The AGN-host galaxy connection: New insights from the extended ionised gas

Bernd Husemann
Astrophysikalisches Institut Potsdam

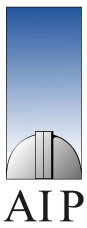

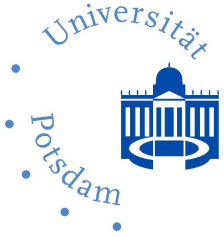

Dissertation
zur Erlangung des akademischen Grades
doctor rerum naturalium (Dr. rer. nat.)
in der Wissenschaftsdisziplin Astrophysik

Eingereicht an der Mathematisch-Naturwissenschaftlichen Fakultät
der Universität Potsdam

31 März 2011

Published online at the
Institutional Repository of the University of Potsdam:
URL http://opus.kobv.de/ubp/volltexte/2011/5555/
URN urn:nbn:de:kobv:517-opus-55556
http://nbn-resolving.de/urn:nbn:de:kobv:517-opus-55556

Contents

Abstract

Active Galactic Nuclei (AGN) are powered by gas accretion onto supermassive Black Holes (BH), that are suspected to reside at the centre of all galaxies with a bulge component. The luminosity of AGN can exceed the integrated luminosity of their host galaxies by orders of magnitude, which are then classified as Quasi-Stellar Objects (QSOs). Some mechanisms are needed to trigger the nuclear activity in galaxies and to feed the nuclei with gas. Among several possibilities, such as gravitational interactions, bar instabilities, and smooth gas accretion from the environment, the dominant process has yet to be identified. Feedback from AGN may be important for the evolution of galaxies, since the BH mass is correlated with several bulge properties and the fraction of AGN among galaxies is the highest for host galaxies with intermediate colours between blue star forming and red quiescent galaxies. Theoretical studies showed that the local galaxy population can be better reproduced assuming that a fraction of the AGN luminosity is transferred onto the host galaxies to suppress star formation or even to expel a large fraction of the gas. However, the details of this coupling between AGN and their host galaxies remain unclear. In this work we aim to investigate the connection between the AGN and their host galaxies by studying the properties of the extendend ionised gas around AGN. Our study is based on observations of ∼50 luminous, low-redshift ($z < 0.3$) QSOs using the novel technique of integral field spectroscopy that combines imaging and spectroscopy. This is the largest dataset of its kind to date. In order to deblend the bright QSO light from the emission of their host galaxies, we develop an efficient algorithm optimised for this observing technique.

After spatially separating the emission of AGN-ionised gas from HII regions, ionised solely by recently formed massive stars, we demonstrate that the specific star formation rates in several disc-dominated AGN hosts are consistent with those of normal star forming galaxies, while others display no detectable star formation activity. Whether the star formation has been actively suppressed in those particular host galaxies by the AGN, or their gas content is intrinsically low, remains an open question. By studying the kinematics of the ionised gas, we find evidence for non-gravitational motions and outflows on kpc scales only in a few objects. The gas kinematics in the majority of objects however indicate a gravitational origin. It suggests that the importance of AGN feedback may have been overrated in theoretical works, at least at low redshifts.

The [OIII] λ5007 line is the strongest optical emission line for AGN-ionised gas, which can be extended over several kpc scales, usually called the Narrow-Line Region (NLR). We perform a systematic investigation of the NLR size and determine a NLR size-luminosity relation of $R_{\rm NLR} \propto L_{\rm [OIII]}^{0.49\pm0.09}$ which is consistent with the scenario of a constant ionisation parameter throughout the NLR. We show that previous narrow-band imaging with the Hubble Space Telescope underestimated the NLR size by a factor of > 2 and that the continuum AGN luminosity is better correlated with the NLR size than the [OIII] luminosity. These affects may account for the different NLR size-luminosity relations reported in previous studies. On the other hand, we do not detect extended NLRs around all QSOs, and demonstrate that the detection of extended NLRs goes along with radio emission. We discuss whether the covering factor for the gas to be illuminated by the AGN radiation is increased by an expanding radio jet due to the expansion and destruction of gas clouds. This may be important for theoretical models of AGN feedback.

We employ emission line ratios as a diagnostic for the abundance of heavy elements in the gas, i.e. its metallicity, and find that the radial metallicity gradients are always flatter than in inactive disc-dominated galaxies. This can be interpreted as evidence for radial gas flows from the outskirts of these galaxies to the nucleus. Recent or ongoing galaxy interactions are likely responsible for this effect and may turn out to be a common prerequisite for QSO activity. The metallicity of bulge-dominated hosts are systematically lower than their disc-dominated counterparts, which we interpret as evidence for minor mergers, supported by our detailed study of the bulge-dominated host of the luminous QSO HE 1029−1401, or smooth gas accretion from the environment. In this line another new discovery is that HE 2158−0107 at $z = 0.218$ is the most metal poor luminous QSO ever observed. The host galaxy is also offset from the BH mass-bulge relations towards a lower stellar mass. Together with a large (30 kpc) extended structure of low metallicity ionised gas, we propose smooth cold gas accretion as the most likely scenario. Theoretical studies suggested that this process is much more important at earlier epochs of the universe, so that HE 2158−0107 might be an ideal laboratory to study this mechanism of galaxy and BH growth at low redshift more detailed in the furture.

Zusammenfassung

Aktive Galaxienkerne (AGN) entstehen durch die Akkretion von Gas auf massive Schwarze Löcher, welche im Zentrum jeder Galaxie mit einer spherodialen Komponente vermutet werden. Die Leuchtkraft eines AGN kann die seiner gesamten Muttergalaxie um Größenordnungen übersteigen. In diesem Fall werden AGN oft als Quasi-Stellare Objekte (Quasare) bezeichnet. Spezielle Mechanismen müssen für das Auslösen dieser Kernaktivität in Galaxien verantwortlich sein. Verschiedene Prozesse wurden bereits identifiziert, aber der entscheidende Mechanismus wurde bisher noch nicht entdeckt. Die Wechselwirkung mit einem AGN könnte außerdem einen entscheidenden Einfluss auf die Entwicklung von Galaxien haben. Ein Anzeichen dafür ist zum Beispiel die starke Korrelation zwischen verschiedenen Eigenschaften von Galaxien mit der Masse ihres zentralen Schwarzen Loches. Theoretische Arbeiten zeigten, dass die Eigenschaften der lokalen Galaxienpopulation oft besser beschrieben werden können, wenn ein Teil der AGN-Leuchtkraft mit ihrer Muttergalaxie wechselwirkt. Es ist noch unklar wie diese Wechselwirkung genau abläuft und ob es die Sternentstehung in Galaxien beeinflusst. In dieser Arbeit studieren wir die Eigenschaften des ausgedehnten ionisierten Gases in AGN-Muttergalaxien, um mögliche Wechselwirkungen zu untersuchen. Wir benutzen dazu eine Stichprobe von ∼50 Quasaren bei geringer Rotverschiebung ($z \sim 0.3$), die mit der neuartigen Technik der Integralfeld-Spektroskopie beobachtet wurden. Diese Technik kombiniert bildgebende und spektroskopische Verfahren.

Wir können mit unserer Analyse zeigen, dass die spezifische Sternentstehungsrate in einigen Scheiben-dominierten AGN-Muttergalaxien vergleichbar mit denen von normalen Galaxien ohne Kernaktivität ist. Allerdings können wir in einigen AGN-Muttergalaxien keine Anzeichen von Sternentstehung feststellen. Ob Sternentstehung in diesen Galaxien momentan durch die Wechselwirkung mit dem AGN unterdrückt wird, ist daher nicht eindeutig. Hinweise auf Gasausflüsse liefert die Kinematik des ionisierten Gases für einige wenige Objekte, doch die Kinematik für die meisten AGN-Muttergalaxien kann allein durch das Wirken der Gravitation erklärt werden. Daraus schließen wir, dass der Einfluss von AGN auf ihre Muttergalaxien geringer sein könnte als theoretisch angenommen wird.

Die [OIII] λ5007 Emissionslinie ist die stärkste optische Linie für AGN-ionisiertes Gas und kann sich über eine Region von mehreren kpc vom Kern erstrecken, die als "Narrow-Line Region" (NLR) bezeichnet wird. Durch eine systematische Untersuchung der NLR-Ausdehnung können wir eine Beziehung zwischen NLR-Radius und AGN-Leuchtkraft bestimmen, $R_{\mathrm{NLR}} \propto L_{[\mathrm{OIII}]}^{0.49\pm0.09}$. Diese Relation ist konsistent mit einem konstanten Ionisationsparameter, das Verhältnis zwischen ionisierenden Photonen und neutralem Wasserstoff, über die gesamte Ausdehnung der NLR. Frühere Studien mit dem Hubble Weltraumteleskop unterschätzten die Größe der NLR um mehr als einen Faktor 2. Andererseits können wir nicht für alle Quasare eine ausgedehnte NLR nachweisen, wobei eine NLR-Detektion bei einer höheren Radioleuchtkraft des Quasars wahrscheinlicher ist. Dies deutet auf eine Wechselwirkung eines Radio-Jets mit dem kernumgebenden Gas hin und könnte für eine theoretische Betrachtung der Wechselwirkung von AGN mit ihrer Umgebung von Wichtigkeit sein.

Wir benutzen Emissionslinien des ionisierten Gases, um den Anteil von schweren Elementen im Gas, die so genannte Metallizität, zu bestimmen. Dabei finden wir, dass die radialen Metallizitätsgradienten in Scheiben-dominierten AGN-Muttergalaxien deutlich flacher sind als in vergleichbaren Galaxien ohne Kernaktivität, was wir als Anzeichen für radialen Gastransport vom Rand der Galaxien zum Kern interpretieren. Dies könnte durch kürzliche oder immernoch andauernde gravitative Wechselwirkungen zwischen Nachbargalaxien entstanden sein und stellt eventuell eine Voraussetzung für Kernaktivität dar. Sehr interessant ist unser Ergebnis, dass die Spheroid-dominierten AGN-Muttergalaxien eine geringere Metallizität aufweisen als die Scheiben-dominierten Galaxien. Dies könnte z.B. durch das Verschmelzen mit kleinen Nachbargalaxien induziert werden, welche eine intrinsisch geringe Metallizität aufweisen. Am Beispiel der elliptischen Muttergalaxie des Quasars HE 1029−1401 können wir durch eine detaillierte Analyse des ionisierten Gases verschiedene Indizien für einen solchen Prozess nachweisen. Eine weiteres Resultat dieser Arbeit ist die Entdeckung eines leuchtkräftigen Quasars mit der geringsten Metallizität, die bisher für solche Objekte nachgewiesen werden konnte. Die Muttergalaxie hat eine geringere Masse als sie von der beobachteten Relation zwischen den Massen von Schwarzen Löchern und den Massen der Muttergalaxien erwartet würde. Wir interpretieren die geringe Metallizität und die Ausdehnung des ionisierten Gases über 30 kpc als deutliche Indizien für die Akkretion von intergalaktischem Gas. Dieser Prozess findet viel häufiger im frühen Universum statt. HE 2158−0107 könnte daher ein ideales Objekt sein, um diesen Prozess im nahen Universum detaillierter studieren zu können.

Chapter 1

Introduction

B. Husemann

ABSTRACT

Active Galactic Nuclei (AGN) have been intensively studied over the last decades. They provided the first evidence for the existence of Super Massive Black Holes (SMBH) at the centre of galaxies. Initially, the prime focus of research was to understand the accretion of matter onto the SMBH and the details in the structure of AGN to explain the various observational signatures in the entire electromagnetic spectrum. Although those issues have not been solved completely and continue to be deeply studied, the main area of AGN research has shifted towards the understanding of how AGN couple to their host galaxies and influence the evolution of each other.
This short introduction should provide the scientific framework for the work presented in this thesis. A comprehensive review of the entire field of AGN research should not be expected since we try to provide a concise overview of the most relevant topics for our investigation including some general background. The introduction features a brief outline of the AGN phenomenon, our current knowledge about the link to their host galaxies and outline the efforts to resolve these question by studying the warm-ionised gas surrounding AGN on host galaxy scales and beyond.

1.1. Active Galactic Nuclei

1.1.1. Types of Active Galactic Nuclei and their unification

Several distinct types of Active Galactic Nuclei (AGN) have historically been defined depending on the used spectral passband at their discovery. As the first class of AGN, Seyfert galaxies were identified from optical spectroscopy and divided into Seyfert 1 and Seyfert 2 galaxies according to their different nuclear spectra (Seyfert 1943). Seyfert 1's display broad permitted emission lines with a Full Width at Half Maximum (FWHM) greater than $2000\,\mathrm{km\,s^{-1}}$ in addition to highly ionised, narrow forbidden emission lines (FWHM smaller than $1000\,\mathrm{km\,s^{-1}}$) and an underlying non-stellar power-law continuum contribution. In contrast, Seyfert 2's lack the broad emission lines and the power-law continuum typical for Seyfert 1 nuclei. A small fraction of Seyfert's were found to have characteristics of both types, so that intermediate classes were additionally introduced later on.

The first radio surveys detected strong extragalactic radio sources, which are now know to originate from powerful relativistic jets. Depending on whether the jets could be associated with galaxies or appeared to originate from bright point-like sources with Seyfert 1 characteristics, those objects were called radio galaxies or quasi-stellar radio sources (quasars), respectively. Similar point-like objects in the optical without associated radio emission were subsequently detected and termed Quasi-Stellar Objects (QSOs). Since QSOs and quasars were measured from their redshifts to be of extragalactic origin and their underlying host galaxies could be recovered, they have been considered as higher luminosity analogs of Seyfert 1 galaxies (Kristian 1973).

Considering the variability of the nuclear emission on timescales of days to years and the required energy to account for the luminosity, accretion onto Super Massive Black Holes (SMBHs), or short Black Holes (BHs), were identified as the only viable powering mechanism for the AGN phenomenon. The Unified Model of AGN (Barthel 1989; Antonucci 1993) tries to explain most of the different AGN types by introducing an optically thick torus of gas and dust around an accreting BH. Depending on the inclination of the torus with respect to our line of sight, the torus obscures the accretion disc and the ionised gas clouds of the Broad-Line Region (BLR), while the Narrow-Line Region (NLR) at larger distances remains unobscured, which results in the observational distinction between Seyfert 1 and 2 galaxies as well as between quasars and radio galaxies. Throughout this work we will thus only distinguish between type 1 (or unobscured) AGN on the one hand and type 2 (or obscured) AGN on the other hand. Since the presence of an evolved radio jet is an additional property of AGN within the inclination-dependent framework, we will use the terms Radio Loud (RL) and Radio Quiet (RQ) to specify their radio properties. In order to emphasise a high optical luminosity of an AGN, we will refer to it as a QSO[1], always corresponding to a type 1 QSO if not specified otherwise.

Although the basic Unified Model of AGN has been quite successful, it is probably simplified in some aspects so that several modification and refinements were proposed, of which we want to highlight a few. In the "receding torus" model (Lawrence 1991), the dust sublimation temperature defines the inner radius of the torus, which is increasing with AGN luminosity and introduces a luminosity-dependent covering factor of the torus. Furthermore, the distribution of gas and dust in the torus is most likely clumpy and not homogeneous (Krolik & Begelman 1988) because the required velocities to support the structure imply either gas temperatures above dust sublimation or supersonic speeds of almost collisionless gas streams of a clumpy medium. Indeed, interferometric observations in the mid-infrared were able to resolve the dusty torus in the Circinus galaxy and found

[1] The term QSO and quasars have often been synonymously used in this sense independent of their radio properties.

evidence for a clumpy distribution (Tristram et al. 2007). On the other hand, it is still an ongoing discussion how the environment of the galaxy affects the type of AGN. An evolutionary connection between ultraluminous infrared galaxies (ULIRGs), which are ongoing gas-rich major mergers, and luminous QSOs was proposed (Sanders et al. 1988; Canalizo & Stockton 2001). The idea is that an AGN is fuelled during the merger, but obscured by the large amount of gas and dust. As star formation decays, the AGN becomes unobscured after it sheds its dust cocoon and appears as a type 1 QSO.

1.1.2. Radio emission from AGN

RL AGN usually stand out through their intense radio emission, which was identified to be synchrotron radiation of relativistic particles in powerful jets reaching out to 1 Mpc distance from the AGN. Depending on the morphology and luminosity of the large scale radio structures, they were classified into two different types. The radio emission is edge-darkened/lobe-dominated for Fanaroff-Riley Class I and edge-brightened/core-dominated for Fanaroff-Riley Class II objects. Because the characteristic spectral slope of the radio power-law continuum $f_\nu \propto \nu^{\alpha_r}$ is steeper for lobe-dominated sources, RL AGN were alternatively divided into steep and flat spectrum radio sources at a radio spectral index of $\alpha_r = -0.5$.

In order to homogeneously characterise the RL AGN population, two different criteria have been commonly used in the literature to distinguish between RL and RQ objects. The rest-frame radio-to-optical flux density ratio $R = f_\nu(6\,\mathrm{cm})/f_\nu(4400\,\text{Å})$ was defined for type 1 AGN, where $R > 10$ correspond to RL AGN and $R < 1$ to RQ AGN (e.g. Kellermann et al. 1989). Alternatively, the total radio luminosity has been used to define a minimum luminosity for RL AGN, e.g. $P(1.4\,\mathrm{GHz}) > 10^{23}\,\mathrm{W\,Hz^{-1}}$ (Best et al. 2005), which is applicable also for type 2 AGN. However, the selected RL AGN sample are not directly comparable, because only 20% of the RL AGN selected with the latter criterion would be classified as such based on the R parameter (Rafter et al. 2009). In any case, the fraction of RL QSOs (RLQs) in optically-selected low-redshift samples is only 10–20% (Kellermann et al. 1989; Urry & Padovani 1995; Ivezić et al. 2002) and decreases further with increasing redshift and AGN luminosity (Jiang et al. 2007). Whether the population of RLQs and radio-quiet QSOs (RQQ) are actually bimodal in nature (Kellermann et al. 1989; Miller et al. 1990) or rather a result of selection effects (Cirasuolo et al. 2003; White et al. 2007) remains an ongoing discussion.

The majority of QSOs are classified as RQQs, the origin of their faint radio emission is not yet well understood. Radio emission originating from ongoing star formation in the host galaxy could potentially contribute. Considering a typical RQQs at $z = 0.15$, e.g. PG 0052+251, with a *total* radio flux of $f_\nu(1.4\,GHz) = 7.1$ mJy. This radio emission would correspond to an ongoing star formation rate (SFR) of more than $200\,\mathrm{M_\odot\,yr^{-1}}$ adopting the SFR-radio calibration of (Bell et al. 2003). Since the far-IR emission, another independent SFR tracer, often implies lower ongoing SFRs, other processes than star formation must significantly contribute to radio emission even for RQQs. The radio emission could be spatially resolved in several RQQs on sub-arcsecond scales (Kukula et al. 1995; Leipski et al. 2006). It often displays distinct radio hotspots, indicating low-power jets. The morphology of their radio structure resembles those of small-scale jets that are commonly detected in the nuclei of nearby Seyfert nuclei (e.g. Ulvestad & Wilson 1989; Falcke et al. 1998; Kinney et al. 2000; Ulvestad & Ho 2001). On the other hand, the radio emission was found to be still unresolved for a significant fraction of RQQs even at milliarcsecond resolution (Ulvestad et al. 2005), which questions the existence of a radio jet in these sources. Laor & Behar (2008) therefore suggested that the radio emission is produced by magnetically heated AGN coronae. This interpretation differs from the standard interpretation of the correlation between X-ray and radio luminosity (Merloni et al. 2003; Falcke et al. 2004; Panessa et al. 2007), which is usually thought to be the result of an intimate coupling between the hot corona of the accretion disc and the ejection of relativistic particles.

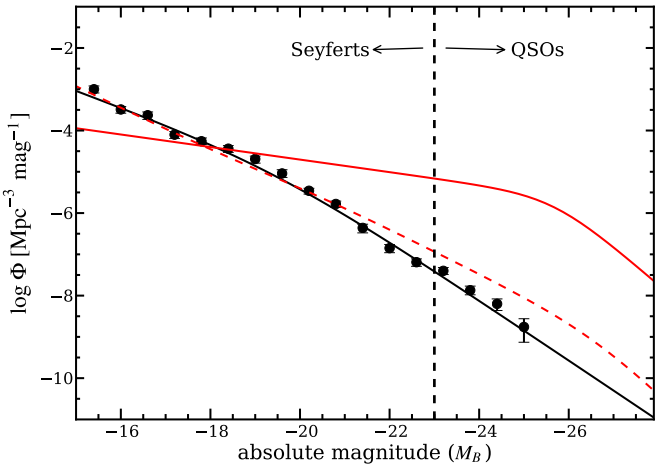

Fig. 1.1. The local AGN luminosity function. Black solid points correspond to the combined HES+SDSS AGN LF at $z = 0$ (Schulze et al. 2009). The black solid line represents the best-fit double power-law model to that LF. For comparison, the model to the AGN LF at $z = 1.5$ (Croom et al. 2009) is indicated by the red solid line, which was extrapolated toward $z = 0$ assuming a luminosity dependent density evolution (LDDE) model (red dashed line). The division line between QSO and Seyfert galaxies has typically been set at $M_V \sim -23$ being highlighted by the vertical dashed line.

1.1.3. AGN population demographics

With the advent of large photometric and spectroscopic surveys, like the Hamburg-ESO Survey (HES, Wisotzki et al. 1996), the Sloan Digital Sky Survey (SDSS, York et al. 2000) and the 2dF/6dF QSO Redshift survey, complete samples of AGN could be constructed to characterise the AGN population as a whole and its evolution over cosmic time.

The local type 1 AGN luminosity function (LF) was most recently presented by Schulze et al. (2009) as a combination of the AGN samples from HES and SDSS (Fig. 1.1). Obviously, the number density of AGN is steeply declining with increasing luminosity, and can be well described by a double power-law function. A commonly used division in luminosity between QSOs and Seyferts was arbitrarily set at an absolute magnitude of $M_B = -23$ (for $H_0 = 50\mathrm{km\,s^{-1}}$ Mpc, e.g. Schmidt & Green 1983). This means that QSOs are rather rare objects and vastly outnumbered by Seyfert galaxies in the present universe. The AGN LF at higher redshifts $z \sim 2$ (e.g. Bongiorno et al. 2007; Croom et al. 2009) indicates that QSOs were much more abundant at earlier epochs, while the space density of Seyfert galax-

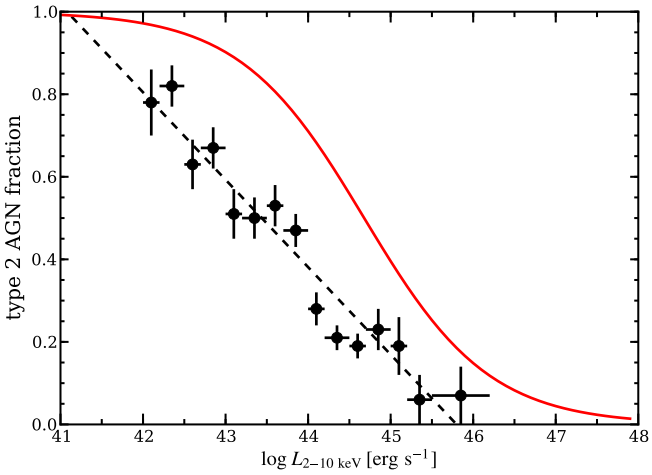

Fig. 1.2. Fraction of type 2 AGN as a function of hard X-ray (2-10 keV) luminosity. Black symbols are measurements from Hasinger (2008) based on all X-ray selected AGN with available optical identification. The dashed line is a linear fit to the data, which should saturate at an obscured fraction of either 1 and 0. The red solid line shows a model of the type 2 AGN fraction inferred from MIR observations by Maiolino et al. (2007) assuming a physically motivated luminosity dependence.

ies appears to be roughly unchanged. This phenomenon is frequently referred to as "AGN cosmic downsizing".

In order to characterise the ratio of obscured and unobscured AGN, comparable and homogeneous samples of both AGN types need to be constructed. X-ray selected samples are well suited for this task, because hard X-rays penetrate the obscuring material even for optically classified type 2 AGN unless the absorption becomes Compton-thick at column densities above $> 10^{24}$ cm^{-2}. Ueda et al. (2003) and Steffen et al. (2003) independently found a decreasing type 1 AGN fraction with increasing X-ray luminosity based on X-ray selected AGN samples. Figure 1.2 shows the latest results from Hasinger (2008), who combined all available X-ray AGN samples comprising more than 1200 AGN detected in the hard X-ray band (2-10 keV). The decrease of the type 1 AGN fraction is qualitatively in agreement with independent results by Maiolino et al. (2007) from AGN observations in the mid-IR with *Spitzer* at a rest-frame wavelength of 6.7μm. The IR emission in that passband is assumed to directly trace the AGN-heated dust as a diagnostic for the dust covering fraction via the thermal IR to the primary AGN radiation ratio. Both observations provide strong evidence for the receding torus model that most likely complements the Unified Model of AGN. Furthermore, it implies that type 2 QSOs become increasingly scarce at higher luminosities and are difficult to find. A sample of 291 luminous type 2 QSOs could be identified by Zakamska et al. (2003) from the SDSS at $0.3 < z < 0.84$, which allow to study the host galaxy properties of luminous QSOs without the problem of being blended with the bright nuclear points source.

Most of the massive galaxies at $z = 0$ probably host a SMBH in their bulges and are therefore potential AGN. The AGN fraction among galaxies is thus physically important for our understanding of the AGN phenomenon itself. Kauffmann et al. (2003a) employed the large spectroscopic and photometric dataset of the SDSS to study the fraction of type 2 AGN among the galaxy population with unprecedented detail. One of their main results is that the AGN fraction strongly depends on the stellar mass of the host. Although ~85% of galaxies with stellar masses of $M_* < 10^{10}$M$_\odot$ have detectable emission-lines only a few percent could be classified as AGN. Contrary, 80% of emission-line galaxies with $M_* > 10^{11}$M$_\odot$ were classified as AGN. The overall fraction of detected AGN peaks around $M_* \sim 10^{11}$M$_\odot$ with a maximum of about 30% due to a general decrease in the fraction of emission-line galaxy at higher stellar masses. These numbers are likely to be lower limits, because the nuclear spectrum of the galaxies might be diluted by emission-lines from star forming regions within the 3″ aperture of the SDSS fibres. For comparison, Ho et al. (1997) inferred an active fraction of 43% in their entire sample of 420 emission-line galaxies, though it includes a substantial fraction of very low luminosity AGN.

1.1.4. AGN properties from type 1 AGN spectra

The spectrum of type 1 AGN offers important diagnostic tools to infer the properties in the very circumnuclear region, since the light of the accretion disc and the emission-lines of the BLR are strongly affected by obscuring material. For example, the radius of the BLR (R_{BLR}) can be estimated from the time lag between luminosity variation of the BLR and the continuum, known as the reverberation mapping technique (Blandford & McKee 1982). A tight correlation between R_{BLR} and the continuum luminosity (e.g. L_{5100} at 5100Å) could be established in this way, for which the latest results by Bentz et al. (2009) imply a relation of the form

$$\log\left(\frac{R_{\mathrm{BLR}}}{\mathrm{lt-days}}\right) = (0.52\pm0.06)\log\left(\frac{L_{5100}}{10^{44}\,\mathrm{erg\,s^{-1}}}\right)+(1.58\pm2.9) \quad (1.1)$$

The slope of this relation is consistent with naïve expectations when all AGN have a similar ionising spectrum, similar ionisation parameter and gas densities in the BLR region. Considering the definition of the ionisation parameter U,

$$U = \frac{Q(\mathrm{H})}{4\pi r^2 c n_{\mathrm{e}}}\,, \quad (1.2)$$

where $Q(H)$ is the number of ionising photons above 13.6 eV per second from the ionising source, c is the speed of light and n_{e} is the electron density of the medium. Rearranging the definition of U results in

$$r = \left(\frac{Q(\mathrm{H})}{4\pi c n_{\mathrm{e}} U}\right)^{0.5} \propto Q(\mathrm{H})^{0.5}\,. \quad (1.3)$$

This relation can be turned into a dependence with luminosity,

$$r \propto L^{0.5}\,, \quad (1.4)$$

if the shape of the ionising continuum is independent of the luminosity.

The BLR radius-luminosity relation can be complemented with the assumption of virialised BLR clouds, so that the width of the broad lines, in particular Hβ, and the continuum luminosity of the type 1 AGN spectrum is sufficient to obtain a BH mass estimate. Despite the fact that the geometry and kinematics of the BLR are currently uncertain and the host galaxy light may contaminate the AGN continuum, the "virial" method (e.g. Wandel et al. 1999; Vestergaard 2002) became a standard technique. It is particularly important to homogeneously estimate BH masses for large spectroscopic AGN samples where direct measurements based on gas or stellar kinematics cannot be obtained.

Other properties of type 1 AGN spectra were investigated by Boroson & Green (1992) by means of a principal component analysis on various QSO parameters, like emission line widths and line fluxes. These authors found that most of the variance among the parameters can be expressed with only a few principal vectors in the parameter space. The strongest one is known as "Eigenvector 1", which represents an anti-correlation between the Fe II emission-line strength and the [O III] λ5007 (hereafter [O III]) emission-line strength (either luminosity or peak height) as well as a correlation between [O III] strength and the FWHM of the broad Hβ line. The same behaviour was noticed by Yip et al. (2004) from the Eigenspectra of a large sample of SDSS QSO spectra. Eigenvector 1 is also implicitly linked with the radio luminosity due to a correlation between [O III] and radio luminosity (e.g. Miller et al. 1993). The main physical driver for those correlations, which imply a physical connection between BLR and NLR properties, has not been identified yet. Initial speculations that the [O III] emission may be anisotropic and orientation dependent could not be confirmed due to a correlation with the orientation-independent [O II] $\lambda\lambda$3727, 3729 lines (Kuraszkiewicz et al. 2000). Instead, Boroson (2002) suggested that BH mass and Eddington ratio are the main driver for Eigenvector 1, but this does not provide a physically meaningful answer.

Hu et al. (2008) systematically studied the redshift and line width of the Fe II emission in type 1 SDSS QSOs and found that those lines are, on average, narrower and red-shifted with respect to the broad Hβ line. Thus, they claim that broad Fe II emission originates from a different region, likely exterior to the Hβ emitting region of the BLR and that the Fe II emitting clouds are flowing inwards to the nucleus. Since the Fe II strength was found to correlate with the Eddington ratio, substantial shielding of the clouds would be required to prevent them from being pushed away. Indeed, a positive correlation between Fe II column density and Eddington ratio was reported by Sameshima et al. (2011), who proposed that an increasing fraction of ionising photons could be absorbed by those large column density clouds before they reach the NLR. This is qualitatively in agreement with the fact that the covering factor of the NLR was identified to be the main driver for the [O III] line strength (Baskin & Laor 2005) and might physically explain the correlation imprinted in Eigenvector 1.

1.2. AGN host galaxies

1.2.1. Triggering of AGN activity

A long standing question in the research of AGN is to identify the physical process(es) that actually ignite the AGN activity in galaxies. Due to the conservation of angular momentum, no gas would be able to sink towards the central SMBH, if the host galaxy is a completely relaxed system. Gravitational torques or instabilities are therefore required to funnel gas towards the galaxy centre. How the accretion disc of an AGN is locally fuelled and whether this process is triggered by an external event on galaxy scales are two related, but independent questions in that respect. AGN cover several order of magnitude in bolometric luminosities from $L_{\rm bol} = 10^{41}\,{\rm erg\,s^{-1}}$ for low-luminosity AGN up to $L_{\rm bol} = 10^{48}\,{\rm erg\,s^{-1}}$ for the most luminous QSOs, which corresponds to mass accretion rates of $\dot{M}_{\rm BH} = 10^{-5}\,{\rm M_\odot yr^{-1}}$ and $\dot{M}_{\rm BH} = 100\,{\rm M_\odot yr^{-1}}$, respectively, assuming a canonical radiative efficiency of 10%. Because the matter accretion rate spans several orders of magnitude, various mechanisms are certainly allowed that provide the required fuel over the AGN duty cycle.

While secular processes, such as large-scale bars and instabilities in disc galaxies, have been proposed to trigger low-luminosity AGN, more violent triggering events may be required to achieve the high mass accretion rate for QSO activity. Major mergers have therefore attracted much attention, because lots of gas is transported towards the nucleus by the imposed gravitational torques during the interaction as highlighted by numerical simulations (e.g Barnes & Hernquist 1991; Mihos & Hernquist 1996). In fact, ongoing major mergers or post-merger features were frequently associated with QSO activity (e.g. Stockton 1982; Hutchings et al. 1984; Hutchings & Neff 1992) that gained strength after the evolutionary connection between ULRIGs and QSO was proposed. The major-merger hypothesis has come into question, since a considerable number of low-redshift QSOs could be associated with undisturbed disc galaxies or rather smooth ellipticals (McLure et al. 1999; Dunlop et al. 2003; Floyd et al. 2004). However, deeper images of elliptical QSO hosts revealed low surface brightness features (Bennert et al. 2008). These structure were interpreted as evidence for past galaxy interactions either minor companions being tidally disrupted or a major merger event.

One caveat of most of those morphological studies was that no control sample of inactive galaxies could be used to statistically compare the morphological merger signatures, of which Dunlop et al. (2003) and Sánchez et al. (2004) stand out as positive exceptions. Recently, a comprehensive morphological study of X-ray selected AGN hosts at $z \sim 1$ was presented by Cisternas et al. (2011) in relation to a statistically matched control sample. They found that more than 85% of AGN hosts do not display strong distortion indicative of major mergers and that no statistically significant difference in the fraction of distortions exists between inactive and active galaxies. Thus, their conclusions was that secular evolution processes or minor mergers, as opposed to major mergers, play the leading role in triggering episodes of high BH accretion. This is supported by the results of Reichard et al. (2009), which indicate that the most luminous AGN are preferentially found in lopsided galaxies. A similar result has been obtained for local elliptical radio galaxies in comparison to their inactive population (Tal et al. 2009), though two different modes of BH accretion (cold vs. hot) in radio galaxies possibly need to be distinguished concerning their merger signatures (Ramos Almeida et al. 2010).

Another powerful tool for quantifying the role of galaxy interactions in triggering AGN activity is to statistically compare the properties of paired and isolated galaxies in large samples (Barton et al. 2000; Alonso et al. 2007; Woods & Geller 2007; Li et al. 2008; Ellison et al. 2008; Rogers et al. 2009). All those studies consistently found that the star formation in galaxy pairs is significantly enhanced compared to isolated objects which is in line with theory and simulations. On the other hand, the results on the AGN fraction were controversial. While most studies found no or only a small enhancement in the AGN fraction, Woods & Geller (2007) found a higher AGN fraction in paired galaxies with respect to their control sample. Focussing in particular on early-type galaxies, Rogers et al. (2009) reported that the AGN fraction increases for apparently interacting galaxies. From all these studies a common scenario emerged in which (minor) galaxy interaction mainly trigger AGN activity, but slightly delayed up to several 100 Myr after the peak of star formation. In any case, gas at large galactic radii is driven towards the nucleus during the interaction which systematically dilutes the central gas-phase metallicity (Ellison et al. 2008), which could poten-

tially be used to track inflow of low-metallicity gas within the galaxy using spatially resolved data.

A further step to investigate how the accretion disc is actually fuelled is to directly study the distribution and dynamics of the gas in the very circumnuclear region. This is observationally challenging given the small physical scales and because the optical emission lines probe only the ionised gas phase which may be subject to an outflow induced by radio-jet coupling or AGN radiation pressure. Recent near-IR Integral Field Unit (IFU) observations highlighted their ability to disentangle the kinematics of molecular and ionised gas down to 30 pc scales in the nearest Seyfert galaxies (Riffel et al. 2008, 2010; Hicks et al. 2009). These new observations provide the first glimpse on a molecular gas disc with a radius of < 100 pc that possibly feeds the BH accretion disc and circumnuclear star formation.

1.2.2. BH mass-bulge relationships

Using the first determinations of accurate dynamical BH masses for local inactive galaxies, Kormendy & Richstone (1995) and Magorrian et al. (1998) found evidence for a correlation between BH mass ($M_{\rm BH}$) and bulge luminosity ($L_{\rm bulge}$) of the host galaxy. Since then, numerous studies have confirmed these results with increasing accuracy and another tight correlation with the stellar velocity dispersion σ_* of the bulge was discovered by Ferrarese & Merritt (2000) and Gebhardt et al. (2000). The $M_{\rm BH}$-σ_* appears to have the lowest scatter compared to the others with a best-fit relation of

$$\left(\frac{M_{\rm BH}}{10^8 {\rm M}_\odot}\right) = (1.32 \pm 0.18) \times \left(\frac{\sigma_*}{200\,{\rm km\,s^{-1}}}\right)^{4.24\pm0.41} \quad (1.5)$$

as most recently determined by Gültekin et al. (2009), which is consistent with a $M_{\rm BH} \propto \sigma_*^4$ dependence. Figure 1.3 highlights that the scatter in the $M_{\rm BH}$-σ_* is larger than the measurement errors, which implies a significant contribution of intrinsic scatter ("cosmic scatter") to the relation. Gültekin et al. (2009) quantified the intrinsic scatter to be 0.44 dex for the entire sample, but slightly lower for elliptical galaxies and higher for spiral galaxies, respectively. Only the $M_{\rm BH}$-$L_{\rm bulge}$ relation at near-IR luminosities were found to have a comparable scatter (Marconi & Hunt 2003) with a best-fit relation of

$$\left(\frac{M_{\rm BH}}{10^8 {\rm M}_\odot}\right) = (2.80 \pm 0.49) \times \left(\frac{L_{\rm H,bul}}{10^{11}\,{\rm L}_\odot}\right)^{1.16\pm0.12} . \quad (1.6)$$

The lower scatter compared to relations using optical passbands can be explained by the lower sensitivity of the near-IR mass-to-light ratios to actual star formation history of the stellar population.

Currently, the common interpretation of the emergence of all these BH-bulge relations is that the evolution of BHs and bulges are intimately linked (e.g. Kauffmann & Haehnelt 2000; Wyithe & Loeb 2003; Hopkins et al. 2007; Somerville et al. 2008). In the co-evolution picture, every episode of bulge growth, due to mergers and star formation, is accompanied by a self-regulated growth of the SMBH for which AGN feedback processes are thought to be responsible. An alternative option has been pointed out by Peng (2007), who used a thought experiment to show that the BH mass and bulge mass distributions will converge to a certain correlation after a sufficiently long sequence of galaxy mergers, even when they were initially uncorrelated. Jahnke & Macciò (2011) recently confirmed with dedicated simulations

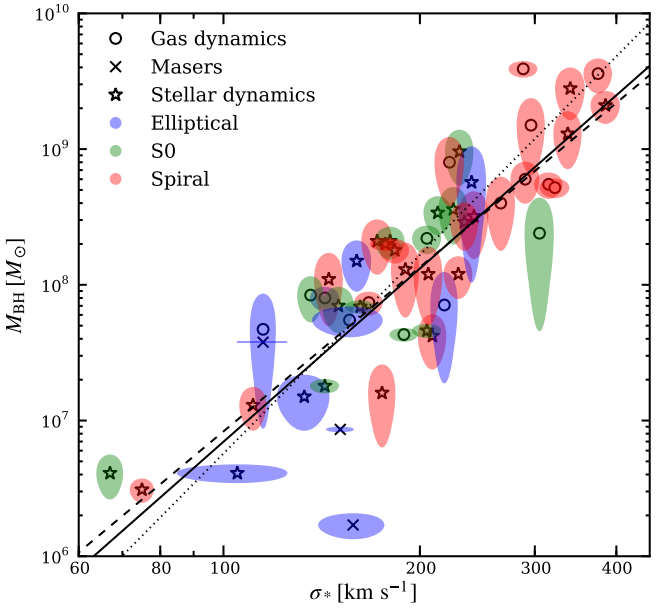

Fig. 1.3. The $M_{\rm BH}$-σ_* relation for galaxies with dynamical $M_{\rm BH}$ measurements. Data and figure style were adapted from Gültekin et al. (2009). Different techniques for BH mass measurements are indicated by the symbols: gas dynamical modelling (*open circles*), stellar dynamical modelling (*open stars*), masers (*crosses*). The corresponding errors are indicated by the coloured ellipses, where the colour represent the Hubble type of the host galaxy: elliptical (*red*), S0 (*green*), spiral (*blue*). The solid line marks the best-fit relation (Eq. 1.5) of Gültekin et al. (2009). In comparison are also shown the relation reported by Tremaine et al. (2002) (dashed line) and Ferrarese & Ford (2005) (dotted line).

that a tight $M_{\rm BH}$-$M_{\rm bulge}$ relation can indeed be established at redshift $z = 0$ by this simple process within the framework of a Λ-dominated cold dark matter (ΛCDM) cosmology. Nevertheless, physical processes, such as star formation, BH accretion and feedback processes, may well play an important role in shaping the BH-bulge relation and possibly lead to the observed intrinsic scatter of the relation.

The evolution of the BH-bulge relations with cosmic time is therefore subject to intense investigation in order to understand the nature of the apparent linkage between BHs and their hosts and how it is established. Because the measurement of BH masses *simultaneously* with host properties remains challenging at high redshifts, no consistent picture has emerged yet. Direct kinematic BH mass measurements are only possible for local galaxies, so that mainly type 1 AGN are used to estimate $M_{\rm BH}$ from their spectra which introduces the burden to recover their bulge properties from the AGN-contaminated host light. Several groups have tackled this problem at various redshifts with different techniques, for example by recovering σ_* in the spectra of low-redshift ($z \leq 0.6$) low-luminosity type 1 AGN (Woo et al. 2006, 2008), using the line dispersion of [O III] as a surrogate for σ_* (Shields et al. 2003; Salviander et al. 2007), or using high spatial resolution optical/near-IR broad-band imaging to deblend AGN and host light (e.g. Schramm et al. 2008; Jahnke et al. 2009; Merloni et al. 2010), which can be further aided by magnification due to gravitational lensing (Peng et al. 2006). Most of these studies found that the mean $M_{\rm BH}/M_{\rm bulge}$ ratio increases with redshift/lookback time implying a more rapid

growth of SMBH at early epochs, but also no evolution with redshift was reported (Shields et al. 2003).

One additional difficulty in the interpretation of those results is a particular selection bias for QSOs at high redshifts (Lauer et al. 2007). Because only the brightest QSOs with the most massive BHs can be detected at high redshifts at a given flux limit, the probability of their hosts to be less massive galaxies than the mean is significantly higher due to the steeply decreasing galaxy mass function combined with the cosmic scatter in the BH-bulge relation. To infer the value of the cosmic scatter and understand its origin, observationally and theoretically, is therefore essential to properly take this bias into account when interpreting the observations at various redshifts.

1.2.3. AGN hosts in transition from the blue cloud to the red sequence?

A striking feature in the overall galaxy population is its apparent bimodality. In the colour-magnitude diagram (CMD), a blue cloud of galaxies is well separated from the population of luminous red galaxies forming a well defined red sequence. For the galaxy sample constructed from SDSS, Kauffmann et al. (2003b) investigated a more physical version of the CMD. They replaced the colour with the age-sensitive $D_n(4000)$ index (the Balmer break strength) and the dust-corrected absolute magnitude with the stellar mass of the host using individually determined mass-to-light ratios based on the $D_n(4000)$ index and the strength of the Balmer absorption ($H\delta_A$). Figure 1.4 shows that blue cloud galaxies are young systems with recent or ongoing star formation, while the red sequence constitutes of old galaxies that are known to be ellipticals or bulge-dominated/early-type galaxies. This bimodality in the CMD of galaxies has been found to exist already at $z \leq 2.5$ (Franzetti et al. 2007; Cassata et al. 2008; Brammer et al. 2009). However, the number of galaxies on the red sequence and their stellar mass density rose by about a factor of 2 from $z \simeq 1$ to $z = 0$, whereas the number and stellar mass density of blue galaxies remained roughly constant (Bell et al. 2004; Arnouts et al. 2007). This has been interpreted as a continuous build-up of the red sequence population over cosmic time via the truncation of star formation in blue cloud galaxies, while early-type galaxies within the red sequence may grow further by gas-poor ("dry") mergers leading to their well-defined colour-magnitude relation (e.g. Skelton et al. 2009).

In order to place AGN hosts within the emerging framework of the entire galaxy population, a cornerstone result was achieved by Kauffmann et al. (2003a). They statistically compared type 2 AGN hosts and inactive galaxies in SDSS using $D_n(4000)$ as the stellar age indicator. Despite the problem of possible SDSS aperture biasses, they found that type 2 AGN hosts generically exhibit younger stellar populations with respect to inactive galaxies at least over several kpc. That result extended the previously known nuclear-starburst phenomenon in type 2 AGN (Schmitt et al. 1999; González Delgado et al. 2001; Cid Fernandes et al. 2004; Wild et al. 2007) to recent star formation episode on scale of the entire galaxy. In fact, Kauffmann et al. (2007) showed that AGN were almost always associated with a blue extended disc based on *GALEX* near-UV light profiles, which is difficult to explain with either secular evolution scenarios or strong galaxy interactions. Due to their young stellar population mixed with an ancient population of stars, AGN hosts appear to be preferentially located in between the blue cloud and the red sequence (Fig. 1.4). Subsequent studies consistently found that the AGN fraction among galaxies is the highest in that so-called "green valley" of the CMD (Martin et al. 2007; Salim et al. 2007; Silverman et al. 2008). After carefully deblending the nucleus and host emission for type 1 AGN, the colours of bulge-dominated host were similarly found to be significantly bluer than their inactive counterparts (Jahnke et al. 2004; Sánchez et al. 2004).

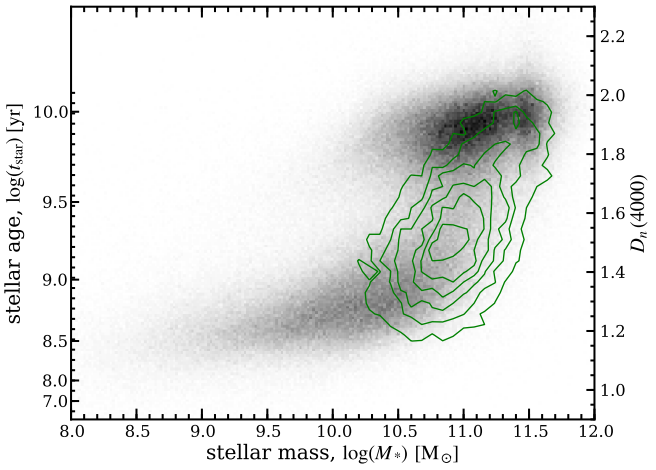

Fig. 1.4. Distribution of galaxies in the stellar age vs. stellar mass plane. The data were taken from the SDSS DR7 value-added MPA/JHU galaxy catalogue (*http://www.mpa-garching.mpg.de/SDSS/*) containing more than 600 000 galaxies and more than 100 000 AGN. The 2D histogram of non-AGN galaxies is shown as the grey scale image highlighting the bimodality of the galaxy population. The overplotted green countours correspond to the distribution of the luminous AGN population, for which the AGN fraction among the galaxies is the highest in the region between the two branches of the bimodal galaxy population.

The high fraction of AGN hosts in the green valley, combined with the assumption that mergers are their main triggering mechanism, leads to a scenario in which AGN are the driver for the rapid migration of galaxies from the blue cloud to the red sequence (top panel of Fig. 1.5) due to AGN related quenching of star formation (e.g. Faber et al. 2007; Nandra et al. 2007). The timescale for the shutdown of star formation was estimated to be of the order of 100–500 Myr (Schawinski et al. 2009; Wild et al. 2010), which was shown to be faster than can be explained by gas depletion from star formation alone (Kaviraj et al. 2010). On the other hand, semi-analytic models of AGN evolution are still unable to reproduce the cosmic downsizing of AGN with a merger-driven evolution of galaxies at low-redshifts. Furthermore, the extended blue discs of AGN hosts indicate the presence of a substantial reservoir of cold gas that can be accreted onto the bulge and possibly cause recurrent episodes of BH growth and star formation due to gravitational interactions or local instabilities. Major mergers cannot explain these blue discs and the merger timescale of ∼1 Gyr is too short to account for the large number of galaxies in the transient phase at low redshifts. As a result, Hasinger (2008) outlined a different scenario for low-luminosity AGN and their hosts: Pre-formed bulge-dominated galaxies depart from their red sequence (bottom panel of Fig. 1.5) due to gas accretion which produces low levels of star formation accompanied with modest rates of BH growth. Nevertheless, the major merger scenario still appears to be the dominant process for the evolution of galaxies and the triggering of luminous QSOs at high redshift ($z \sim 2$).

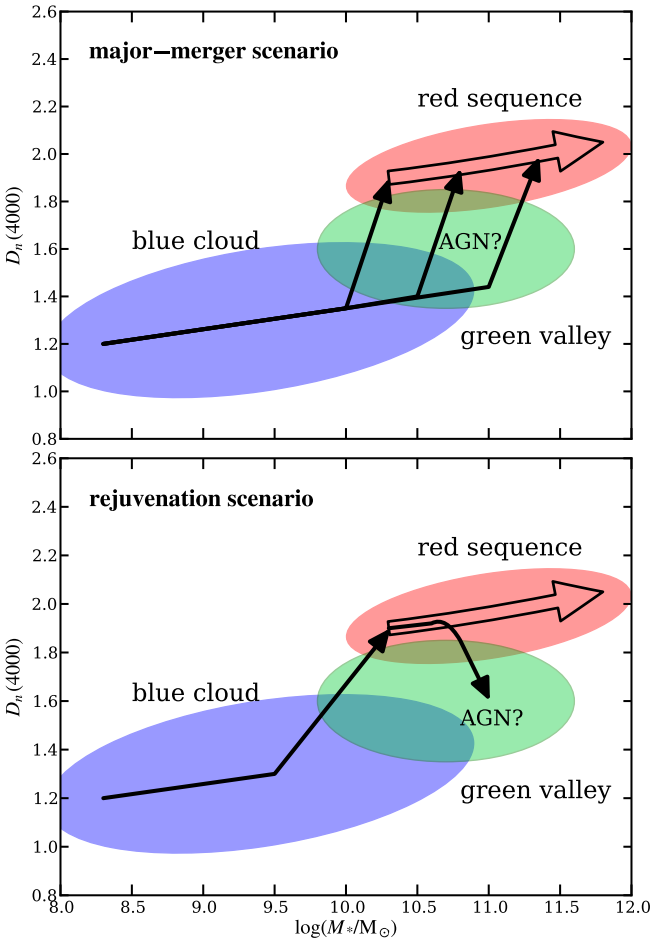

Fig. 1.5. Schematic diagrams of two proposed evolutionary galaxy tracks. *Top panel:* Major mergers initially transfrom disc-dominated to bulge-dominated systems and trigger AGN activity that might be responsible for the truncation of star formation as discussed by Faber et al. (2007). Major mergers can occur at various stellar masses that build up the red sequence and lead to the observed green valley population as a transient phase. *Buttom panel:* "Rejuvenation" scenario as proposed by Hasinger (2008). Bulge-dominated red sequence galaxies migrate along the red-sequence, but were initially formed from major mergers of blue cloud galaxies. A fraction of red sequence galaxies may depart towards the green valley in case its stellar population is "rejuvenated" due to the accretion of gas from its environment, which may possibly fuel an AGN as well.

An additional complication in the whole interpretation of those observations is the effect of dust on the galaxy colours. Dust corrections based on stellar population modelling of a few broad-band passband may be insufficient. Cardamone et al. (2010) analysed the colours of galaxies based on 32 optical to infrared passbands including several medium-band filters that allowed a significantly more accurate determination of the dust extinction. Their dust-corrected CMD shows a clear bimodality even for AGN hosts without any green valley population, which appears to be in conflict, if confirmed, with the usual interpretation of the green valley to be a transient phase.

1.2.4. The hunt for AGN feedback

Although the observational facts presented in the previous subsections already indicate that some sort of AGN feedback might be important for the evolution of galaxies, the results of numerical simulations and semi-analytic models were the main driver for the concept of AGN feedback. Early semi-analytic models in the ΛCDM cosmological model overpredicted the space density of the faintest and most luminous galaxies due to the continuous accretion and condensation of gas onto dark matter halos. While supernova feedback is energetic enough to remove the gas from low-mass systems and stall star formation, feedback from AGN was suggested by Silk & Rees (1998) to produce a galactic superwind that is capable of removing a significant fraction of gas from massive galaxies and thereby truncate star formation. AGN feedback was subsequently introduced into semi-analytic models and the observed galaxy luminosity function and several BH-bulge relations could be simultaneously reproduced (Benson et al. 2003; Bower et al. 2006; Croton et al. 2006). Numerical simulation of major mergers were able to produce red elliptical remnants in agreement with the apparent colour bimodality only after AGN feedback was included (Springel et al. 2005; Khalatyan et al. 2008).

However, the actual efficiency and physical processes with which the AGN transfers energy or momentum to the ambient medium is largely unconstrained from observations and remained so far an adjustable parameter in all simulations. One possible process are "energy-driven" AGN winds, which can be produced either by photoionisation of metal or hydrogen atoms leading to a thermal expansion of the gas or via shock-heating by a radio jets. On the other hand, radiation pressure is able to drive "momentum-driven" wind that can be important in the vicinity of the nucleus. King (2003) showed that for such a momentum-driven wind the accretion onto the BH stalls at a certain BH mass which scales as σ_*^4, assuming an isothermal sphere for the dark matter halo in which the host galaxy resides. However these momentum-driven winds are only efficient at super-Eddington accretion except if dust or absorption at resonance lines enhance the effective cross-section for the radiation. Jets may be more efficient in that respect as they can transport momentum to large distances via their ram pressure.

Simulations frequently adopted two different modes of AGN feedback, the so-called "quasar mode" and "radio mode", where the former was assumed to operate during a merger-induced AGN phase and the later for the most massive galaxies when they accrete hot gas from their halos. With dedicated 1D numerical simulations of a model elliptical galaxy, Ciotti et al. (2009) found that neither radiative nor mechanical feedback alone are able to match with observations. Either the mechanical feedback is too strong, blowing out the entire gas before the SMBH could grow to the observed masses, or is too weak so that strong cooling flows develop resulting in too young stellar population as observed at $z = 0$. They therefore argued that both types of feedback are required, where the radiative feedback heats the gas on kpc scales to prevent cooling flows and mechanical feedback from winds on scales of a few 100 pc self-regulates the accretion and luminosity of the SMBH.

Observational evidence for radiation supported momentum-driven winds come from broad absorption troughs in the UV or X-ray spectra of broad-absorption line QSOs (BAL QSOs) with blue-shifts of up to several thousand km s^{-1} (e.g. de Kool et al. 2001; Chartas et al. 2007) that make up ≤10% of the QSO population. Whether these winds provide enough kinetic energy to remove the entire gas content from the system remains contro-

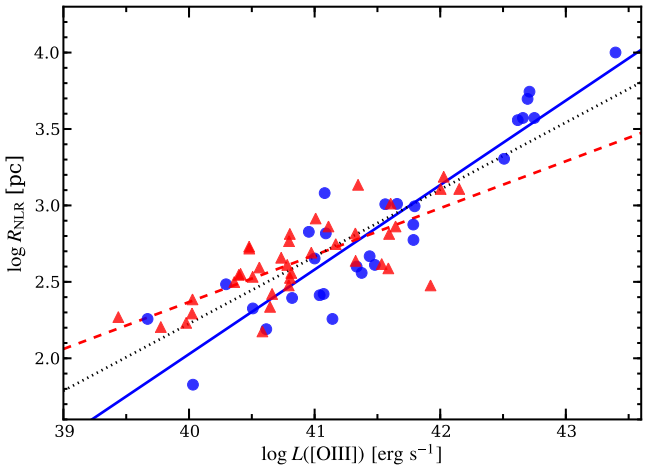

Fig. 1.6. Size-luminosity relation of the (E)NLR as measured from *HST* narrow-band imaging combining data from Schmitt et al. (2003a) and Bennert et al. (2002). The red triangles correspond to Seyfert 2 galaxies and the blue circles denote Seyfert 1 galaxies and type 1 QSOs at high luminosities. Best-fit relations for the type 1, type 2 and all AGN, are shown as the blue solid, red dashed and black dotted line, respectively.

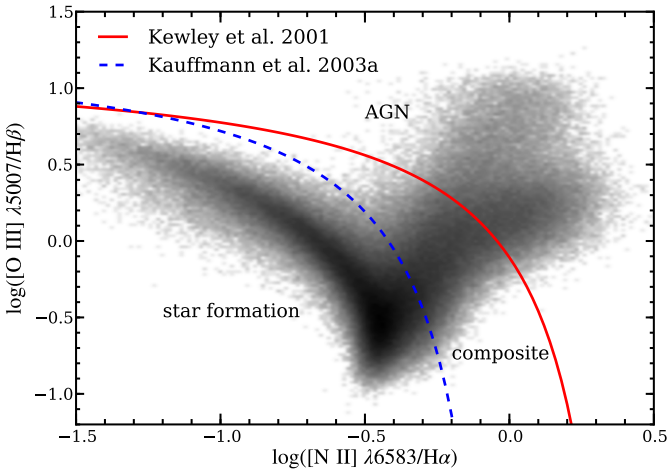

Fig. 1.7. BPT diagnostic diagram comparing the [O III]/Hβ emission-line ratios against the [N II]/Hα ratios. The grey scale image is a logarithmic 2D histogram of emission-line galaxies from the SDSS DR7 value-added MPA/JHU galaxy catalogue (*http://www.mpa-garching.mpg.de/SDSS/*). Only galaxies where all four emission lines could be detected with a S/N > 3 were considered. The demarcation curves defined by Kewley et al. (2001) and Kauffmann et al. (2003a) are shown by the red solid line and the blue dashed line, respectively. The AGN and star forming branches are clearly visible with a lot of galaxies within a composite region.

versial due to the large uncertainties in their total mass loading factor and their distances ($\lesssim$ 1 pc to several kpc). Circumstantial evidence for the radio-mode feedback comes from X-ray observations of nearby galaxies cluster. Hot cavities and ripples were detected in the X-ray images of clusters, which could be associated with bubbles inflated by the jets of the radio galaxy at the cluster centre (e.g. Fabian et al. 2006). Combining the radio-luminosity function of galaxies with mechanical energy output as implied by the X-ray cavities, Best et al. (2006) concluded that the radio-mode heating is able to balance the observed cooling rate of the hot gas for all massive elliptical galaxies with $M_* \geq 2-3\times10^{11}\mathrm{M}_\odot$ due to *recurrent* radio-loud activity.

As another part of the puzzle, Tremonti et al. (2007) discovered that the majority of massive post-starburst galaxies at $z \sim 0.6$ display Mg II $\lambda\lambda$2796, 2803 absorption lines blueshifted by 500–2000 km s^{-1} indicative for fossil galactic superwinds possibly due to radio-quiet AGN. Still, "smoking gun" evidence for AGN feedback that causally links the quenching of star formation directly to AGN activity and galactic winds is observationally scarce, in particular for isolated field galaxies. Thus, it remains unclear whether AGN feedback is really as important for the evolution of galaxies as initially thought and other possibilities, like gravitational heating (Johansson et al. 2009), have been raised as alternative scenarios for the quenching of star formation.

1.3. Tracing the AGN–host interplay via ionised gas

1.3.1. Size and properties of the Narrow-Line Region

A direct signature of gas heating due to AGN photoionisation is the bright narrow optical emission from ionised gas in the NLR, which implies the presence of a warm, ionised ISM with gas temperatures of more than 10 000 K. The NLR could be resolved on physical scales of $\lesssim$1 kpc with narrow-band imaging of the [O III] line in nearby Seyfert galaxies. The NLR light distribution is often of biconical shape in Seyfert 2 galaxies (e.g. Pogge 1988; Storchi-Bergmann et al. 1992) which were considered as evidence for the validity of the Unified Model of AGN. The integrated [O III] is quite important for the studies of type 2 AGN, since it is the best tracer for the bolometric luminosity of the AGN (Zakamska et al. 2003; Heckman et al. 2004). Most of the AGN SED is obscured by the torus, but emission of forbidden lines, like [O III], can be assumed to be isotropic as it is optically thin and the corresponding NLR region is too extended to be obscured by the dusty torus, although dust extinction of the host may introduce a systematic error.

The size of the NLR certainly needs to be dependent on the AGN luminosity given the budget of ionising photons. Extended NLRs (ENLRs) with sizes larger than 1 kpc were imaged for the most luminous Seyfert galaxies (Mulchaey et al. 1996; Schmitt et al. 2003a) and could be resolved for a small sample of 7 type 1 QSOs with *HST* (Bennert et al. 2002). As a puzzling result, the size-luminosity relation for the NLR were found to be significantly different for Seyfert galaxies and type 1 QSOs. While Bennert et al. (2002) determined a dependence of $R_{\mathrm{NLR}} \propto L_{[\mathrm{O\,III}]}^{0.52\pm0.06}$ for their QSOs, Schmitt et al. (2003b) estimated $R_{\mathrm{NLR}} \propto L_{[\mathrm{O\,III}]}^{0.33\pm0.04}$ based on their large sample of Seyfert galaxies. While the former relation would be similar to the relation for the BLR that could be theoretically explained by a constant ionisation parameter (recall Section 1.1.4), the later is close to the relation for a Strömgren sphere that assumes a constant density of the ambient gas. One possible solution proposed by Bennert et al. (2006c) is that type 1 and type 2 AGN follow an *apparently* different size-luminosity relation due to the inclination-dependent projection of the ionisation cones in the receding-torus model. As an initial result for a subsample of our QSOs presented in this work, we found that an ENLR is detected in only ~50% of the QSOs, where the detection is related to the properties of the QSO spectrum itself (Husemann et al. 2008).

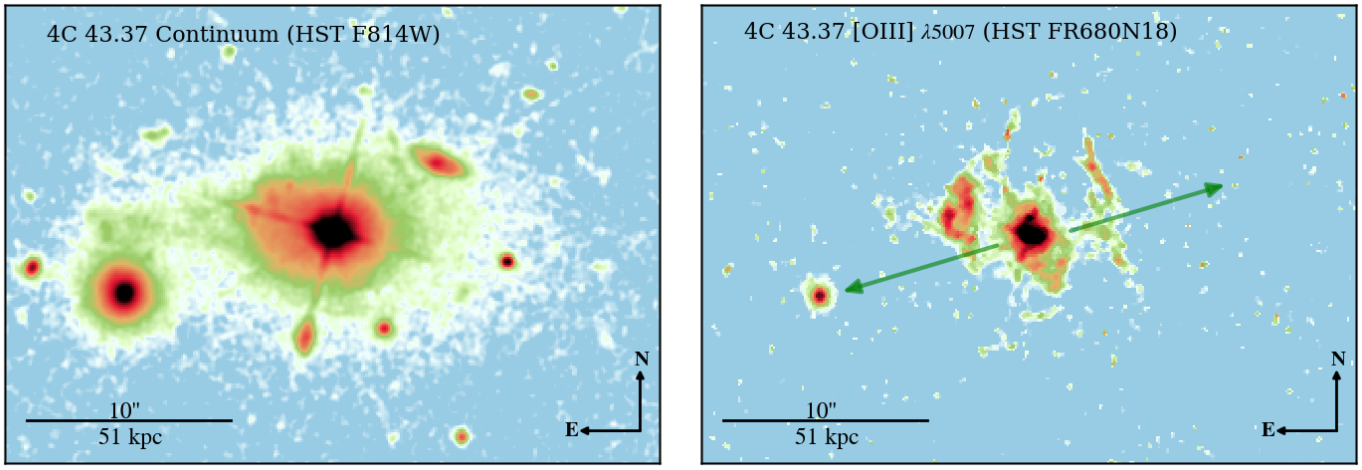

Fig. 1.8. Archival *HST* Wide Field Channel images of 4C 37.43 obtained with WFPC2. *Left panel:* Broad-band image in the F814W filter with 10% peak response at Hα. A loopsided host galaxy is recovered underneath the bright QSO. A prominent "tail" of emission is seen that extends 10″ to the East. *Right panel:* Narrow-band, linear-ramp filter image centred on the [O III] λ5007 emission line. An EELR with several filamentary structures of ionised gas is detected up to a distance of ~30 kpc from the QSO. The orientation of the radio lobes axis is indicated by the green arrows.

Thus, more than just the inclination is probably required to explain the different sizes of the ENLR.

One particular problem of the [O III] narrow-band imaging studies is that only the light distribution of a single emission line can be studied. However, H II regions that are ionised by hot massive stars within star forming regions also emit in [O III], which possibly contaminate and enlarge the apparent NLR. Emission-line ratios are a powerful tool to discriminate between different ionisation sources. The most famous one is the [O III]/Hβ vs. [N II]/Hα diagnostic diagram (Fig. 1.7), known as the BPT diagram (Baldwin et al. 1981). The distribution of line ratios appear to be clearly bimodal for emission-line galaxies, including star forming ones and type 2 AGN, leading to its characteristic seagull-like shape. The branch on the left side is solely associated with emission from star forming galaxies. The tight sequence in line ratios has been identified to correlate with the gas-phase nitrogen and oxygen abundances and several strong-line abundance indicators were empirically calibrated as a diagnostic tools. Both abundances are positively correlated with the [N II]/Hα ratios and negatively with the [O III]/Hβ. The AGN branch on the other side appears to merge with the H II branch at low [O III]/Hβ. Thus, the apparent sequence is thought to be partially the result of aperture effects, in particular for SDSS, where the emission of the NLR is diluted by ongoing star formation in the galaxy captured within a single fibre. Because AGN are associated with massive galaxies, the tight mass-metallicity relation of galaxies (Tremonti et al. 2004) implies that the two branches should merge at a point corresponding to high gas-phase metallicites, which is apparently observed. Nevertheless, demarcation curves were determined to classify object into star forming, AGN and composite objects based on the emission-line ratios (Kewley et al. 2001; Kauffmann et al. 2003a). For spatially resolved spectroscopy, the dilution of the NLR signal is much less a problem with sufficient spatial and spectral resolution and the radial transition zone from the NLR to star forming region within a galaxy can be determined (Bennert et al. 2006a,b). Thus, integral field spectroscopy would be an ideal method to map out the size and properties of the NLR almost unbiassed against star formation contamination.

Whether the NLR regions represent the radiative AGN feedback as required and predicted by the simulations is unclear, but the size-luminosity relation would be an important empirical constraint on how far out the AGN ionising radiation reaches to heat the ISM. Its size may reach the boundary of the bulge in late-type Seyfert galaxies, but certainly not the edge of their stellar discs, for which more luminous QSOs would be needed. If the gas is just heated and not expelled by a wind, the gas would be able to cool again introducing episodic star formation and BH growth phases, governed by the AGN duty cycle. Indication for a reduced specific star formation in QSO hosts was found by Ho (2005), who argued that the contribution of star formation to the [O II] λ3727 line of the NLR was smaller than the expected SFR from the molecular gas content of the host galaxy. This might be just an observational bias due to the aperture size of the spectroscopic fibre, which made it difficult to disentangle the different emission components. Whether those biases can account for the apparent discrepancy with an *enhanced* SFR inferred for the same QSO based on the near-IR continuum and Polycyclic Aromatic Hydrocarbon (PAH) emission (Schweitzer et al. 2006) or rather point to additional systematics, is not understood yet.

1.3.2. Extended Emission Line Regions of radio-loud QSOs

Long before the ENLRs were characterised, huge Extended Emission Line Regions (EELRs) with sizes of several tens of kpc were detected around RLQs (Wampler et al. 1975; Stockton 1976). Spectroscopic observations (Boroson & Oke 1984; Boroson et al. 1985) and narrow-band imaging (Stockton & MacKenty 1987) for a sample of RLQs revealed that EELRs are found in ~50% of steep-spectrum RLQ with highly ionised gas most likely due to the AGN radiation. *HST* images of the EELR around 4C 37.43 are shown in Fig. 1.8 as an example. The origin of the filamentary structures of ionised gas in the EELR has been discussed ever since. Several scenarios have been proposed as explanations for the distribution of physical properties of the EELR gas.

Given the similarities of the filaments with tidal tails in simulations of galaxy collision and interactions, it was suggested

that the gas might be tidal debris of two merging galaxies. A potential problem with this scenario is that the relatively high gas densities of the filaments, in the range of $10\,\mathrm{cm}^{-3}$ up to few$\times100\,\mathrm{cm}^{-3}$, imply that the clouds would dissipate within a short time ($\sim$10 000 yr), unless they are gravitationally bound or confined by the pressure of a hot ambient medium. Thus, Fabian et al. (1987) suggested that the warm gas of the EELR had been consended from and is embedded in a hot high-pressure medium, e.g. a cooling flow. X-ray observations with *Chandra* however failed to detect the diffuse host X-ray halos (Stockton et al. 2006), and the implied upper limits were insufficient to account for the required cooling. Whether cold accretion along cosmic filaments (Kereš et al. 2005) could be an explanation for the missing hot gas to rescue that scenario is still unclear. Recently, Fu & Stockton (2007) found that the BLR metallicity, inferred from UV emission-line ratios, is systematically lower for RLQ with an EELR compared to those without, which they attributed to an inflow of low metallicity gas from large radii towards the nucleus during a major merger. Together with the kinematics of the EELRs, obtained from IFU observations, Fu & Stockton (2009) argued that EELRs are possibly remants of AGN-driven superwinds and that AGN activity was triggered by the merger of a gas-rich galaxy with a massive, gas-poor galaxy.

At higher redshifts EELR appear as giant Lyα halos around RLQs (Heckman et al. 1991) and radio galaxies (e.g. McCarthy et al. 1990; Reuland et al. 2003; Villar-Martín et al. 2003, 2007) often extending on scales of 100 kpc. Whether their origin is similar to those of low redshift counterparts remains elusive, since cooling flows or cold accretion is likely more prevalent at earlier cosmic times than in the local universe (Haiman & Rees 2001). Because Lyα is a resonance line, photons will be scattered due to a cascade of absorption and re-emission events, requiring extensive radiative transfer modelling to accurately determine the physical properties of the gas. It is therefore difficult to assess whether radio-jets provide additional energy for the EELR in these sources. The detection of Lyα halos in a small sample of RQQs at redshift $2.7 < z < 4.5$ by Christensen et al. (2006) allowed a direct comparison of their properties to obtain insights into their nature. They found that the Lyα halos around RQQs were less luminous and less extended compared to RLQs at a given nuclear luminosity. Thus, they concluded that the Lyα luminosity in RLQs may indeed be enhanced due to a coupling of the jet with its ambient intergalactic medium or the environment of the two population are different. This is further supported by the alignment between the radio and Lyα morphologies (Heckman et al. 1991; McCarthy et al. 1995; Sánchez & Humphrey 2009). A similar systematic investigation of the properties of RQQs at low redshift has not been performed yet.

1.3.3. Jet–cloud interaction and galactic superwinds

The coupling of radio jets with the ambient gas has been detected and studied on 100 kpc scales in RL AGN down to sub-kpc scales for the low-power radio jets in Seyfert galaxies. Jets in RL AGN were found to be well aligned with the primary axis of elongated EELRs above $z > 0.6$, the so-called "alignment-effect" (McCarthy et al. 1987). It suggests a prominent role of radio jets in shaping their associated EELR possibly due to ram pressure and shocks that either compress or ionise the gas on large scales. Spectroscopic observations of radio-galaxies revealed extreme kinematics of the gas with line widths exceeding $1000\,\mathrm{km\,s}^{-1}$ in high-redshift radio galaxies (e.g McCarthy et al. 1996; Villar-Martín et al. 1999) and a few hundred $\mathrm{km\,s}^{-1}$ in low-redshift ones (e.g. Tadhunter et al. 1989). These jets are usually assumed to be quite collimated, so that their working surface against the ISM within the host galaxy would be to small for blowing out significant amounts of gas. With near-IR IFU observations of a $z = 2.2$ radio galaxy, Nesvadba et al. (2006) studied the kinematics and energetics of jet-cloud interaction with emission lines in the rest-frame optical window. They found a galactic superwind on scales of tens of kpc covering a large solid angle with an injection energy of more than $10^{60}\,\mathrm{erg\,s}^{-1}$, which is enough to remove almost 50% of the gas from the galaxy within 100 Myr. The AGN was identified as the only source, which can reasonably provide enough energy to power the wind.

The EELRs around RLQs at much lower redshifts ($z \lesssim 0.3$) have certainly quite different properties compared to their high redshift counterparts. Recent optical IFU spectroscopy observations showed that their kinematics are more quiescent with line width of 30 to $100\,\mathrm{km\,s}^{-1}$, albeit some clouds with velocities of $500\,\mathrm{km\,s}^{-1}$ appear to be common (e.g. Fu & Stockton 2006, 2009). These high-velocity clouds were interpreted as signatures for a galactic superwind remnant produced at the very early phase of radio activity. Such young radio sources appear as Compact Steep Spectrum (CSS) radio sources or Gigahertz-Peaked Sources (GPS) in the low-redshift universe and were also extensively studied spectroscopically (e.g. Holt et al. 2003). They represent a phase where the radio-jet is currently passing through the dense and dusty interstellar medium of the host galaxy leading to strong interactions with outflowing material accelerated up to $\sim$2000 $\mathrm{km\,s}^{-1}$. However, the mass outflow rate in the warm ionised medium of PKS 1334+12 and its corresponding kinetic energy in the associated galactic wind was estimated to be 2 order of magnitude lower than expected from theory (Holt et al. 2011). The energy appears insufficient to blow out the warm gas from the bulge of the galaxy unless a large portion of energy is hidden in the neutral or molecular phase of the ISM. Thus, it is certainly not yet clear how EELRs develop and what they imply in the sense of AGN feedback processes.

In Seyfert galaxies, jet-cloud interaction could also be resolved, but on much smaller scales (<1 kpc). The well-studied archetypal Seyfert 2 galaxy NGC 1068 shows multiple kinematic components along the jet axis out to 250 pc with line widths up to $\sim$3000 $\mathrm{km\,s}^{-1}$ (FWHM) and outflowing velocities of more than $2000\,\mathrm{km\,s}^{-1}$ (Cecil et al. 2002; Gerssen et al. 2006). Due to the low mass loading factor, these jet-driven interactions do not play a major role in the energy budget of the galaxy. The situation for RQQs is less clear due to lack of observations, but accelerated gas clouds associated with resolved, low-power radio sources were detected in individual cases (e.g. Mrk 1014, Leipski & Bennert 2006; Fu & Stockton 2009). Even if the energy coupling between AGN and ambient medium via jet-cloud interaction is energetically insufficient, that process could possibly drive a wind in the warm or hot medium leading to instabilities and fragmentation of massive cold gas clouds and enhance their effective cross-section for radiative AGN feedback processes in a second stage as proposed by Hopkins & Elvis (2010).

1.4. Goals and outline of this work

The main aim of this thesis is to exploit the potential of IFUs to map out and study the properties of the warm-ionised ISM around luminous low-redshift ($z < 0.3$) QSOs in order to understand the evolution of their host galaxies. IFU data for more than 50 type 1 QSOs were collected at major telescopes that represent the largest sample of this kind to date. Our sample contains mainly RQQs as their properties have yet been much less inves-

tigated compared to their radio-loud counterparts. The type of observational data combined with the sample size has been an additional challenge in terms of data reduction and data analysis, which demanded new software solutions in order to attack our main scientific objectives:

- Revise the NLR size-luminosity relation for type 1 QSOs
- Search for kinematic signatures of galactic winds
- Constrain the origin of the gas: external vs. internal
- Detect signatures of recent star forming activity

The main part of the thesis is structured into four Chapters which are designed to be stand-alone articles, which are either accepted, submitted or to be submitted in the near future for publication in the Journal *Astronomy & Astrophysics*. Therefore, each Chapter features a dedicated introduction, more focused on the particular content of the Chapter, but a certain level of redundancy will be unavoidable. The Appendix provides complementary material including a description of our developed software tool, sample tables and figures as well as small side studies/projects, which are either still ongoing and of preliminary nature or do not qualify for a dedicated publication.

Chapter 2 is devoted to the investigation of the ionised gas around the luminous radio-quiet QSO HE 1029−1041, which is the brightest QSO on the southern sky ($m_V = 13.7$) and actually the first one discovered by HES. The exceptionally low redshift of the object ($z = 0.08$) allows to study the ISM around such a luminous QSO with unprecedented spatial resolution from the ground. The analysis of our entire QSO sample and the interpretation of results is split into two Chapters according to the QSO subsample selection and the IFU instrument used for observation. In Chapter 3 we analyse the properties of the ionised ISM gas phase around luminous QSOs observed with the PMAS IFU at the Calar Alto observatory. The investigation is focused on the gas kinematics, the ENLR size/luminosity and their connection to radio activity. Chapter 4 contains a detailed analysis of VIMOS IFU observations of a well-defined sample of low-luminosity QSO hosts, which were already intensively studied by means of multi-colour broad-band imaging (Jahnke et al. 2004). Following up on the results presented in Chapter 3, the NLR size-luminosity relation is studied including archival VIMOS IFU observations of type 1 Seyfert galaxies that were analysed and kindly provided by Daniel Kupko. Furthermore, we investigate gas-phase metallicity gradients and absolute O/H abundances to understand the past and current evolutionary stage of the host galaxies in conjunction with signatures of recent star formation activity. Chapter 5 is again focused on a single object, the radio-quiet QSO HE 2158−0107, which stand out of the sample by its extraordinary large EELR compared to the host galaxy size. We combined our IFU observations with archival optical and near-IR broad-band imaging to constrain the origin of this EELR and the evolution of the host galaxy in the context of the BH-bulge relations and its scatter. The main conclusions of this work are summarised in Chapter 6 with a brief outlook for future perspectives in that particular area of research.

References

Alonso, M. S., Lambas, D. G., Tissera, P., & Coldwell, G. 2007, MNRAS, 375, 1017
Antonucci, R. 1993, ARA&A, 31, 473
Arnouts, S., Walcher, C. J., Le Fèvre, O., et al. 2007, A&A, 476, 137
Baldwin, J. A., Phillips, M. M., & Terlevich, R. 1981, PASP, 93, 5
Barnes, J. E. & Hernquist, L. E. 1991, ApJ, 370, L65
Barthel, P. D. 1989, ApJ, 336, 606
Barton, E. J., Geller, M. J., & Kenyon, S. J. 2000, ApJ, 530, 660
Baskin, A. & Laor, A. 2005, MNRAS, 358, 1043
Bell, E. F., McIntosh, D. H., Katz, N., & Weinberg, M. D. 2003, ApJS, 149, 289
Bell, E. F., Wolf, C., Meisenheimer, K., et al. 2004, ApJ, 608, 752
Bennert, N., Canalizo, G., Jungwiert, B., et al. 2008, ApJ, 677, 846
Bennert, N., Falcke, H., Schulz, H., Wilson, A. S., & Wills, B. J. 2002, ApJ, 574, L105
Bennert, N., Jungwiert, B., Komossa, S., Haas, M., & Chini, R. 2006a, A&A, 459, 55
Bennert, N., Jungwiert, B., Komossa, S., Haas, M., & Chini, R. 2006b, A&A, 456, 953
Bennert, N., Jungwiert, B., Komossa, S., Haas, M., & Chini, R. 2006c, New A Rev., 50, 708
Benson, A. J., Bower, R. G., Frenk, C. S., et al. 2003, ApJ, 599, 38
Bentz, M. C., Peterson, B. M., Netzer, H., Pogge, R. W., & Vestergaard, M. 2009, ApJ, 697, 160
Best, P. N., Kaiser, C. R., Heckman, T. M., & Kauffmann, G. 2006, MNRAS, 368, L67
Best, P. N., Kauffmann, G., Heckman, T. M., & Ivezić, Ž. 2005, MNRAS, 362, 9
Blandford, R. D. & McKee, C. F. 1982, ApJ, 255, 419
Bongiorno, A., Zamorani, G., Gavignaud, I., et al. 2007, A&A, 472, 443
Boroson, T. A. 2002, ApJ, 565, 78
Boroson, T. A. & Green, R. F. 1992, ApJS, 80, 109
Boroson, T. A. & Oke, J. B. 1984, ApJ, 281, 535
Boroson, T. A., Persson, S. E., & Oke, J. B. 1985, ApJ, 293, 120
Bower, R. G., Benson, A. J., Malbon, R., et al. 2006, MNRAS, 370, 645
Brammer, G. B., Whitaker, K. E., van Dokkum, P. G., et al. 2009, ApJ, 706, L173
Canalizo, G. & Stockton, A. 2001, ApJ, 555, 719
Cardamone, C. N., Urry, C. M., Schawinski, K., et al. 2010, ApJ, 721, L38
Cassata, P., Cimatti, A., Kurk, J., et al. 2008, A&A, 483, L39
Cecil, G., Dopita, M. A., Groves, B., et al. 2002, ApJ, 568, 627
Chartas, G., Brandt, W. N., Gallagher, S. C., & Proga, D. 2007, AJ, 133, 1849
Christensen, L., Jahnke, K., Wisotzki, L., & Sánchez, S. F. 2006, A&A, 459, 717
Cid Fernandes, R., Gu, Q., Melnick, J., et al. 2004, MNRAS, 355, 273
Ciotti, L., Ostriker, J. P., & Proga, D. 2009, ApJ, 699, 89
Cirasuolo, M., Celotti, A., Magliocchetti, M., & Danese, L. 2003, MNRAS, 346, 447
Cisternas, M., Jahnke, K., Inskip, K. J., et al. 2011, ApJ, 726, 57
Croom, S. M., Richards, G. T., Shanks, T., et al. 2009, MNRAS, 399, 1755
Croton, D. J., Springel, V., White, S. D. M., et al. 2006, MNRAS, 365, 11
de Kool, M., Arav, N., Becker, R. H., et al. 2001, ApJ, 548, 609
Dunlop, J. S., McLure, R. J., Kukula, M. J., et al. 2003, MNRAS, 340, 1095
Ellison, S. L., Patton, D. R., Simard, L., & McConnachie, A. W. 2008, AJ, 135, 1877
Faber, S. M., Willmer, C. N. A., Wolf, C., et al. 2007, ApJ, 665, 265
Fabian, A. C., Celotti, A., & Erlund, M. C. 2006, MNRAS, 373, L16
Fabian, A. C., Crawford, C. S., Johnstone, R. M., & Thomas, P. A. 1987, MNRAS, 228, 963
Falcke, H., Körding, E., & Markoff, S. 2004, A&A, 414, 895
Falcke, H., Wilson, A. S., & Simpson, C. 1998, ApJ, 502, 199
Ferrarese, L. & Ford, H. 2005, Space Sci. Rev., 116, 523
Ferrarese, L. & Merritt, D. 2000, ApJ, 539, L9
Floyd, D. J. E., Kukula, M. J., Dunlop, J. S., et al. 2004, MNRAS, 355, 196
Franzetti, P., Scodeggio, M., Garilli, B., et al. 2007, A&A, 465, 711
Fu, H. & Stockton, A. 2006, ApJ, 650, 80
Fu, H. & Stockton, A. 2007, ApJ, 664, L75
Fu, H. & Stockton, A. 2009, ApJ, 690, 953
Gebhardt, K., Bender, R., Bower, G., et al. 2000, ApJ, 539, L13
Gerssen, J., Allington-Smith, J., Miller, B. W., Turner, J. E. H., & Walker, A. 2006, MNRAS, 365, 29
González Delgado, R. M., Heckman, T., & Leitherer, C. 2001, ApJ, 546, 845
Gültekin, K., Richstone, D. O., Gebhardt, K., et al. 2009, ApJ, 698, 198
Haiman, Z. & Rees, M. J. 2001, ApJ, 556, 87
Hasinger, G. 2008, A&A, 490, 905
Heckman, T. M., Kauffmann, G., Brinchmann, J., et al. 2004, ApJ, 613, 109
Heckman, T. M., Miley, G. K., Lehnert, M. D., & van Breugel, W. 1991, ApJ, 370, 78
Hicks, E. K. S., Davies, R. I., Malkan, M. A., et al. 2009, ApJ, 696, 448
Ho, L. C. 2005, ApJ, 629, 680
Ho, L. C., Filippenko, A. V., & Sargent, W. L. W. 1997, ApJ, 487, 568
Holt, J., Tadhunter, C. N., & Morganti, R. 2003, MNRAS, 342, 227
Holt, J., Tadhunter, C. N., Morganti, R., & Emonts, B. H. C. 2011, MNRAS, 410, 1527
Hopkins, P. F. & Elvis, M. 2010, MNRAS, 401, 7
Hopkins, P. F., Hernquist, L., Cox, T. J., Robertson, B., & Krause, E. 2007, ApJ, 669, 45

Hu, C., Wang, J., Ho, L. C., et al. 2008, ApJ, 687, 78
Husemann, B., Wisotzki, L., Sánchez, S. F., & Jahnke, K. 2008, A&A, 488, 145
Hutchings, J. B., Crampton, D., & Campbell, B. 1984, ApJ, 280, 41
Hutchings, J. B. & Neff, S. G. 1992, AJ, 104, 1
Ivezić, Ž., Menou, K., Knapp, G. R., et al. 2002, AJ, 124, 2364
Jahnke, K., Bongiorno, A., Brusa, M., et al. 2009, ApJ, 706, L215
Jahnke, K., Kuhlbrodt, B., & Wisotzki, L. 2004, MNRAS, 352, 399
Jahnke, K. & Macciò, A. V. 2011, ApJ, 734, 92
Jiang, L., Fan, X., Ivezić, Ž., et al. 2007, ApJ, 656, 680
Johansson, P. H., Naab, T., & Ostriker, J. P. 2009, ApJ, 697, L38
Kauffmann, G. & Haehnelt, M. 2000, MNRAS, 311, 576
Kauffmann, G., Heckman, T. M., Budavári, T., et al. 2007, ApJS, 173, 357
Kauffmann, G., Heckman, T. M., Tremonti, C., et al. 2003a, MNRAS, 346, 1055
Kauffmann, G., Heckman, T. M., White, S. D. M., et al. 2003b, MNRAS, 341, 33
Kaviraj, S., Schawinski, K., Silk, J., & Shabala, S. S. 2010, ArXiv e-prints
Kellermann, K. I., Sramek, R., Schmidt, M., Shaffer, D. B., & Green, R. 1989, AJ, 98, 1195
Kereš, D., Katz, N., Weinberg, D. H., & Davé, R. 2005, MNRAS, 363, 2
Kewley, L. J., Dopita, M. A., Sutherland, R. S., Heisler, C. A., & Trevena, J. 2001, ApJ, 556, 121
Khalatyan, A., Cattaneo, A., Schramm, M., et al. 2008, MNRAS, 387, 13
King, A. 2003, ApJ, 596, L27
Kinney, A. L., Schmitt, H. R., Clarke, C. J., et al. 2000, ApJ, 537, 152
Kormendy, J. & Richstone, D. 1995, ARA&A, 33, 581
Kristian, J. 1973, ApJ, 179, L61+
Krolik, J. H. & Begelman, M. C. 1988, ApJ, 329, 702
Kukula, M. J., Pedlar, A., Baum, S. A., & O'Dea, C. P. 1995, MNRAS, 276, 1262
Kuraszkiewicz, J., Wilkes, B. J., Brandt, W. N., & Vestergaard, M. 2000, ApJ, 542, 631
Laor, A. & Behar, E. 2008, MNRAS, 390, 847
Lauer, T. R., Tremaine, S., Richstone, D., & Faber, S. M. 2007, ApJ, 670, 249
Lawrence, A. 1991, MNRAS, 252, 586
Leipski, C. & Bennert, N. 2006, A&A, 448, 165
Leipski, C., Falcke, H., Bennert, N., & Hüttemeister, S. 2006, A&A, 455, 161
Li, C., Kauffmann, G., Heckman, T. M., White, S. D. M., & Jing, Y. P. 2008, MNRAS, 385, 1915
Magorrian, J., Tremaine, S., Richstone, D., et al. 1998, AJ, 115, 2285
Maiolino, R., Shemmer, O., Imanishi, M., et al. 2007, A&A, 468, 979
Marconi, A. & Hunt, L. K. 2003, ApJ, 589, L21
Martin, D. C., Wyder, T. K., Schiminovich, D., et al. 2007, ApJS, 173, 342
McCarthy, P. J., Baum, S. A., & Spinrad, H. 1996, ApJS, 106, 281
McCarthy, P. J., Spinrad, H., Dickinson, M., et al. 1990, ApJ, 365, 487
McCarthy, P. J., Spinrad, H., & van Breugel, W. 1995, ApJS, 99, 27
McCarthy, P. J., van Breugel, W., Spinrad, H., & Djorgovski, S. 1987, ApJ, 321, L29
McLure, R. J., Kukula, M. J., Dunlop, J. S., et al. 1999, MNRAS, 308, 377
Merloni, A., Bongiorno, A., Bolzonella, M., et al. 2010, ApJ, 708, 137
Merloni, A., Heinz, S., & di Matteo, T. 2003, MNRAS, 345, 1057
Mihos, J. C. & Hernquist, L. 1996, ApJ, 464, 641
Miller, L., Peacock, J. A., & Mead, A. R. G. 1990, MNRAS, 244, 207
Miller, P., Rawlings, S., & Saunders, R. 1993, MNRAS, 263, 425
Mulchaey, J. S., Wilson, A. S., & Tsvetanov, Z. 1996, ApJS, 102, 309
Nandra, K., Georgakakis, A., Willmer, C. N. A., et al. 2007, ApJ, 660, L11
Nesvadba, N. P. H., Lehnert, M. D., Eisenhauer, F., et al. 2006, ApJ, 650, 693
Panessa, F., Barcons, X., Bassani, L., et al. 2007, A&A, 467, 519
Peng, C. Y. 2007, ApJ, 671, 1098
Peng, C. Y., Impey, C. D., Rix, H.-W., et al. 2006, ApJ, 649, 616
Pogge, R. W. 1988, ApJ, 328, 519
Rafter, S. E., Crenshaw, D. M., & Wiita, P. J. 2009, AJ, 137, 42
Ramos Almeida, C., Tadhunter, C. N., Inskip, K. J., et al. 2010, MNRAS, 1609
Reichard, T. A., Heckman, T. M., Rudnick, G., et al. 2009, ApJ, 691, 1005
Reuland, M., van Breugel, W., Röttgering, H., et al. 2003, ApJ, 592, 755
Riffel, R. A., Storchi-Bergmann, T., & Nagar, N. M. 2010, MNRAS, 404, 166
Riffel, R. A., Storchi-Bergmann, T., Winge, C., et al. 2008, MNRAS, 385, 1129
Rogers, B., Ferreras, I., Kaviraj, S., Pasquali, A., & Sarzi, M. 2009, MNRAS, 399, 2172
Salim, S., Rich, R. M., Charlot, S., et al. 2007, ApJS, 173, 267
Salviander, S., Shields, G. A., Gebhardt, K., & Bonning, E. W. 2007, ApJ, 662, 131
Sameshima, H., Kawara, K., Matsuoka, Y., et al. 2011, MNRAS, 410, 1018
Sánchez, S. F. & Humphrey, A. 2009, A&A, 495, 471
Sánchez, S. F., Jahnke, K., Wisotzki, L., et al. 2004, ApJ, 614, 586
Sanders, D. B., Soifer, B. T., Elias, J. H., Neugebauer, G., & Matthews, K. 1988, ApJ, 328, L35
Schawinski, K., Virani, S., Simmons, B., et al. 2009, ApJ, 692, L19
Schmidt, M. & Green, R. F. 1983, ApJ, 269, 352
Schmitt, H. R., Donley, J. L., Antonucci, R. R. J., Hutchings, J. B., & Kinney, A. L. 2003a, ApJS, 148, 327
Schmitt, H. R., Donley, J. L., Antonucci, R. R. J., et al. 2003b, ApJ, 597, 768
Schmitt, H. R., Storchi-Bergmann, T., & Cid Fernandes, R. 1999, MNRAS, 303, 173
Schramm, M., Wisotzki, L., & Jahnke, K. 2008, A&A, 478, 311
Schulze, A., Wisotzki, L., & Husemann, B. 2009, A&A, 507, 781
Schweitzer, M., Lutz, D., Sturm, E., et al. 2006, ApJ, 649, 79
Seyfert, C. K. 1943, ApJ, 97, 28
Shields, G. A., Gebhardt, K., Salviander, S., et al. 2003, ApJ, 583, 124
Silk, J. & Rees, M. J. 1998, A&A, 331, L1
Silverman, J. D., Mainieri, V., Lehmer, B. D., et al. 2008, ApJ, 675, 1025
Skelton, R. E., Bell, E. F., & Somerville, R. S. 2009, ApJ, 699, L9
Somerville, R. S., Hopkins, P. F., Cox, T. J., Robertson, B. E., & Hernquist, L. 2008, MNRAS, 391, 481
Springel, V., Di Matteo, T., & Hernquist, L. 2005, ApJ, 620, L79
Steffen, A. T., Barger, A. J., Cowie, L. L., Mushotzky, R. F., & Yang, Y. 2003, ApJ, 596, L23
Stockton, A. 1976, ApJ, 205, L113+
Stockton, A. 1982, ApJ, 257, 33
Stockton, A., Fu, H., Henry, J. P., & Canalizo, G. 2006, ApJ, 638, 635
Stockton, A. & MacKenty, J. W. 1987, ApJ, 316, 584
Storchi-Bergmann, T., Wilson, A. S., & Baldwin, J. A. 1992, ApJ, 396, 45
Tadhunter, C. N., Fosbury, R. A. E., & Quinn, P. J. 1989, MNRAS, 240, 225
Tal, T., van Dokkum, P. G., Nelan, J., & Bezanson, R. 2009, AJ, 138, 1417
Tremaine, S., Gebhardt, K., Bender, R., et al. 2002, ApJ, 574, 740
Tremonti, C. A., Heckman, T. M., Kauffmann, G., et al. 2004, ApJ, 613, 898
Tremonti, C. A., Moustakas, J., & Diamond-Stanic, A. M. 2007, ApJ, 663, L77
Tristram, K. R. W., Meisenheimer, K., Jaffe, W., et al. 2007, A&A, 474, 837
Ueda, Y., Akiyama, M., Ohta, K., & Miyaji, T. 2003, ApJ, 598, 886
Ulvestad, J. S., Antonucci, R. R. J., & Barvainis, R. 2005, ApJ, 621, 123
Ulvestad, J. S. & Ho, L. C. 2001, ApJ, 558, 561
Ulvestad, J. S. & Wilson, A. S. 1989, ApJ, 343, 659
Urry, C. M. & Padovani, P. 1995, PASP, 107, 803
Vestergaard, M. 2002, ApJ, 571, 733
Villar-Martín, M., Sánchez, S. F., Humphrey, A., et al. 2007, MNRAS, 378, 416
Villar-Martín, M., Tadhunter, C., Morganti, R., Axon, D., & Koekemoer, A. 1999, MNRAS, 307, 24
Villar-Martín, M., Vernet, J., di Serego Alighieri, S., et al. 2003, MNRAS, 346, 273
Wampler, E. J., Burbidge, E. M., Baldwin, J. A., & Robinson, L. B. 1975, ApJ, 198, L49
Wandel, A., Peterson, B. M., & Malkan, M. A. 1999, ApJ, 526, 579
White, R. L., Helfand, D. J., Becker, R. H., Glikman, E., & de Vries, W. 2007, ApJ, 654, 99
Wild, V., Heckman, T., & Charlot, S. 2010, MNRAS, 405, 933
Wild, V., Kauffmann, G., Heckman, T., et al. 2007, MNRAS, 381, 543
Wisotzki, L., Koehler, T., Groote, D., & Reimers, D. 1996, A&AS, 115, 227
Woo, J., Treu, T., Malkan, M. A., & Blandford, R. D. 2006, ApJ, 645, 900
Woo, J., Treu, T., Malkan, M. A., & Blandford, R. D. 2008, ApJ, 681, 925
Woods, D. F. & Geller, M. J. 2007, AJ, 134, 527
Wyithe, J. S. B. & Loeb, A. 2003, ApJ, 595, 614
Yip, C. W., Connolly, A. J., Vanden Berk, D. E., et al. 2004, AJ, 128, 2603
York, D. G., Adelman, J., Anderson, Jr., J. E., et al. 2000, AJ, 120, 1579
Zakamska, N. L., Strauss, M. A., Krolik, J. H., et al. 2003, AJ, 126, 2125

Chapter 2

Mapping the ionised gas around the luminous QSO HE 1029−1401: Evidence for minor merger events?⋆

B. Husemann[1], S. F. Sánchez[2], L. Wisotzki[1], K. Jahnke[3], D. Kupko[1], D. Nugroho[3], and M. Schramm[4]

[1] Astrophysikalisches Institut Potsdam, An der Sternwarte 16, 14482 Potsdam, Germany
[2] Centro Astronómico Hispano-Alemán, Calar Alto,(CSIC-MPG), C/Jesús Durbán Remón 2-2, E-04004 Almeria, Spain
[3] Max-Planck-Institut für Astronomie, Königsstuhl 17, D-69117 Heidelberg, Germany
[4] Department of Astronomy, Kyoto University, Kyoto 606-8502, Japan

ABSTRACT

We present VIMOS integral field spectroscopy of the brightest radio-quiet QSO on the southern sky HE 1029−1401 at a redshift of $z = 0.086$. Standard decomposition techniques for broad-band imaging are extended to integral field data in order to deblend the QSO and host emission. We perform a tentative analysis of the stellar continuum finding a young stellar population (< 100 Myr) or a featureless continuum embedded in an old stellar population (10 Gyr) typical for a massive elliptical galaxy. The stellar velocity dispersion of $\sigma_* = 320 \pm 90$ km/s and the estimated black hole mass $\log(M_{\rm BH}/M_\odot) = 8.7 \pm 0.3$ are consistent with the local $M_{\rm BH}$–σ_* relation within the errors. For the first time we map the two-dimensional ionised gas distribution and the gas velocity field around HE 1029−1401. While the stellar host morphology is purely elliptical we find a highly structured distribution of ionised gas out to 16 kpc from the QSO. The gas is highly ionised solely by the QSO radiation and has a significantly lower metallicity than would be expected for the stellar mass of the host, indicating an external origin of the gas most likely due to minor mergers. We find a rotating gas disc around the QSO and a dispersion-dominated non-rotating gas component within the central 3 kpc. At larger distances the velocity field is heavily disturbed, which could be interpreted as another signature of past minor merger events. Alternatively, the arc-like structure seen in the ionised gas might also be indicative of a large-scale expanding bubble, centred on and possibly driven by the active nucleus.

2.1. Introduction

Since the underlying host galaxies of several quasi-stellar objects (QSOs) were resolved by Kristian (1973), QSO host galaxies have been extensively studied to understand their properties and their relevance for the evolution of the overall galaxy population over cosmic time. Most of our knowledge of QSO host galaxies comes from numerous ground and space-based imaging studies (e.g. Malkan 1984; Smith et al. 1986; McLeod & Rieke 1994; Bahcall et al. 1997; Dunlop et al. 2003; Sánchez & González-Serrano 2003), which provide basic information on the host galaxies like the morphology or the luminosity. Narrow-band images centred on luminous emission lines have been obtained to infer the distribution and size of the ionised gas surrounding the QSO (e.g. Stockton & MacKenty 1987; Mulchaey et al. 1996; Falcke et al. 1998; Bennert et al. 2002; Schmitt et al. 2003). However, optical and/or near-infrared spectroscopy is required for a more detailed investigation of the properties of the stellar population and the ionised gas.

Boroson & Oke (1982) were the first to detect strong Balmer absorption lines in the off-nuclear spectrum of the QSO 3C 48 and highly ionised gas was already found long ago in off-nuclear spectra of many QSOs (e.g. Wampler et al. 1975; Stockton 1976; Boroson & Oke 1984; Boroson et al. 1985) indicating large amount of gas being photoionised by the QSO radiation. Unfortunately, spectroscopy of QSO hosts suffers invariably from the contamination of the spectrum by the emission of the active galactic nucleus (AGN) even when observed some arcseconds away from the nucleus. Various spectroscopic studies circumvented this problem by looking at obscured (type 2) AGN (e.g. González Delgado et al. 2001; Kauffmann et al. 2003; Cid Fernandes et al. 2004; Bennert et al. 2006; Stoklasová et al. 2009), which are thought to have the same properties as unobscured (type 1) AGN in the framework of the unification model of AGN (Antonucci 1993; Urry & Padovani 1995). They often find a young stellar population in the AGN host galaxies, in particular for the most luminous AGN, suggesting a connection between star formation and nuclear activity in agreement with photometric studies of type 1 QSOs at all redshifts (Jahnke & Wisotzki 2003; Jahnke et al. 2004a,b; Sánchez et al. 2004b).

Letawe et al. (2007) and Jahnke et al. (2007), hereafter Let07 and Jah07 respectively, developed two different methods to decompose the AGN and host spectra in long-slit observations and applied them to a sample of luminous QSOs. However, long-slit spectroscopy covers only a small part of the host and depend on the chosen position angle and slit width. Only integral field unit (IFU) observations allow to study the properties of the entire host galaxy in an unbiased way. Dedicated AGN-host decomposition

⋆ This Chapter is published as an article in journal *Astronomy & Astrophysics*: Husemann et al., A&A, Volume 519, page A115, 2010, reproduced with permission ©ESO. Please note that the style of all figures were refurbished with respect to the published article without changing the content of the published article.

techniques have already been developed and were successfully applied to IFU data of luminous QSOs at low and high redshift (Sánchez et al. 2004a; Christensen et al. 2006; Husemann et al. 2008).

In this Chapter, we report on optical IFU spectroscopy of the luminous radio-quiet QSO HE 1029−1401 with the VIMOS IFU at the Very Large Telescope (VLT). HE 1029−1401 was discovered by the Hamburg-ESO survey (HES; Wisotzki et al. 1991, 2000) to be the brightest QSOs in the southern hemisphere with an apparent magnitude of $V = 13.7$ at a redshift of only $z = 0.086$.

Observations with the Hubble Space Telescope (*HST*) revealed a bright elliptical (E1) host galaxy (Bahcall et al. 1997) with an effective radius of $r_e = 3.2''$ (5.1 kpc). Jahnke et al. (2004a) found from multi-colour imaging that the host colours are significantly bluer than inactive galaxies at the same luminosity and inferred an intermediate-age stellar population of 0.7 Gyr (luminosity weighted) by modelling the Spectral Energy Distribution (SED) with template Single Stellar Populations (SPPs).

Spatially resolved on-nuclear longslit spectroscopy for this object was presented by Let07 and Jah07. Both studies consistently found highly ionised gas in the host galaxy on kpc scales. Jah07 found that the stellar component is non-rotating, but the velocity curve of the ionised gas indicated the presence of a rotating gas disc on kpc scales around the nucleus. Let07 argued instead that the velocity curve does not fit with a pure rotational velocity field based on inclination arguments.

The main focus of this paper is to present an in-depth analysis of the ionised gas in the host galaxy of HE 1029−1401, but we also perform a tentative analysis of the stellar continuum. Throughout the paper we assume a cosmological model with $H_0 = 70$ km/s, $\Omega_m = 0.3$, and $\Omega_\Lambda = 0.7$. This corresponds to a physical scale of 1.6 kpc/″ at $z = 0.086$.

2.2. Morphology of the host galaxy of HE 1029−1401

A high resolution *HST* image of HE 1029−1401 in the F606W band was published by Bahcall et al. (1997). We retrieved the archival *HST* image from the Hubble Legacy Archive[1] in order to re-analyse the image. An analytic Point Spread Function (PSF) for the observations was created with the TinyTim software package (Krist 1995), because no sufficiently bright star was covered by the *HST* observation. We used `GALFIT` (Peng et al. 2002) to decompose the host and QSO contributions assuming a de Vaucouleurs light profile (de Vaucouleurs 1948) for the host plus a point source for the nucleus. The effective radius and ellipticity of our best-fitting model was $r_e = 3.5''$ (5.6 kpc) and $e = 0.1$, respectively, which are consistent with the parameters derived by Bahcall et al. (1997).

The nucleus-subtracted image of HE 1029−1401 is shown in Fig. 2.1. A strong negative residual is still visible at the QSO position due to the saturated QSO core. We cleaned the image of residuals from the usual diffraction spikes by replacing each affected pixel with the median value of the unaffected pixels within a radius of 6 pixels. Wisotzki (1994) obtained redshifts for 13 galaxies in the field finding 4 physical companions which indicate that the HE 1029−1401 is part of a loose group of galaxies. None of these confirmed companions were covered with our IFU observations. Neither C1 nor C2 have redshift information

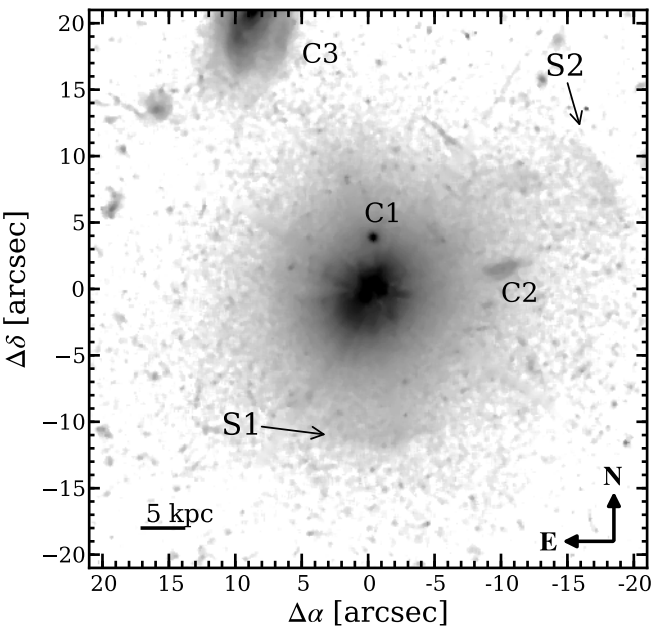

Fig. 2.1. Nucleus-subtracted *HST* F606W broad-band image of the host galaxy of HE 1029−1401. Residuals of the diffraction spikes have been taken out by interpolation and the image is smoothed by a median filter (boxsize of 4 pixels) for display purposes. Three apparent nearby companion galaxies are labelled as C1, C2 and C3 of which only C3 is confirmed to be at a different redshift (Wisotzki 1994). The location of the two faint shells reported by Bahcall et al. (1997) are highlighted with arrows.

available, but C3 was found to be at a different redshift than HE 1029−1401 (Wisotzki 1994).

Bahcall et al. (1997) also reported the detection of two faint shells located roughly 11″ and 19″ away from the nucleus. These shells are hardly visible in Fig. 2.1, but we highlighted their position by arrows for guidance and labelled them as S1 and S2, respectively. Note that the shell S2 is outside the field-of-view of our IFU observations.

We also performed an isophotal analysis of the host using the *ellipse* task of `IRAF`[2] (Tody 1993) after masking the 2 closest apparent companions. As the image is strongly affected by decomposition residuals over the central 2″, we only took into account isophotes within a range of 2″–10″ in the semi-major axis. We found that the ellipticity of the host is slightly decreasing outwards from 0.2–0.1 and that the a_4/a Fourier coefficient is consistent with 0. Thus, the deviation from pure elliptical isophotes is marginal.

2.3. IFU Observations and Data Reduction

We employed the IFU mode of the VIMOS instrument (LeFevre et al. 2003) on the VLT to perform optical 3-D spectroscopy of HE 1029−1401. The observations were conducted on the 18th and 24th of December 2003 at a seeing of ∼ 1.1″, with the high-resolution blue and orange grisms covering the spectral regions around Hβ and Hα with a spectral resolution of $R \sim 2600$. We

[1] http://hla.stsci.edu/

[2] `IRAF` is distributed by the National Optical Astronomy Observatories, which are operated by the Association of Universities for Research in Astronomy, Inc., under cooperative agreement with the National Science Foundation.

chose a spatial sampling of 0.66″/fibre resulting in a field-of-view of 27″×27″ that matches well with the angular size of the QSO host galaxy. The exposure times were split into 3 × 300s for the blue and 6 × 450s for the orange grism. A dither pattern was used in order to correct for dead fibres within the field-of-view. Additionally, a blank sky exposure of 300s was obtained in between of the target exposure series. Arc lamp and continuum lamp exposures were acquired for each configuration directly after the target exposures for calibration purposes. Standard star exposures were taken for each night according to the instrumental setup.

The VIMOS instrument is a complex IFU with 1600 operating fibres in the high-resolution mode. These are split up into 4 bundles of 400 fibres densely projected onto each of the 4 spectrograph CCDs. Instrument flexure and cross-talk between adjacent fibres are important issues for VIMOS which need to be carefully taken into account in the data reduction. As this is not the case for the standard reduction pipeline provided by ESO, we used our own flexible reduction package R3D (Sánchez 2006) designed to reduce fibre-fed IFU raw data, complemented by custom Python scripts. The basic reduction steps performed with R3D include: Bias subtraction, visually checked fibre identification, fibre tracing, spectra extraction, wavelength calibration, fibre flatfielding and flux calibration.

Flexure of the instrument causes substantial shifts of the fibre traces in the cross-dispersion direction between the continuum lamp exposure and the science exposure. This is a severe problem for an accurate extraction of the science spectra. We measured the fibre trace positions in the individual science exposures and continuum lamp exposure by modelling the cross-dispersion profile at 5 different locations on the dispersion axis with multiple Gaussians. The cross-dispersion profiles were generated by co-adding 200 pixels in the dispersion direction, preferentially encompassing bright sky lines, to increase the S/N. The offset between the science and continuum lamp fibre traces were measured to be in the range of −2.5 to 2.5 pixels. 2nd order Chebychev polynomials were used to extrapolate the offsets to the whole dispersion axis range.

In order to reduce the effect of cross-talk we used an iterative and fast algorithm that is part of the R3D package, based on Gaussian profile fitting to each of the fibres in the cross-dispersion direction. The centroids were fixed for each fibre to the position on the continuum lamp taking into account the position offsets due to the flexure. The width of the Gaussians was fixed. Details of the spectra extraction algorithm can be found in the R3D user guide[3]. The width of the fibre profiles is different for each of the four CCDs as it depends on the optical calibration of the four independent VIMOS spectrograph units. Thus, we estimated the fibre dispersion separately for each unit by simultaneously fitting each fibre with a Gaussian profile in the cross-dispersion direction at a single dispersion position for each CCD.

The continuum lamp exposure was used to create a fibre-flat that corrects for the differences in the fibre-to-fibre transmission. Sky subtraction and the correction for the differential atmospheric refraction were done with custom Python scripts. Taking advantage of the dithered exposures we were able to increase the spatial sampling by a factor of 2 and to correct for dead fibres within the field-of-view. The flux calibrated datacubes were rescaled in flux to match with the QSO *V*-band photometry and corrected for Galactic extinction applying the Cardelli et al. (1989) extinction curve with an extinction of $A_V = 0.221$ (Schlegel et al. 1998) in the sightline to HE 1029−1401.

[3] http://www.caha.es.sanchez/r3d/R3D_user_guide.pdf

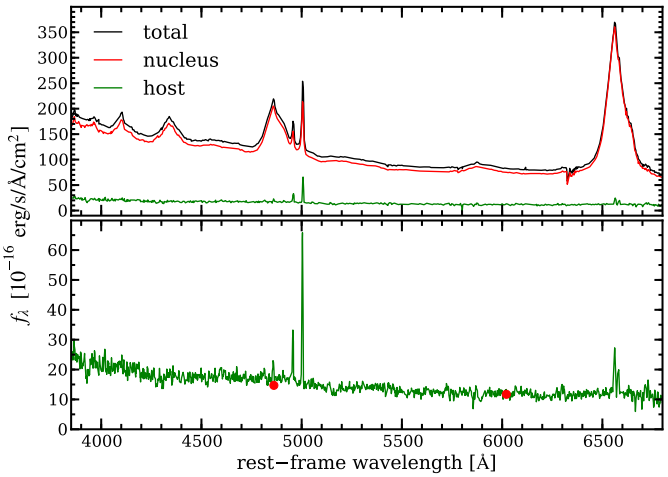

Fig. 2.2. Result of the decomposition process for HE 1029−1401. The integrated spectrum and the decomposed QSO and host spectra are shown in the top panel. A zoomed version on the host spectrum is provided in the bottom panel. The red points indicate the host magnitudes in the V and R band measured by Jahnke et al. (2004a). They are offset by 0.5 mag to put them on the same absolute scale as the IFU photometry. All spectra have been smoothed with a median filter of 7 pixels for display purposes.

2.4. IFU decomposition of host and QSO emission

In order to study the emission from the stars and the gas in the host of HE 1029−1401 it is important to properly subtract the contribution of the bright QSO. Broad-band imaging studies of QSO hosts have successfully used a two-dimensional analytical modelling scheme to decompose the point-like nucleus and different spatial extended host components to study the properties of QSO host galaxies (e.g. McLure et al. 1999; Kuhlbrodt et al. 2004; Sánchez et al. 2004b; Kim et al. 2008; Jahnke et al. 2009). We have extended this method to model each monochromatic image of an IFU datacube in order to obtain the clean optical spectrum of the radio jet of 3C 120 (García-Lorenzo et al. 2005; Sánchez et al. 2004a, 2006) and to deblend the components of a gravitationally lensed quasar (Wisotzki et al. 2003).

Broad-band imaging studies usually estimate the PSF empirically from stacked images of stars within the field-of-view. The field-of-view of current IFU instruments is generally too small so that no star can usually be captured simultaneously with the target. In light of time variable seeing, the QSO itself therefore needs to be used to construct a PSF. Fortunately, the spectral shape of the QSO is, in the absence of atmospheric dispersion, exactly the same in each spatial pixel of the IFU, only scaled by a factor according to the PSF. In particular, the broad emission lines of type 1 QSOs are a unique feature of the point like nucleus, which can be used to empirically estimate a PSF for IFU data (Jahnke et al. 2004c).

Having obtained a PSF for the IFU data from the broad emission lines and the morphological parameters of the host inferred from the *HST* images, we proceeded to model each monochromatic IFU narrow-band image by a linear combination of the PSF and host model. In this way we reconstructed a *pure* QSO and host datacube containing the QSO and mean host spectrum.

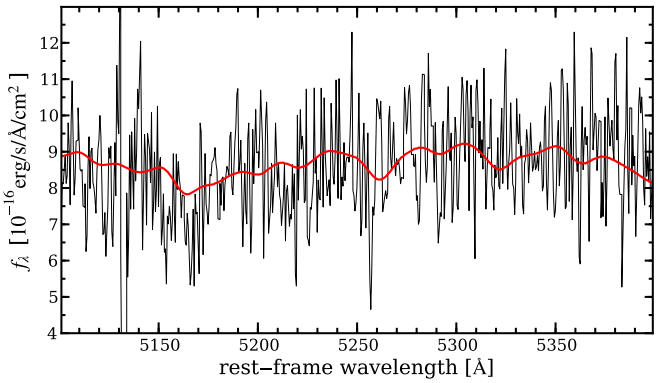

Fig. 2.3. Host spectrum of HE 1029−1401 in the rest-frame wavelength between 5100 and 5400Å. The best-fitting model spectrum is overplotted as the red solid line. Note that the strong residual of the bright [O I] 5577 night sky emission line appearing at ∼5135Å in the deredshifted spectrum was masked out for the modelling.

Afterwards, we subtracted the QSO datacube from the observed one to obtain a datacube uncontaminated by the QSO. The result of this decomposition process for HE 1029−1401 is presented in Fig. 2.2.

We found the IFU spectrum of the QSO and host component to be of higher quality than the long-slit spectra presented by Let07. The stellar absorption lines around MgI λ5166 are clearly visible in our host spectrum, and the noise in the spectrum is greatly reduced compared to the long-slit spectrum, due to the much larger galaxy area captured. IFU spectroscopy improves the quality of the decomposition due to the large spatial coverage of almost the entire host galaxy and the on-source PSF estimation based on QSO features. The decomposition of the long-slit spectra particularly suffered as the only available PSF star near HE 1029−1401 is 2 mag fainter than the QSO (Let07).

2.5. Analysis

2.5.1. The host spectrum and stellar velocity dispersion

Comparing the V and R band apparent magnitudes reported by Jahnke et al. (2004a) with the magnitudes inferred from our host spectrum, we found a constant offset of 0.5 mag in both bands. This difference can be easily explained by the brightness variability of the QSO as we matched the overall IFU photometry to the archival magnitude of the QSO with a difference in observation time of several years. Note that our measured $V - R$ colour in the observed frame of 0.36 mag is consistent with the $V - R$ broad-band colour of 0.4 ± 0.05 mag measured by Jahnke et al. (2004a).

While we found consistent colours with the previous broad-band study, we noticed a steep increase in the blue part of the total host spectrum. This feature is even more pronounced for the host spectra within 1.5″ around the nucleus. Whether this blue part of the spectrum originates from a young stellar population around the nucleus, or from scattered QSO light due to circumnuclear dust (e.g Antonucci & Miller 1985; Zakamska et al. 2005), or whether it is an artifact of a systematic PSF mismatch in the decomposition process in that spectral region, we are currently unable to say. However, we do resolve the strong absorption lines around MgI λ5166 even at the low level of signal as shown in Fig. 2.3, so the stellar component has a significant contribution to the continuum emission.

We modelled the integrated host spectrum excluding the central 1.5″ with a linear combination of high spectral resolution SSP spectra employing the STARLIGHT spectral synthesis code (Cid Fernandes et al. 2005; Mateus et al. 2006). The SSP spectra with a spectral sampling of 0.3Å were generated with the Sed@ code[4] as presented in González Delgado et al. (2005) with the following inputs: initial mass function from Salpeter (1955) in the mass range 0.1-120 $M_\odot$; the high resolution library from Martins et al. (2005) based on atmosphere models from PHOENIX (Hauschildt & Baron 1999; Allard et al. 2001), ATLAS9 (Kurucz 1991) computed with SPECTRUM (Gray & Corbally 1994) and the ATLAS9 library computed with TLUSTY (Lanz & Hubeny 2003). Our input grid contains 39 SSP spectra with ages of $1, 3, 5, 10, 25, 40, 100, 300, 600, 900, 2\,000, 5\,000$ and 10 000 Myr and metallicities of 0.004, 0.02 and 0.04 Z.

Monte Carlo simulations were used to determine the errors of the best-fit parameters, the flux-weighted stellar age $\langle t_* \rangle$ and metallicity $\langle Z \rangle$ at a normalisation wavelength of $\lambda_0 = 5075$Å, the extinction (A_V) and the stellar velocity dispersion (σ_*). We generated 200 mock spectra of the host on the basis of the observed host spectrum combined with its wavelength dependent noise budget. These 200 artificial host spectra were analysed with STARLIGHT exactly as the observed host spectrum itself. Finally, a linear combination of only 5–7 SSP spectra was sufficient for modelling all spectra. The other SSP base spectra of the grid were discarded from the modelling in the first iteration by STARLIGHT as their total contribution to the flux density at the normalisation wavelength were less then 2%. The resulting parameters were $\langle t_* \rangle = 5 \pm 0.5$ Gyr, $\langle Z \rangle = 0.024 \pm 0.003$, $A_V = 0.5 \pm 0.2$ and $\sigma_* = 320 \pm 90$ km/s (corrected for the instrumental resolution of ∼42 km/s). We repeated the same analysis excluding the blue part of the host spectrum (3800–4700Å rest-frame wavelength) and arrived at consistent results within the errors. To our knowledge this is the first time that σ_* was estimated for the host galaxy of such a luminous QSO. Jahnke et al. (2004a) derived a younger stellar population with 0.7-2 Gyr based on SSP modeling of the *VRIJHK* multi-colour spectral energy distribution. A direct comparison with our result needs to be taken with caution due to the completely different analysis method used to infer the characteristic age of the stellar population. However, we note that the distribution of stellar populations that contribute to the composite spectrum is clearly bimodal and consists of a young stellar population with ages <100 Myr (53 ± 5% of the total flux at λ_0) in addition to an old stellar population with 10 Gyr age (47 ± 5% of the total flux at λ_0). This indicates the presence of a young stellar component if the main contribution to the blue continuum of the spectrum is of stellar origin and not due to a featureless continuum that can hardly be distinguished from such a young stellar component (e.g Storchi-Bergmann et al. 2000).

2.5.2. The QSO spectrum

The top panel of Fig. 2.2 shows the QSO spectrum of HE 1029−1401 in the full wavelength range covered by our observations. We now focus on the analysis of the Hβ-[O III] region using a multi-component fitting scheme to deblend the various

[4] Sed@ is a synthesis code included in the *Legacy Tool project* of the *Violent Star Formation Network*; see *Sed@ Reference Manual* at `http://www.iaa.es/~mcs/sed@` for more information

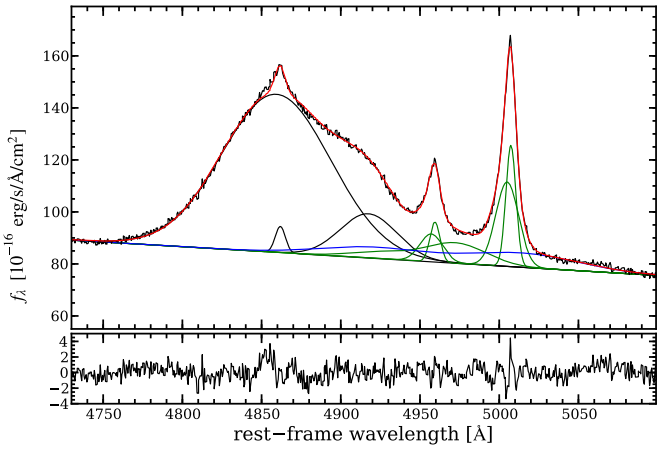

Fig. 2.4. Multi-component fit to the Hβ-[O III] spectral region of the QSO spectrum. The best-fit model is indicated by the red solid line and the individual Gaussian components are plotted above the local linear continuum with the following colour coding: Hβ line (black), [O III] doublet lines (green), Fe II doublet lines (blue). The residuals of the model are shown below with a refined scaling.

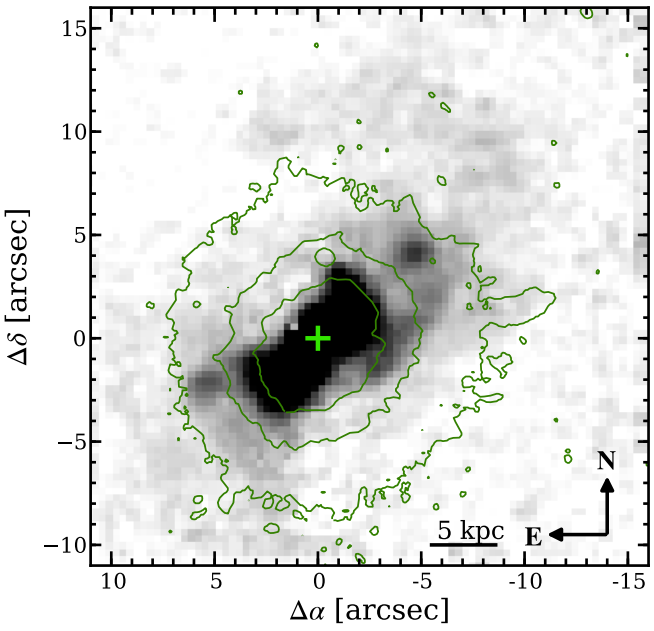

Fig. 2.5. Nucleus-subtracted continuum-free [O III] λ5007 narrow-band image. The 20Å wide band was centred on the nuclear [O III] λ5007 wavelength. A green cross marks the position of the QSO. The contours indicate the position and morphology of the host in comparison to the ionised gas morphology.

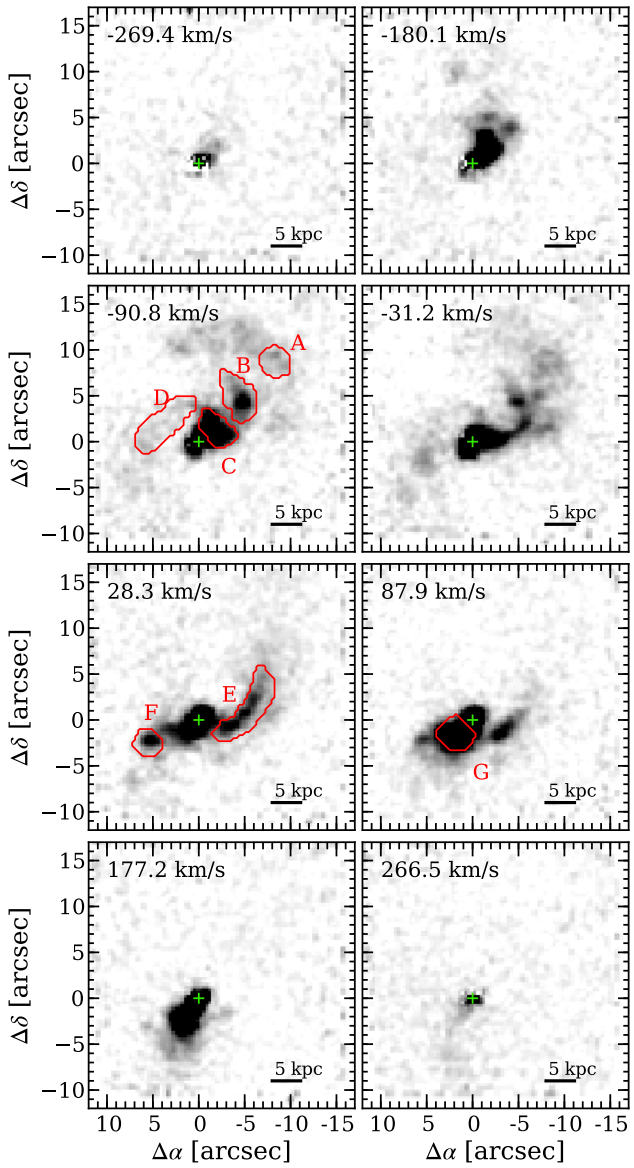

Fig. 2.6. [O III] channel maps created from monochromatic datacube slices corresponding to rest-frame radial velocities of −269.4, −180.1, −90.8, −31.2, +38.3, +87.9, +177.2, +266.5 km/s, respectively. The main distinct emission line regions are labelled alphabetically from A to G and the red boxes indicate regions that were co-added to obtain their characteristic spectrum (Fig. 2.7). The position of the QSO is marked in each map by the green cross.

emission lines in this spectral region. Our model consists of several Gaussian components and a simple linear relation to approximate the local continuum. The best-fit model to the spectrum and its individual components are shown in Fig. 2.4.

The Hβ line exhibits an asymmetric line profile with enhanced emission on its red wing, which can be well described by a redshifted Gaussian component. From the model we measured a line width of the broad Hβ line of 6195±80 km/s (FWHM) and 2352±30 km/s (σ). Furthermore, the [O III] λ5007 (hereafter [O III])line profile is asymmetric to the blue side requiring a second Gaussian component. The two [O III] components are separated by 120±50 km/s in rest-frame and have FWHM values of 421±50 km/s and 975±129 km/s, respectively. Additionally, a third extremely broad and blueshifted component is required to reach an acceptable fit. We are not sure whether this component is physical, representing a true extension of the asymmetric [O III] line profile, or whether it should be rather attributed to the complex and asymmetric line profile of the Hβ line. The continuum flux density at 5100Å (rest-frame) is $(93.4 \pm 11.6) \times 10^{-16}$ ergs^{-1}cm^{-2}Å^{-1} corresponding to a luminosity of $\log(\lambda L_\lambda/[\mathrm{erg/s}]) = 44.97 \pm 0.05$.

With these measurements we estimated a black-hole mass from the single epoch QSO spectrum using the virial method. This calculation is based on the empirical relation between the broad-line region radius and the continuum luminosity at 5100 Å calibrated by Bentz et al. (2006), and the prescription by Collin et al. (2006) to infer the velocity of the broad line clouds from the Hβ line dispersion adopting a scale factor of 3.85. This yields a black hole mass of $\log(M_{\rm BH}/M_\odot) = 8.7$ for HE 1029−1401. The measurement errors for the black hole mass are much smaller in this case than the systematic errors of the method, thus we adopted a canonical error of 0.3 dex. Assuming the $M_{\rm BH}$-σ_* relation of Tremaine et al. (2002) our measured stellar velocity dispersion σ_* predicts a black hole mass of $\log(M_{\rm BH}/M_\odot) = 8.9^{+1.0}_{-0.4}$, which is perfectly consistent with our virial black hole mass estimate.

Adopting a bolometric correction of $L_{\rm Bol} = 9 \times \lambda L_\lambda(5100\text{Å})$ (Kaspi et al. 2000), we estimated a bolometric luminosity of $\log(L_{\rm Bol}/[\rm erg/s]) = 46.0 \pm 0.2$ and an Eddington ratio of $\log(L_{\rm Bol}/L_{\rm Edd}) = -0.9 \pm 0.2$ for the QSO.

2.5.3. Ionised gas distribution and channel maps

In Fig. 2.5 we present an [O III] narrow-band image (20Å bandwidth) extracted from the datacube after subtracting the QSO contribution. Continuum emission from the host galaxy was previously subtracted to obtain a pure emission-line image. This is the first two-dimensional map of the ionised gas distribution around HE 1029−1401.

The image reveals ionised gas on scales of several kpcs. We find a highly structured distribution of the ionised gas. The brightest structure is a symmetric circumnuclear bicone suggestive of an ionisation cone by the QSO. Furthermore, we detect ionised gas in several knots and arms and in a faint giant arc-like feature north-west to the galaxy centre at a projected distance of 16 kpc. Most of the distinct emission-line regions are well located inside the visible light distribution of the early-type host galaxy when compared with the *HST* image in Fig. 2.1. The prominent bicone-like structure is roughly aligned with the major axis of the host galaxy, although the orientation of the latter is not well constrained due to the low ellipticity of the host.

The integrated extended [O III] line flux is $(328 \pm 88) \times 10^{-16}\,\rm erg\,s^{-1}cm^{-2}$ corresponding to an [O III] luminosity of $\log(L([\rm O\,III])/[\rm erg/s]) = 41.78 \pm 0.12$. This is one of the most luminous extended emission-line regions (EELRs) around a radio-quiet QSO compared to other radio-quiet ones, e.g. in the sample of Stockton & MacKenty (1987).

In Fig. 2.6 we present [O III] channel maps corresponding to monochromatic images at specific radial velocities with respect to the rest-frame of the objects. In this way we can identify low-surface brightness emission-line regions that are relatively faint in the integrated line image or that spatially overlap but are separated in velocity space. The main emission line regions are labelled alphabetically from A to G and their characteristic spectra were obtained by co-adding several spatial pixels within the boundary indicated by the red boxes. These regions are a symmetric bicone-like structure around the nucleus (regions C and G), two arm-like structures (regions D and E), two emission-line knots (regions B and F) and part of the giant arc-like feature ∼16 kpc north-west of the nucleus (region A). We excluded the central ∼1″ region around the QSO from these spectra because of significant residuals of the QSO subtraction.

2.5.4. Spectral analysis of specific regions

Co-added spectra of the regions A–G as defined in the previous subsection are shown in Fig. 2.7. These were split up into two narrow wavelength ranges bracketing the Hβ and Hα emission lines. No signatures of the broad emission lines of the QSO are visible in any of the extracted spectra after the spectral decomposition. The Hβ, [O III] $\lambda\lambda$4959, 5007, Hα and [N II] $\lambda\lambda$6549, 6585 emission lines are clearly detected in most of the selected regions. The [S II] $\lambda\lambda$6716, 6731 emission lines are only visible in the spectra of region C and G.

We modelled each spectrum with Gaussian profiles for the emission lines and scaled the best-fitting stellar population spectrum (cf. Sect. 2.5.1) to the continuum. We found that stellar absorption lines have no significant effect on the Balmer emission line. The flux ratio of the [O III] and [N II] doublets were fixed to their theoretical values and all emission lines were kinematically coupled to have the same redshift and line dispersion. We utilised Monte Carlo simulations to estimate realistic errors for all free fit parameters. 100 mock spectra were generated for each spectrum according to the noise of the spectrum as estimated from the adjacent continuum. These mock spectra were consistently analysed and the standard deviation of the resulting distribution for each fitted parameter was taken as its 1σ error. A 3σ upper limit is given for the flux of the Hβ line in region A as it falls below the detection limit. The measured emission line fluxes are given in Table 2.1.

We noticed that all emission lines in the spectrum of region G display an asymmetric line profile. A two component Gaussian model for each line provided an excellent fit to the data. The appearance of a second system of kinematically distinct emission-line in region G will be further analysed later in Sect. 2.6.4.

2.6. Results

2.6.1. Source of ionisation and gas metallicity

To infer the dominant ionisation source for the gas we employ the commonly used emission-line ratio diagnostic diagram [O III] λ5007/Hβ vs. [N II]λ6582/Hα (Baldwin et al. 1981; Veilleux & Osterbrock 1987). The diagram distinguishes gas being ionised by the hard UV radiation field of an AGN from gas ionised by radiation from hot stars in star forming H II regions. A theoretically motivated and conservative boundary between both mechanisms was derived by Kewley et al. (2001). The diagnostic diagram is shown in Fig. 2.8 for the emission-line ratios inferred from the spectra of region A–G.

We found that photoionisation by star forming regions can be excluded for all regions as the inferred line ratios are above the Kewley et al. demarcation curve. Of course, this does not imply there is no current star formation in the host, only that AGN ionisation of the ISM dominates strongly over any other ionisation mechanisms. We can also exclude shock ionisation based on the kinematics and the emission-line ratios. The line ratios for the broad shocked gas components in powerful radio galaxies are observed to have a much lower ionisation state with [O III]/Hβ∼2–4 (e.g. Villar-Martín et al. 1999) than observed here. Furthermore, shock-ionisation models (Dopita & Sutherland 1995; Allen et al. 2008) indicate that an [O III]/Hβ line ratio around 10 would require shock velocities > 500 km/s for which we find no evidence in our observations (cf. Sect. 2.6.3). Thus, photoionisation by the central QSO is the dominant ionisation mechanism for the gas in HE 1029−1401 *at least* within a radius of 16 kpc around the nucleus.

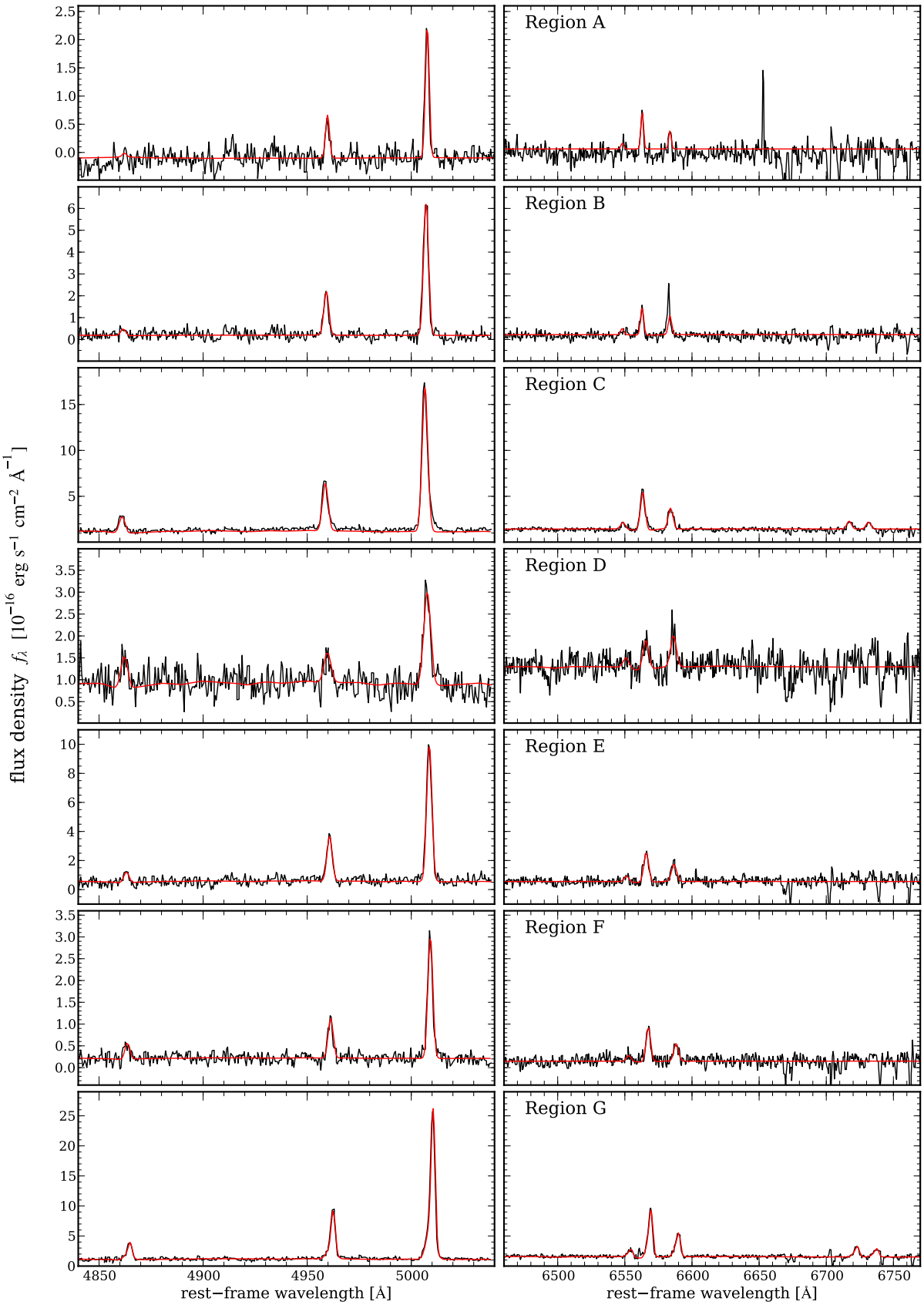

Fig. 2.7. Co-added spectra of the regions A-G (as defined in Fig. 2.6) are shown from top to bottom split up into two wavelength ranges bracketing Hβ (left panels) and Hα (right panels). The black line corresponds to the observed spectrum and the red line to the fitted model. Two systems of Gaussians were required to model the spectrum of region G. The apparent mismatch between the model and the [N II] λ6585 line in region B is due to an artifact, but the model is still constrained due to the doublet nature and the kinematical coupling of the lines.

Table 2.1. Emission line fluxes for the Hβ, [O III] λ5007, Hα,[N II] λ6583 and the [S II] $\lambda\lambda$6716, 6731 lines as measured from Gaussian fits to the spectra of the region A to G.

Region	Hβ	[O III] λ5007	Hα	[N II] λ6583	[S II] λ6716	[S II] λ6731
	line fluxes in units of 10^{-16} erg s^{-1} cm^{-2}					
A	< 0.5	5.9 ± 0.2	1.9 ± 0.2	1.1 ± 0.1	–	–
B	1.0 ± 0.2	19.5 ± 0.3	4.1 ± 0.3	2.8 ± 0.3	–	–
C	7.2 ± 0.2	56.8 ± 0.4	21.7 ± 0.3	11.9 ± 0.3	4.7 ± 0.3	3.8 ± 0.3
D	2.9 ± 0.4	8.5 ± 0.5	4.9 ± 0.5	4.2 ± 0.5	–	–
E	2.7 ± 0.4	32.0 ± 0.5	10.5 ± 0.4	6.1 ± 0.3	–	–
F	1.3 ± 0.1	9.0 ± 0.1	3.8 ± 0.2	2.0 ± 0.2	–	–
G (narrow)	5.7 ± 0.5	52.7 ± 1.7	19.1 ± 3.4	7.5 ± 2.3	2.8 ± 1.1	1.9 ± 0.9
G (broad)	5.2 ± 0.6	29.9 ± 1.8	14.7 ± 2.5	10.6 ± 2.2	4.8 ± 1.2	4.5 ± 1.1

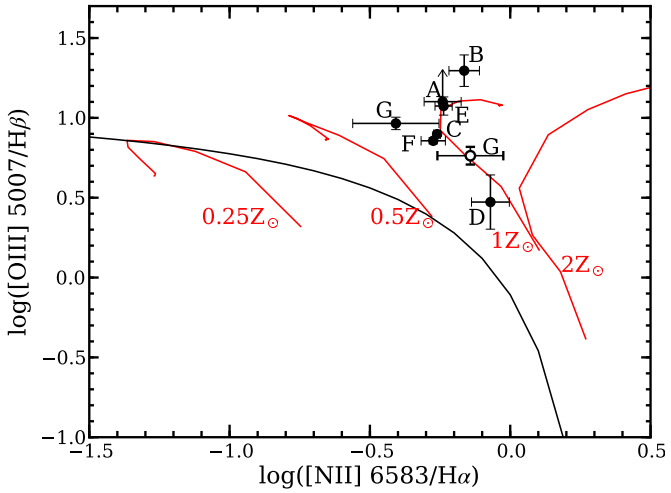

Fig. 2.8. Diagnostic diagram for the emission-line ratios of the regions A-G in HE 1029−1401. The narrow emission-line ratios are indicated by black circles and the broad component in region G is indicated by the black opened circle. The commonly used demarcation curve between AGN and H II regions by Kewley et al. (2001) is indicated as the black solid line. Dusty radiation pressure-dominated photoionisation models (Groves et al. 2004) are indicated by the red tracks for four gas-phase metallicities with $0.25Z_\odot$, $0.5Z_\odot$, $1Z_\odot$ and $2Z_\odot$ with physical parameters as described in the text.

In order to infer the metallicity of the gas we compared the emission-line ratios with the dusty radiation pressure-dominated photoionisation models by Groves et al. (2004). These models are represented by red tracks in Fig. 2.8 corresponding to gas-phase metallicities of $0.25Z_\odot$, $0.5Z_\odot$, $1Z_\odot$ and $2Z_\odot$ assuming an electron density of $n = 100\mathrm{cm}^{-3}$ for the emitting clouds and a power-law index $\alpha = -1.4$ for the ionising QSO continuum. The line ratios do not strongly depend on the electron density, so we chose the model grid with the lowest density close to the estimated value as discussed in the next section. Note that the true metallicities of the photoionisation models are a factor of 2 higher than the gas-phase metallicities, since half of the overall metal content is depleted into dust in the models. The comparison with the photoionisation models revealed that the emission-line ratios follow quite closely the model with a solar metallicity. Only the gas in region B appears to have a systematically different ionisation state and/or metallicity.

2.6.2. Total ionised gas mass

To estimate the total ionised gas mass in HE 1029−1401 we followed the prescription and assumptions of Osterbrock & Ferland (2006). By measuring the luminosity of the Hβ recombination line one can estimate the ionised gas mass $M_{\rm ion}$ using the following formula:

$$M_{\rm ion} = \frac{1.4 m_{\rm p}}{n_e \alpha^{\rm eff}_{\rm H\beta} h\nu_{\rm H\beta}} L_{\rm H\beta}\,, \tag{2.1}$$

where $m_{\rm p}$ is the proton mass, h is Planck's constant, n_e is the electron density, $\alpha^{\rm eff}_{\rm H\beta}$ is the effective recombination coefficient for Hβ and $L_{\rm H\beta}$ is the $H\beta$ line luminosity. Assuming Case B recombination, the low-density limit and a typical gas temperature of $T \approx 10,000$ K for ionised nebulae, we end up with

$$M_{\rm ion} \approx 10^7 \left(\frac{100\,\mathrm{cm}^{-3}}{n_{\rm e}}\right)\left(\frac{L_{\rm H\beta}}{10^{41}\,\mathrm{erg\,s}^{-1}}\right) \tag{2.2}$$

In our case we were able to measure the electron density sensitive [S II] λ6716/λ6731 emission-line ratio only in high-surface brightness regions of the bicone structure (region C and G). The line ratios in region G are rather uncertain due to the line blending of a narrow and broad component, so that we estimated the electron density from region C only. We measured a [S II] λ6716/λ6731 line ratio of 1.2 ± 0.1 for region C. This ratio implies an electron density of $200^{+150}_{-110}\mathrm{cm}^{-3}$ (Osterbrock & Ferland 2006, p. 123) assuming an electron temperature of 10 000 K.

Since the narrow Hβ line is the weakest in all of the spectra, we used the [O III] emission line as a surrogate for the Hβ emission assuming a line ratio of [O III]/Hβ ∼ 10 (cf. Fig. 2.8). With the integrated [O III] line luminosity measured from the [O III] narrow-band image (c.f. Sect. 2.5.3) and our adopted electron density, we estimated an ionised gas mass of $M_{\rm ion} = 3^{+6}_{-2} \times 10^6\,M_\odot$. Note that we did not take reddening due to dust in the host galaxy into account, which would increase $L_{\rm H\beta}$ and hence the ionised gas mass. Our inferred ionised gas mass should be taken as a rough estimate due to the various assumptions needed and can only be used at an order-of-magnitude level.

2.6.3. Global gas kinematics

In order to obtain full 2-D velocity and velocity dispersion maps of the ionised gas we fitted the [O III] doublet lines as they are the brightest emission lines in all of the individual 6400 spectra of the nucleus-subtracted datacube. The measured emission-line

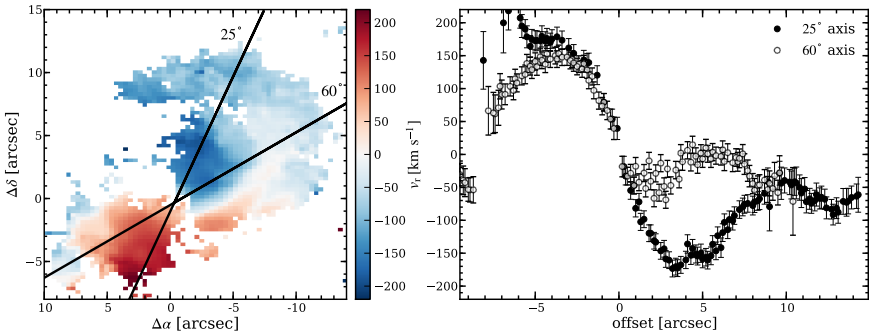

Fig. 2.9. *Left panel:* [O III] velocity map of HE 1029−1401 with respect to its estimated systemic velocity (25670 km/s). The two black lines correspond to position angles of 25° and 60°, respectively. *Right panel:* Velocity curves extracted for these two orientations from the maps. Negative offsets correspond to the South-East side and positive offsets to the North-West side of the nucleus.

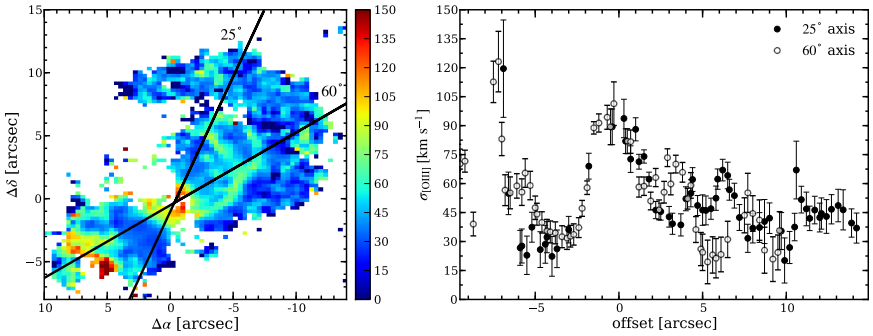

Fig. 2.10. Same as Fig. 2.9, but for the [O III] velocity dispersion, corrected for the spectral resolution of the instrument.

centroids were converted into radial velocities with respect to the systemic redshift for each spatial pixel to construct a 2-D velocity map (Fig. 2.9 left panel). A different visualisation of the velocity field are 'long-slit' velocity curves (Fig. 2.9 right panel) extracted from our velocity map for the position angles (PAs) 25° and 60°. We chose these two PAs such that one shows the velocity curve of the bi-cone structure and the other to cross the arm-like feature. Similarly, we present a 2-D [O III] velocity dispersion map (Fig. 2.10 left panel), corrected for the spectral resolution of the instrument, and the corresponding 'long-slit' curves (Fig. 2.10 right panel). The gaps in the velocity and dispersion curves around the circumnuclear region are due to the strong residuals of the decomposition process which prevent a reliable measurement of the extended emission lines.

The 2-D kinematic information from our IFU data draws a much clearer picture than previous long-slit studies of this object. While the [O III] velocity curve at a PA of 25° appears like a symmetric rotation curve up to 5″ from the galaxy centre, it is highly disturbed at larger distances. At a PA of 60° the velocity curve crosses the arm-like structure detected in the [O III] flux distribution which clearly breaks the symmetry seen at a PA of 25°. We measured a maximum amplitude of ±170 km/s for the radial velocities at a distance of 4.8 kpc (3″) from the nucleus, which is consistent with the measurements by Let07 and Jah07 based on long-slit spectroscopy only. However, the long-slit velocity curve presented by Let07 covers only ±4″ which is less than half of the region we studied with our IFU data. Therefore, they miss the turnover of the velocity curve at 4″–6″from the nucleus. Another major kinematic component is the prominent distortion in the rotational velocity field on the West side of the nucleus, which was missed by the long-slit data of Let07 and Jah07.

The measured velocity dispersion (σ) of the gas after correcting for the instrumental resolution is ∼ 30 km/s on the red- and ∼40 km/s on the blue-shifted side of the velocity curve. On both sides the v/σ ratio is significantly greater than 1, which indicates rotational support of the gas in a disc. This is consistent with the conclusion of Jah07. The velocity dispersion increases significantly up to ∼ 80 km/s between the region of the gas disc and the major kinematic distortion on the West side. This is most probably related to the superposition of the two kinematic components as we find asymmetric and double-peaked emission-lines in this particular region. In the circumnuclear region the velocity dispersion rises steeply towards the centre. We will study the kinematics of this region in greater detail in the next section.

2.6.4. Gaseous kinematics in the inner 3 kpc

As previously mentioned in Sect. 2.5.4, a two component model for the emission lines was required to model the spectrum of region G. We present the model for that spectrum and the individual emission-line components in Fig. 2.11. All the strong emission lines are clearly asymmetric and a second broader Gaussian component is needed to match this asymmetry. Furthermore, we found that all emission lines share the same kinematics and were therefore kinematically coupled in the model. We inferred a velocity dispersion of 45 km/s for the narrow and 110 km/s for the broad component.

From the spatially resolved kinematics assuming only a single Gaussian for the emission line, we note that the velocity dispersion is rising close to the centre. This suggests that the broad component is also spatially resolved. Thus, we modelled each spectrum of the datacube with a two-component Gaussian model for the [O III] doublet emission line. We employed the statistical F-test on the χ^2 values for the two models to decide weather the two component model is a statistically significant better representation of the spectrum than a single component model. The resulting maps of the flux distribution, radial velocity and velocity dispersion for the narrow and broad components are shown in Fig. 2.12.

These maps reveal that the narrow component originates from rotationally supported gas without a major increase in the velocity dispersion as close as 1 kpc to the QSO. The broad com-

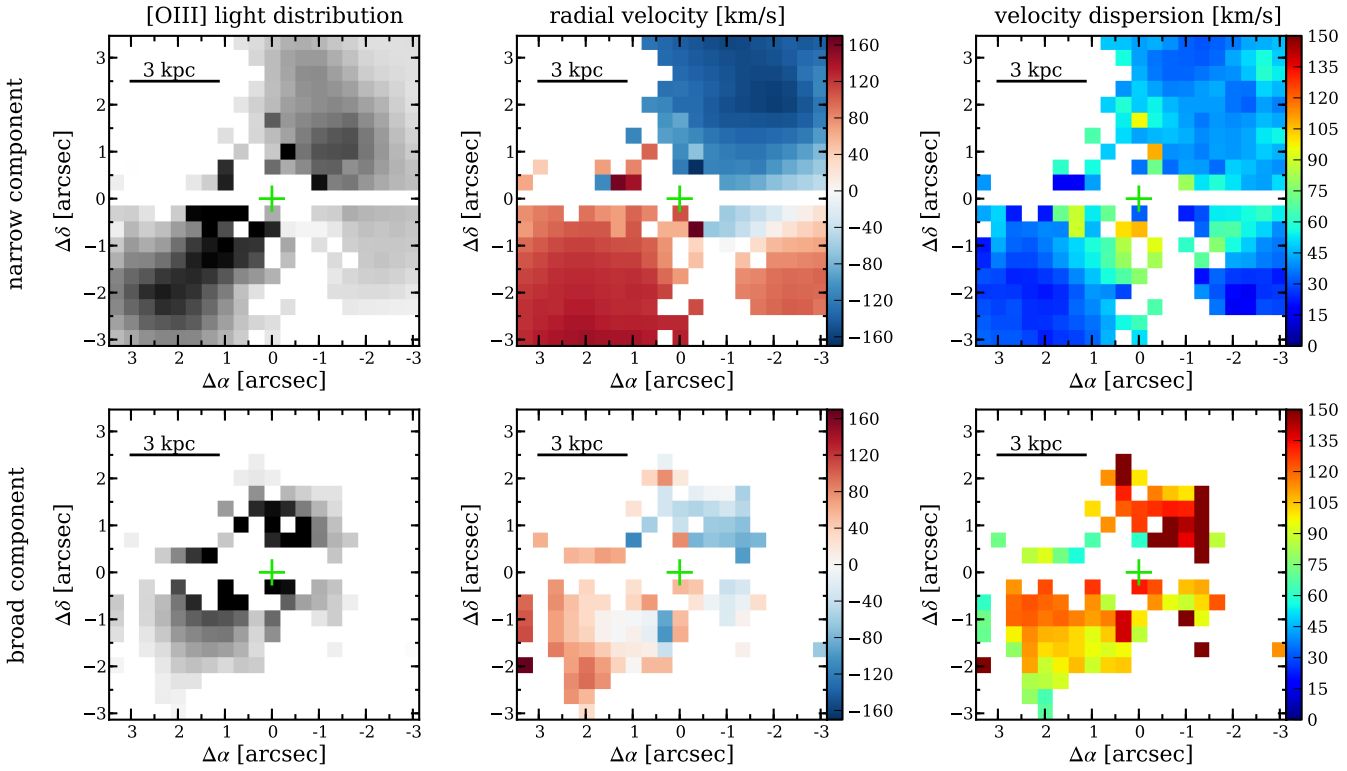

Fig. 2.12. Distribution and kinematics of two kinematically distinct emission line components. The flux distribution (left), radial velocity (middle) and velocity dispersion (right) are shown for the narrow emission line in the top panels and in the bottom panels for the broad component.

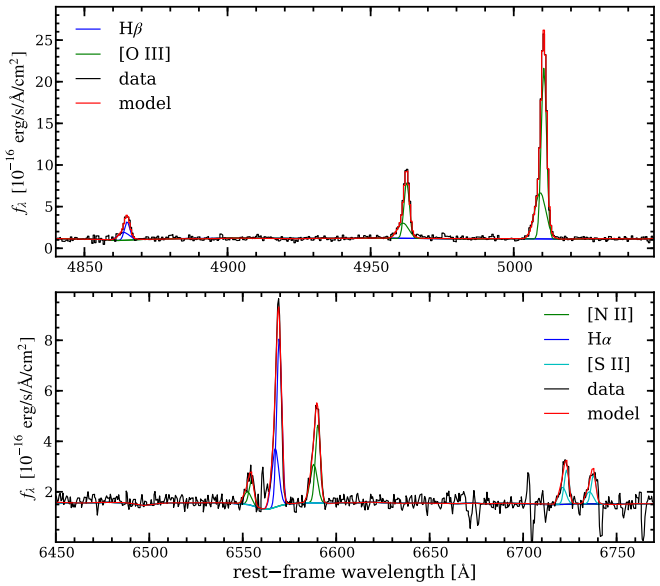

Fig. 2.11. Detailed modelling of the emission lines in the spectrum of region G. The emission lines around Hβ are shown in the top panel and the ones around Hα in the bottom panel. The spectrum and its model together with the individual Gaussian components for the emission lines are plotted with colours given the in legend.

ponent, on the other hand, is almost non-rotating with a velocity gradient of only ±40 km/s compared to ±120 km/s of the rotating gas in the same region. The spatially resolved velocity dispersion of the gas in the broad component were measured to be in the range of $\sigma_g = 100 - 140$ km/s in agreement with the velocity dispersion inferred from the integrated spectrum of region G. Because σ/v is greater than 1 for the broad component, this gas seems to be dispersion dominated and mainly supported by random motion. We also detected the broad component on the blueshifted side of the rotating gas coincident with region C, which is hardly noticeable in the integrated spectrum of that region as the flux in the broad component is much lower than theflux in region G. This dispersion dominated gas component in the circumnuclear region was not detectable in the previous studies by Let07 and Jah07 due to the lower spectral resolution.

2.6.5. Surface brightness profiles and apparent neighbouring galaxies

We measured the radial surface brightness profiles of the stellar continuum emission as seen by *HST* and of the [O III] line emission from the VIMOS data using circular annuli. To account for the biconical structure of the [O III] light distribution we also computed surface brightness profiles within a 70° wide cone along the major and minor axis. Due to the low spatial resolution of the VIMOS date we took the subpixel coverage of the annuli and cones into account. Since the ratio of [O III] to Hβ is constant of ∼10 for the entire galaxy, it is reasonable to assume that the [O III] light distribution is a tracer of the ionised gas distribution. The profiles are compared in Fig. 2.13 after the *HST* surface brightness was scaled to match the total [O III] surface brightness in the radial distance range from 7.5″ to 9″.

Surprisingly, the surface brightness profile of the total ionised gas apparently follows that of the stars on a global scale

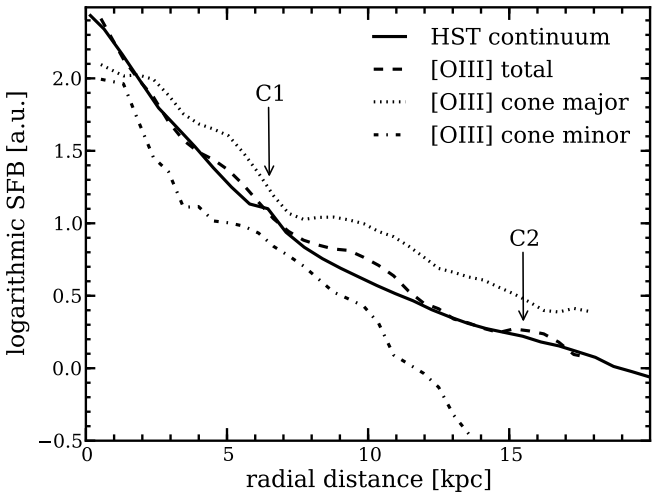

Fig. 2.13. Radial surface brightness profiles of the stellar continuum (solid line) compared with the total ionised gas distribution (dashed line), the ionised gas within a 70° wide cone along the major axis of [O III] (dotted line) and the ionised gas for a similar cone along the minor axis (dashed-dotted line). The surface brightness profile of the stellar continuum was scaled to match that of the total ionised gas between 7.5″ (12 kpc) and 9″ (14.5 kpc) radial distance. The radial distances of the apparent companions C1 and C2 are marked for comparison.

despite the morphological difference. However, the profiles are significantly different for the light distribution in the cones along the major and minor axis. The drop in the [O III] surface brightness along the minor axis is steep with a power-law index of -1.8. This is roughly consistent with the geometrical decrease in the ionising photon density that scales as r^{-2}. On the other hand, the profile along the major axis is much shallower also with respect to the stars indicating that the radial ionised gas distribution is determined by the gas density rather than the amount of available ionising photons in this direction. The distinct [O III] emission line knots and arcs as identified in the [O III] narrowband image and channel maps (cf. Fig. 2.5 and Fig. 2.6) produce excesses in the total [O III] surface brightness profile and along the major axis at around 5 kpc, 10 kpc and 16 kpc radial distance as expected. We do not detect any corresponding features in the continuum surface brightness profile. The stellar surface brightness profile itself is rather smooth except for the bright apparent companion C1 located 4 arcsec away from the host centre, but we do not find any significant excess in the [O III] surface brightness at that location neither in the major nor the minor axis cone.

We consider two explanations for the lack of ionised gas at the location of the bright apparent neighbouring galaxy C1 north to the nucleus: 1.) The galaxy is not a physical companion so its gas cannot be ionised by the QSO. 2.) The galaxy is a physical companion with an intrinsically low amount of gas to be ionised.

The relation of the second faint galaxy to the host galaxy of HE 1029−1401 remains unclear. We detected weak [O III] emission at its position which corresponds to one end of the large arc-like structure seen at a distance of 10″. It is possible that gas is stripped off from the faint companion while it is orbiting around the host galaxy forming a tail of gas that is partially illuminated by the QSO radiation. Since redshift information is not available for this galaxy, a simple projection effect is also a reasonable explanation.

2.7. Discussion

2.7.1. The unexpected anisotropic AGN radiation field

The biconical distribution of the ionised gas in the circumnuclear region of HE 1029−1401 appears to be very similar to the ionisation cones detected in several nearby Seyfert galaxies (e.g. Pogge 1988a,b; Storchi-Bergmann & Bonatto 1991; Storchi-Bergmann et al. 1992). These collimated AGN radiation cones are supporting the unified model for AGN in which the nucleus is thought to be surrounded by a dusty torus providing a partial obscuration of the AGN. This model explains the distinction between type 1 and type 2 AGN solely by the orientation of the obscuring torus with respect to the observers line-of-sight. In this picture, the opening angle of the ionisation cones is simply determined by the covering factor of the torus.

Why is such an anisotropic radiation field on kpc scales unexpected for a luminous type 1 QSO like HE 1029−1401? Firstly, ionisation cones are best seen if they are oriented perpendicular to our line-of-sight, which means that the torus is oriented almost edge-on and the AGN is obscured. This is the reason why most of the known ionisation cones were detected in Seyfert 2 galaxies. Secondly, the 'receding torus' model (Lawrence 1991) predicts the opening angle of the AGN ionisation cones to increase with the AGN luminosity, which is observationally supported by the decreasing fraction of obscured AGN with increasing luminosity in X-ray selected AGN samples (e.g. Ueda et al. 2003; Hasinger 2004, 2008). The X-ray 2–10 keV luminosity of HE 1029−1401 is $2.3{\times}10^{44}$ erg s^{-1} (Reeves & Turner 2000, converted to a concordance cosmology) corresponding to a type 2 fraction of ≃30% (Hasinger 2008, , see Fig. 1.2). From this fraction one would expect a large opening angle of ∼115°, much more than what our observations suggest.

Mulchaey et al. (1996) simulated the apparent emission-line images of the ionisation cones assuming that the ambient gas distribution is a spheroid or disc. They found that for a spheroidal gas distribution the emission-line image may have a V-shape morphology but the apparent opening angle is always equal or greater than the opening angle of the ionisation cones. Due to the rotational motion of the gas, our observations indicate that the gas is more likely to be distributed in a disc rather than in a sphere. In that case, the apparent opening angle from the emission-line images is always *smaller* than the opening angle of the ionisation cones depending on the angle between the disc and cone axis. If the ionisation cones is oriented such that it intercepts the disc almost at its edge, the apparent opening angle would be much smaller and consistent with our observations. Thus, the morphology of the emission-line gas around HE 1029-1401 can be consistent with the expectation of the unifed model of AGN if the ambient gas is distributed in a disc combined with a certain configuration of the AGN ionisation cones with respect to the disc.

2.7.2. The origin of the gas

We inferred from our IFU data that the elliptical host of HE 1029−1401 contains ionised gas with a mass of the order of 5×10^6. The ionised gas mass is rather small compared to the stellar mass of the system that has been measured to be $M_{\rm stellar} \approx 1 \times 10^{11} M_\odot$ based on broad-band SED modelling (M. Schramm, private communication). Unfortunately, the neutral gas fraction of HE 1029−1401 is unknown. Thus, it is unclear if HE 1029−1401 contains more gas than comparable inactive

early-type galaxies, or whether the luminous QSO is just able to ionise a significant fraction of the neutral gas content.

But where did the gas come from? Our emission-line diagnostic analysis showed that the metallicity of the gas is close to solar. We now compare this with the mass-metallicity relation of star-forming galaxies as presented by Tremonti et al. (2004). As the mass-metallicity relation depends critically on the assumed metallicity estimator (Kewley et al. 2006), the Tremonti et al. (2004) relation best matches with our metallicity estimation as it is also based on the CLOUDY photoionisation code (Ferland 1996). What we find is that the expected value for the oxygen abundance for a galaxy with a stellar mass of $10^{11} M_{\odot}$ is $12 + \log(\mathrm{O/H}) = 9.11$. This is more than 0.3 dex larger than the solar oxygen abundance measured for HE 1029−1409. Although the scatter in the mass-metallicity relation is non-negligible, the metallicity of the gas in HE 1029−1409 would correspond to a $>3\sigma$ deviation from the Tremonti et al. (2004) mass-metallicity relation at a stellar mass of $10^{11} M_{\odot}$.

Peeples et al. (2009) and Sol Alonso et al. (2010) recently showed that the high-mass low-metallicity outliners of the mass-metallicity relation are morphologically disturbed galaxies with bluer colours (or younger stellar populations) suggesting an inflow of low-metallicity gas driven by galaxy interactions and accompanied by enhanced star formation. This is consistent with the observations of HE 1029−1401, but the signatures for galaxy interactions are weak with only the faint shells detected by Bahcall et al. (1997). The high stellar mass and smooth surface brightness profile of the host suggest that the last major merger that formed the elliptical galaxy happened at a much earlier epoch. Assuming that the gas originates entirely from a single progenitor galaxy, the solar gas phase metallicity would correspond to a stellar mass of roughly $5 \times 10^9 M_{\odot}$ almost 10 times smaller than the host mass of HE 1029−1401 itself. This is consistent with the picture that ionised gas originates from one or a few minor companions that merged with HE 1029−1401. Therefore, we favour to interpret the low metallicity of the ionised gas in HE 1029−1401 as a clear indication for an *external* origin of the gas via the infall of one or a few minor companions.

Similar results have been obtained for the EELRs around the radio-loud QSOs 4C 37.43 (Fu & Stockton 2007) and 3C 79 (Fu & Stockton 2008). The authors found in both of these cases a solar to sub-solar metallicity of the ionised gas on kpc scales around their massive elliptical host galaxies containing black holes with a mass of the order of $10^9 M_{\odot}$. They also came to the conclusion that the metal-poor gas needs to have an external origin.

2.7.3. The kinematics of the ionised gas – Indications for mergers or AGN outflow?

The [O III] emission-line profile in the nuclear spectrum is asymmetric, which we resolved into two distinct Gaussian components with a FWHM of 421±50 km/s and 975±129 km/s, respectively, where the broader component is blueshifted by 120 ± 50 km/s. Such asymmetric [O III] lines have been previously reported in many other QSOs (e.g. Heckman et al. 1981; Véron-Cetty et al. 2001) and were interpreted as an indication for high ionisation outflows from the nucleus (Zamanov & Marziani 2002). We can not spatially resolve the extended ionised gas closer than ∼1 kpc from the nucleus, but outside this unresolved region we did not find any signatures for a similarly broad and blueshifted ionised gas component indicating that this possibly outflowing component is restricted to scales below ∼1 kpc.

Instead, we find that the majority of the extended ionised gas appears to be bound in a rotationally supported gas disc. The lack of rotational motion in the corresponding stellar component as inferred by Jah07 further supports an external origin of the gas from a kinematically point of view. The non-rotating dispersion-dominated ionised gas within the central 3 kpc could either represent an *intrinsic* reservoir of gas originating from the stars in the host or gas that is directly heated by the AGN.

On larger scales the kinematics of the ionised gas around HE 1029−1401 strongly deviates from the rotational motion of the disc. García-Lorenzo et al. (2005) found a similarly distorted kinematic pattern in the gaseous velocity field and inner shells around the nucleus of 3C 120, which they interpreted as evidence for a merging event. Above we invoked minor mergers to explain the external origin of the gas, which would also provide a consistent explanation for the distortion in the velocity field. On the other hand, morphological distortion in the stellar component should be detected at the location of the kinematical distortions if mergers play the dominant role. It could be that the current *HST* image of HE 1029−1401 is simply too shallow to detect faint morphological distortions. Bennert et al. (2008) found shells and tidal tails in four out of five elliptical QSO host galaxies observed with *HST* in deep exposures suggesting that merger are quite common for such galaxies. But without a matched control sample of inactive elliptical galaxies this result cannot be taken as a direct evidence for a causal link between mergers and QSO activity. Indeed, in a large sample of mainly inactive elliptical galaxies presented by Tal et al. (2009), similar distortions were found in 75% of them with no correlation between AGN activity and large scale distortions. However, their AGN comparison sample consists mainly of low-luminosity radio galaxies which might have a different fuelling mechanisms compared to luminous QSOs.

As an alternative possibility we speculate that these structures could be ionised filaments on the surface of an expanding shell/bubble driven out by the AGN. Two examples of such outflowing bubbles were investigated recently with detailed IFU observations of the Broad Absorption Line QSOs Mrk 231 (Lipari et al. 2009) and HE 0450−2948 (Lípari et al. 2009). They argued that these outflows are part of galactic outflows driven by extreme starbursts as the result of major mergers which possibly lead also to the onset of QSO activity due to an interaction between the nuclear star formation and the central black hole. Such a particular phase of QSO activity has been claimed to be part of an evolutionary sequence of AGN (e.g. Sanders et al. 1988a,b; Lipari 1994; Canalizo & Stockton 2000; Papadopoulos et al. 2008; Lípari & Terlevich 2006, and references therein) as a short transition phase before the QSO becomes dominant. In this scenario HE 1029−1401 would have to be place at the end of a potential AGN evolutionary path, the QSO dominant phase. Yet, due to the unknown geometry and proper motion of these intriguing structures, it is difficult to pin down the nature of the disturbed velocity field as due to an expanding bubble. An interpretation as signatures of (minor) merging appears at least as likely.

2.8. Summary and Conclusions

We presented optical integral field spectroscopy observations of the luminous radio-quiet QSO HE 1029−1401 obtained with the VIMOS instrument at the VLT. A dedicated decomposition technique for IFU data was used to decompose the spectra of the host and the QSO component. This allowed us to perform a detailed spatially-resolved analysis of the ionised gas properties based

on emission-line diagnostics and a tentative analysis of the integrated stellar continuum at a S/N level of ∼10. We draw the following conclusions from our present study of this QSO:

- We found tentative evidence from the stellar continuum for a blue featureless continuum or a young stellar population (<100 Myr) embedded in the old stellar population (10 Gyr) of the massive elliptical host galaxy. The stellar velocity dispersion is estimated to be $\sigma_* = 320$ km/s, although the uncertainty of ±90 km/s is considerable.

- The black hole mass is estimated from QSO spectrum to be $\log(M_{\rm BH}) = 8.7 \pm 0.3$ accreting at an Eddington ratio of $\log(L_{\rm Bol}/L_{\rm Edd}) = -0.9 \pm 0.2$. Our $M_{\rm BH}$ and σ_* measurements are consistent with the $M_{\rm BH} - \sigma_*$ relation of Tremaine et al. (2002) within the uncertainties.

- We detected highly ionised gas in the host galaxy up to a projected distance of at least ∼ 16 kpc that is solely ionised by the QSO radiation. The integrated [O III] luminosity of this EELR is with $\log(L([\mathrm{O\,III}])/[\mathrm{erg/s}]) = 41.78 \pm 0.1$ one of the most luminous EELR detect around a radio-quiet QSO. The total ionised gas mass was estimated to be $3^{+6}_{-2} \times 10^6 M_\odot$, which should be correct at an order-of-magnitude level only.

- The morphology of the ionised gas appears to be biconical with additional faint knots and arcs at larger distances. The rather narrow bicones may imply more collimated ionisation cones of the AGN than predicted by the unification model for such a luminous QSO. Assuming a disc-like distribution of gas, we prefer to interpret the biconical emission-line image as the projection of the partially illuminated gas disc.

- Comparison of photoionisation models with the observed emission-line ratios of the gas indicated that the metallicity of the gas is significantly lower than expected from the mass-metallicity relation of galaxies. We interpret this as an external origin of the gas and argue that this is most likely due to minor merger(s).

- We found that the ionised gas is rotationally-supported with an additional dispersion-dominated component in the circumnuclear region up to ∼3 kpc. The ordered velocity field is clearly distorted on larger scales that either support the scenario of minor mergers or might be speculatively interpreted as filaments on the surface of an AGN-driven outflowing shell/bubble. However, we did not find clear and conclusive evidence for an AGN outflow.

Our observations draw a scenario of HE 1029−1401 in which the massive elliptical host has recently accreted fresh gas from its environment via minor mergers. This process leaves the host morphology almost unchanged, but the black hole accretion can be 're-juvenated' and a disc of gas is formed. If the accretion event is accompanied by a short burst of star formation, the previous red elliptical galaxy would become bluer moving the galaxy back to the 'green valley' in the colour-magnitude diagram. The importance of minor mergers in the late evolution of the early-type galaxies population has recently been highlighted (Naab et al. 2009; Johansson et al. 2009; Bezanson et al. 2009). It might also be an important process to explain a luminous AGN phase in early-type galaxies as indicated by our single-object study.

Acknowledgements. We thank the anonymous referee for his comments that improved the clarity of the manuscript. BH would like to thank the members of the CEFCA institute for their hospitality during a visit were part of this work was done. BH and LW acknowledge financial support by the DFG Priority Program 1177 'Galaxy Evolution', grant Wi 1369/22-1 and Wi 1369/22-2. SFS would like to thanks the 'Ministerio de Ciencia e Innovacion' project ICTS-2009-10, and the 'Junta de Andalucia' projects P08-FWM-04319 and FQM360. KJ and DN are funded through the DFG Emmy Noether-Program, grant JA 1114/3-1.

References

Allard, F., Hauschildt, P. H., Alexander, D. R., Tamanai, A., & Schweitzer, A. 2001, ApJ, 556, 357
Allen, M. G., Groves, B. A., Dopita, M. A., Sutherland, R. S., & Kewley, L. J. 2008, ApJS, 178, 20
Antonucci, R. 1993, ARA&A, 31, 473
Antonucci, R. R. J. & Miller, J. S. 1985, ApJ, 297, 621
Bahcall, J. N., Kirhakos, S., Saxe, D. H., & Schneider, D. P. 1997, ApJ, 479, 642
Baldwin, J. A., Phillips, M. M., & Terlevich, R. 1981, PASP, 93, 5
Bennert, N., Canalizo, G., Jungwiert, B., et al. 2008, ApJ, 677, 846
Bennert, N., Falcke, H., Schulz, H., Wilson, A. S., & Wills, B. J. 2002, ApJ, 574, L105
Bennert, N., Jungwiert, B., Komossa, S., Haas, M., & Chini, R. 2006, A&A, 456, 953
Bentz, M. C., Peterson, B. M., Pogge, R. W., Vestergaard, M., & Onken, C. A. 2006, ApJ, 644, 133
Bezanson, R., van Dokkum, P. G., Tal, T., et al. 2009, ApJ, 697, 1290
Boroson, T. A. & Oke, J. B. 1982, Nature, 296, 397
Boroson, T. A. & Oke, J. B. 1984, ApJ, 281, 535
Boroson, T. A., Persson, S. E., & Oke, J. B. 1985, ApJ, 293, 120
Canalizo, G. & Stockton, A. 2000, AJ, 120, 1750
Cardelli, J. A., Clayton, G. C., & Mathis, J. S. 1989, ApJ, 345, 245
Christensen, L., Jahnke, K., Wisotzki, L., & Sánchez, S. F. 2006, A&A, 459, 717
Cid Fernandes, R., Gu, Q., Melnick, J., et al. 2004, MNRAS, 355, 273
Cid Fernandes, R., Mateus, A., Sodré, L., Stasińska, G., & Gomes, J. M. 2005, MNRAS, 358, 363
Collin, S., Kawaguchi, T., Peterson, B. M., & Vestergaard, M. 2006, A&A, 456, 75
de Vaucouleurs, G. 1948, Annales d'Astrophysique, 11, 247
Dopita, M. A. & Sutherland, R. S. 1995, ApJ, 455, 468
Dunlop, J. S., McLure, R. J., Kukula, M. J., et al. 2003, MNRAS, 340, 1095
Falcke, H., Wilson, A. S., & Simpson, C. 1998, ApJ, 502, 199
Ferland, G. J. 1996, Hazy, A Brief Introduction to Cloudy 90, ed. Ferland, G. J.
Fu, H. & Stockton, A. 2007, ApJ, 666, 794
Fu, H. & Stockton, A. 2008, ApJ, 677, 79
García-Lorenzo, B., Sánchez, S. F., Mediavilla, E., González-Serrano, J. I., & Christensen, L. 2005, ApJ, 621, 146
González Delgado, R. M., Cerviño, M., Martins, L. P., Leitherer, C., & Hauschildt, P. H. 2005, MNRAS, 357, 945
González Delgado, R. M., Heckman, T., & Leitherer, C. 2001, ApJ, 546, 845
Gray, R. O. & Corbally, C. J. 1994, AJ, 107, 742
Groves, B. A., Dopita, M. A., & Sutherland, R. S. 2004, ApJS, 153, 9
Hasinger, G. 2004, Nuclear Physics B Proceedings Supplements, 132, 86
Hasinger, G. 2008, A&A, 490, 905
Hauschildt, P. H. & Baron, E. 1999, Journal of Computational and Applied Mathematics, 109, 41
Heckman, T. M., Miley, G. K., van Breugel, W. J. M., & Butcher, H. R. 1981, ApJ, 247, 403
Husemann, B., Wisotzki, L., Sánchez, S. F., & Jahnke, K. 2008, A&A, 488, 145
Jahnke, K., Bongiorno, A., Brusa, M., et al. 2009, ApJ, 706, L215
Jahnke, K., Kuhlbrodt, B., & Wisotzki, L. 2004a, MNRAS, 352, 399
Jahnke, K., Sánchez, S. F., Wisotzki, L., et al. 2004b, ApJ, 614, 568
Jahnke, K. & Wisotzki, L. 2003, MNRAS, 346, 304
Jahnke, K., Wisotzki, L., Courbin, F., & Letawe, G. 2007, MNRAS, 378, 23
Jahnke, K., Wisotzki, L., Sánchez, S. F., et al. 2004c, AN, 325, 128
Johansson, P. H., Naab, T., & Ostriker, J. P. 2009, ApJ, 697, L38
Kaspi, S., Smith, P. S., Netzer, H., et al. 2000, ApJ, 533, 631
Kauffmann, G., Heckman, T. M., Tremonti, C., et al. 2003, MNRAS, 346, 1055
Kewley, L. J., Dopita, M. A., Sutherland, R. S., Heisler, C. A., & Trevena, J. 2001, ApJ, 556, 121
Kewley, L. J., Groves, B., Kauffmann, G., & Heckman, T. 2006, MNRAS, 372, 961
Kim, M., Ho, L. C., Peng, C. Y., et al. 2008, ApJ, 687, 767
Krist, J. 1995, in Astronomical Society of the Pacific Conference Series, Vol. 77, Astronomical Data Analysis Software and Systems IV, ed. R. A. Shaw, H. E. Payne, & J. J. E. Hayes, 349–+
Kristian, J. 1973, ApJ, 179, L61+

Kuhlbrodt, B., Wisotzki, L., & Jahnke, K. 2004, MNRAS, 349, 1027
Kurucz, R. L. 1991, in NATO ASIC Proc. 341: Stellar Atmospheres - Beyond Classical Models, 441–+
Lanz, T. & Hubeny, I. 2003, ApJS, 146, 417
Lawrence, A. 1991, MNRAS, 252, 586
LeFevre, O., Saisse, M., Mancini, D., et al. 2003, in Society of Photo-Optical Instrumentation Engineers (SPIE) Conference Series, Vol. 4841, Society of Photo-Optical Instrumentation Engineers (SPIE) Conference Series, ed. M. Iye & A. F. M. Moorwood, 1670–1681
Letawe, G., Magain, P., Courbin, F., et al. 2007, MNRAS, 378, 83
Lipari, S. 1994, ApJ, 436, 102
Lípari, S., Bergmann, M., Sanchez, S. F., et al. 2009, MNRAS, 398, 658
Lipari, S., Sanchez, S. F., Bergmann, M., et al. 2009, MNRAS, 392, 1295
Lípari, S. L. & Terlevich, R. J. 2006, MNRAS, 368, 1001
Malkan, M. A. 1984, ApJ, 287, 555
Martins, L. P., González Delgado, R. M., Leitherer, C., Cerviño, M., & Hauschildt, P. 2005, MNRAS, 358, 49
Mateus, A., Sodré, L., Cid Fernandes, R., et al. 2006, MNRAS, 370, 721
McLeod, K. K. & Rieke, G. H. 1994, ApJ, 431, 137
McLure, R. J., Kukula, M. J., Dunlop, J. S., et al. 1999, MNRAS, 308, 377
Mulchaey, J. S., Wilson, A. S., & Tsvetanov, Z. 1996, ApJS, 102, 309
Naab, T., Johansson, P. H., & Ostriker, J. P. 2009, ApJ, 699, L178
Osterbrock, D. E. & Ferland, G. J. 2006, Astrophysics of gaseous nebulae and active galactic nuclei (2nd. ed. by D.E. Osterbrock and G.J. Ferland. Sausalito, CA: University Science Books, 2006)
Papadopoulos, P. P., Feain, I. J., Wagg, J., & Wilner, D. J. 2008, ApJ, 684, 845
Peeples, M. S., Pogge, R. W., & Stanek, K. Z. 2009, ApJ, 695, 259
Peng, C. Y., Ho, L. C., Impey, C. D., & Rix, H.-W. 2002, AJ, 124, 266
Pogge, R. W. 1988a, ApJ, 328, 519
Pogge, R. W. 1988b, ApJ, 332, 702
Reeves, J. N. & Turner, M. J. L. 2000, MNRAS, 316, 234
Salpeter, E. E. 1955, ApJ, 121, 161
Sánchez, S. F. 2006, AN, 327, 850
Sánchez, S. F., García-Lorenzo, B., Jahnke, K., et al. 2006, New Astronomy Review, 49, 501
Sánchez, S. F., Garcia-Lorenzo, B., Mediavilla, E., González-Serrano, J. I., & Christensen, L. 2004a, ApJ, 615, 156
Sánchez, S. F. & González-Serrano, J. I. 2003, A&A, 406, 435
Sánchez, S. F., Jahnke, K., Wisotzki, L., et al. 2004b, ApJ, 614, 586
Sanders, D. B., Soifer, B. T., Elias, J. H., et al. 1988a, ApJ, 325, 74
Sanders, D. B., Soifer, B. T., Elias, J. H., Neugebauer, G., & Matthews, K. 1988b, ApJ, 328, L35
Schlegel, D. J., Finkbeiner, D. P., & Davis, M. 1998, ApJ, 500, 525
Schmitt, H. R., Donley, J. L., Antonucci, R. R. J., Hutchings, J. B., & Kinney, A. L. 2003, ApJS, 148, 327
Smith, E. P., Heckman, T. M., Bothun, G. D., Romanishin, W., & Balick, B. 1986, ApJ, 306, 64
Sol Alonso, M., Michel-Dansac, L., & Lambas, D. G. 2010, A&A, 514, A57+
Stockton, A. 1976, ApJ, 205, L113+
Stockton, A. & MacKenty, J. W. 1987, ApJ, 316, 584
Stoklasová, I., Ferruit, P., Emsellem, E., et al. 2009, A&A, 500, 1287
Storchi-Bergmann, T. & Bonatto, C. J. 1991, MNRAS, 250, 138
Storchi-Bergmann, T., Raimann, D., Bica, E. L. D., & Fraquelli, H. A. 2000, ApJ, 544, 747
Storchi-Bergmann, T., Wilson, A. S., & Baldwin, J. A. 1992, ApJ, 396, 45
Tal, T., van Dokkum, P. G., Nelan, J., & Bezanson, R. 2009, AJ, 138, 1417
Tody, D. 1993, in Astronomical Society of the Pacific Conference Series, Vol. 52, Astronomical Data Analysis Software and Systems II, ed. R. J. Hanisch, R. J. V. Brissenden, & J. Barnes, 173–+
Tremaine, S., Gebhardt, K., Bender, R., et al. 2002, ApJ, 574, 740
Tremonti, C. A., Heckman, T. M., Kauffmann, G., et al. 2004, ApJ, 613, 898
Ueda, Y., Akiyama, M., Ohta, K., & Miyaji, T. 2003, ApJ, 598, 886
Urry, C. M. & Padovani, P. 1995, PASP, 107, 803
Veilleux, S. & Osterbrock, D. E. 1987, ApJS, 63, 295
Véron-Cetty, M.-P., Véron, P., & Gonçalves, A. C. 2001, A&A, 372, 730
Villar-Martín, M., Tadhunter, C., Morganti, R., Axon, D., & Koekemoer, A. 1999, MNRAS, 307, 24
Wampler, E. J., Burbidge, E. M., Baldwin, J. A., & Robinson, L. B. 1975, ApJ, 198, L49
Wisotzki, L. 1994, A&A, 292, 45
Wisotzki, L., Becker, T., Christensen, L., et al. 2003, A&A, 408, 455
Wisotzki, L., Christlieb, N., Bade, N., et al. 2000, A&A, 358, 77
Wisotzki, L., Reimers, D., & Wamsteker, W. 1991, A&A, 247, L17
Zakamska, N. L., Schmidt, G. D., Smith, P. S., et al. 2005, AJ, 129, 1212
Zamanov, R. & Marziani, P. 2002, ApJ, 571, L77

Chapter 3

The properties of extended emission-line regions around low-redshift QSOs and the lack of high-velocity AGN outflows⋆

B. Husemann[1], L. Wisotzki[1], S. F. Sánchez[2], and K. Jahnke[3]

[1] Astrophysikalisches Institut Potsdam, An der Sternwarte 16, 14482 Potsdam, Germany
[2] Centro Astronómico Hispano Alemán de Calar Alto (CSIC-MPIA), E-4004 Almería, Spain
[3] Max-Planck-Institut für Astronomie, Königsstuhl 17, D-69117 Heidelberg, Germany

ABSTRACT

We present a detailed analysis of a large sample of 31 low-redshift, mainly radio-quiet type 1 QSOs observed with the PMAS integral field spectrograph with the aim to study their Extended Emission-Line Regions (EELRs). Following up on our previous work, we focus on the ionisation state, the kinematics of the ionised gas, the size and luminosity of Extended Narrow Line Regions (ENLRs) and their connection to low power radio jets. EELRs are detected around 19 of our 31 QSOs (61%) after deblending the unresolved QSO emission from the extended host galaxy light in our integral field data with our new software `QDeblend`^{3D}. Based on standard emission-line diagnostics we identify 14 EELRs to be entirely ionised by the QSO radiation, 3 EELRs are composed of H II regions due to ongoing star formation and 3 EELRs display signatures of both ionisation mechanisms at different locations. With a morphological characterisation of the host galaxies from broad-band images we find that ongoing star formation with rates up to $4\,M_\odot\,yr^{-1}$ occurs exclusively in disc-dominated hosts. The kinematics of the EELRs are quiescent and likely gravitationally driven in most cases. We determine dynamical masses of $> 2\times10^{10}\,M_\odot$ for 6 objects with a rotational pattern matching with expected masses of galaxies with luminous QSOs. Only 5 objects display line width or radial velocities exceeding $> 400\,km\,s^{-1}$ in specific regions of the EELR that can often be associated jet-cloud interaction of low-power radio jets. These are significantly lower velocities and detection rates as seen in starburst and post-starburst galaxies. The typical size of the ENLR is ∼10 kpc at the given QSO luminosity, at least a factor of ∼2 larger than determined with the Hubble Space Telescope, consistent with the ENLR sizes of type 2 QSOs at similar [O III] luminosities. ENLRs of obscured and unobscured QSOs therefore need to follow the same ENLR size-luminosity relation. We show that the ENLR size is much better correlated with the QSO continuum luminosity than the [O III] luminosity. Given the potential correlation between the ENLR luminosity and the radio luminosity we tentatively argue that the even the low-power radio jets in radio-quiet QSOs are another important factor to shape the properties of the ENLR including its kinematics.

3.1. Introduction

Extended emission line regions (EELRs) with sizes of several tens of kpc were initially discovered around luminous radio-loud QSOs by Wampler et al. (1975) and Stockton (1976). Follow-up longslit spectroscopy presented by Boroson & Oke (1984) and Boroson et al. (1985) confirmed that a substantial part of the extended warm ionised gas is predominantly photoionised by the hard radiation of the active nuclei with line ratios similar to the compact narrow-line region (NLR) of AGN. Stockton & MacKenty (1987) conducted a large ground-based narrow-band imaging survey of 47 luminous, mainly radio-loud QSOs at $z < 0.5$ in the [O III] line and detected EELRs around 25% of those systems. A strong alignment effect between the major EELR axis and the radio axis was found for RLQs at $z > 0.6$ (McCarthy et al. 1987) suggesting that radio jets have a strong impact on the EELR properties and may directly enhance their brightnesses. On the other hand, EELRs have been claimed to be preferentially found around radio-loud QSOs with a systematically lower broad line region (BLR) metallicity (Fu & Stockton 2007). The nature of EELRs and the origin of the gas are not yet clear and remain strongly debated.

The properties of the extended ionised gas around radio-quiet QSOs has been studied much less intensively. Bennert et al. (2002) imaged a sample of 7 objects in the [O III] line with the Hubble Space Telescope (*HST*) and detected ionised gas on scale of up to 10 kpc, significantly smaller than EELRs around radio-loud QSOs. Including NLR sizes in low luminosity Seyfert galaxies, Bennert et al. (2002) found a strong correlation between the [O III] luminosity and the size of the NLR, which is often referred to as the extended NLR (ENLR) if it extents over more than 1 kpc. Another large *HST* narrow-band snap-shot survey focussing of Seyfert galaxies confirmed the existence of such a relation (Schmitt et al. 2003b), but the exact slope and zero-point still remains controversial. Potential caveats of the *HST* images are the low sensitivity and the lack of spectroscopy information to confirm the association of emission to the NLR of the AGN. For example, longslit spectroscopy of Seyfert galaxies allowed Bennert et al. (2006a,b) to determine the radius of the transition zone between AGN photoionisation and H II region at 0.7 – 4 kpc.

The study of extended emission around luminous QSOs is significantly hampered by the severe contamination due to the

⋆ This Chapter will be submitted to the journal *Astronomy & Astrophysics* within a few month time frame.

bright unresolved nuclei. Recent studies therefore focused on rare type 2 QSOs for which the emission of the nucleus is obscured by an optical thick torus as proposed in the Unified Model of AGN (Antonucci 1993). For example, Villar-Martín et al. (2010) detected a huge EELR (180 kpc) around the luminous type 2 QSO SDSS J0123+00 ($z = 0.399$) and determined an ENLR size of ∼25 kpc from longslit spectra using emission line diagnostics. Furthermore, small samples of type 2 QSOs were recently studied by means of longslit (Greene et al. 2011) and integral field spectroscopy (Humphrey et al. 2010) for which typical ENLR sizes of ∼10 kpc were reported, almost 2 times larger than the ENLRs of unobscured (type 1) QSOs observed with *HST*.

The extended emission of the warm ionised gas phase around AGN has attracted further attention, because it may allow to directly study the impact of the AGN on its surrounding host galaxy. Complex kinematics of the EELR are found around radio-loud QSOs and radio galaxies with line widths up to 1000 km s^{-1} and high velocity clouds exceeding the escape velocity being able to potentially expel a large fraction of gas from the host galaxy (e.g. McCarthy et al. 1996; Villar-Martín et al. 1999; Tadhunter et al. 2001; Holt et al. 2003, 2006; Nesvadba et al. 2006; Fu & Stockton 2009). This has been interpreted as a clear signature for AGN feedback which is theoretically invoked to explain the observed scaling relation between the black hole (BH) mass and host galaxy properties (e.g. Magorrian et al. 1998; Gebhardt et al. 2000; Tremaine et al. 2002; Häring & Rix 2004; Gültekin et al. 2009), and to efficiently quench star formation required to prevent the overprediction of massive young galaxies in cosmological simulation (e.g. Croton et al. 2006; Khalatyan et al. 2008). Given the short duty cycle of radio-loud AGN and the low radio-loud fraction of the order of 10%, it remains unclear if this particular mode of AGN activity can be the primary channel for AGN feedback. Furthermore, the coupling of kinematic jet energy to the ambient medium may be significantly less efficient than currently required by numerical simulation (Holt et al. 2011). Although individual radio-quiet QSOs like Mrk 231 were also discovered to display extremely complex extended ionised gas kinematics similar to their radio-loud counterparts (Hamilton & Keel 1987; Lipari et al. 2009), the pilot studies of radio-quiet type 2 QSOs (Humphrey et al. 2010; Greene et al. 2011) consistently found much more quiescent gas kinematics.

Given that type 1 QSOs are much more frequent and allow to directly infer basic AGN properties directly from the spectrum of the nucleus, we took the challenge to deal with deblending of the QSO and extended host galaxy emission. In our early work (Husemann et al. 2008, hereafter Hu08) we studied a sample of 20 mainly radio-quiet QSOs observed with the PMAS integral field unit (IFU) and reported that 8 of 20 QSOs are surrounded by a luminous EELR and emphasised that the EELR detection is linked with the spectral properties of the nucleus itself. Since then, we further extended our sample with additional observations of 11 radio-quiet QSOs. In this Chapter we present a detailed analysis of the ionisation mechanisms of the extended ionised gas, the ionised gas kinematics and the ENLR size and luminosity for the complete sample. It is organised as follows: In section 3.2 we report on the characteristics of the sample including its selection and host galaxy properties. The IFU observations, data reduction and QSO-host deblending are described in section 3.3. Basic properties of the AGN are determined from the QSO spectra in section 3.4 and we apply standard emission-line diagnostics to infer the ionisation mechanism of the extended gas in section 3.5. We then turn to the kinematics of the extended gas (section 3.6) and focus on various properties of the ENLR in section 3.7. We close this Chapter with a discussion of our main conclusions within a broader context. Throughout the Chapter we assume a cosmological model with $H_0 = 70\,\mathrm{km\,s^{-1}}$ Mpc, $\Omega_\mathrm{m} = 0.3$, and $\Omega_\Lambda = 0.7$.

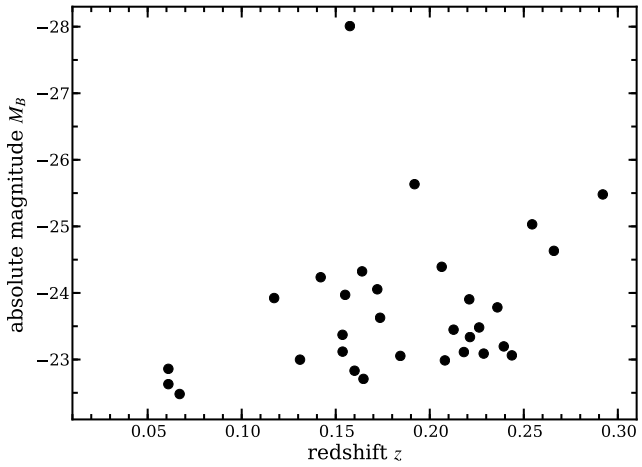

Fig. 3.1. Absolute B band magnitude against the redshift for all objects in our QSO sample.

3.2. The QSO sample and characteristics

3.2.1. Sample selection

Our QSO sample consists of 31 objects in the redshift range $0.06 < z < 0.3$ which we observed with the Potsdam Multi-Aperture Spectro-photometer (PMAS, Roth et al. 2005) mounted to the Cassegrain focus of the 3.5 m telescope at the Calar Alto observatory. The QSOs were drawn from two samples that were constructed with different selection criteria. An initial sample of 21 low-redshift QSOs was randomly selected from the Palomar-Green Survey (PG, Schmidt & Green 1983) and from the Hamburg/ESO survey (HES Wisotzki et al. 2000) with an absolute magnitude of $M_B \leq -23$ (computed with $H_0 = 50\,\mathrm{km\,s^{-1}\,Mpc^{-1}}$), a classical but arbitrary division line between Seyfert galaxies and QSOs, and a declination of $\delta > -10°$ to be observable from the Calar Alto observatory. An additional sample 10 QSOs were drawn from the Sloan Digital Sky Survey (SDSS) DR6 (Adelman-McCarthy et al. 2008). These QSOs were selected to be brighter than $g < 17$ within the redshift range $0.13 < z < 0.3$ and to have an [O III]/Hβ peak flux density ratio greater than 1.5 as measured from the SDSS spectra. This last criterion is based on early results from the initial sample (Hu08) and should give preference to QSOs surrounded by an EELR. The complete list of our observed objects is given in Table 3.1 including information of some of their main characteristics.

The redshift-luminosity diagram of our observed QSO sample is shown in Fig. 3.1. We computed absolute magnitudes (M_B) from the apparent B band magnitudes taking into account Galactic foreground extinction (Schlegel et al. 1998) and an appropriate k-correction (Wisotzki 2000). The B band magnitudes and redshifts were either taken from the available catalogues or directly measured from publicly available SDSS spectra. The absolute magnitudes are in the range of $-26 < M_B < -22.3$ with a median value of -23.45. The median redshift of the sample is $z = 0.184$. The majority of our objects are relatively luminous low-redshift QSOs.

Table 3.1. Characteristics of the QSO sample.

Name	Alt. Name	α (J2000)	δ (J2000)	z^a	$m_B{}^b$	$M_B{}^c$	$f_{1.4\,\mathrm{GHz}}{}^d$	$f_{5\,\mathrm{GHz}}{}^e$	R^f	Class.^{g}
PG 0026+129		$00^h29^m13\overset{s}{.}8$	13°16′05.″0	0.142	14.95	-24.24	7.1	5.1	1.08	RI
PG 0050+124	I Zw 1	$00^h53^m34\overset{s}{.}9$	12°41′35.″0	0.061	14.39	-22.86	8.3	2.6	0.33	RQ
PG 0052+251		$00^h54^m52\overset{s}{.}2$	25°25′39.″0	0.155	15.42	-23.97	7.1	0.7	0.24	RQ
SDSS J0057+1446		$00^h57^m09\overset{s}{.}9$	14°46′10.″2	0.172	15.58	-24.05	2.4	1.3†	0.48	RQ
HE 0132-0441		$01^h35^m27\overset{s}{.}0$	-04°26′36.″2	0.154	16.25	-23.12	7.4	2.9	2.03	RI
SDSS J0155-0857		$01^h55^m30\overset{s}{.}0$	-08°57′04.″1	0.165	16.83	-22.71	<0.9	< 0.5†	<0.58	RQ
HE 0157-0406		$01^h59^m49\overset{s}{.}0$	-03°52′00.″4	0.218	17.09	-23.11	<0.9	< 0.5†	<0.75	RQ
PG 0157+001	Mrk 1014	$01^h59^m50\overset{s}{.}2$	00°23′41.″0	0.164	15.20	-24.32	26.2	8.0	2.12	RI
SDSS J0836+4426		$08^h36^m58\overset{s}{.}9$	44°26′02.″3	0.254	15.54	-25.03	10.0	5.3†	1.93	RI
SDSS J0948+4335		$09^h48^m59\overset{s}{.}5$	43°35′19.″0	0.226	16.81	-23.48	<0.9	< 0.5†	<0.56	RQ
SDSS J1131+2632		$11^h31^m09\overset{s}{.}2$	26°32′07.″9	0.244	17.41	-23.06	2.7	1.4†	2.90	RI
HE 1217+0220	PKS 1217+023	$12^h20^m11\overset{s}{.}9$	02°03′41.″7	0.239	17.23	-23.20	652.0	440.0	757.18	RL
HE 1226+0219	3C 273	$12^h29^m06\overset{s}{.}7$	02°03′07.″9	0.158	11.42	-28.01	55296.0	37000.0	302.22	RL
SDSS J1230+6621		$12^h30^m22\overset{s}{.}2$	66°21′54.″7	0.184	16.75	-23.05	<2.5	< 1.3†	<1.46	RQ?
HE 1228+0131		$12^h30^m50\overset{s}{.}0$	01°15′21.″8	0.117	14.82	-23.92	1.4	0.2	0.04	RQ
SDSS J1230+1100		$12^h30^m54\overset{s}{.}1$	11°00′11.″2	0.236	16.61	-23.78	<1.0	< 0.5†	<0.52	RQ
PG 1427+480		$14^h29^m43\overset{s}{.}1$	47°47′27.″0	0.221	16.33	-23.90	<0.9	0.0	0.02	RQ
SDSS J1444+0633		$14^h44^m14\overset{s}{.}7$	06°33′06.″8	0.208	17.10	-22.99	<1.0	< 0.5†	<0.81	RQ
HE 1453-0303		$14^h56^m11\overset{s}{.}5$	-03°15′27.″8	0.206	15.68	-24.39	2.7	1.4†	0.58	RQ
PG 1545+210	PKS 1545+210	$15^h47^m43\overset{s}{.}5$	20°52′17.″0	0.266	16.05	-24.63	1560.0	720.0	418.15	RL
PG 1612+261	TON 256	$16^h14^m13\overset{s}{.}2$	26°04′16.″0	0.131	16.00	-23.00	17.9	5.1	2.81	RI
SDSS J1655+2146		$16^h55^m51\overset{s}{.}4$	21°46′01.″8	0.154	16.00	-23.37	6.6	3.5†	1.94	RI
PG 1700+518		$17^h01^m24\overset{s}{.}9$	51°49′21.″0	0.292	15.43	-25.48	21.6	7.2	2.36	RI
PG 2130+099	Mrk 1513	$21^h32^m27\overset{s}{.}8$	10°08′19.″0	0.061	14.62	-22.63	6.0	2.0	0.32	RQ
HE 2152-0936		$21^h55^m01\overset{s}{.}5$	-09°22′24.″5	0.192	14.26	-25.63	1.2	0.6†	0.07	RQ
HE 2158-0107		$22^h01^m03\overset{s}{.}1$	-00°53′01.″0	0.213	16.69	-23.45	1.6	0.8†	0.88	RQ
HE 2158+0115		$22^h01^m29\overset{s}{.}7$	01°29′56.″1	0.160	16.63	-22.83	<0.9	< 0.5†	<0.48	RQ
PG 2214+139	Mrk 304	$22^h17^m11\overset{s}{.}6$	14°14′28.″0	0.067	14.98	-22.48	<2.5	0.2	0.05	RQ
HE 2307-0254		$23^h10^m29\overset{s}{.}7$	-02°38′13.″0	0.221	16.90	-23.34	<2.5	< 1.3†	<1.68	RQ?
HE 2349-0125	PKS 2349-014	$23^h51^m56\overset{s}{.}0$	-01°09′13.″6	0.174	16.03	-23.63	1623.2	622.7	355.46	RL
HE 2353-0420		$23^h56^m32\overset{s}{.}9$	-04°04′00.″7	0.229	17.23	-23.09	<2.5	< 1.3†	<2.27	RQ?

Notes. [a] QSO redshift taken from the PG, HES, or SDSS catalogue. [b] Apparent B band magnitudes taken from the catalogues or synthesised from the SDSS spetrum. [c] Absolute magnitudes M_B taking into account Galactic foreground extinction and an appropriate k-correction (Wisotzki 2000). [d] Radio fluxes at 1.4 GHz in mJy as measured by the NVSS all-sky survey or the FIRST survey when covered. [e] Radio fluxes at 5 GHz in mJy taken from Kellermann et al. (1989) and an unpublished Catalog (Gopal-Krishna et al. private communication), if available. Values marked with † were estimated from the radio flux at 1.4 GHz assuming a spectral index of $\alpha = -0.5$. [f] Ratio R of the 5 GHz radio to optical flux density at 4400Å. The optical flux density f_ν(4400Å) in mJy was estimated from the optical B band magnitude with the relation $m_B = -2.5 \log f_\nu(4400\,\text{Å}) - 48.36$ Schmidt & Green (1983). [g] Radio classification of the QSO following Kellermann et al. (1989) into radio loud (RL) and radio quiet (RQ) and intermediate radio (RI) QSOs. An unambigous classification for a few object cannot be made due to upper limits in R.

3.2.2. Radio properties

Radio-loud and radio-quiet QSOs (RLQs and RQQs, respectively) are often distinguished based on the R parameter, which is defined as the ratio of the radio (at 6 cm/5 GHz) to the optical flux density (at 4400 Å). We adopt the classification of Kellermann et al. (1989), who separated RQQs with $R < 1$, RLQs with $R > 10$ and a few radio-intermediate objects in between the two classes. Not every object of our sample has been observed at 5 GHz, but the NRAO VLA Sky Survey (NVSS Condon et al. 1998) and the FIRST survey (Becker et al. 1995) provide radio measurements at 1.4 GHz (21 cm) for a large fraction of the sky with a completeness level of 2.5 mJy and 1 mJy, respectively. We adopt a power-law dependence of the radio flux densities ($f_\nu \propto \nu_\mathrm{r}^\alpha$) with a spectral index of $\alpha_\mathrm{r} = -0.5$, at the border line between steep and flat-spectrum radio sources, to estimate the flux density at 5 GHz from measurements at 1.4 GHz when required. Only 4 objects in the sample can be classified as RLQs, 8 objects have intermediate radio properties, and the majority of objects within the sample are clearly RQQs.

Table 3.2. Tadio imaging for our RQQs.

Name	ν^a	Beam^b	Size^c	PA^d	Reference
PG 0026+129	8.4 GHz	0.″35	0.″60	...	(1)
PG 0052+251	4.8 GHz	0.″59	< 0.″09	...	(1)
Mrk 1014	8.4 GHz	0.″36	2.″6	90°	(1)
PG 1612+261	8.4 GHz	0.″28	1.″0	66°	(2)
PG 1700+518	8.4 GHz	0.″28	1.″0	-86°	(2)
PG 2130+099	4.8 GHz	0.″35	2.″9	-48°	(1)

Notes. [a] Observing frequency ν of the radio observations. [b] Beam size of the interferometric radio observations. [c] Maximum size of the extended radio emission. [d] Position angle of the major radio axis. 90° points to the East and 0° to the North.

References. (1) Leipski et al. (2006); (2) Kukula et al. (1998)

Besides the integrated radio measurements, archival high spatial resolution images for 6 of our RQQs were obtained

with the VLA interferometer at subarcsecond resolution and presented by Kukula et al. (1998) and Leipski et al. (2006). We retrieved most of the processed images from the VLA image archive[1], some were kindly provided by the authors. The characteristics of these images are listed in Table 3.2. All except PG 0052+251 display extended radio emission with sizes up to 3″. Triple radio sources were identified in Mrk 1014 and PG 2130+099 that confirm the presence of low-power radio jets in these sources.

3.2.3. QSO host morphologies

Available broad-band imaging

High spatial resolution broad-band images were obtained with the Hubble Space Telescope (*HST*) for most of the PG QSO over the last decade, except PG 1427+490, PG 1612+261 and PG 2214+139. These *HST* images were initially published in various unrelated articles (see Table 3.3), but a homogeneous analysis of all the public data was presented by Kim et al. (2008). Furthermore, broad-band images in the 5 Sloan bands (*u*,*g*,*r*,*i*,*z*) are obviously available for all SDSS QSOs, and additionally also for a few HES and PG QSOs covered by the SDSS footprint. These short survey images (effective exposure time of 54s) were usually obtained at a seeing around ∼1.″2 (*r*) and it has not yet been attempted to recover the underlying host galaxies. This is a difficult task due to the short exposure time and the low spatial resolution of the images.

No broad-band images have so far been presented for most of the HES QSOs in our sample. Ground-based *H* band images were obtained for a few QSOs in 2003 with the SOFI IR spectrograph and imaging camera (Moorwood et al. 1998) mounted on the New Technology Telescope (NTT) and are publicly available in the ESO archive, which we reduced with the corresponding standard ESO pipeline. Additionally, we obtained *R* band images for three HES QSOs with the 60 cm telescope of the Lightbuckets robotic telescope network (LB-0001, hereafter LB1). This small telescope is equipped with an Apogee Alta U42 CCD camera providing a spatial resolution of 0.″57 pixel^{-1}. With an exposure time of ∼1 h, these images are nominally deeper than SDSS, but suffer from a seeing of ≳2″. We reduced these images following the standard process including bias subtraction, flat-fielding and combination of the dithered exposures with custom `Python` scripts.

QSO-host deblending

In order to perform a consistent analysis of the available broad-band images we deblended the QSO and host emission using `GALFIT` (Peng et al. 2002). We emphasise that our main aim here is only to recover the stellar light surface brightness distribution of the underlying host galaxies and distinguish between bulge-dominated and disc-dominated host galaxies whenever possible. A more detailed analysis of the images would be beyond our scope and hardly possible given the low spatial resolution for most of the images.

We created an empirical Point Spread Function (PSF) from bright stars in the field close to the target. Dedicated PSF stars were observed with *HST* only for a few objects, so that we usually relied on synthetic PSFs generated with the `TinyTim` software package (Krist 1995). First, we used `GALFIT` to model each object with a PSF component only, to check whether any significant residuals of a host could actually be detected. This was the case for all QSOs except for HE 2158−0107 (see Chapter 5 for more details) In a second step, we modelled the images with a superposition of a Sersić light profile (Sersic 1968) for the host and a PSF for the QSO component. Two examples of the deblending results for the ground-based SDSS image are presented in Fig. 3.2.

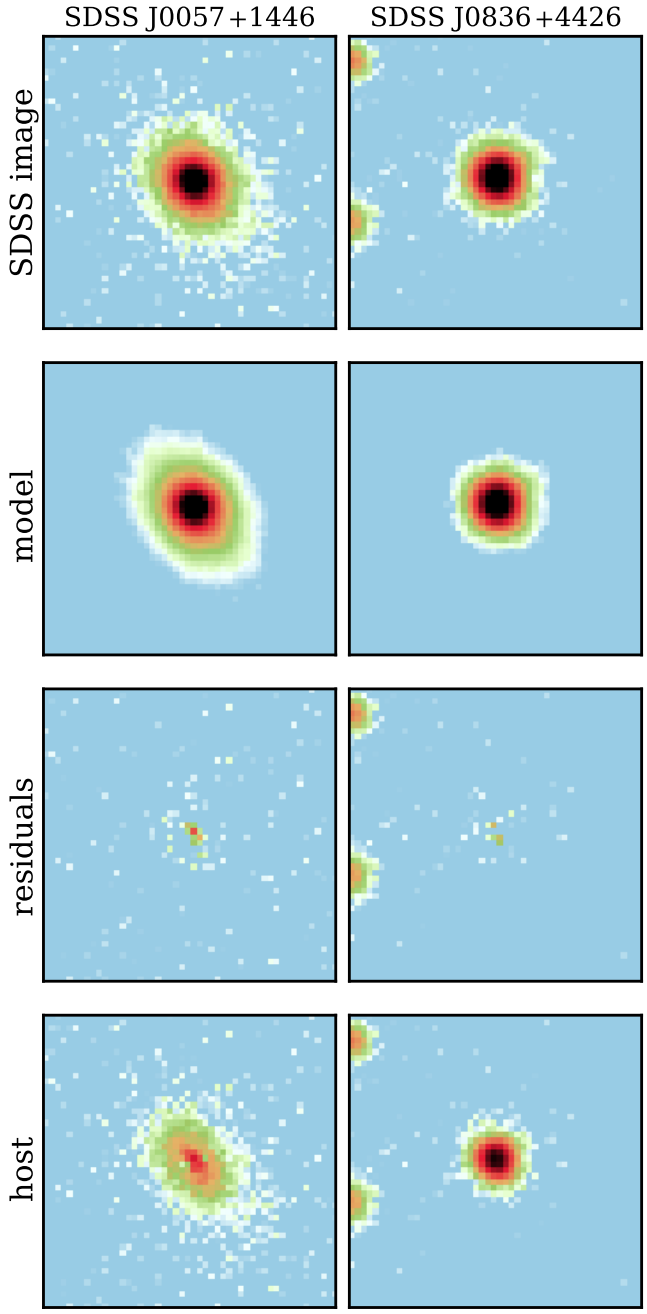

Fig. 3.2. Two examples of the QSO-host deblending process for SDSS *i* band images. The PSF was constructed from a bright nearby star in the field. A best-fitting Sersić surface brightness model plus a PSF for the nucleus was obtained with `GALFIT` and subtracted from the original SDSS image to highlight the residuals. The host galaxy is recovered after subtracting the best-fit PSF component from the original image.

[1] https://archive.nrao.edu/archive/archiveimage.html

Table 3.3. Broad-band imaging analysis results – Structural parameters and morphological host galaxy classification.

Name	Telescope/Instrument	Ref.[a]	$\chi^2_\nu(n=1)$	$\chi^2_\nu(n=4)$	$\chi^2_\nu(n)$	r_e[b]	b/a[c]	PA[d]	Class.[e]
PG 0026+129	HST NICMOS (F160W)	(1)	4.400	3.566	3.563 (3.6)	1.″2 (3.0 kpc)	0.82	85°	B
PG 0050+124	HST WFPC2 (F814W)		2.826	2.684	2.669 (2.8)	8.″7 (10.2 kpc)	0.73	-58°	B+D
PG 0052+251	HST WFPC2 (F606W)	(2)	2.705	3.368	2.704 (1.0)	3.″5 (9.4 kpc)	0.65	-8°	D
SDSS J0057+1446	SDSS (i')		1.002	0.990	0.989 (2.7)	3.″7 (10.8 kpc)	0.52	-50°	B?
	SDSS (r')		1.018	0.985	0.984 (6.7)	2.″2 (6.4 kpc)	0.62	-49°	
HE 0132−0441	LB1 Apogee U42 (R)		1.505	1.508	1.505 (1.1)	3.″8 (10.1 kpc)	0.79	28°	D(V)
SDSS J0155−0857	SDSS (i')		1.180	1.150	1.148 (5.4)	1.″3 (3.4 kpc)	0.62	32°	B?
	SDSS (r')		1.136	1.139	1.132 (1.7)	2.″4 (6.8 kpc)	0.57	31°	
PG 0157+001	HST WFPC2 (F675W)	(3)	6.406	6.471	6.360 (1.5)	4.″9 (13.8 kpc)	0.89	15°	D/M
SDSS J0836+4426	SDSS (i')		0.984	0.979	0.980 (6.1)	0.″2 (0.8 kpc)	0.52	-83°	?
	SDSS (r')		0.994	0.984	0.984 (12.0)	0.″2 (0.8 kpc)	0.90	16°	
SDSS J0948+4335	SDSS (i')		1.244	1.259	1.243 (1.2)	2.″4 (8.7 kpc)	0.80	-31°	D(V)
	SDSS (r')		1.052	1.083	1.051 (0.8)	2.″7 (9.8 kpc)	0.79	-27°	
SDSS J1131+2632	SDSS (i')		1.213	1.255	1.212 (0.8)	3.″7 (14.2 kpc)	0.74	-70°	M(V)
	SDSS (r')		1.111	1.174	1.105 (0.7)	3.″4 (13.1 kpc)	0.75	-73°	
PKS 1217+023	HST WFPC2 (F675W)	(4)	4.850	4.722	4.719 (3.15)	2.″5 (9.7 kpc)	0.79	85°	B
3C 273	HST WFPC2 (F606W)	(5)	1.941	1.823	1.814 (2.8)	5.″0 (13.7 kpc)	0.80	78°	B
SDSS J1230+6621	SDSS (i')		1.340	1.340	1.339 (1.7)	1.″8 (5.6 kpc)	0.85	15°	D?
	SDSS (r')		1.047	1.052	1.047 (1.1)	1.″8 (5.6 kpc)	0.73	24°	
HE 1228+0131	SDSS (i')		1.038	1.006	0.992 (9.9)	0.″3 (0.6 kpc)	0.66	-48°	?
	SDSS (r')		1.122	1.110	1.104 (9.0)	0.″8 (1.7 kpc)	0.68	-63°	
SDSS J1230+1100	SDSS (i')		0.878	0.867	0.864 (6.1)	0.″2 (0.8 kpc)	0.77	-86°	?
	SDSS (r')		1.055	1.047	1.043 (8.5)	0.″2 (0.8 kpc)	0.82	-30°	
SDSS J1444+0633	SDSS (i')		0.982	0.975	0.972 (12.1)	1.″3 (4.4 kpc)	0.68	85°	?
	SDSS (r')		0.981	0.974	0.974 (7.2)	1.″7 (5.4 kpc)	0.70	90°	
PG 1427+480	SDSS (i')		1.438	1.408	...	0.″9 (3.2 kpc)	0.90	34°	B?
	SDSS (r')		1.039	1.033	1.032 (6.8)	0.″6 (2.1 kpc)	0.79	20°	
PKS 1545+210	HST WFPC2 (F606W)	(5)	2.667	2.606	2.603 (3.0)	1.″8 (7.4 kpc)	0.85	77°	B
PG 1612+261	SDSS (i')		1.057	1.053	1.047 (2.2)	1.″6 (3.7 kpc)	0.37	10°	D(V)
	SDSS (r')		1.057	1.068	1.047 (1.7)	1.″7 (3.96 kpc)	0.40	11°	
SDSS J1655+2146	SDSS (i')		1.795	1.662	...	0.″2 (0.5 kpc)	0.94	51°	?
	SDSS (r')		1.188	1.140	...	0.″6 (1.6 kpc)	0.82	30°	
PG 1700+518	HST WFPC2 (F547M)	(1)	1.800	1.742	...	1.″4 (6.2 kpc)	0.80	23°	M(V)
PG 2130+099	HST WFPC2 (F606W)	(6)	1.870	1.875	1.833 (1.8)	12.″0 (14 kpc)	0.36	60°	B+D
	NTT SOFI (H)		1.417	1.372	1.360 (2.4)	7.″3 (8.6 kpc)	0.31	51°	
HE 2152−0936	NTT SOFI (H)		1.156	1.128	1.091 (9.6)	0.″7 (2.2 kpc)	0.48	59°	D(V)
	LB1 Apogee U42 (R)		1.263	1.248	1.243 (8.5)	1.″7 (5.3 kpc)	0.59	60°	
HE 2158−0107[f]	SDSS (z)		0.884	0.880	0.880 (6.2)	0.″2 (0.7 kpc)	0.93	43°	B?
	NTT SOFI (H)		...	...	...	...	...	...	
PG 2214+139	NTT SOFI (H)		1.014	1.063	0.950 (1.8)	2.″9 (3.7 kpc)	0.97	64°	B
	SDSS (i')		1.825	1.380	1.299 (5.4)	4.″2 (5.4 kpc)	0.94	63°	
	SDSS (r')		2.326	1.814	1.684 (5.8)	4.″1 (5.3 kpc)	0.94	56°	
HE 2307−0254	NTT SOFI (H)		0.542	0.542	0.542 (6.2)	0.″2 (0.7 kpc)	0.67	35°	B?
PKS 2349−014	HST WFPC2 (F606W)	(7)	2.649	2.441	2.436 (3.3)	5.″6 (16.5 kpc)	0.81	83°	B/M
HE 2353−0420	LB1 Apogee U42 (R)		0.940	0.957	0.939 (0.7)	3.″8 (13.9 kpc)	0.49	15°	D(V)

Notes. [(a)] References to the articles in which a morphological analysis of these data was initally presented. [(b)] Effective radius r_e of the best-fitting realistic host-galaxy model given in apparent and physical scale. [(c)] Axis ratio of the minor to major axis of the best-fitting model. [(d)] Position angle of the major axis of the best-fitting model oriented such that 0° is North and 90° is East. [(e)] Our host galaxy morphological classification into: B (bulge-dominated), D (disc-dominated), B+D (bulge+disc component), M (Merger or strongly interacting), B?/D? (only tentative classifications), ? (unconstrained). We append (V) to the classification, if it is due to a visiual inspection of the image. [(f)] unrsolved host galaxy

References. (1) Veilleux et al. (2009); (2) Bahcall et al. (1996); (3) McLure et al. (1999); (4) Dunlop et al. (2003); (5) Bahcall et al. (1997); (6) Kim et al. (2008); (7) Bahcall et al. (1995)

Each QSO host was modelled with three different radial Sersić surface brightness profiles where the Sersić index was fixed to $n = 1$ (exponential profile), to $n = 4$ (de Vaucouleurs profile) or left as a free parameter, respectively. The resulting χ^2 values and the best-fit structural parameters are reported in Table 3.3. In the cases of PG 2130+099 and I Zw 1, a bulge+disc model provides a significantly better fit to the surface brightness distribution in the *HST* images than a single component. The structural parameters reported in Table 3.3 for these two QSO hosts refer to the disc component of the model.

The QSO hosts observed with *HST* are all well resolved and we recover the host galaxies also for the majority of the ground-based observation. PSF-subtracted host galaxy images are presented below in Fig. 3.6 for all objects. The ground-based images clearly suffer from their low spatial resolution, so that the models are strongly affected by PSF mismatch in compact galaxies that sometimes lead to nonphysically high Sersić in-

dices. The comparison of the SDSS *i* and *r* images allow us to judge the robustness of the results. A strong deviation indicates that the structural parameter could not be well constrained. Furthermore, a close apparent companion affected the modelling of SDSS J1655+2146, so that a reasonable model could only be inferred for the host with a fixed Sersić indices.

Morphological classification

Discriminating between a bulge- or disc-dominated QSO host galaxy is not always straightforward, even for the high spatial resolution images obtained with *HST*. Commonly used criteria are the best-fitting Sersić index n to distinguish bulge-dominated ($n > 2.5$) and disc-dominated ($n < 2.5$) systems (e.g. Bell et al. 2004) or the lowest χ^2 value of different models to identify the best one (e.g. McLeod & McLeod 2001; Dunlop et al. 2003; Jahnke & Wisotzki 2003; Guyon et al. 2006). However, the statistical significance for the favoured model needs to be considered. On the other hand, a visual classification of the host is often preferred to identify spiral structures of disc-dominated systems, or apparently disturbed merging system.

For the *HST* images, the χ^2 value robustly discriminate between the models. We adopt the criterion by Guyon et al. (2006), which demands a significant difference in the reduced χ^2 of $|\chi^2_\nu(n = 1) - \chi^2_\nu(n = 4)| > 0.05$. The χ^2 classification always agreed with the best-fit Sersić index and we achieved good agreement with literature results. The situation is more difficult for the ground-based observations, where the χ^2 values sometimes differ only marginally. A visual inspection of the images, together with large axis ratios (b/a), may provide evidence in some cases for disc-dominated host even when a bulge-dominated model was formally preferred as in the case of HE 0132−0441, PG 1612+261, HE 2152−0936 and HE 2353−0420. When the best-fitting Sersić index is $n > 7$, we doubt that any reliable classification can be made, because probably severe flux transfer between the PSF and a compact host happened. In the other cases, we refer to the best-fitting Sersić indices for our classification, but consider these classifications as tentative.

From the 28 QSOs with available broad-band imaging, we classified 17 host galaxies into 5 bulge-dominated, 8 disc-dominated and 4 ongoing merging galaxies. 5 of the remaining hosts are likely bulge-dominated systems and one is probably disc-dominated. For the rest of the host galaxies we were not able to constrain the morphology. Our sample seems to be almost evenly split up into bulge- and disc-dominated systems without any preference.

3.3. Spatially resolved spectroscopy of QSOs

3.3.1. PMAS IFU observations

IFU observations for the initial sample were carried out with PMAS in the nights from the 2th to 7th of April in 2002 and from the 2nd to 4th of May 2003. The QSOs of the extended sample were observed in night from the 13th to 17th of March and from the 5th to 8th of September in 2008. In all cases we used the PMAS lens-array with the highest magnification providing a seeing-limited sampling of $0\farcs5 \times 0\farcs5$ and a field of view of $8'' \times 8''$ for the 256 spaxels[2]. The host galaxies of the observed QSOs effectively fill the field of view in most cases (see Fig. 3.6), but are significantly larger for the three nearest objects ($z < 0.10$) and a few extended systems at higher redshift.

The low resolution V300 grating was used for the observations of the initial QSO sample covering a large wavelength range including the major diagnostic spectral features around the Hβ and Hα emission lines simultaneously. Higher spectral resolution observations with the V600 grating were taken for the extension of the sample, but then centred on the Hβ emission line only. For both setups we estimated the spectral resolution from the O I λ5577 night-sky emission line to be 6.1 Å (FWHM) and 3.2 Å (FWHM), respectively. At least two exposures were usually taken for each QSO with individual integration times in the range of 900 s up to 2400 second reaching a total integration time of 1-2 hours per object. Table 3.4 summarises the details of the observations including notes on the ambient observing conditions.

A set of arc lamp (HgNe) and continuum lamp exposures were acquired before or after the target frames for fibre tracing and wavelength calibration. Skyflats were taken during twilight to measure the variations in the fibre-to-fibre transmission, and spectro-photometric standard stars were regularly observed at the beginning and at the end of the nights with the same instrumental setups as the QSOs.

3.3.2. Data reduction

The basic data reduction was performed with the `R3D` reduction package (Sánchez 2006) designed to reduce fibre-fed integral field spectroscopy data. We used the independent modular tasks of the package for the following basic reduction steps: 1. bias subtraction, 2. fibre tracing on the continuum lamp exposure, 3. extraction of the fibre spectra, 4. wavelength calibration with the arc-lamp exposures, 5. fibreflat correction based on observed skyflats, 6. flux calibration of the spectra using spectrophotometric standard star observations, and 7. creation of a datacube from the row-stacked spectra.

As discussed in Roth et al. (2005), the PMAS instrument suffers from flexure depending on the hour angle of the observations. This inevitably leads to shifts between different exposures of the same target in dispersion and/or cross-dispersion direction of the spectra on the CCD detector. We measured those shifts in both direction between the science exposures with the `IRAF` task *imalign* by comparing the position of ~20 sky emission lines distributed across the whole CCD in the raw image. The shifts between individual exposures were of the order of subpixels up to a few pixels. If only one set of calibration frames (continuum+arc lamp) was available for a sequence of observations, we resampled the calibration frames to match with position of the individual exposures. The science frame taken right after or before the calibration frames was used as the reference for the zero position.

Because of the various rebinning processes along the basic `R3D` reduction tasks, it is mandatory to clean the raw frames from the majority of cosmic rays. To combine the frames at the raw level is impossible for PMAS due to the shifts caused by flexure. We thus detected and removed cosmics rays from the individual raw frames with the DCR routine (Pych 2004). As emission line features and cosmic rays can appear very similar on raw IFU data we used a balanced configuration of DCR, so that most of the cosmics rays were removed without affecting night sky lines or emission-line features of our target itself. This procedure needs to be applied carefully as pixels affected by a cosmic ray are replaced by surrounding pixels, but the "true" information is still

[2] spectral pixel, a single spatial resolution element containing a spectrum along the entire wavelength range

Table 3.4. PMAS IFU observational log.

Object	Date	t_{exp} [sec]	Grating	Wavelength coverage	Seeing	Condition
PG 0026+129	2002–09–05	1×1200, 1×2400	V300	4600–7800Å	1.″1	photometric
I Zw 1	2002–09–03	1×900, 2×1800	V300	3900–7200Å	1.″0–1.″4	mainly clear
PG 0052+251	2002–09–06	2×1800	V300	4600–7800Å	1.″0	photometric
SDSS J0057+1446	2008–09–05	5×1800	V600	5100–6600Å	1.″5	part. cloudy
HE 0132−0441	2002–09–02	1×1200, 1×1800	V300	4600–7800Å	1.″2–1.″8	photometric
SDSS J0155−0857	2008–09–07	4×1800	V600	5100–6600Å	1.″4–1.″8	photometric
		2×1800			1.″2	photometric
HE 0157−0406	2002–09–02	1×1200, 1×1800	V300	5400–8600Å	1.″2–1.″3	photometric
Mrk 1014	2002–09–07	1×1200, 1×1800	V300	5400–8600Å	1.″2–1.″3	photometric
	2008–09–06	4×1800	V600	5100–6600Å	1.″4	mainly clear
SDSS J0836+4426	2008–03–16	3×1800	V600	5500–7000Å	1.″1	part. cloudy
SDSS J0948+4335	2008–03–13	3×1800	V600	5250–6750Å	1.″1	cloudy
SDSS J1131+2623	2008–03–13	3×1800	V600	5250–6750Å	1.″1	part. cloudy
PKS 1217+023	2003–05–02	4×1800	V300	5600–8900Å	1.″0–1.″2	mainly clear
3C 273	2003–05–03	3×1200	V300	4350–7650Å	1.″4–1.″9	mainly clear
HE 1228+0131	2003–05–04	4×1800	V300	4350–7650Å	1.″0–1.″3	part. cloudy
SDSS J1230+6621	2008–03–16	2×1800	V600	5000–6500Å	1.″0	mainly clear
SDSS J1230+1100	2008–03–13	1×1800	V600	5250–6750Å	1.″1	cloudy
PG 1427+490	2003–05–01	3×1200	V300	5600–8900Å	0.″9–1.″2	mainly clear
SDSS J1444+0633	2008–03–16	1×1800	V600	5250–6750Å	1.″3–1.″5	cloudy
HE 1453−0303	2003–05–02	2×1800	V300	5600–8900Å	1.″2–1.″5	mainly clear
	2003–05–03	2×1800			1.″3–1.″6	mainyl clear
PKS 1545+21	2003–05–03	3×1800	V300	5600–8900Å	1.″2–1.″5	mainly clear
PG 1612+261	2008–09–07	3×1800	V600	5100–6600Å	1.″1	mainly clear
SDSS J1655+2146	2008–03–16	3×1200	V600	5000–6500Å	1.″3–1.″6	part. cloudy
		1×1800			1.″0	photometric
PG 1700+518	2003–05–02	2×1800	V300	5600–8900Å	0.″9–1.″2	photometric
	2003–05–03	2×1800			1.″6	mainly clear
PG 2130+099	2002–09–04	2×2400	V300	3900–7200Å	1.″3	photometric
HE 2152−0936	2002–09–06	2×1800	V300	5400–8600Å	1.″2	photometric
HE 2158−0107	2002–09–06	2×1800	V300	5400–8600	1.″1	photometric
HE 2158+0115	2002–09–04	1×2400	V300	4600–7800Å	1.″5	photometric
	2002–09–05	2×2400			1.″6–2.″0	mainly clear
PG 2214+139	2002–09–02	2×2400, 1×1800	V300	3900–7200Å	1.″3–1.″4	photometric
HE 2307−0254	2002–09–06	2×1800	V300	5400–8600Å	1.″2	photometric
PKS 2349−014	2002–09–06	3×900	V300	5400–8600Å	1.″0–1.″1	photometric
HE 2353−0420	2002–09–07	2×1800	V300	5400–8600Å	1.″1–1.″4	photometric

lost for that pixel. Thus, we always required that emission lines must be spatially extended, that they had a line width equal or greater than the instrumental resolution, and that the doublet line ratios were consistent with their theoretical values.

A median sky spectrum was created from spaxels uncontaminated by extended emission lines of the QSO host. That sky spectrum was then subtracted from the whole datacube. We thus excepted a contamination of the sky spectrum by stellar continuum emission of the QSO host galaxy for several QSO hosts if it filled the entire field of view. This has no strong impact on our emission line analysis, but the Balmer emission lines need to be corrected for the underlying stellar absorption lines. We address the issue of the inaccurate sky subtraction and how it affects our emission-line measurements in Sect. 3.3.4.

The datacubes were further corrected for differential atmospheric refraction (DAR) by resampling each monochromatic slice such that the position of the QSO is aligned to a common reference point at all wavelengths. We flux-calibrated the datacubes based on the mean sensitivity functions of all observed standard stars for a certain instrumental setup taking into account the airmass and the atmospheric extinction law for the Calar Alto observatory (Sánchez et al. 2007). Finally, we combined the datacubes using either a variance weighted mean or a clipping method whenever 3 or more exposures were available to reject remaining cosmic rays and artifacts.

Most of the data were taken under clear or photometric conditions. In order to check the quality and uncertainty of the spectrophotometry, we compared the flux-calibrated QSO spectra with available SDSS spectra taking into account the size of SDSS fibre. The deviation between the QSO spectra in the continuum over the whole wavelength range was 20% at most, which we adopt as our spectro-photometric uncertainty.

3.3.3. QSO-host deblending with QDeblend^{3D}

Similar to the deblending of the broad-band images we need to decompose the QSO and host emission also in our IFU data to study and interpret the emission of the host galaxy without the QSO contamination. The three-dimensional nature of the IFU date requires new analysis techniques and software. We devel-

oped the software tool QDeblend^{3D} for this particular task[3]. At the core of the program is an iterative deblending algorithm which is a significant improvement of a simple technique introduced by Christensen et al. (2006).

The basic concept is to treat the spaxels of the IFU datacube as a set of independent spectra rather than as a sequence of monochromatic images. In the absence of atmospheric dispersion the spectrum of a point source would then be the same in each spaxel, multiplied by a scale factor according to the PSF. In the case of QSO observations, the scale factors of the PSF can be directly determined from the strength of the broad emission lines with respect to the adjacent continuum as described by Jahnke et al. (2004) at the specific wavelength of the broad emission lines (see Fig. A.1 in the Appendix). Here we will briefly outline the iterative algorithm implemented in QDeblend^{3D}. A more detailed explanation of the iterative process can be found in Appendix A.

In a first step a high S/N nuclear QSO spectrum is extracted from the datacube. After a PSF has been determined from a broad QSO emission line, the nuclear QSO spectrum is subtracted from each spaxel after multiplied by the corresponding PSF scale factor. However, oversubtraction will occur, since the nuclear QSO spectrum is usually contaminated by extended host galaxy light. With the iterative scheme of QDeblend^{3D} we try to subtract this host galaxy contamination from the nuclear spectrum, by estimating a *mean* host galaxy spectrum from the residual datacube after QSO subtraction. Usually a rectangular aperture is used to extract the QSOs around which an rectangular annulus defines the region of the host galaxy spectrum. However, any set of the spaxel for the QSO and host galaxy spectrum can be defined with QDeblend^{3D}. Since the host galaxy becomes brighter towards the galaxy centre, the mean host spectrum in an extended region should to be scaled in brightness before it is subtracted from the initial nuclear QSO spectrum. That scale factor is unconstrained from the IFU data itself. One may either adopt an analytic surface brightness profile, a constant surface brightness, or a manually set scale factor which fulfils a certain criterion. The decontaminated nuclear QSO spectrum is then used as the starting point for another iteration until the decontaminated nuclear QSO spectra converge.

For our PMAS spectra we use the broad Hα or Hβ lines of the QSOs to perform a QSO-host deblending with QDeblend^{3D}. Since we focus on the emission lines of the ionised gas around Hβ and Hα region in this work, we restrict the QSO-host deblending to small wavelength regions around the two Balmer lines. This almost entirely avoids the problem of PSF mismatch due to the wavelength dependence of the atmospheric seeing. The nuclear QSO spectra are taken from the brightest spaxel in the data, and the surrounding 8 spaxels are used to estimate a mean host galaxy spectrum from the residuals. Here we assume a constant surface brightness to extrapolate the host galaxy emission towards the central spaxel. The QSO spectra converged already after 4 iterations at which we stopped the iterative process.

3.3.4. Imperfect sky subtraction and Balmer absorption

One problem with our observations is the imperfect subtraction of the sky background, because the PMAS lens-array has no dedicated sky fibres and our host galaxies frequently fill the entire field of view. Since no blank sky fields were obtained together with the science exposures, we were forced to estimate the sky directly from the science exposures itself. We used areas free of extended emission lines to avoid any oversubtraction of these lines, but those regions may contain significant emission from stellar continuum of the host. Thus, the stellar continuum is usually oversubtracted and we are unable to reliably infer directly the "real" stellar continuum from our data.

Although we do not aim to analyse the stellar continuum in this work, the apparent strength of the Balmer emission-lines depend on the strength of their underlying stellar absorption lines. This needs to be always taken into account when using the Balmer lines for a quantitative analysis and diagnostic purposes. In order to explore the impact of the Balmer absorption line on our measurements, we combined synthetic single stellar population (SSP) models from Bruzual & Charlot (2003) with the absolute surface brightness photometry of the *HST* broad-band images. In a first step, we convolved the nucleus-subtracted *HST* images with the PSF of the corresponding PMAS observation and rebinned the image to the spatial sampling of our PMAS data. Afterwards, we scaled a suite of SSP spectra to the surface brightness in several specific regions. As an example we show in Fig. 3.3 two SSP models (300 Myr and 5Gyr) matched

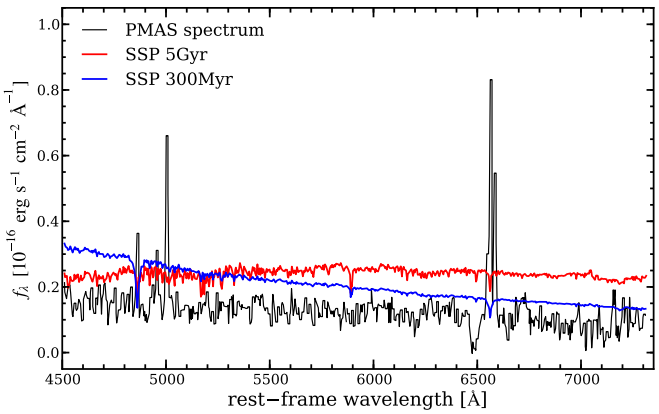

Fig. 3.3. Comparing the PMAS spectra of PKS 2349−014 (region A) with two SSP model spectra matched to the *HST* photometry. The systematic offset between the SSP models and the PMAS spectra is caused by an oversubtraction of the sky background in the PMAS observations.

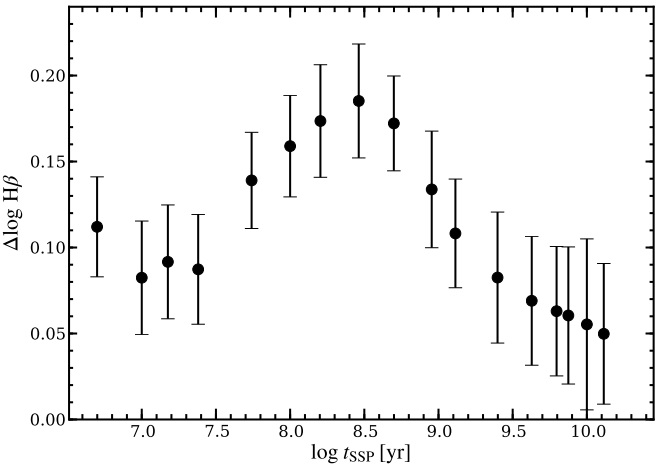

Fig. 3.4. Underestimation of the Hβ emission line flux (Δ log(Hβ)) due to the stellar absorption line as a function of the stellar population age for the PMAS spectrum of PKS 2349−014 (region A).

[3] available for download at http://sourceforge.net/projects/qdeblend/

to the *HST* photometry in comparison to the PMAS spectrum of PKS 2349−014 (region A as defined in Fig. 3.6). The PMAS spectrum is well below both SSP model spectra, which can be entirely attributed to the oversubtracted sky.

The strengths of the Balmer absorption lines depend on the age of the stellar population. We measured the differences between the Hβ emission line fluxes of the continuum subtracted and unsubtracted PMAS spectra expressed as $\Delta\log(\mathrm{H}\beta) = \log(\mathrm{H}\beta_{\mathrm{sub.}}) - \log(\mathrm{H}\beta_{\mathrm{unsub.}})$ for 18 SSP spectra with ages of the order of 300 Myr $< t_{\mathrm{SSP}} <$ 5 Gyr assuming solar metallicity. We show the dependence of ΔHβ on t_{SSP} for PKS 2349−014 (region A) as an example in Fig. 3.4. We find that the Hβ emission line flux is underestimated due to the corresponding stellar absorption line by 0.07-0.2 dex in this case of PKS 2349−014. The redshift of that object ($z = 0.174$) is close to the median redshift of our sample and representative for the majority of objects. The Hβ emission-line flux is more severely affected for the few object at $z = 0.06$ given the lower equivalent width of their emission line.

Due to the unconstrained age of the stellar population, we used the average of $\Delta\log(\mathrm{H}\beta)$ taken over all SSP ages with an error corresponding to the possible range of values. For the host that fill the PMAS field of view and were not observed with *HST*, we corrected all Hβ lines by an average factor of $\Delta\log(\mathrm{H}\beta) = 0.13 \pm 0.08$ dex, determined from all objects with reliable *HST* photometry. Although the Hα emission line is also affected by the stellar absorption, we made not correction given that the correction factor is negligible with 0.03 ± 0.01 dex only.

3.4. AGN parameters from the QSO spectra

Our PMAS data provide high S/N spectra of the central QSOS without any wavelength-dependent slit losses, because the IFU covers the entire seeing disc of a point source even under bad seeing conditions. We used those spectra to derive some fundamental AGN parameters, like redshifts, black hole masses M_{BH}, and Eddington ratios $\lambda = L_{\mathrm{bol}}/L_{\mathrm{Edd}}$. The contamination of the QSO spectrum by host galaxy light was removed or at least minimised by our QSO-host deblending process described above. For a few QSOs where the SDSS spectra had significantly higher S/N we used these instead. From the SDSS broad-band images we estimated a host contamination of only ∼15% for their SDSS spectra and corrected the estimated continuum luminosities correspondingly.

3.4.1. Spectral modelling of the Hβ-[O III] region

All of the AGN parameters we are interested in have been calibrated to spectral features around the broad Hβ. We therefore concentrated our analysis of the AGN spectra to the rest-frame wavelength region between 4700–5100Å. A multi-component model of the Hβ, [O III] and Fe II emission-lines was fitted to our QSO spectra. Several Gaussian components were used to deblend the various emission line, plus a straight line for the local continuum as described in Appendix B. Instead of using an iron template we directly modelled the two prominent Fe II lines in our wavelength range.

The best-fitting set of parameters was found by searching for the lowest χ^2 of the residuals with a downhill simplex algorithm (e.g. Press et al. 1992). Two representative examples of these models are presented in Fig. 3.5, while the models for all QSO spectra in our sample are shown in Fig. B.2. We measured the continuum flux at 5100Åand the width of the broad Hβ component expressed in terms of FWHM (FWHM$_{\mathrm{H}\beta}$) and line dispersion ($\sigma_{\mathrm{H}\beta}$) from the best-fitting model. These values are listed in Table B.1 for the entire sample.

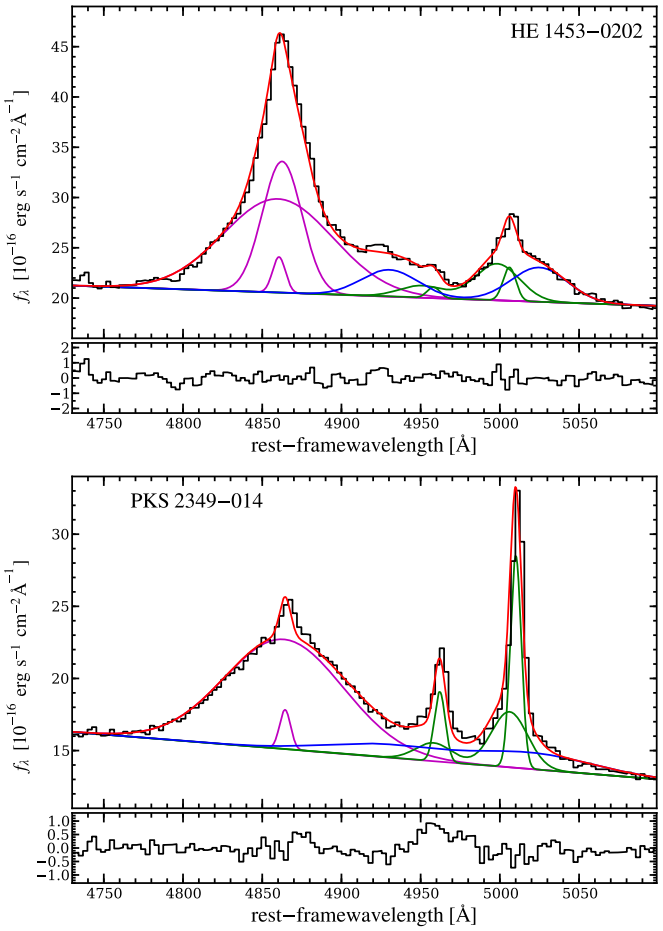

Fig. 3.5. Spectral modelling of the Hβ-[O III] region for two representative QSO spectra. The black line correspond to the observed QSO spectra and the red curve represents our best fit model. The model consists of individual Gaussian components for the emission lines (Hβ–magenta, [O III]–green, Fe II–blue) above a straight line for the local continuum. The residual of the model are shown in a dedicated panel below.

3.4.2. Black hole masses and Eddington ratios

Black hole masses can be estimated from single epoch broad-line AGN spectra using the so-called virial method (Peterson & Wandel 2000; Vestergaard 2002). It combines the empirically derived size-luminosity relation of the BLR as determined via reverberation mapping (e.g. Kaspi et al. 2000; Peterson et al. 2004; Kaspi et al. 2005; Bentz et al. 2006, 2009) and the kinematics of the BLR estimated from the width of the broad emission-lines assuming virial motion of the clouds. We adopted the empirical relation between the BLR size and the continuum luminosity at 5100 Å calibrated by Bentz et al. (2009), and the prescription of Collin et al. (2006) to infer the kinematics of the broad line clouds from the Hβ line dispersion ($\sigma_{\mathrm{H}\beta}$). A virial scale factor of 3.85 was estimated by Collin et al. (2006) to match the virial BH masses with the M_{BH}-σ_* relation of local inactive galaxies

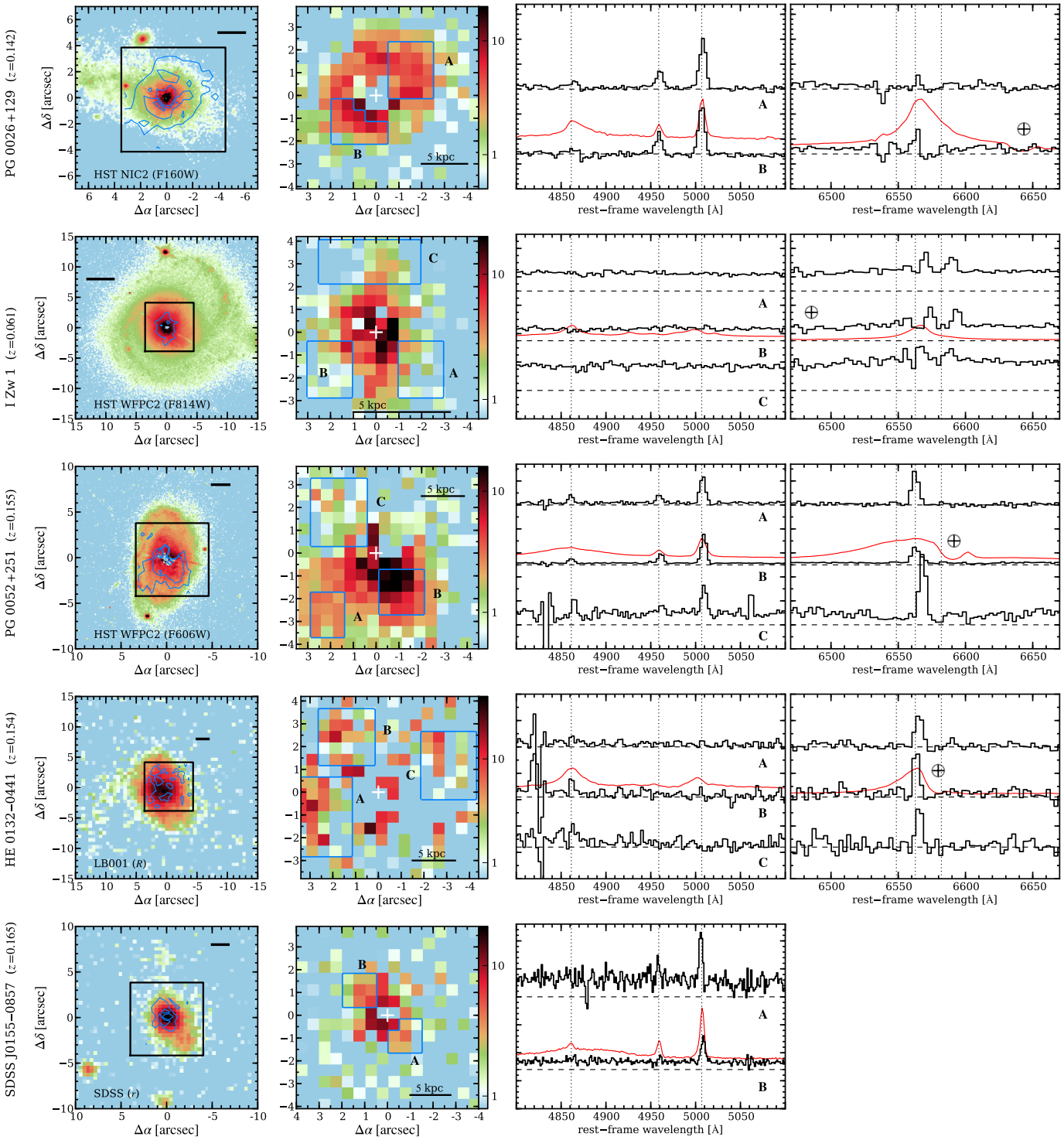

Fig. 3.6. Overview of the individual objects with extended emission. *Left panels:* Nucleus-subtracted broad-band images with overplotted countours of extended line emission within the PMAS field of view (black box). A scale bar represents 5 kpc at the object redshift and the image is oriented such that North is up and East is to the left. *Middle panels:* Nucleus-subtracted [O III] narrow-band PMAS images with a logarithmic scaling in units of 10^{-16} erg s^{-1}cm^{-2}arcsec^{-2}. Note that in the case of I Zw 1, HE 0132−0441 and HE 2152−0936, the Hα narrow-band images are shown instead. The blue boundaries indicate the spatial regions defined to obtain the co-added spectra shown in the right panels. A white cross marks the position of the QSO. *Right panels:* Co-added spectra of the specific spatial regions around the Hβ and Hα line. The different spectra are arbitrarily scaled and offset from each other, for which the dashed lines indicate their corresponding zero flux density. Vertical dotted lines mark the position of emission lines at the QSO redshift. The arbitrarily scaled QSO spectrum is shown as a red line for comparison. Telluric absorption line features are highlighted by a crossed circle symbol.

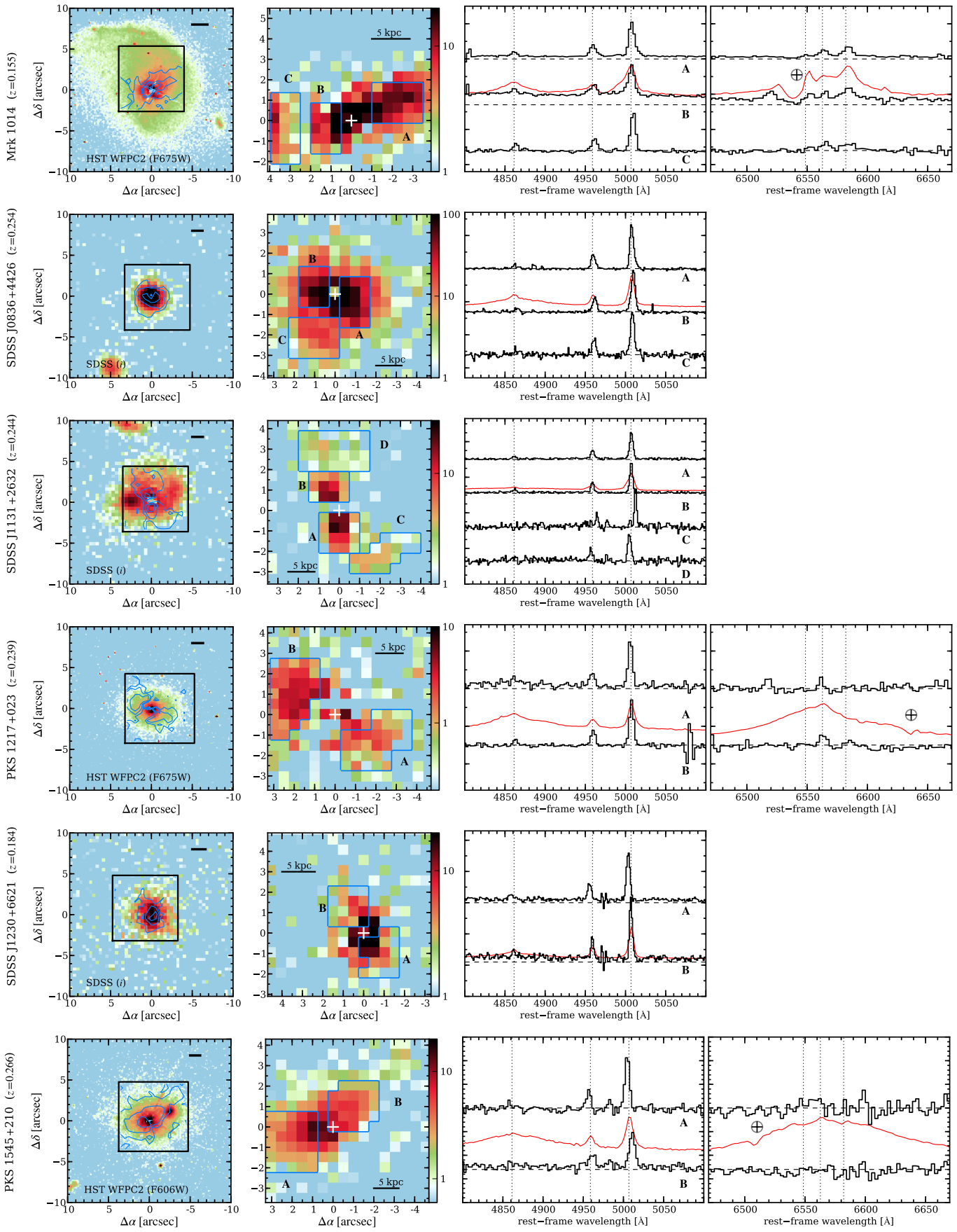

Fig. 3.6. Continued.

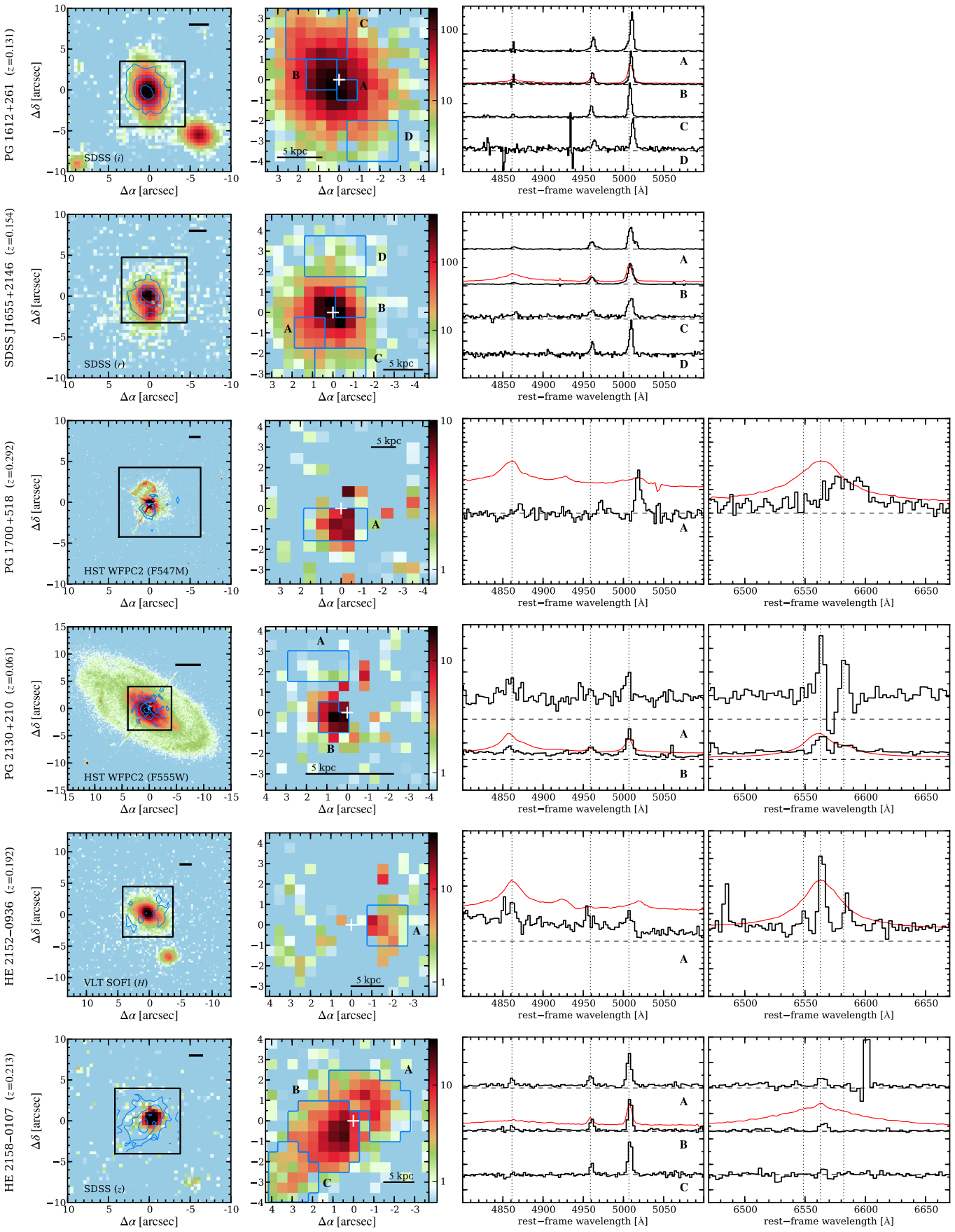

Fig. 3.6. Continued.

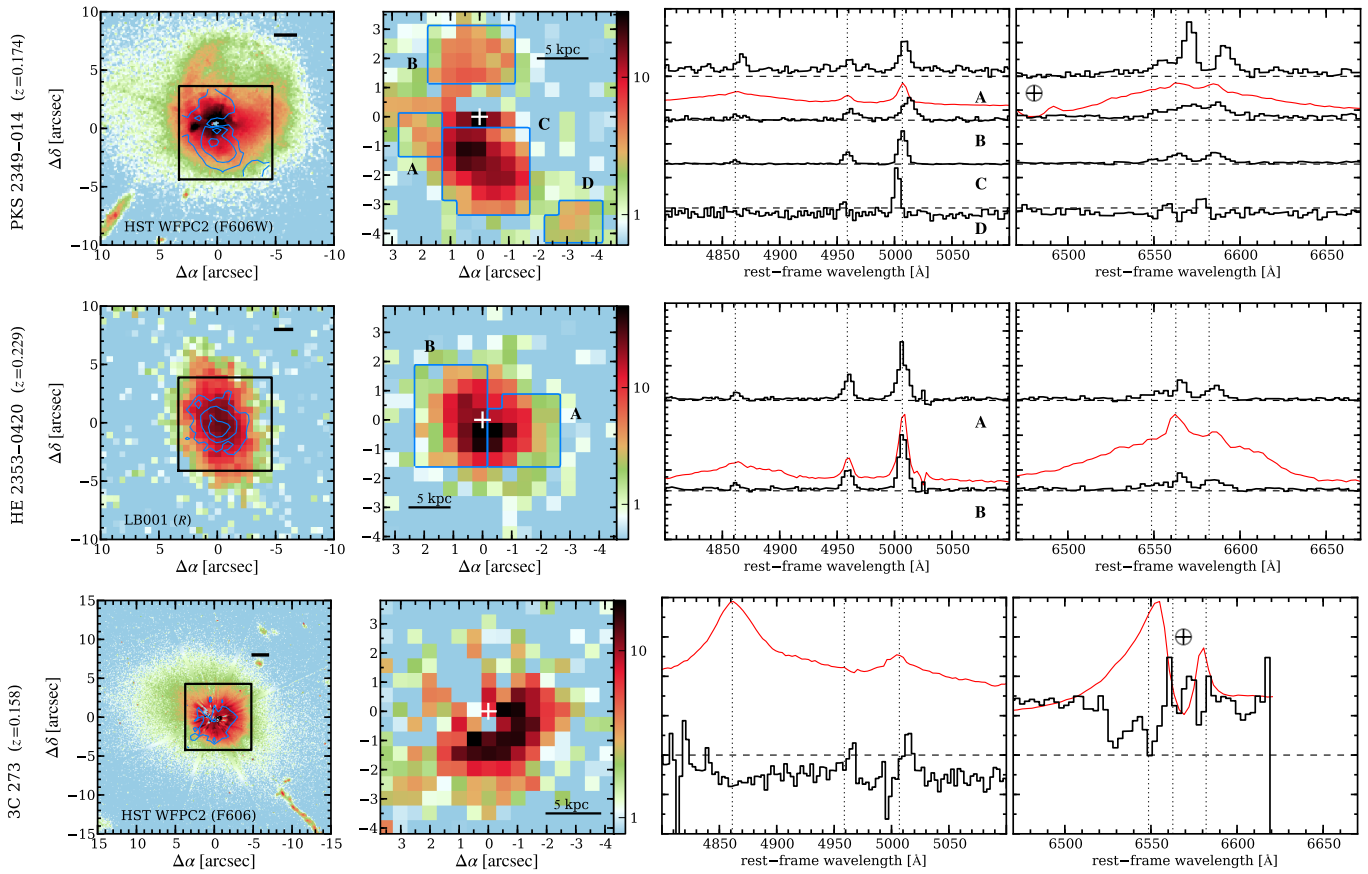

Fig. 3.6. Continued.

(Tremaine et al. 2002). This yields a black hole mass calibration of

$$M_{\rm BH} = 10^{7.41} \left(\frac{\sigma_{\rm H\beta}}{1000\,{\rm km\,s^{-1}}}\right)^2 \left(\frac{\lambda L_\lambda(5100)}{10^{44}{\rm erg/s}}\right)^{0.52} M_\odot\,. \quad (3.1)$$

The error on the estimated BH masses using the virial method is dominated by systematic errors rather than measurement errors from high S/N QSO spectra. In addition to the intrinsic uncertainties in the adopted scaling relations and the adopted line profile model, the unknown geometry and kinematics of the BLR and the correct determination of the QSO continuum flux are sources of the uncertainty. The BH masses estimated in this way are usually assumed to be accurate within a factor of ∼2.

Furthermore, we estimated the bolometric luminosity of the QSOs adopting an often used bolometric correction of

$$L_{\rm bol} = 9 \times \lambda L_\lambda(5100\text{Å})\,, \quad (3.2)$$

following Kaspi et al. (2000). From the BH masses we also calculated the Eddington luminosities $L_{\rm Edd}$ and Eddington ratios $\lambda \equiv L_{\rm bol}/L_{\rm Edd}$. The derived values for the $M_{\rm BH}$ and λ are given in Table B.1. Almost all of our QSOs have black hole masses of $M_{\rm BH} \gtrsim 10^8 M_\odot$ and Eddington ratios in between $0.1 \lesssim \lambda < 1$ without any QSO accreting above the Eddington limit, which is in agreement with the results of recent low-redshift QSO studies (Schulze & Wisotzki 2010; Steinhardt & Elvis 2010). The median BH mass and median Eddington ratio for our sample are $M_{\rm BH} \simeq 4 \times 10^8 M_\odot$ and $\lambda \simeq 0.15$. In individual cases, $M_{\rm BH}$ are found to be 0.5 dex larger than previous estimates based on the FWHM of Hβ (e.g. Vestergaard & Peterson 2006), but the values based on $\sigma_{H\beta}$ should be more robust as argued by Peterson et al. (2004) and Collin et al. (2006).

3.5. Emission line diagnostics of EELRs

3.5.1. Mapping of EELRs and their corresponding spectra

After subtracting the QSO contribution with QDeblend^{3D} from the observed data we took could study the properties of ionised gas around the QSOs. We started by extracting 40 Å wide narrow-band images centred on the [O III] λ5007 ([O III] hereafter) and Hα lines of the QSO after subtracting any underlying stellar continuum contribution. The synthetic passband of our narrow-band images roughly correspond to ±900 km s^{-1} in the rest frame at the median redshift of the sample, so that extended emission even with non-gravitational kinematics would be captured. We detect EELRs in [O III] around 16 of 31 QSOs (∼50%), of which a high fraction have also detectable Hα emission (when covered by our observations). Additionally, Hα emission is detected around three objects, I Zw 1, HE 0132−0441 and HE 2152−0936, without corresponding [O III] emission

In Fig. 3.6 we present the PMAS narrow-band images for all objects with detected EELRs in comparison to the nucleus-subtracted broad-band host images, when available. The EELRs generally do not extend beyond the size of the host galaxies at the surface brightness limits of our observations. The only exception is HE 2158−0107 for which the EELR is much more extended than the host galaxy and reaches even beyond the PMAS field of view with a projected size of >22 kpc. We therefore study this interesting object more detailed in Chapter 5.

As the Hβ, Hα, and [N II] lines are rather weak in individual spaxels we decided to co-add several spaxels to increase their S/N. Based on the morphology of the EELR we defined up to 4 characteristic spatial regions, avoiding spaxels with obvious

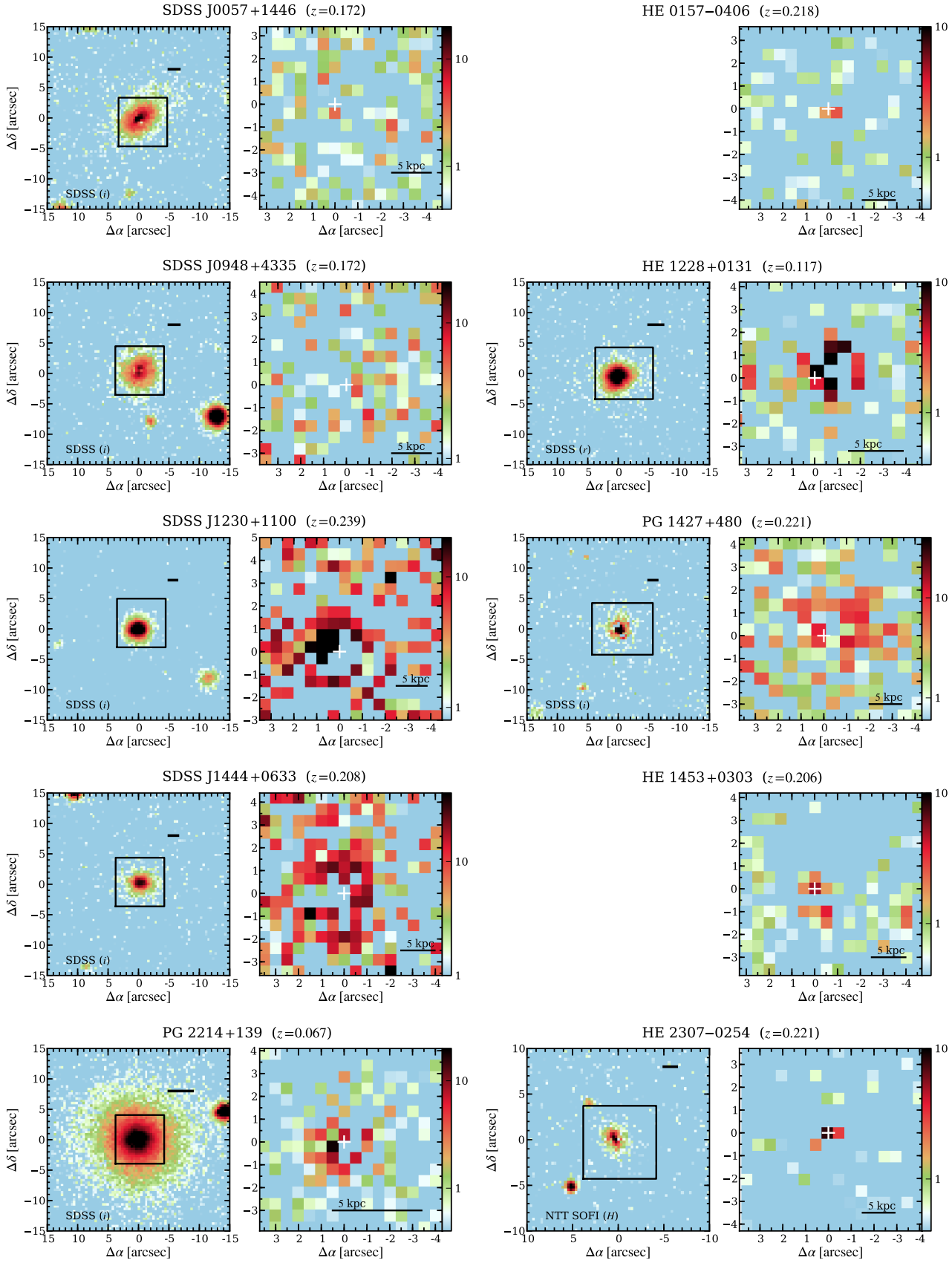

Fig. 3.7. Overview of the individual objects without detected extended emission. For each object the nucleus-subtracted broad-band images is presented, if available, in the left panel with the PMAS field of view indicated by the black rectangle. The black scale bar indicates a physical size of 5 kpc at the redshift of the object. The nucleus-subtracted [O III] narrow-band images is presented in the right panels with the a white cross indicating the QSO position.

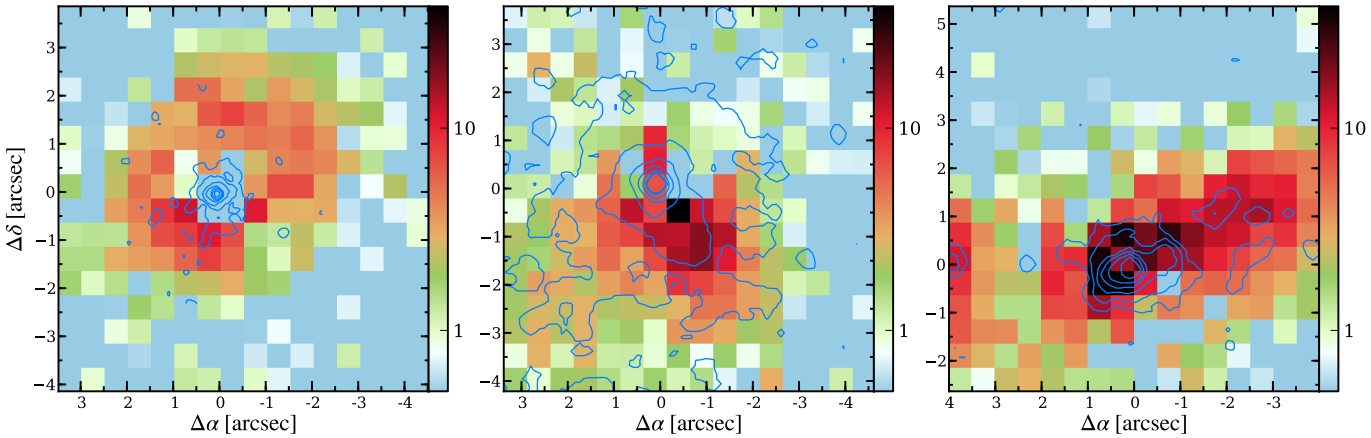

Fig. 3.8. Direct comparison of PMAS and *HST* [O III] narrow-band images. PMAS narrow-band images of PG 0026+129 (left panel), PG 0052+251 (middle panel) and Mrk 1014 (right panel) are shown in units of 10^{-16} erg s^{-1} cm^{-2} arcsec^{-2}. The corresponding *HST* narrow-band images of Bennert et al. (2002) are overplotted as blue contours also in a logarithmic scaling.

signs of artifacts or QSO residuals that could affect the emission line measurements. The region boundaries are shown in Fig. 3.6 together with the corresponding co-added spectra in the rest-frame wavelength intervals 4800–5100Å and 6450–6750Å, if covered by our observation. The Hβ and [O III] emission lines were clearly detected in most of these objects. Essentially no contamination of the broad Hβ emission was left in these extended spectra, which demonstrates the high quality of the deblending process at least beyond 0.″5 around the QSO position. The Hα and [N II] lines are often redshifted into one of the atmospheric absorption bands, which prevent a detection of these lines in those cases.

To quantitatively measure the observed emission lines, we modelled each line in the spectra with a Gaussian profile taking into account the theoretically fixed line ratios of the [O III] $\lambda\lambda$4960, 5007 and [N II] $\lambda\lambda$6548, 6583 doublets. Furthermore, we assumed that the lines are kinematically coupled having the same redshift and linewidth. This may not be true in all cases, because distinct ionised gas clouds with different kinematics and ionisation states can be aligned along our line-of-sight. The seeing may enhance this apparent confusion and in a few cases the redshift of the extended Balmer and [O III] lines do not agree in some regions of the host galaxy. Measured line fluxes, line widths and the rest-frame velocity offset with respect to the redshift of the narrow QSO [O III] emission line are reported in Table 3.6. Statistical errors on the flux measurements and 3σ upper limits for undetected emission lines were obtained based on the noise in the adjacent continuum.

We note that the Hβ line flux for the region A and B of PG 1612+261 is unreliable due to a bad column on the PMAS CCD, but regions C and D remain unaffected. Off-nuclear long-slit spectra presented already by Boroson et al. (1982) showed that the [O III]/Hβ line ratio is ∼10 out to several arcseconds away from the nucleus. Thus, we assume that the gas is at least as highly ionised closer to the nucleus, although we were not able to reliably constrain the line ratios in that region. Furthermore, we find that the [O III] emission line in region A is significantly asymmetric requiring two independent Gaussian components to model the line profile.

The QSO 3C 273 actually appears to be surrounded by some ionised gas, but it is by far the brightest object in our sample and was observed under poor seeing conditions. To check whether this feature may simply be an artifact we analysed the 3 individual exposures obtained for this target separately. The apparent structure could only be recovered in 1 of the 3 exposures implying that this may not be a real detection. Until observation with higher quality exists for 3C 273 we will treat it only as a candidate detection.

No extended line emission was detected around the remaining 12 objects in the sample. We present their narrow-band images and available broad-band images in Fig. 3.7 for completeness.

3.5.2. Comparison with *HST* narrow-band imaging

From the 7 QSOs of an *HST* narrow-band snapshot survey by Bennert et al. (2002) 3 objects are included in our PMAS sample. This enables us to directly compare the narrow-band images obtained from both telescope (Fig. 3.8). We applied a median smoothing filter with a box size of 5×5 pixels to the *HST* images in order to catch lower surface brightness (SFB) features. The 3σ SFB limits for the *HST* and PMAS narrow-band images are listed in Table 3.5. The estimated SFB limits support our visual impression from the comparison of the narrow-band images that the PMAS images are at least a factor of 4 deeper than the *HST* images even after smoothing.

PG 0026+129 was observed with the Planetary Camera (PC) that has a sampling of 0.″05 pixel^{-1} instead of 0.″1 pixel^{-1} compared to Wide Field Channel (WFC). Thus, the PMAS image for this particular object is roughly 20 times deeper than the one of *HST*, which was most likely the reason why the extended [O III] emission is completely missed by *HST*. The lowest SFB filaments around the nucleus in the *HST* image may tentatively correspond to the high SFB structures in our PMAS images. It is obvious that Bennert et al. (2002) underestimated the size of the extended [O III] emission for this object at least by factor of 3.

The *HST* images of PG 0052+251 and Mrk 1014 obtained with the WFC are deeper so that high SFB structures of extended [O III] emission could be detected. Nevertheless, our groundbases PMAS narrow-band images reach a lot deeper, in particular in the case of Mrk 1014 where diffuse emission is present between the high SFB structures. Similar IFU observation of Mrk 1014 obtained by Fu & Stockton (2008) display the same [O III] light distribution as our PMAS observation suggesting

Table 3.5. 3σ SFB limits of [O III] narrow-band images.

Name	HST	smoothed[a] HST	PMAS
	$\left[10^{-15}\ \mathrm{erg\ s^{-1}\ cm^{-2}\ arcsec^{-2}}\right]$		
PG 0026+129	10.73	3.79	0.14
PG 0052+251	2.77	0.80	0.18
Mrk 1014	2.74	0.91	0.21

Notes. [(a)] A median filter of 5×5 pixel box size was used.

that the structures are real. The low SFB regions south-east of PG 0052+251 was missed by Bennert et al. (2002) and became visible only after smoothing the HST data. The maximum [O III] size was thus underestimated by a factor of ∼2 in these two cases. We return to the issue of NLR sizes in section 3.7.

For PG 0052+215 we note further that the contours of the smoothed *HST* images do not agree with the [O III] light distribution in our PMAS images north of the nucleus. We carefully checked that this is not introduced by our data reduction or data analysis. A possible origin for the rather symmetric diffuse light in the *HST* image around the nucleus might be continuum emission of the host. Bennert et al. (2002) subtracted only the contribution of the QSO using a PSF-star image, because the S/N in the much shallower continuum image of the host was insufficient. The unavailability of a continuum image also hampered the analysis of the narrow-band *HST* image of PKS 1545+210 (3C 323.1) as part of large *HST* snapshot program to study extended gas around radio galaxies (Privon et al. 2008).

We conclude that *HST* is of course much better in terms of spatial resolution than any optical ground-based observations, but its narrow-band images suffer from low sensitivity which has already been noted by several authors (e.g. Bennert 2005; Privon et al. 2008). Additionally, narrow-band images require off-band images which are often not sufficiently deep or absent to subtract the stellar continuum contribution from the on-band images.

3.5.3. Ionisation sources of the EELRs

Narrow-band imaging observations of large AGN samples have been the main tool for detecting and characterising EELRs (e.g Stockton & MacKenty 1987; Baum et al. 1988; Mulchaey et al. 1996a; Bennert et al. 2002; Schmitt et al. 2003a,b; Privon et al. 2008). Most of these projects focused on a single emission line, which does not allow to constrain the origin of the gas ionisation. Three different ionisation mechanisms for the ISM on galactic scales need to be distinguished: 1. Photoionisation by the hard UV radiation field of an AGN leading to a resolved NLR. 2. Shock ionisation due to radio jets of an AGN. 3. Photoionisation of the ISM in star-forming regions due to the ionising UV photons of young and massive OB stars leading to classical H II regions. With the aid of diagnostic emission-line ratio diagrams it is possible to distinguish between different excitation mechanisms (Baldwin et al. 1981; Veilleux & Osterbrock 1987; Villar-Martin et al. 1997; Allen et al. 1998). The most commonly used diagnostic diagram in the optical is the [O III] λ5007/Hβ vs. [N II] λ6583/Hα diagram (Veilleux & Osterbrock 1987), also known as the BPT diagram (Baldwin et al. 1981). Those lines are usually the strongest in the optical spectrum and their ratios are most insensitive to reddening. AGN ionised gas and H II regions populate two distinct branches on this BPT diagram as shown in Fig. 3.9. A theoretical limit for the emission-line ratios of H II

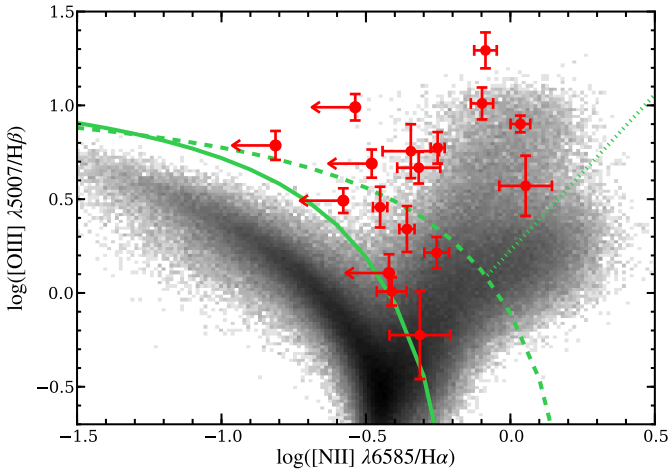

Fig. 3.9. The standard BPT [O III]λ5007/Hβ vs. [N II]λ6583/Hα diagram. The 2D histogram of the line ratios for more than 800 000 emission-line galaxies taken from the SDSS DR7 value-added MPA/JHU galaxy catalogue are shown in the grey (logarithmic) scale image. All EELR regions of our sample for which both line ratios could be measured, even if one ratio is just a limit, are plotted as red symbols. Demarcation curves by Kewley et al. (2001), Kauffmann et al. (2003) and Stasińska et al. (2008) are drawn as solid, dashed and dotted green line, respectively.

regions that can be reached during a maximum starburst event was derived by Kewley et al. (2001) for the BPT diagram:

$$\log([\mathrm{O\,III}]/\mathrm{H}\beta) = 0.61/(\log([\mathrm{N\,II}]/\mathrm{H}\alpha) - 0.47) + 1.19\ . \quad (3.3)$$

Based on a large sample of SDSS emission-line galaxies, Kauffmann et al. (2003) found that the AGN branch in the BPT diagram separates from H II branch well below the Kewley et al. demarcation curve and empirically defined a new line that tightly encloses the H II branch being parametrised as

$$\log([\mathrm{O\,III}]/\mathrm{H}\beta) = 0.61/(\log([\mathrm{N\,II}]/\mathrm{H}\alpha) - 0.05) + 1.3\ . \quad (3.4)$$

The region in between the two demarcation lines is often referred to as a composite region (Kauffmann et al. 2003; Kewley et al. 2006) where the emission-line gas could be partially ionised by both mechanisms. However, this classification approach may be oversimplified as pointed out by Cid Fernandes et al. (2010), because even emission-line ratios in the AGN area above the Kewley et al. curve may have some hidden contribution from H II region. Conversely, a region below that curve could be entirely powered by a massive starburst without requiring an AGN contribution. Furthermore, the AGN branch is composed of Seyfert type emission lines and Low Ionisation Nuclear Emission Regions (LINERs Heckman 1980) with lower [O III]/Hβ at a given [N II]/Hα ratio. Stasińska et al. (2008) defined a demarcation line between the two classes at a angle of 59°, counter clock-wise from a line of constant [O III]/Hβ, going through the point ($\log$ [N II]/Hα = −0.43, $\log$ [O III]/Hβ = −0.49). The nature of LINER emission is still strongly debated. Possible origins are AGN photoionisation, photoionisation from evolved stars or shock ionisation. Anyway, LINER-type line ratios are not found in our QSO sample.

We created a BPT diagram (Fig. 3.9) for all the co-added spectra in which we could measure both line ratios, [O III] λ5007/Hβ *and* [N II] λ6583/Hα. In the case that either Hβ or [N II] λ6538 was below the detection limit we used the 3σ up-

Table 3.6. Kinematics and line fluxes for specific regions of extended emission

Object[a]		Δv_r[b]	σ_{line}[c]	Hβ	[O III] λ5007	Hα	[N II] λ6585	Classification
		[km s^{-1}]	[km s^{-1}]	[10^{-16} erg s^{-1} cm^{-2}]				
PG 0026+129	A	48 ± 34	158 ± 14	2.4 ± 0.9	25.1 ± 1.0	...	...	AGN
	B	136 ± 32	153 ± 9	2.5 ± 0.4	19.8 ± 0.5	...	...	AGN
PG 0050+124	A	−312 ± 27	83 ± 24	...	...	9.3 ± 1.4	7.9 ± 0.3	H II
	B	−475 ± 28	18 ± 23	...	...	6.9 ± 2.8	7.7 ± 0.4	H II
	C	−215 ± 36	80 ± 30	...	...	9.8 ± 1.9	5.8 ± 0.7	H II
PG 0052+251	A	−127 ± 36	110 ± 31	3.0 ± 0.5	9.4 ± 0.2	9.5 ± 0.4	< 2.5	H II
	B	−232 ± 32	82 ± 27	6.3 ± 1.1	38.5 ± 0.2	22.1 ± 0.8	< 3.4	H II?
	C	−264 ± 41	65 ± 28	5.5 ± 1.2	7.0 ± 0.4	14.1 ± 1.1	< 5.3	AGN
HE 0132−0441	A	−95 ± 40	76 ± 22	...	...	12.1 ± 1.2	< 2.5	H II
	B	17 ± 39	0 ± 25	...	...	5.8 ± 1.7	< 4.6	H II
	C	−105 ± 47	0 ± 39	...	...	4.7 ± 2.9	< 8.3	H II
Mrk 1014	A	−100 ± 28	155 ± 22	9.1 ± 1.8	53.9 ± 0.5	26.1 ± 5.1[d]	14.6 ± 0.7	AGN
	B	67 ± 32	229 ± 17	14.0 ± 3.5	40.1 ± 0.9	40.2 ± 10.0[d]	14.2 ± 0.8	AGN
	C	−222 ± 31	113 ± 28	5.0 ± 1.0	23.0 ± 0.5	14.2 ± 2.7[d]	6.8 ± 1.0	AGN
SDSS J0846+4426	A	−88 ± 46	132 ± 3	18.2 ± 2.2	198.2 ± 2.3	...	...	AGN
	B	−229 ± 46	143 ± 3	14.2 ± 1.4	146.0 ± 1.5	...	...	AGN
	C	−154 ± 50	130 ± 8	< 5.4	58.6 ± 1.8	...	...	AGN
SDSS J1131+2623	A	−44 ± 69	117 ± 3	1.9 ± 0.9	32.6 ± 0.6	...	...	AGN
	B	−32 ± 68	87 ± 4	1.6 ± 0.3	25.7 ± 0.4	...	...	AGN
	C	−424 ± 72	54 ± 8	< 1.3	8.6 ± 0.4	...	...	AGN
	D	131 ± 76	105 ± 10	< 2.4	13.9 ± 0.8	...	...	AGN
PKS 1217+023	A	45 ± 35	75 ± 27	2.5 ± 0.6	9.3 ± 0.3	...	...	AGN
	B	−61 ± 37	80 ± 27	3.4 ± 1.1	19.4 ± 0.7	6.1 ± 0.8	2.8 ± 0.5	AGN
SDSS J1230+6621	A	299 ± 24	114 ± 6	4.0 ± 0.9	35.3 ± 0.9	...	...	AGN
	B	67 ± 23	80 ± 5	2.9 ± 0.4	19.5 ± 0.5	...	...	AGN
PKS 1545+210	A	309 ± 47	93 ± 29	4.5 ± 2.4	36.9 ± 1.8	...	...	AGN
	B	−134 ± 64	212 ± 51	6.0 ± 4.1	35.5 ± 4.7	...	...	AGN
PG 1612+261	A	70 ± 29	77 ± 5	< 18.9	111.0 ± 4.7	...	...	AGN
	B	54 ± 28	91 ± 3	< 8.2	289.1 ± 2.0	...	...	AGN
	C	248 ± 28	82 ± 4	18.2 ± 3.7	199.8 ± 1.2	...	...	AGN
	D	−92 ± 33	105 ± 8	< 4.8	29.3 ± 1.2	...	...	AGN
SDSS J1655+2146	A	−85 ± 26	161 ± 2	1.3 ± 0.8	127.9 ± 0.9	...	...	AGN
	B	−85 ± 27	183 ± 3	20.4 ± 2.6	319.3 ± 3.0	...	...	AGN
	C	−78 ± 31	197 ± 7	8.1 ± 1.0	44.3 ± 1.2	...	...	AGN
	D	−128 ± 30	94 ± 5	< 4.1	43.5 ± 1.4	...	...	AGN
PG 1700+518	A	−889 ± 67	158 ± 39	2.1 ± 0.6	9.2 ± 0.8	...	...	AGN
PG 2130+099	A	−99 ± 68	180 ± 105	5.9 ± 3.0	3.5 ± 0.7	7.7 ± 1.6	3.8 ± 0.4	H II
	B	−262 ± 36	176 ± 32	10.1 ± 2.8	22.1 ± 1.3	21.6 ± 1.1	9.5 ± 0.3	AGN?
HE 2152−0936	A	49 ± 27	33 ± 15	3.4 ± 0.4	3.4 ± 0.4	14.6 ± 1.0	5.7 ± 0.5	AGN
HE 2158−0107	A	42 ± 44	69 ± 26	8.1 ± 1.4	39.6 ± 1.5	11.5 ± 1.6	< 3.8	AGN
	B	−50 ± 39	39 ± 23	11.2 ± 1.8	108.5 ± 1.9	28.4 ± 3.6	< 8.2	AGN
	C	−50 ± 47	0 ± 30	< 3.6	18.7 ± 1.2	...	...	AGN
PKS 2349−014	A	−33 ± 49	172 ± 24	4.2 ± 0.8	6.9 ± 0.3	10.3 ± 0.7	5.7 ± 0.4	H II
	B	−269 ± 57	299 ± 21	5.6 ± 2.1	20.8 ± 1.1	11.7 ± 2.2	13.2 ± 1.2	AGN
	C	97 ± 39	146 ± 22	12.2 ± 1.2	96.6 ± 0.9	34.0 ± 2.2	36.8 ± 1.6	AGN
	D	418 ± 47	0 ± 26	1.3 ± 0.1	5.8 ± 0.3	...	...	AGN
HE 2353−0420	A	85 ± 51	225 ± 17	7.6 ± 1.5	77.9 ± 2.0	22.5 ± 1.6	18.0 ± 1.0	AGN
	B	66 ± 46	189 ± 18	6.0 ± 1.3	116.5 ± 1.8	32.5 ± 2.2	26.6 ± 1.6	AGN

Notes. [a] Name of QSOs followed with the alphabetically ordered character of the specific co-added spectra. [b] Radial velocity offset with respect to the rest-frame of the nuclear [O III] line. Negative values corresponds to a blue shift. [c] Emission line dispersion after the instrumental dispersion was subtracted in quadrature. A zero dispersion means that the line was unresolved. [d] The Hα line was strongly affected by telluric absorption and its flux was estimates from the Hβ line assuming zero dust extinction (Hα/Hβ=2.87).

per limit to constrain at least an upper/lower limit on the corresponding line ratio. Most of the emission-line ratios are on the AGN side above the Kewley et al. line for which we assume that AGN ionisation is the *dominant* process to ionise the gas. Region C of PG 0052+251, region A of PG 2130+099 and region A of HE 2152−0936 are almost directly on the H II branch

and represent regions of ongoing star formation. Region A of PKS 2349−014 correspond to a physical companion located 4″ West of the nucleus and its emission-line ratios would place it in the composite region of the BPT diagram. However, the Hβ and Hα lines are redshifted by ∼200 km s^{-1} with respect to the [O III] lines. This can be explained most likely due to an seeing induced superposition of emission lines corresponding to an H II region and AGN ionised gas. Thus, we classify this particular emission-line region as solely being due to star formation.

For the majority of regions we are only able to infer a single emission line ratio, either [O III] λ5007/Hβ or [N II] λ6583/Hα, so that the ionisation mechanism can generally not be determined unambiguously. We assumed that all regions with only an Hα detection are characteristic for H II regions. If these regions were instead ionised by AGN, the [O III] line would be at least as bright as the Hα line assuming a theoretical Balmer decrement of Hα/Hβ ∼ 2.87 (Osterbrock & Ferland 2006) and a [O III]/Hβ line ratio of >3 as a threshold for AGN ionised gas. Dust extinction along our line-of-sight within the host galaxy can dilute the [O III] and Hβ emission further, but a high dust extinction is often found around H II regions and is directly proportional to the current star formation rate (SFR) (e.g. Hopkins et al. 2001; Sullivan et al. 2001). Thus AGN ionisation would be an unlikely scenario in those cases.

On the other hand, it is clear from the two branches in the BPT diagram that the [O III] λ5007/Hβ line ratio alone is not sufficient to constrain the ionisation mechanism. An emission-line ratio of log([O III] λ5007/Hβ) > 0.9 can still be securely assigned to AGN ionisation which is the case for 7 objects. Ho et al. (1997) defined a threshold value of [O III] λ5007/Hβ > 3 above which AGN photoionisation is likely to be the dominant process. This can be physically explained by the fact that the star forming branch in the BPT diagram represents actually a sequence of increasing gas-phase metallicity from high to low [O III]/Hβ line ratios (e.g. Pettini & Pagel 2004). A high [O III] λ5007/Hβ line ratio can reasonably excluded as a signature for star formation for luminous AGN by considering the mass-metallicity relation of galaxies (e.g. Tremonti et al. 2004). Luminous AGN reside almost exclusively in massive galaxies above $M_* > 10^{10} M_\odot$ (Kauffmann et al. 2003), corresponding to a high gas-phase metallicity ($Z > Z_\odot$). Thus, we will rely on the Ho et al. criterion to classify the ionisation of our EELRs, but we caution that the argument as outlined above might not be correct for all EELRs as the gas-phase metallicity typically decreases with distance from the galaxy centre (e.g. Henry & Worthey 1999).

From the detected EELRs we classified 12/18 EELRs to be entirely ionised by the AGN, 3/18 EELRs to be powered by H II regions only, and 3 of 18 exhibit signatures for both mechanisms dominating in spatially separated regions. Interestingly, all the H II regions are located in disc-dominated galaxies and in the strongly interacting system PKS 2349−014. Letawe et al. (2007) reported from their on-axis longslit spectroscopy of luminous QSOs that the ISM was in most cases ionised either by young stars or shocks. They found a completely AGN-ionised ISM only in the case of bulge-dominated galaxies, while their disc-dominated system or morphological disturbed galaxies show signatures of H II regions in almost every case. Since inactive disc-dominated galaxies are known to have young stellar population and continue to from star in their disc, it may not be surprising that this is true also for AGN hosts.

Table 3.7. Ongoing SFR from the integrated Hα luminosity.

Name	f(Hα) [10^{-16} erg s^{-1} cm^{-2}]	log L(Hα) [erg s^{-1}]	SFR [$M_\odot$ yr^{-1}]
PG 0050+124	43.5±11.2	40.6±0.2	0.3±0.1
PG 0052+251	75.6±5.5	41.7±0.1	3.9±1.1
HE 0132−0441	22.7±5.8	41.2±0.2	1.2±0.5
PG 2130+099	7.7±1.6	39.9±0.2	0.1±0.0
HE 2152−0936	14.6±1.0	41.2±0.1	1.2±0.3
PKS 2349−014	10.3±0.7	40.9±0.1	0.7±0.2

3.5.4. Ongoing star formation in QSO hosts

H II regions are a direct signature of ongoing star formation as the required energetic ionising photons can only be produced by massive OB stars with life times of <5 Myr. The integrated Hα luminosity of H II regions within a galaxy is directly proportional to the current star formation rate (SFR). We adopt the calibration of Kennicutt (1998)

$$\mathrm{SFR}\ (\mathrm{M_\odot yr^{-1}}) = \frac{L(\mathrm{H}\alpha)}{1.26 \times 10^{41}\ \mathrm{erg\,s^{-1}}} \quad , \tag{3.5}$$

which is based on a Salpeter initial mass function. It would be desirable to take the dust extinction of Hα into account, but that is unconstrained from our data in most cases and we decided to use the uncorrected Hα fluxes. We obtained the integrated Hα fluxes by co-adding the spectra of the entire field of view excluding the confirmed AGN ionised region. In case of HE 2152−0936, HE 0132−0441, and PKS 2349−014 the integrated values simply correspond to the summed flux in the specific emission-line regions. The resulting Hα luminosities and estimated SFRs can be found in Table 3.7.

The SFRs we infer for the disc-dominated host galaxies of PG 0052+251, HE 0132−0441 and HE 2152−0936 are of the order of 1M$_\odot$ yr^{-1} in agreement with typical star-forming galaxies at stellar masses around 10^{10}M$_\odot$ (e.g. Brinchmann et al. 2004). For I Zw 1 and PG 2130+099 the SFRs are of the order of 0.1M$_\odot$ yr^{-1} only. These values need to be considered as lower limits because the PMAS field of view centred on the QSO covered only the bulge and not the extended discs in which most of current star formation activity is expected to take place. Deep off-axis spectroscopy ($\gtrsim$ 9 kpc) of QSOs were presented by Nolan et al. (2001) and Wold et al. (2010) including PG 0052+251 and PKS 2349−014. They reported a high contribution (43 ± 19% in flux) of young stars (< 100 Myr) to the spectrum of PG 0052+251 matching well with our detected signatures of ongoing star formation in the disc of the host galaxy. On the other hand, they found a predominantly old stellar population with only a small contribution of young stars (6–11% in flux) for PKS 2349−014 and missed the region of ongoing star formation as it was not covered by their slit. It demonstrates what impact the limited spatial coverage of long-slit observations might have on the characterisation of such systems.

Another aspect of our study is that luminous QSOs can reside in disc-dominated host galaxies with quite typical SFRs compared to their inactive counterparts. Among those HE 2152−0936 is one of the most luminous QSOs in our sample ($M_B = -25.93$). It supports the notion that local luminous QSOs with $M_V < -23.5$ are not necessarily associated with passively evolving, massive bulge-dominate galaxies as proposed by different studies (e.g. McLure et al. 1999; Nolan et al. 2001; Dunlop et al. 2003).

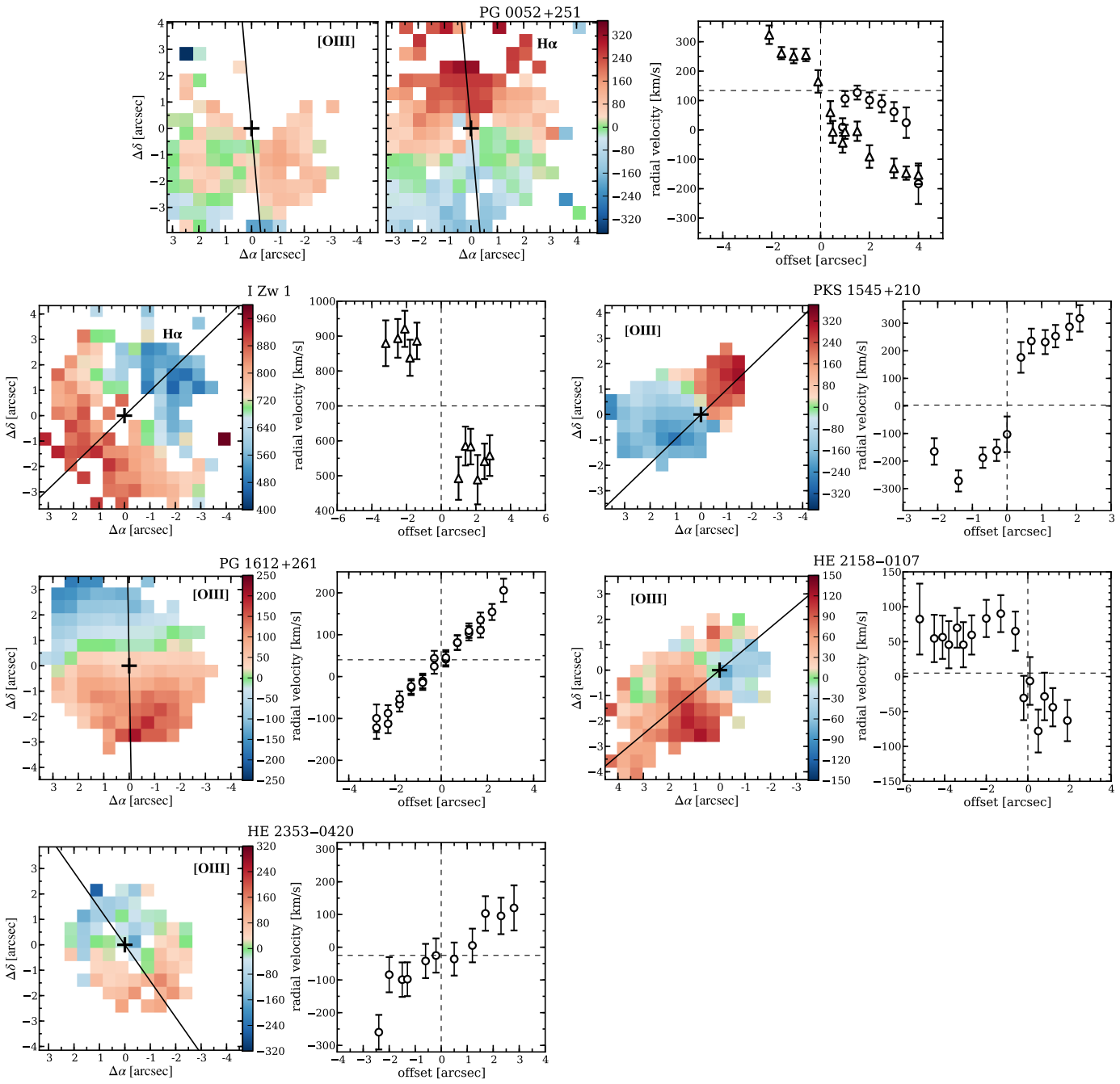

Fig. 3.10. 2D velocity maps for objects with apparently large-scale rotational motion gas motion. A "longslit" velocity curves along the major kinematic axis is extracted from the maps as described in the text. A solid black line indicates the orientation of the major kinematic axis. The radial velocity are estimated for each spaxel by modelling the corresponding emission line with a Gaussian profile. The vertical dashed line highlights the position of the QSO along the synthetic slit and the horizontal dashed line indicates the measured velocity zeropoint of the velocity curve.

3.6. Kinematics of the EELRs

3.6.1. Construction of 2D velocity fields

In the previous section we focused on integrated spectra of specific region to study the physical properties of the ISM. Now we discuss the 2D radial velocity distribution of the EELRs based based on the brightest emission lines. We modelled the [O III] λ4960, 5007 doublet and/or the Hα emission line with Gaussian profiles independently for each spaxel in the nucleus-subtracted datacubes. The line widths of the [O III] doublet were coupled and the [O III] line ratio was fixed to the theoretical value. We use the narrow [O III] emission in the QSO spectrum for the systemic redshift of the objects to compute rest-frame radial velocities. In section E.2. of the Appendix we investigate whether the nuclear emission lines are really a good proxy for the systemic redshift from the zero-point in the extended velocity field. Previous studies showed that the [O III] lines are often systematically blueshifted (e.g. Eracleous & Halpern 2004; Boroson 2005) potentially caused by circumnuclear outflows. Whether

Table 3.8. Kinematic properties of rotational velocity fields.

Name	PA[a] [°]	Δv_r[b] [$\frac{km}{s}$]	v_0[c] [$\frac{km}{s}$]	R[d] [″/kpc]	$v_r(R)$[e] [$\frac{km}{s}$]	log $M_{dyn}(R)$[f] [$M_\odot$]
I Zw 1	−28	88	704	3/3.5	166	10.7
PG 0052+251	2	94	134	3/8.1	284	11.3
PKS 1545+210	−46	165	3	2/8.2	299	> 11.2
PG 1612+261	6	57	39	3/7.0	119	10.4
HE 2158−0107	−49	17	5	2/6.9	49	> 9.6
HE 2353−0420	20	70	−25	2/7.3	138	10.6

Notes. [(a)] Position angle along the highest velocity gradient. [(b)] Radial velocity gradient along the major kinematic axis per arcseconds. [(c)] Radial velocity zero point that the QSO position with respect to the rest-frame defined by the nuclear [O III] line. [(d)] Characteristic radius from the centre used for a dynamical mass estimate [(e)] Radial velocity at the radius given given in (d). [(f)] Rough dynamical mass estimates following Eq. 3.6.

outflow signatures can be detected on kpc scales is one of the issues we want to address in the following.

We excluded PG 1700+518, HE 2152−0936 and PG 2130−099 from a detailed analysis since their EELRs appear to be nearly unresolved. Furthermore, the S/N of the emission lines in HE 0132−0441 and SDSS J0155−0857 was not sufficient to perform a spatially resolved analysis. We present the velocity fields for the 13 remaining EELRs in three categories: 1. Large scale rotational motions (Fig. 3.10), 2. Velocity fields of morphologically identified major mergers (Fig. 3.11), and 3. Peculiar velocity fields (Fig. 3.12). In addition to the 2D velocity maps we constructed synthetic "longslit" curves along a certain PA directly from the maps in a geometrically manner. The angular distance of spaxels, covered by a hypothetical slit of 1.″3 width, was computed with respect to the QSO position. Finally, the velocities within bins of 0.″3 in angular distances along the slit were averaged. In the following we discuss the results for each of the three categories separately.

EELRs dominated by rotational motion

Signatures of large scale rotational motion of the extended ionised gas are detected around I Zw 1, PG 0052+251, PKS 1545+21, PG 1612+261, HE 2158−0107 and HE 2353−0420. Their velocity fields are shown in Fig. 3.10. Since the turn-off point is not reached in most cases, we modelled the synthetic longslits curves with a straight line ($v_r = \Delta v_r \cdot r + v_0$) to search for the major kinematic axis with the steepest gradient among all $-90° < PA < 90°$ in steps of 3°. The velocity curves along that axis and perpendicular to it are also shown in Fig. 3.10. The estimated kinematic parameters along the primary kinematic axis are given in Table 3.8 including a dynamical mass estimate. The majority of these systems (4/6) are morphological disc-dominated galaxies for which the kinematic major axis is aligned with the photometric major axis within ±14° (rms). It is thus reasonable to assume that the ionised gas is following the gravitational motion of the stellar disc in these cases. We are thus able to roughly estimate dynamical masses (corrected for the inclination) within a certain radius R assuming purely circular motion

$$M_{dyn}(< R) = v_r(R)^2 \, R \, G^{-1} \sin(i)^{-1} \quad , \tag{3.6}$$

where G is the gravitational constant and i is the inclination of the rotating gas disc with respect to our line-of-sight.

PKS 1545+210 and possibly also HE 2158−0107 are bulge-dominated host galaxies for which the inclinations of the potential rotating gas discs are unknown and their dynamical masses can only be hard lower limits. The minimum dynamical mass of $M_{dyn}(< 8.2\,kpc) > 1.6 \times 10^{11} M_\odot$ for PKS 1545+210 is a typical value for a RLQ host (e.g. Best et al. 2005) and already close to the expected bulge mass (within a factor of 2) of the BH mass-bulge mass relation of Häring & Rix (2004). An alternative scenario of AGN-driven bipolar outflows to produce the same kinematics is rather unlikely because the radio-jets are oriented perpendicular to the kinematic major axis (see section 3.6.2). Interestingly, an apparent companion galaxy is located ∼3″ to the West of PKS 1545+210 in the direction of the kinematic major axis. We speculate whether the companion galaxy might be the origin of the gas in the elliptical galaxies and defines the plane of rotation. A spectroscopic confirmation of the companion redshift is still missing to confirm or reject that scenario.

The reliability of our velocity fields, intimately linked to the QSO-host deblending process, can be best tested in comparison to independent results of other studies. From our objects only the kinematics of I Zw 1 were previously studied. Schinnerer et al. (1998) obtained ^{12}CO(1-0) data for I Zw 1 on scales of 1″–14″, and H I data on scales of 20″–40″ was studied by Lim & Ho (1999). Our PMAS observation of I Zw 1 complement the previous kinematic information with that of the ionised gas within the central < 3″. A radial Hα velocity of $v_r = 166 \pm 22\,km\,s^{-1}$ at a distance of 2″ from the centre corresponds to a circular velocity of $v_{circ} \approx 260 \pm 34\,km\,s^{-1}$ after correcting for an inclination of 40°. This circular velocity and corresponding dynamical mass estimate for I Zw 1 are in good agreement with the result for the molecular gas (Schinnerer et al. 1998).

Among those 6 objects a direct comparison of the Hα and [O III] kinematics is only possible for PG 0052+251. While the Hα velocity exhibit a clear pattern of disc-like rotation, the velocity field of [O III] does not follow the same rotational pattern and is redshifted by up to $\sim 100\,km\,s^{-1}$. The kinematic separation of the two emission lines into distinct components support our previous interpretation from the emission-line ratio, that the Hα emission originates dominantly from H II regions in the extended disc of the host, whereas the [O III] emission is mainly powered by the AGN ionisation. We speculate that either the ionisation cone of the AGN points outside the main disc of the galaxy and ionises a separate gas region, or that the gas is outflowing almost perpendicular to our line-of-sight. Both scenarios would be able to explain the differences in the observed radial velocities.

Generally, our estimated dynamical masses underline that host galaxies of luminous QSOs are massive systems with masses of at least $> 10^{10} M_\odot$ in agreement with the SDSS results of Kauffmann et al. (2003). That this measurement is only possible for 6 out of 31 observed QSO hosts can be explained by several observational limitations: 1. Only half of the objects display extended emission lines at our given sensitivity limit, 2. Several host galaxies are currently interacting and not relaxed systems, 3. The velocity fields in [O III] depend on the geometry of the AGN ionisation cones and can be subject to non-gravitational motion.

Velocity fields of interacting QSO host galaxies

In Fig. 3.11 we present velocity fields of the three QSO hosts, Mrk 1014, SDSS J1131+2632 and PKS 2349−012, which we identified to be ongoing major merger based on their broad-band images. Due to the tidal forces and complex mass distribution

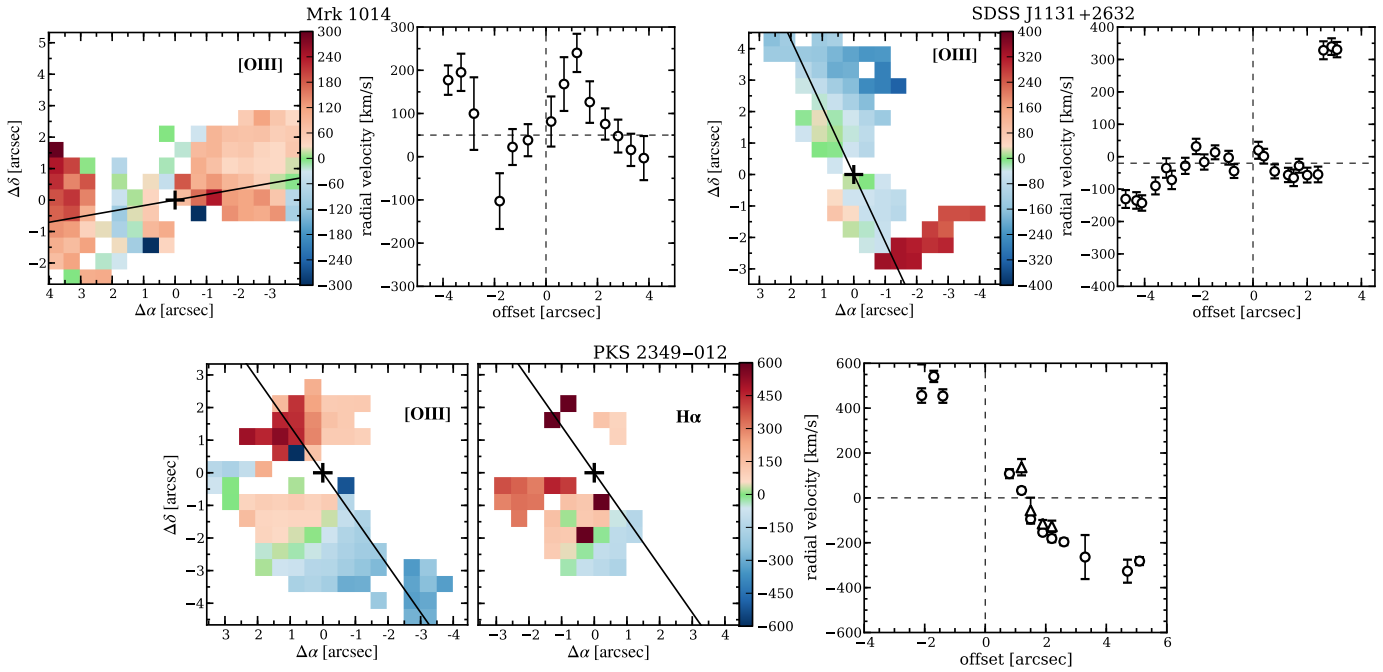

Fig. 3.11. Same as Fig. 3.10 showing the velocity fields of the 3 QSO hosts morphologically classified as ongoing major mergers.

we do not necessarily expect a clear rotational pattern for the gas velocity field even though it could still be driven by gravitation.

Our PMAS observation of Mrk 1014 covers only the central part of the QSO host (cf. Fig. 3.6), so that we are not able to trace the bulk motion of the ionised gas across the whole galaxy. The [O III] velocity curve along the major axis of the elongated EELR appears to be unusual. The symmetric curve displays two sharp peaks in the radial velocity at ±2″ distance from the nucleus and the radial direction of motion changes from receding to approaching and vice versa at larger distances. These features can possibly explained by jet-cloud interactions as discussed later in section 3.6.2.

Since the EELR of SDSS J1131+2632 is quite collimated, we have only limited knowledge about the kinematics of this object. The most striking feature is a giant shell or arc of ionised gas 4″ South-East of the nucleus, redshifted by 352 ± 33 km s^{-1} from the systemic velocity in the rest-frame. It is a unique feature among all the objects studied in this work. This kinematic peculiarity does not correspond to any photometric substructure in the broad-band image of the complex merging system like a prominent spiral or tidal arm. We are not able to say whether the gas belongs to a faint companion galaxy illuminated and ionised by the AGN radiation or to an outflowing shell of gas.

A strong velocity gradient is detected in the ionised gas of PKS 2349−014. The main axis of this gradient follows the large curved wisps that were found in the HST images by Bahcall et al. (1995). Thus, the gas kinematics are likely to be following the complex gravitational potential of the galaxy. However, the radio-jet axis of this RLQ is oriented North-South and may kinematically disturb the ionised gas at a certain region.

Peculiar velocity fields

The radial velocity fields of the remaining four QSO hosts, PG 0026+129, SDSS J0836+4426, PKS 1217+023 and SDSS J1655+2146, are either asymmetric or lack a significant velocity gradient across the galaxy. All four hosts tend to be morphologically bulge-dominated, for which the gas could be kinematically hot and slowly rotating consistent with the observed velocity fields. However, the SDSS images of J1655+2146 and J0836+4426 do not rule out a disc component in their morphology, which would need to be studied with higher spatial resolution imaging. At least we do not find any strong evidence for non-gravitational motion of the ionised gas.

3.6.2. Evidence for jet-cloud interactions on kpc scales

In order to study whether radio jets could directly influence the kinematics of the ionised gas, Fig. 3.13 compares the spatially resolved radio maps with the light distribution of the EELR in the [O III] line. Since the radio lobes of the RLQs extend far beyond the field of view we only indicate the direction of the large-scale bipolar radio jets. The radio emission is unresolved for 2 of the 6 RQQs with available subarcsecond radio images, for which we also find no kinematic indication of a possible jet-cloud interaction. In the case of PG 1700+518 the radio structure do not seem to coincide with the EELR light distribution. Whether the high receding radial velocity of ∼800 km s^{-1} for this EELR structure (cf. Table 3.6) is driven by jet-cloud interaction therefore remains unclear. Canalizo & Stockton (1997) obtained longslit spectra covering almost the same region, but did not report a high velocity offset of the ionised gas with respect to the stars. Since we can only use broad QSO lines as a reference for the systemic redshift, we cannot rule out a mismatch between the "true" systemic redshift of the galaxy and the redshift of the QSO for this particular object.

In the case of Mrk 1014 and PG 1612+261, we detect distinct blue-shifted component in the [O III] line at the location of the extended radio emission in the spectra of the corresponding regions (Fig. 3.13). The line width and radial velocity offset are 508 ± 84 km s^{-1} and −1012 ± 48 km s^{-1} for Mrk 1014 and 424 ± 24 km s^{-1} (FWHM) and −220 ± 20 km s^{-1} for PG 1612+261, respectively. These clearly non-gravitational motions coincident with radio emission are strong evidence for

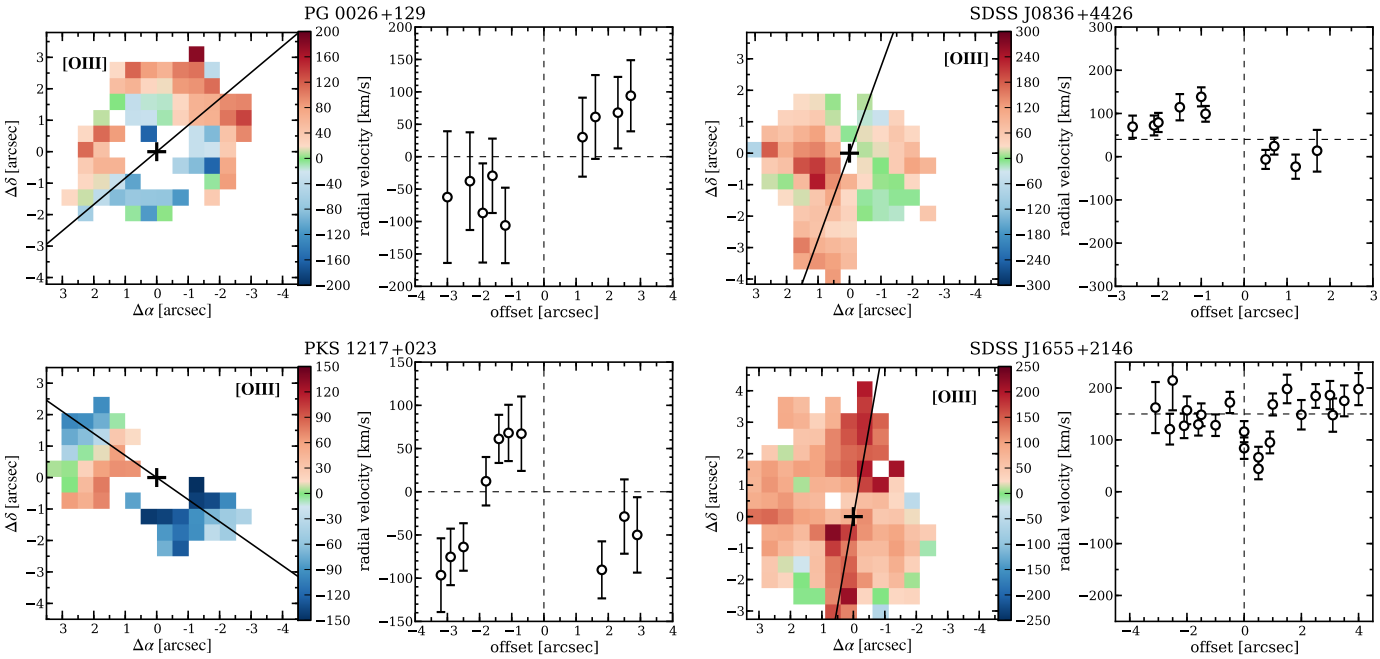

Fig. 3.12. Same as Fig. 3.10, presenting the velocity fields of the remaining objects with peculiar gas kinematics.

ongoing jet-cloud interactions. In addition to the blue-shifted component, a broad redshifted component is blended with the [O III] narrow component of Mrk 1014. We speculate that the approaching and receding gas emission might originate from the two sides of the bow shock superimposed along our line-of-sight for the significantly inclined jet. The asymmetry of the [O III] line is partially responsible for the peculiar 2D velocity field for which we assumed a simply Gaussian line profile. The extended ionised gas kinematics of Mrk 1014 was already studied in detail by means of long-slit (Leipski & Bennert 2006) and IFU spectroscopy (Fu & Stockton 2009). Our data for this object confirms their results. The brightest region of the EELR around the RQQ PG 2130+099 is matching with the southern hot spot of the triple radio source. However, we could not find any kinematic impact on the EELR from a possible jet-cloud interaction as in the other cases. Since the region is only 1″ away from the nucleus and the object was observed with the low-resolution V300 grism, we may have missed important substructures below our spatial and spectral resolution.

The [O III] kinematics of the major merger host of PKS 2349−012 are mainly quiescent. However, the extremely redshifted [O III] emission ($397 \pm 70\,\mathrm{km\,s^{-1}}$) 2″ North of the nucleus is matching with the radio axis and might be due to an interaction with the radio jet. In support of this non-gravitational origin, the [O III] emission lines are broad with $\sim 700\,\mathrm{km\,s^{-1}}$ (FWHM) in this particular region (Region B), which could be a signature for a turbulent medium and shocks at this position. Higher spectral resolution would be required to study the kinematics of the gas in more detail and to resolve individual emission line components.

The RLQs PKS 1217+023 and PKS 1545+210 reside both in bulge-dominated galaxies. The radio jet axis for PKS 1217+023 is aligned with the major axis of its associated EELR and velocity curve along the primary axis dos not agree with rotational motion. Whether the gas is directly interacting with the jets remains uncertain due to the low emission line width $<200\,\mathrm{km\,s^{-1}}$ (FWHM) of an undisturbed medium. A interaction of the jet with the EELR around PKS 1545+210 is most unlikely as the radio jet is aligned with the rotation axis of the gas disc. Such rotating gas discs are common in low-redshift radio galaxies (e.g. Baum et al. 1992) with Centaurus A being the most prominent example.

3.6.3. The incidence of non-gravitational motions among RQQs

Our IFU observations allow for the first time to study the kinematics of extended ionised gas in a large sample of RQQs. Off-axis spectroscopy campaigns were focused on the stellar populations and the ionisation state of the gas, but were not able to provide a census of the gas kinematics given the very low covering factor of the observations. Letawe et al. (2007) studied the kinematics of 12 RQQs with their on-axis spectra. They interpreted all ionised gas velocity curves not matching with an ordered rotation as signatures of gravitational interactions given the disturbed morphology of their hosts. Greene et al. (2011) recently presented long-slit kinematics of the ionised gas for their sample of type 2 QSOs, but otherwise there is quite a lack of spatially resolved gas kinematics for RQQs in the literature.

AGN feedback has become an important ingredient in cosmological simulations of galaxy formation to efficiently stall star formation on short timescales. Significant amounts of gas are thought to be expelled from the host galaxy by AGN outflows in order to prevent recurrent star formation episodes. Galactic superwinds have been detected in Ultra Luminous Infrared Galaxies (ULRIGs) reaching up to $1000\,\mathrm{km\,s^{-1}}$ (Rupke et al. 2005) and massive post-starburst galaxies (Tremonti et al. 2007). Although ULRIGs can often be starburst-AGN composites, the impact of the AGN on the outflows is unclear.

We find signatures of non-gravitational motion in the warm-ionised gas on kpc scales, that could be identified with AGN-driven outflows, only around 5 out of 31 QSOs (16%) of which one object is a RLQs. The two most striking cases of potential AGN outflows are PG 1700+518 and SDSS J1131+2632 with ionised gas clouds reaching more than $400\,\mathrm{km\,s^{-1}}$ in ra-

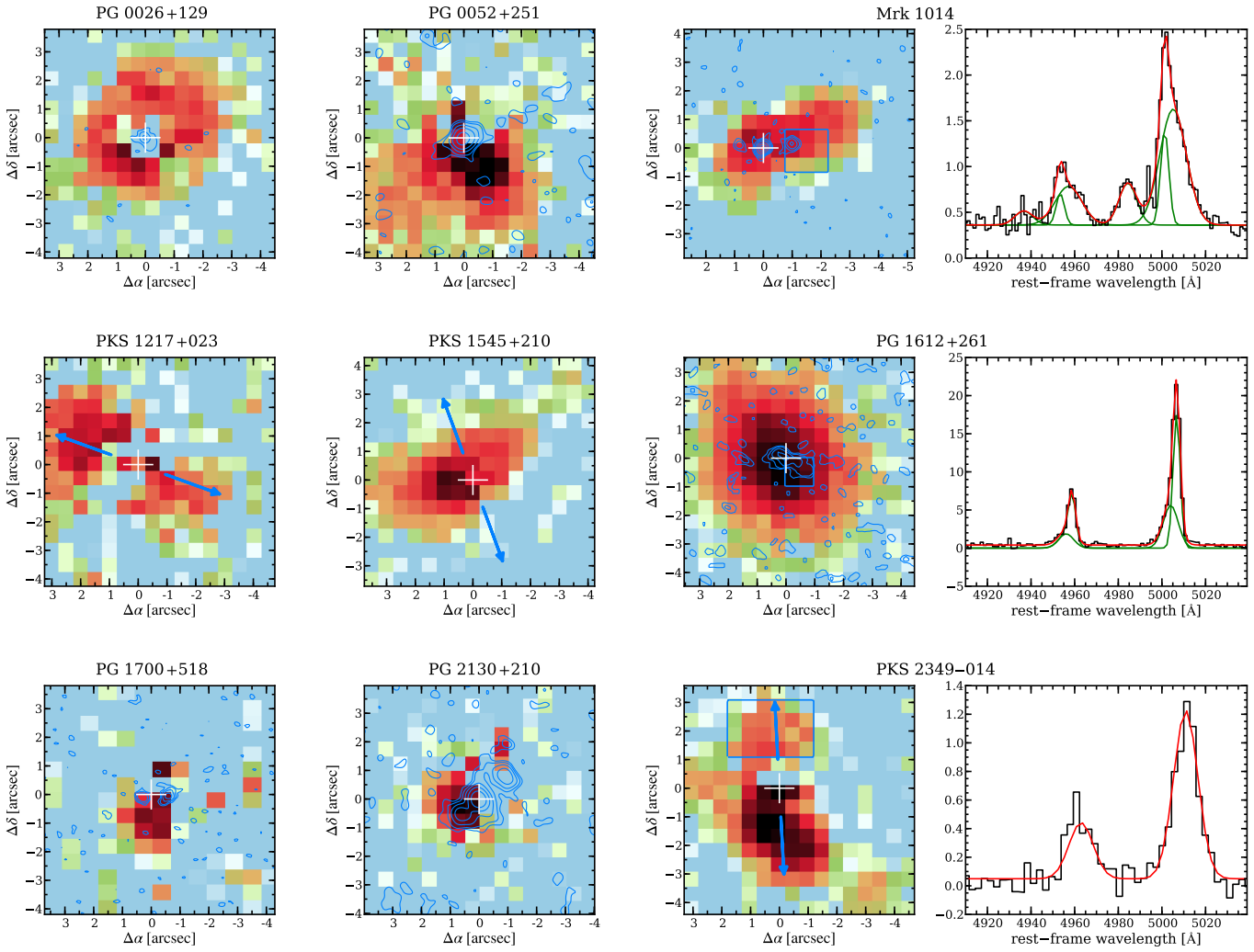

Fig. 3.13. The EELR light distribution of the [O III] line in comparison to the resolved radio emission. For the RQQs the high spatial resolution VLA radio images are overplotted as blue countours, while the primary radio axis of the radio lobes in RLQs is indicated by the blue arrows. In the case of Mrk 1014, PG 1612+261 and PKS 2349−012, the [O III] line profile in the co-added spectrum (of the spaxels in the blue box) is presented to highlight the gas kinematics at the location of the a potential jet cloud interaction. The red line is the model to the spectrum, and the green line represents the individual Gaussian components.

dial velocity. Other signatures of outflows are associated with rather localised jet-cloud interaction, which are often embedded in an otherwise still quiescent medium (e.g. PG 1612+261). Greene et al. (2011) also reported mainly quiescent kinematics of the extended gas around type 2 QSOs with radial velocities of <400 km s^{-1} typically below the escape velocity for those systems. These low detection rates agree with the results of Krug et al. (2010). They determined the radial velocity of the Na I D absorption line in the spectra of infrared-faint (SFR<10 M$_\odot$ yr^{-1}) Seyfert galaxies at $z < 0.05$ and reported an outflow detection rate of 6% for Seyfert 1 and 18% for Seyfert 2 galaxies compared to more than 50% for starburst galaxies.

3.7. The extended narrow-line region

In the previous sections we studied the general properties of extended line emission around QSOs, which are usually called Extended Emission Line Regions (EELRs) independently of the ionisation mechanism for the gas. Now we want to focus our attention only to the AGN ionised part of the EELRs which represent the extension of the AGN NLR to sizes of $\gtrsim$1 kpc and are usually called extended narrow-line regions (ENLR). We identified the AGN ionised regions among the EELRs with the BPT emission-line diagnostic diagram already in section 3.5.3. In the following we study the morphologies, sizes and luminosities of ENLRs in relation to the nuclear and radio properties of their QSOs.

3.7.1. ENLR morphologies

As a first step, we classified the ENLR morphologies by eye into three categories: 'one-sided' (3 objects), 'biconical' (6 objects) and 'round' (7 objects). Assuming elliptical isophotes, we measured the ellipticity of the ENLR from the light distribution in the narrow-band images 2σ above the background noise. Furthermore, we obtained the PA of the major ENLR axis by searching for the maximum flux within bipolar cones of 20° opening angle. All results are reported in Table 3.9. The mea-

Table 3.9. Luminosities and morphological parameters of the ENLR.

Name	$\log L_{\rm ENLR}$([O III]) [erg/s]	Morph.	e	PA [°]
PG 0026+129	41.80 ± 0.14	round	0.30	−57
PG 0052+251	41.75 ± 0.13	one-sided	–	34
SDSS J0155−0857	41.43 ± 0.19	round	0.39	5
Mrk 1014	42.22 ± 0.14	biconical	0.60	−65
SDSS J0846+4426	43.08 ± 0.09	round	0.09	83
SDSS J1131+2623	42.11 ± 0.14	biconical	0.64	18
PKS 1217+023	41.82 ± 0.16	biconical	0.44	62
SDSS J1230+6621	41.90 ± 0.15	round	0.32	5
PKS 1545+210	42.35 ± 0.13	biconical	0.45	−49
PG 1612+261	42.80 ± 0.12	round	0.20	39
SDSS J1655+2146	43.03 ± 0.09	round	0.19	43
PG 1700+518	41.81 ± 0.18	one-sided	–	−27
PG 2130+099	40.90 ± 0.32	one-sided	–	−28
HE 2158−0107	42.32 ± 0.13	biconical	0.46	−46
PKS 2349−014	42.11 ± 0.11	biconical	0.18	6
HE 2353−0420	42.47 ± 0.12	round	0.15	57

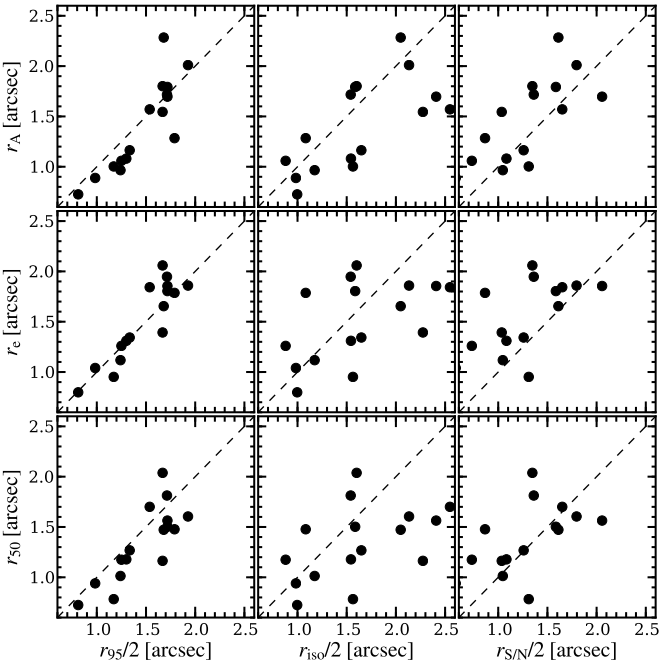

Fig. 3.14. Comparison of six different ENLR size definitions. Compared are the effective radius r_e, the half-light radius r_{50}, the semi-major axis A, the maximum radius radius r_{95}, the isophotal radius $r_{\rm iso}$, and the SN-based radius $r_{\rm SN}$. The latter three are divided by a factor of 2 to be roughly at the same scale compare to the first three ENLR size definitions. The dashed line indicates a one-to-one relation.

sured ellipticities of the ENLRs reproduce our visual impression of round and biconical ENLR morphologies where the transition of our visual classification occurs at $e \simeq 0.4$. An exception is PKS 2349−014 because its ENLR is quite lopsided and the southern high SFB region dominates the whole ENLR structure.

An intrinsically biconical ENLR structure is predicted by the Unified Model of AGN (Antonucci 1993; Urry & Padovani 1995). Elongated or biconical ENLRs were often observed (e.g. Unger et al. 1987; Mulchaey et al. 1996b; Veilleux et al. 2001; Schmitt et al. 2003b) in agreement with the picture of the Unified Model. However, the ENLR of type 1 AGN is expected to be round or "halo"-like more frequently as we should look almost directly along the AGN ionisation cone to the nucleus. The situation is a bit more complex because the gas density distribution may strongly influence ENLR morphologies (Mulchaey et al. 1996b), in particular when the ENLR exceeds beyond the size of its host galaxy.

We found a large fraction of 37.5% biconical ENLRs which even increases to 56% when the the one-sided ENLRs are assumed to be intrinsically biconical. Such a large fraction of biconical ENLRs for type 1 AGN is not in agreement with naïve predictions of the Unified Model. Similar results have been reported by Schmitt et al. (2003b) and Mulchaey et al. (1996b), who studied the ENLR by narrow-band imaging of large samples of Seyfert 1 and Seyfert 2 galaxies and found that the morphology of their ENLRs are statistically indistinguishable. Thus, either the Unified Model is oversimplistic in that respect or the ENLR morphology is significantly affected by secondary properties, like the gas density distribution with respect to the ionisation cones or the presence and direction of radio jets. From the 7 objects where the PA of the radio jet is known from radio imaging, only two ENLR are unaligned with the radio axis, while the axes are aligned within ±20° (rms) for the other objects.

3.7.2. ENLR sizes

All previous ENLR surveys used different definitions to estimate the ENLR sizes. Schmitt et al. (2003a) estimated the maximum projected size by eye from the [O III] light distribution of their *HST* narrow-band images. Circular apertures were used by Bennert et al. (2002) to infer the ENLR radius at which the [O III] surface brightness in an annulus dropped below the background surface brightness limit. Finally, ground-based narrow-band images of 47 Seyfert galaxies were analysed by Mulchaey et al. (1996a), who defined isophotal ENLR sizes at a surface brightness of 2×10^{-16} erg cm^{-2} arcsec^{-2}. Clearly, different ENLR size definitions are not directly comparable with each other, and some of them critically depend on the depth of the data. We now investigate the robustness of six different ENLR size definitions based on the [O III] light distribution, 2σ above the background noise, to check their impact on the results and utilise future comparisons. We measured the radius of circular apertures r_{50} and r_{95} centred on the QSO, containing 50% and 95% of the ENLR [O III] flux. An effective radius ($r_{\rm e}$) is defined as the luminosity-weighted projected distance of each pixel with respect to the QSO position. We adopted the definition of `Sextractor` (Bertin & Arnouts 1996) to estimate a semi-major axis (r_A) from the light distribution of the [O III] image,

$$r_A^2 = \frac{\langle x^2\rangle + \langle y^2\rangle}{2} + \sqrt{\left(\frac{\langle x^2\rangle - \langle y^2\rangle}{2}\right)^2 + \langle xy\rangle^2}\,, \tag{3.7}$$

where $\langle x^2\rangle$, $\langle y^2\rangle$, and $\langle xy\rangle$ are the QSO-centred second-order moments of the light distribution. Furthermore, we measure the maximum radius out to a limiting isophotal [O III] surface brightness of 2×10^{-16} erg cm^{-2} arcsec^{-2} ($r_{\rm iso}$) and out to a limiting S/N of 5 ($r_{\rm S/N}$). The measured ENLR sizes with all 6 size definitions are reported in Table 3.10 with errors based on Monte Carlo simulations of the QSO-host deblending process. We generated 200 realisations for each object datacube according to the observed signal and its variance, which we consistently analysed to infer 1σ errors for the sizes from their standard deviations. Due to the

Table 3.10. ENLR sizes based on several different size definitions.

Name	r_A ["]	r_{50} ["]	r_{95} ["]	r_e ["]	r_{iso} ["]	$r_{S/N}$ ["]
PG 0026+129	1.7 ± 0.4	1.8 ± 0.3	3.4 ± 0.7	1.9 ± 0.3	3.1 ± 0.8	2.7 ± 0.8
PG 0052+251	2.3 ± 1.3	1.5 ± 0.4	3.4 ± 0.6	1.7 ± 0.4	4.1 ± 0.8	3.2 ± 0.8
SDSS J0155−0857	0.9 ± 0.7	0.9 ± 0.3	2.0 ± 1.3	1.0 ± 0.4	2.0 ± 1.5	1.1 ± 0.8
Mrk 1014	> 2.0	> 1.6	> 3.9	> 1.9	> 4.3	> 3.6
SDSS J0846+4426	1.1 ± 0.4	1.2 ± 0.3	2.6 ± 1.1	1.3 ± 0.4	3.1 ± 1.4	2.2 ± 0.9
SDSS J1131+2623	1.5 ± 0.4	1.2 ± 0.4	3.3 ± 0.8	1.4 ± 0.4	4.5 ± 1.0	2.1 ± 0.7
PKS 1217+023	1.8 ± 0.4	2.0 ± 0.4	3.3 ± 0.6	2.1 ± 0.4	3.2 ± 0.7	2.7 ± 0.9
SDSS J1230+6621	0.7 ± 0.4	0.7 ± 0.3	1.6 ± 0.9	0.8 ± 0.4	2.0 ± 0.8	1.1 ± 0.7
PKS 1545+210	1.8 ± 0.9	1.5 ± 0.3	3.4 ± 0.7	1.8 ± 0.4	3.2 ± 0.7	3.2 ± 0.9
PG 1612+261	> 1.2	> 1.3	> 2.7	> 1.3	> 3.3	> 2.5
SDSS J1655+2146	1.0 ± 0.3	0.8 ± 0.3	2.3 ± 0.6	1.0 ± 0.3	3.1 ± 0.7	2.6 ± 0.7
PG 1700+518	1.3 ± 0.2	1.5 ± 0.4	3.6 ± 1.0	1.8 ± 0.4	2.2 ± 1.8	1.7 ± 0.8
PG 2130+099	1.1 ± 0.2	1.2 ± 0.5	2.5 ± 1.1	1.3 ± 0.5	1.8 ± 1.4	1.5 ± 1.1
HE 2158−0107	> 1.7	> 1.6	> 3.4	> 1.9	> 4.8	> 4.1
PKS 2349−014	1.6 ± 0.4	1.7 ± 0.3	3.1 ± 0.6	1.8 ± 0.3	5.1 ± 1.2	3.3 ± 0.6
HE 2353−0420	1.0 ± 0.3	1.0 ± 0.3	2.5 ± 0.6	1.1 ± 0.3	2.3 ± 0.6	2.1 ± 0.7

low spatial sampling of our reconstructed PMAS narrow-band images, we further added 0.″5 to the uncertainty of r_{95}, r_{iso}, and $r_{S/N}$ as well as 0.″25 to the uncertainty of r_A, r_{50}, and r_e. The seeing certainly increases the apparent size of the ENLR, but its strength strongly depends on the intrinsic emission line distribution and also on the size definition. We emphasise that due to the large apparent ENLR sizes of several arcseconds in our sample any correction for the seeing would be a small effect, so that we did not perform a seeing correction.

The measurements for all 6 size definitions are compared with each other in Fig. 3.14. We note some significant scatter between the ENLR sizes of different size definitions. Except that r_{95}, r_{iso}, $r_{S/N}$ are about 2 times larger than all the other according to their definitions, $r_{95}/2$, r_{50} and r_e and r_A display low deviations from each other with a scatter of about 15% (rms). The deviations with the r_{iso} and $r_{S/N}$ size definitions is significantly higher than the other with a scatter of up to 35% (rms) as they are suspected to be more strongly dependent on the depth of the images. Anyway, the deviations appear still small and should not strongly affect the results of large samples except the absolute scaling of the ENLR size.

Given the high frequency of elongated ENLR structures, we investigated by how much longslit spectroscopy observation can underestimate the ENLR size. We extracted synthetic longslit SFB distribution from the narrow-band images in the same way as the velocity curves along the major and minor axis of the ENLR. We find that the ENLR size is underestimated on average by a factor of 2 in the worst case where the slit is always oriented perpendicular to the major axis. For individual objects even a factor of 6 can be reached. Thus, the choice of the position angle of a longslit can have a strong impact on the estimated ENLR size, certainly much more than reported by Greene et al. (2011) based on their observations of type 2 QSOs with multiple slit orientations. One possible explanation for this discrepancy could be the confusion of extended and unresolved [O III] emission of the nucleus, which is symmetrically smeared out by the seeing. We subtracted this unresolved emission with our QSO-host deblending technique before we analysed the extended emission, but this was not done for the type 2 QSOs.

3.7.3. ENLR size-luminosity relation

After converting the angular ENLR sizes into projected physical sizes at the redshift of the objects, we compare in Fig. 3.15 the r_{95}, r_e, and r_{iso} ENLR sizes with the *total* [O III] luminosity (ENLR+QSO) (left panels) and with the bolometric luminosity L_{bol} of the QSO (right panels). The ENLR sizes are totally uncorrelated with the [O III] luminosity in our case with a low Spearman rank correlation coefficient and a high probability for no correlation ($\varrho = 0.27, P = 0.3$, for r_{95}). On the other hand, a much higher correlation coefficient is found for the QSO continuum luminosity L_{5100} ($\varrho = 0.65, P = 6 \times 10^{-3}$, for r_{95}). The correlation between the ENLR size and the AGN continuum luminosity has not been investigated yet, because all previous studies focused either on type 2 AGN for which the AGN continuum is obscured, or on low-luminosity Seyfert nuclei with a substantial contamination of the continuum by the underlying host galaxy. Bennert et al. (2002) compared their ENLR size also with the broad Hβ luminosity of the QSOs that is well correlated with the QSO continuum luminosity (e.g. Greene & Ho 2005; Schulze et al. 2009; Punsly & Zhang 2011). Their data imply a slightly higher correlation coefficient for the ENLR size as a function of Hβ luminosity which they however did not notice in their paper.

We find that the isophotal ENLR sizes have a larger error than the two others and the r_{iso} sizes appear smaller than the others for objects at high AGN continuum luminosities. These high luminosity QSOs are usually at the highest redshifts among our sample, hence the surface brightness of their ENLR was dimmed so that their sizes are underestimated if a constant surface brightness limit is used at all redshifts. r_{iso} is therefore not a good ENLR size definition and we will discuss in the following only the results for r_{95} and r_e.

The average size of the detected ENLR among our type 1 QSOs is 5 kpc ± 2 kpc for the effective radius (r_e) and 10 kpc ± 3 kpc for the maximum projected size (r_{95}) or the isophotal radius (r_{iso}) at a median [O III] luminosity of $\log L([\mathrm{O\,III}]) = 42.7 \pm 0.15$. Although a few objects are in agreement with the scaling relation of Bennert et al. (2002), the majority are a factor of 2 larger than the extrapolation of their relation for the given [O III] luminosity. The discrepancy is even much larger for the scaling relation of Schmitt et al. (2003b) as determined for their Seyfert 1 subsample. This is not surprising given the fact that the limiting surface brightness of the *HST* narrow-band images are

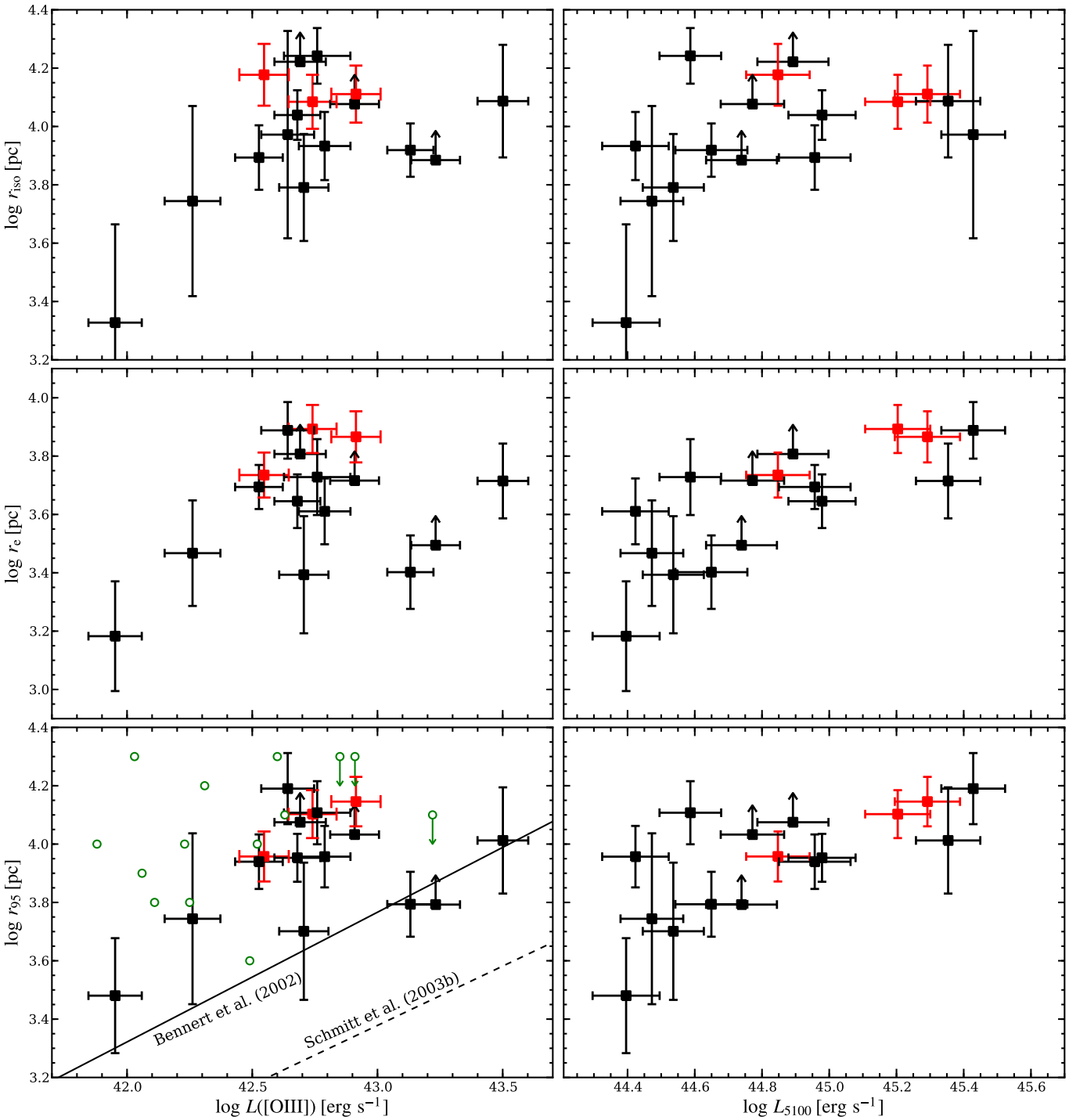

Fig. 3.15. ENLR sizes as a function of total [O III] luminosity (left panels) and the QSO continuum luminosity at 5100Å (right panels). The used size definitions are isophotal radius r_{iso} (upper panels), effective radius r_e (middle panels), and the radius containing 95% of the ENLR flux r_{95} (lower panels). The solid and dashed lines in the lower left panel correspond to the ENLR size-luminosity relations of Bennert et al. (2002) and Schmitt et al. (2003b), respectively. The black filled symbols represent RQQs whereas the red filled symbols highlight the few RLQs in our sample. The green opened circles are recent measurement for luminous type 2 QSOs as reported by Greene et al. (2011).

at least a factor of 10 higher and that Schmitt et al. (2003b) used a S/N-based size definition.

Due to the narrow luminosity range covered by our sample, we do not provide a revised scaling relation because no robust spectroscopically determined ENLR sizes exist in the literature for a significant number of lower luminosity Seyfert 1 galaxies at present. The type 2 QSO in the longslit sample of Greene et al. (2011) have [O III] luminosities close to our type 1 QSOs with

a limiting surface brightness of $\sim 1{\times}10^{-16}$ erg s^{-1} cm^{-2} arcsec^{-2} similar to our observations. As can be seen in Fig. 3.15, the reported ENLR sizes of their type 2 QSOs are of the order of 10 kpc, almost consistent with our type 1 QSOs albeit their sizes are higher at lower [O III] luminosities. This strongly suggests that the scaling relations for the ENLR of type 1 and type 2 AGN cannot be as different as implied by the results of Schmitt et al. (2003b). Their extrapolated relations to an [O III] luminosity $\log L([\mathrm{O\,III}]) = 42.5$ would imply ENLR sizes for type 2 AGN at least a factor of 2 lower than the ones of type 1 AGN. Interestingly, Greene et al. (2011) determined an ENLR size-luminosity relation with a rather shallow power-law slope of 0.22 using extrapolated SFB profiles of the NLR for Seyfert 2 galaxies determined by Fraquelli et al. (2003) based on longslit spectroscopy. However, these cannot be considered as robust estimates, because the ionisation mechanisms of the ISM likely changes from AGN ionisation to ionisation by massive stars at a certain distance from the nucleus. A simple extrapolation from the high SFB regions of the NLR might therefore be too simplified and their NLR sizes can be easily overestimated in this way.

Furthermore, we find that the ENLR size is much better correlated with the AGN continuum luminosity. Albeit the [O III] luminosity is often found to scale well with the QSO luminosity (e.g. Zakamska et al. 2003; Heckman et al. 2004), our result suggest that the [O III] luminosity is a less reliable proxy for the amount of ionising photons compared to the continuum luminosity. Netzer et al. (2004) emphasised that the ENLR size-luminosity relation should not be a universal law. The ENLR sizes implied by the current relations would exceed the size of the host galaxies for luminous QSOs at high redshift by more than an order of magnitude. Our QSOs are just at the limit where the ISM of the entire host galaxies is ionised, so that we do not see a break in the size-luminosity relation. On the other hand, we were not able to resolve or detect an ENLR for a lot of QSOs in our sample. A few of them have rather compact host galaxies, such as PG 1427+480 (cf. Fig 3.6), which may provide an explanation for a non-detection if the size of the host galaxy imposes a natural limit for the ENLR due to the sharp decline in gas density. But since we found in Hu08 a clear correspondence between resolving the ENLR and the spectral properties of the QSO spectrum, we think that another fundamental property of the nuclei, yet to be identified, needs to play an additional role.

3.7.4. ENLR luminosities

In Fig. 3.16 we compare the [O III] luminosities of the ENLRs ($L_{\mathrm{ENLR}}([\mathrm{O\,III}])$) as reported in Table 3.9 with the unresolved [O III] luminosities of the QSOs ($L_{\mathrm{QSO}}([\mathrm{O\,III}])$). For the ENLR non-detections among our sample, we derived 3σ upper limits for $L_{\mathrm{ENLR}}([\mathrm{O\,III}])$ via Monte Carlo simulation. We artificially added ENLRs to the datacubes using all the different empirical morphologies inferred form our detected ENLRs until the input ENLR luminosity reached the detection limit. We consider an ENLR to be detected when the flux in 9 adjacent spaxel were above the 2σ background noise level. The 3σ detection limit for the ENLR luminosity is reached when more than 95% ENLR are detected among 200 different realisations for a given ENLR input luminosity. Here we implicitly assume that the ENLR luminosity is the limiting factor to detect an ENLR and not its size. Our measurements indicate a very significant trend that is fully consistent with the upper limits for the non-detections.

With the Astronomy Survival Analysis package (ASURV, Lavalley et al. 1992) we determined a generalised Spearman rank correlation coefficients of $\varrho = 0.76$ taking the censored data into account. The probability for a non-correlation is $P < 10^{-5}$ for the combined data set covering more than 2 orders of magnitude in [O III] luminosity. A linear regression analysis with the Buckley-James method as part of the ASURV yield a relation of

$$\log(L_{\mathrm{ENLR}}([\mathrm{O\,III}])) = (1.7{\pm}0.3)\log(L_{\mathrm{QSO}}([\mathrm{O\,III}]))-(30.4{\pm}2.2) \quad (3.8)$$

which suggests that the extended nebulae are the extensions of the unresolved NLRs powered by the ionising photons of the AGN.

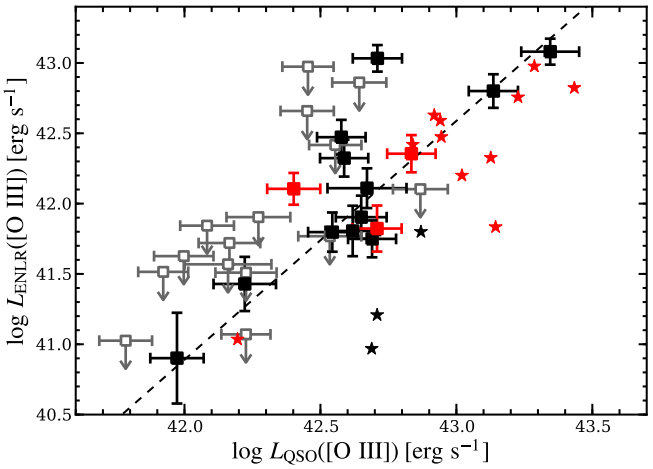

Fig. 3.16. [O III] luminosity of the ENLR as a function of the unresolved QSO [O III] luminosity. Squared symbols indicate our own PMAS measurements and star symbols refer to the literature data of Stockton & MacKenty (1987). Radio-quiet and radio-loud objects are marked as black and red symbols, respectively. The open grey symbol represent upper limits and the dashed line is a linear fit to our PMAS data (squared symbols) only.

A similar trend was already reported from the [O III] narrow-band survey of low-redshift QSOs by Stockton & MacKenty (1987) and the narrow-band survey of local Seyfert galaxies carried out by Mulchaey et al. (1996a). The luminous QSOs in the Stockton & MacKenty (1987) sample, mostly RLQs, appear to follow the scaling relation implied by our data at high [O III] luminosities, but we find that they are *systematically* lower than our relation by up to 0.5 dex. Our ENLR luminosities for PG 0052+251, PG 0157+001 and PKS 1545+210, common to both samples, are 0.5 dex, 0.4 dex, and 0.15 dex higher than reported by Stockton & MacKenty (1987). This discrepancy can be resolved, however, by realising that Stockton & MacKenty (1987) excluded a central aperture with a radius of $\sim 3''$ for their measurements to avoid contamination by QSO light. Thus, they missed the central high luminosity part of the extended nebulae and could only provide upper limits for PG 1700+518 and PKS 1217+023, which we could resolve with our observations.

If the [O III] luminosity is an indicator for the amount of ionising photons emitted by the AGN, we would expect a significant correlation of the ENLR luminosity with the QSO continuum luminosity L_{5100}. We already reported in Hu08 that this is not the case and present the corresponding diagram now for our extended sample in Fig. 3.17. The generalised Spearman rank correlation coefficient computed with ASURV is $\varrho = 0.108$ with a probability of $P = 0.55$ to be completely uncorrelated. This is rather surprising due to strong correlation between the ENLR sizes and the continuum luminosities as shown in Fig. 3.15. Although the amount of ionising photons determines the maxi-

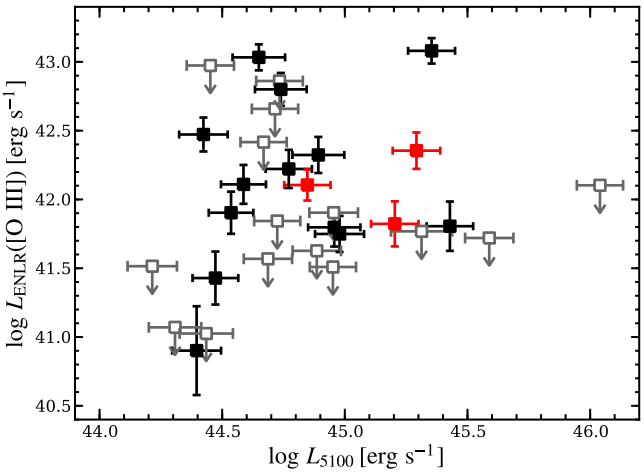

Fig. 3.17. [O III] luminosity of the ENLR as a function of QSO continuum luminosity at 5100Å. Symbols are as defined in Fig. 3.16

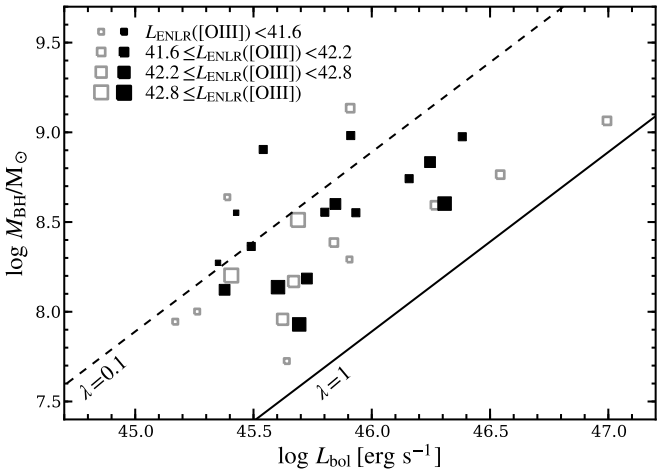

Fig. 3.18. Distribution of QSOs with detected and non-detected ENLRs in the M_{BH}-L_{bol} plane. The ENLR luminosity or its upper limit is encoded in the symbol size. QSO with detected ENLR are indicated by filled symbols and non-detections by grey open symbols, respectively. Solid and dashed lines correspond to constant Eddington ratios of $\lambda = 1$ and $\lambda = 0.1$, respectively.

mum extend of an ENLR this is apparently not true for the ENLR luminosity, which might either be related to the amount and distribution of the gas within the host galaxy or to an anisotropic radiation field outside the nucleus.

We also investigated whether any significant dependence of the ENLR luminosity on BH mass M_{BH} and Eddington ratio λ is present. The distribution of our objects with ENLR detections and non-detection in the M_{BH}-L_{bol} is shown in Fig. 3.18. We defined four bins in ENLR luminosities which are encoded in the size of the symbols. If we consider only the QSOs with an ENLR detection, the most luminous ENLRs are found in QSOs with the highest Eddington ratios. However, many object with non-detected ENLRs and low upper limits appear to populate a similar region. A two dimensional Kolmogorov-Smirnov (K-S) test (Peacock 1983; Fasano & Franceschini 1987) confirmed a high probability of $P = 0.74$ that both samples (ENLR detection and non-detections) are drawn from the same parent population. Neither M_{BH} nor λ play a significant role for the luminosity of the ENLR. Although the QSO luminosity is certainly important by limiting the available amount of ionising photons, there must be an additional physical parameter controlling the ENLR and nuclear [O III] luminosity, possibly the covering factor of the ionising radiation (Baskin & Laor 2005).

3.7.5. Dependence on radio properties

Radio observations have shown that the nuclear [O III] luminosity is correlated with the continuum radio luminosity in radio galaxies and RLQs (e.g. Baum & Heckman 1989; Rawlings & Saunders 1991; Xu et al. 1999) as well as in RQQs (e.g. Miller et al. 1993; Xu et al. 1999; Ho & Ulvestad 2001). The radio (6 cm) to optical (4400 Å) flux ratio, the R parameter, has often been used to distinguish between RQQs ($R < 1$) and RLQs ($R > 10$), so that their [O III] scaling relations often appear significantly offset from each other in terms of radio luminosity. Since the radio emission in RLQs is often dominated by their extended lobes, the two classes may follow a common relation only if the radio core power is considered (Xu et al. 1999). Here we compare L_{ENLR}([O III]) with the radio luminosity at 1.4 GHz in Fig. 3.19. It is difficult to argue about a possible correlation between these two quantities due to the numerous upper limits in both, radio and ENLR luminosity. The generalised Spearman rank correlation coefficient is $\varrho = 0.56$ with $P = 0.003$ for the non-correlation case. However, it is obvious that the ENLR luminosity depends much stronger on the radio luminosity than on the QSO continuum luminosity. We want emphasise three facts:

1. ENLRs are detected around *all* QSOs with log $L(1.4\,\mathrm{GHz}) > 23.6$ (8 objects).
2. 10/13 RQQs with a detected ENLR (77%) have a radio detection, while only 5/14 RQQs with a non-detected ENLR (40%) are detected in the radio.
3. In terms of radio-loudness, we detected an ENLR only around 26% of the RQQs with $R < 1$, but around 87.5% of the QSOs with $1 < R < 10$.

The ENLR luminosity of the RLQs (not included in Fig. 3.19) is of the same order compared to their radio-quiet counterparts, although the integrated radio luminosity is more than two orders of magnitude higher for the RLQs. Whether this is an intrinsic property or caused by the limited field of view of our IFU observation is something we are not able to say at present.

Sulentic et al. (2000) found that the broad Hβ line width of RLQs is almost always $\gtrsim 4000\,\mathrm{km\,s^{-1}}$, and defined two different populations of AGN. Population A with $\mathrm{FWHM_{H\beta}} \gtrsim 4000\,\mathrm{km\,s^{-1}}$ is entirely dominated by RQQs and Population B with $\mathrm{FWHM_{H\beta}} \lesssim 4000\,\mathrm{km\,s^{-1}}$ contains all RLQs and a number of RQQs with otherwise similar characteristics. These two population represent opposite regimes along the famous Eigenvector 1 (Boroson & Green 1992), which ultimately links the width of Hβ, the strength of the Fe II complexes and the relative strength of [O III] with respect to Hβ. The physical driver for this sequence in parameter space is thought to be M_{BH} and λ of the AGN (Boroson 2002; Marziani et al. 2003). In Hu08 we emphasised that a luminous ENLR is preferentially found around QSOs with $\mathrm{FWHM_{H\beta}} > 4000\,\mathrm{km\,s^{-1}}$ and weak Fe II emission that would correspond exclusively to Population A. Our extended sample now contains a few objects, such as the radio-intermediate QSOs PG 1612+261 and SDSS 1655+2146, which are surrounded by a luminous ENLR but have a $\mathrm{FWHM_{H\beta}}$ <

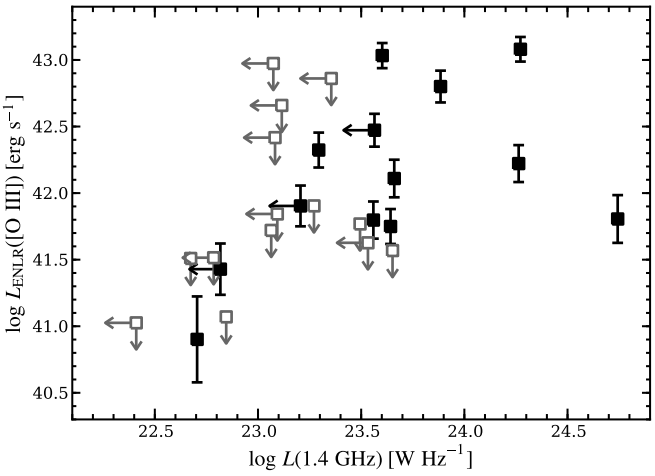

Fig. 3.19. [O III] luminosity of the ENLR against radio luminosity at 1.4 GHz. Black solid symbols refer to objects with detected and grey open symbols to objects with undetected ENLR (upper limits).

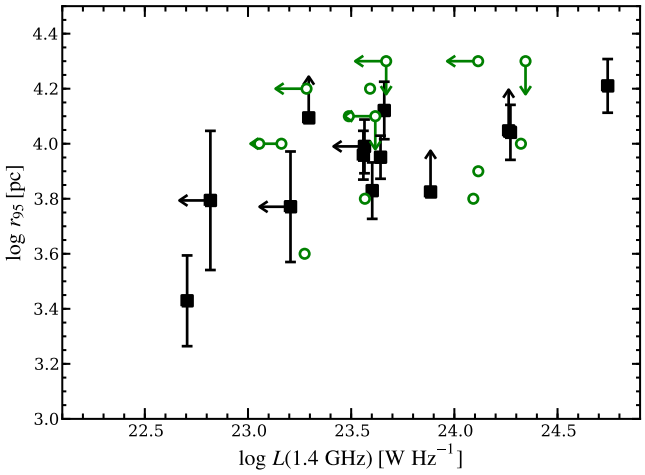

Fig. 3.20. ENLR size as a function of radio luminosity at 1.4 GHz. Measurements for our RQQs with detected ENLR are indicated by the black filled symbols and open green symbols denote measurements for type 2 QSOs as reported by Greene et al. (2011).

3000 km s^{-1} and therefore do not correspond to Population A as one would have naïvely expected. This is in agreement with the results of Zamfir et al. (2008) who found that radio-intermediate QSOs also cover the full range in broad Hβ widths like RQQs and are not restricted to region of Population A like the RLQs.

A close alignment between the EELR and radio axis particularly around high-redshift RLQs and radio galaxies has been well established (McCarthy et al. 1987, 1995), which is also often recognised for the lower luminosity Seyferts (Wilson & Tsvetanov 1994; Capetti et al. 1996; Falcke et al. 1998; Nagar et al. 1999; Schmitt et al. 2003b) on much smaller scales. Furthermore, Leipski et al. (2006) reported a significant trend between the size of the radio and extended [O III] emission. We already mentioned a potential alignment of the major ENLR axis with the PA of radio jets for the few objects with high-resolution radio imaging. Since the sizes of the radio emission are determined only for very few of our object, we investigated whether the size of the ENLR depends on the radio luminosity (Fig. 3.20) including the recent measurements for type 2 QSOs by Greene et al. (2011). No significant correlation is present between the two quantities. Since the radio luminosity might be correlated with the ENLR luminosity but not with its size, we tentatively speculate that radio jets are necessary to increase the covering factor of the gas for the ionising photons of the nucleus.

3.8. Conclusions

In this Chapter we presented a detailed analysis of EELRs around a large sample of 31 low-redshift QSOs observed with the PMAS IFU unit mounted to the 3.5 m telescope at the Calar Alto observatory. It is currently the largest sample of low-redshift QSOs observed with integral field spectroscopy in the optical wavelength regime. In Husemann et al. (2008) we already studied the dependence of the presence of EELRs with the spectral properties of the QSO nuclei using a subsample of objects observed by that time. With the full sample now in hand, we investigated the ionisation state and the kinematics of the EELRs as well as the size and luminosity of the ENLR. In order to separate the unresolved QSO emission from the host galaxy emission we introduced our new software tool `QDeblend`^{3D}. The main results of our analysis can be summarised as follows:

- We detect EELRs around 19 of 31 QSOs (61%), of which 13 are powered entirely by the QSO radiation (the ENLR), 3 are H II-like region produced by ongoing star formation, and the remaining 3 EELRs show signatures of both types in different regions.

- Ongoing star formation is found only in disc-dominated host galaxies and in one ongoing major merger. This supports the notion that luminous QSOs are not necessarily associated with massive elliptical galaxies composed of old stellar populations. The inferred SFRs of the order of 1 M$_\odot$ do not point to ongoing starburst activity in these systems, but are in agreement with SFRs typically inferred for inactive galaxies at comparable stellar masses.

- Signatures of presumably rotational gas kinematics are identified in 6 host galaxies of which 4 are disc-dominated. We roughly estimated dynamical masses for these system in the range of $10 < \log(M_{\rm dyn}/{\rm M}_\odot) < 11.2$. Although the estimates may be lower limits in some cases, they agree with the expected stellar masses of luminous QSOs host galaxies.

- We identify non-gravitational kinematics with emission-line width or radial velocity greater than 400 km s^{-1} only in 5 cases for specific regions within the EELRs. The detection rate and radial velocities are much lower than reported for starburst or post-starburst galaxies. Given the coincidences with extended radio sources, we argue that jet-cloud interactions are the most likely origin for the disturbances in the kinematics in the majority of cases.

- Different definition of ENLR sizes agree with each other at a 30% level, but the depth of the data play a crucial role. Previous ENLRs sizes obtained by Bennert et al. (2002) with *HST* narrow-band images are underestimated by at least a factor of 2 due to their order of magnitude lower limiting surface brightnesses. Nine of sixteen ENLRs in our sample are elongated which means that longslit observations strongly depend on the slit orientation and may underestimate the size by up to a factor of 6 for individual

object, or by a factor of 2 in the mean.

- The typical size of the ENLR is $r_{95} = 10 \pm 3$ kpc for the narrow range in luminosity covered by our QSO sample. Recent ENLR size measurements for type 2 QSOs at comparable luminosity by Greene et al. (2011) are of about the same the ENLR sizes of our type 1 QSOs. This implies that the ENLR size-luminosity relation for type 1 and type 2 AGN should not be as different as the results of Schmitt et al. (2003b) suggested. The reported discrepancy between their extrapolated ENLR sizes of type 2 AGN and that of the luminous QSOs is therefore obsolete.

- We find that the QSO continuum luminosity correlates much better with ENLR size than the total [O III] luminosity, while the [O III] luminosity of the ENLR is totally uncorrelated with the QSO continuum luminosity. Thus, we argue that the [O III] luminosity is not a good proxy for the intrinsic luminosity of the QSO and that the amount of ionising photons does not determine the luminosity of an ENLR. Due to the possible connections with the radio luminosity, we tentatively speculate that low-power radio jets in radio-quiet QSOs may be potentially able increasing the covering factor for the ionising photons of the AGN, which would increases the luminosity of the ENLRs.

One of the main results of our study is the low detection rate of gas outflows around radio-quiet QSOs (RQQs). Together with related work on type 2 QSOs and infrared faint Seyfert galaxies, this is strong evidence that severe AGN-driven outflows are not ubiquitous for radio-quiet AGN. That AGN feedback can strongly affect the properties of the host is most obvious in radio-loud AGN which disturb or expell the gas gas from the host or even drive large cavities in the medium of cluster to prevent cooling flows. The lack of ubiquitous signatures for kinetic AGN feedback in RQQs may have implications for the theoretical scenarios of AGN-related quenching of star formation. Given the presumed time delay between the peak of starburst and AGN activity for a merging galaxy of around a few 100 Myr (Li et al. 2008; Wild et al. 2010), our RQQs could be in a late stage of their evolution after most of the gas has either been heated or was already expelled from the host galaxies. On the other hand, the sizes and luminosities of the ENLRs may provide evidence for the general importance of radio jets to increase the covering factor of the ambient gas for the ionising photons of the nucleus in a pre-stage of feedback. Hopkins et al. (2010) argued that a weak outflow in a hot diffuse medium can possibly increase the AGN feedback in a two-stage process. First, the cold molecular gas clouds expand or are destroyed by the induced pressure gradients and instabilities. Second, the molecular clouds are driven out much more efficiently by the QSO radiation due to their increased cross-sections. It remains speculative if such a process is currently ongoing in our objects, and we simply miss a severe outflowing component in the cold gas phase . To pinpoint AGN feedback in RQQs still remains an open task, and the process may well be not as important as sometimes assumed. For example, AGN feedback might not be required to establish the tight BH mass - bulge correlation (Jahnke & Macciò 2011).

We also performed a systematic analysis of the ENLR sizes for RQQs, which can typically be of the order of 10 kpc and usually does not exceed the size of the host. This now agrees with the size of ENLR around obscured QSOs and solves the problem of the different size-luminosity relations inferred from *HST* data for the two AGN classes. Intriguingly, we discovered that the ENLR is better correlated with the AGN continuum than with the [O III] luminosity. Thus, we caution to use type 2 AGN to study the size-luminosity relation since the [O III] luminosity is only a *secondary* and less accurate proxy for the intrinsic luminosity of the nucleus (e.g. Punsly & Zhang 2011). Furthermore, type 2 QSOs are often found to be radio-intermediate objects and have a much higher incidence of flat-spectrum source (Lal & Ho 2010), which might cause a selection bias of type 2 QSOs due to the enhancement of [O III] luminosity due to an radio-jet at a given intrinsic bolometric luminosity of the AGN. We therefore emphasise the continued need to study unobscured QSOs even though the bright nucleus represents a technical challenge to accurately infer the properties of their hosts.

Acknowledgements. We thank Vardha Nicola Bennert to kindly provide us their analysed narrow-band *HST* as well as Christian Leipski who sent us their reduced radio maps for a few RQQs, which are not available in the VLA archive. BH and LW acknowledge financial support by the DFG Priority Program 1177 "Witnesses of Cosmic History: Formation and evolution of black holes, galaxies and their environment", grant Wi 1369/22-1 and Wi 1369/22-1. KJ is funded through the DFG Emmy Noether-Program, grant JA 1114/3-1.

Funding for the SDSS and SDSS-II was provided by the Alfred P. Sloan Foundation, the Participating Institutions, the National Science Foundation, the U.S. Department of Energy, the National Aeronautics and Space Administration, the Japanese Monbukagakusho, the Max Planck Society, and the Higher Education Funding Council for England. The SDSS was managed by the Astrophysical Research Consortium for the Participating Institutions.

This research has made use of the NASA/IPAC Extragalactic Database (NED) which is operated by the Jet Propulsion Laboratory, California Institute of Technology, under contract with the National Aeronautics and Space Administration.

For the preparation of this paper we have made used of the cosmology calculator "CosmoCalc" (Wright 2006)

References

Adelman-McCarthy, J. K., Agüeros, M. A., Allam, S. S., et al. 2008, ApJS, 175, 297
Allen, M. G., Dopita, M. A., & Tsvetanov, Z. I. 1998, ApJ, 493, 571
Antonucci, R. 1993, ARA&A, 31, 473
Bahcall, J. N., Kirhakos, S., Saxe, D. H., & Schneider, D. P. 1997, ApJ, 479, 642
Bahcall, J. N., Kirhakos, S., & Schneider, D. P. 1995, ApJ, 447, L1+
Bahcall, J. N., Kirhakos, S., & Schneider, D. P. 1996, ApJ, 457, 557
Baldwin, J. A., Phillips, M. M., & Terlevich, R. 1981, PASP, 93, 5
Baskin, A. & Laor, A. 2005, MNRAS, 358, 1043
Baum, S. A. & Heckman, T. 1989, ApJ, 336, 702
Baum, S. A., Heckman, T. M., Bridle, A., van Breugel, W. J. M., & Miley, G. K. 1988, ApJS, 68, 643
Baum, S. A., Heckman, T. M., & van Breugel, W. 1992, ApJ, 389, 208
Becker, R. H., White, R. L., & Helfand, D. J. 1995, ApJ, 450, 559
Bell, E. F., McIntosh, D. H., Barden, M., et al. 2004, ApJ, 600, L11
Bennert, N. 2005, PhD thesis, (University of Bochum, Germany)
Bennert, N., Falcke, H., Schulz, H., Wilson, A. S., & Wills, B. J. 2002, ApJ, 574, L105
Bennert, N., Jungwiert, B., Komossa, S., Haas, M., & Chini, R. 2006a, A&A, 459, 55
Bennert, N., Jungwiert, B., Komossa, S., Haas, M., & Chini, R. 2006b, A&A, 456, 953
Bentz, M. C., Peterson, B. M., Netzer, H., Pogge, R. W., & Vestergaard, M. 2009, ApJ, 697, 160
Bentz, M. C., Peterson, B. M., Pogge, R. W., Vestergaard, M., & Onken, C. A. 2006, ApJ, 644, 133
Bertin, E. & Arnouts, S. 1996, A&AS, 117, 393
Best, P. N., Kauffmann, G., Heckman, T. M., et al. 2005, MNRAS, 362, 25
Boroson, T. 2005, AJ, 130, 381
Boroson, T. A. 2002, ApJ, 565, 78
Boroson, T. A. & Green, R. F. 1992, ApJS, 80, 109
Boroson, T. A. & Oke, J. B. 1984, ApJ, 281, 535
Boroson, T. A., Oke, J. B., & Green, R. F. 1982, ApJ, 263, 32
Boroson, T. A., Persson, S. E., & Oke, J. B. 1985, ApJ, 293, 120
Brinchmann, J., Charlot, S., White, S. D. M., et al. 2004, MNRAS, 351, 1151
Bruzual, G. & Charlot, S. 2003, MNRAS, 344, 1000
Canalizo, G. & Stockton, A. 1997, ApJ, 480, L5+

Capetti, A., Axon, D. J., Macchetto, F., Sparks, W. B., & Boksenberg, A. 1996, ApJ, 469, 554
Christensen, L., Jahnke, K., Wisotzki, L., & Sánchez, S. F. 2006, A&A, 459, 717
Cid Fernandes, R., Stasińska, G., Schlickmann, M. S., et al. 2010, MNRAS, 403, 1036
Collin, S., Kawaguchi, T., Peterson, B. M., & Vestergaard, M. 2006, A&A, 456, 75
Condon, J. J., Cotton, W. D., Greisen, E. W., et al. 1998, AJ, 115, 1693
Croton, D. J., Springel, V., White, S. D. M., et al. 2006, MNRAS, 365, 11
Dunlop, J. S., McLure, R. J., Kukula, M. J., et al. 2003, MNRAS, 340, 1095
Eracleous, M. & Halpern, J. P. 2004, ApJS, 150, 181
Falcke, H., Wilson, A. S., & Simpson, C. 1998, ApJ, 502, 199
Fasano, G. & Franceschini, A. 1987, MNRAS, 225, 155
Fraquelli, H. A., Storchi-Bergmann, T., & Levenson, N. A. 2003, MNRAS, 341, 449
Fu, H. & Stockton, A. 2007, ApJ, 664, L75
Fu, H. & Stockton, A. 2008, ApJ, 677, 79
Fu, H. & Stockton, A. 2009, ApJ, 690, 953
Gebhardt, K., Bender, R., Bower, G., et al. 2000, ApJ, 539, L13
Greene, J. E. & Ho, L. C. 2005, ApJ, 630, 122
Greene, J. E., Zakamska, N. L., Ho, L. C., & Barth, A. J. 2011, ArXiv e-prints
Gültekin, K., Richstone, D. O., Gebhardt, K., et al. 2009, ApJ, 698, 198
Guyon, O., Sanders, D. B., & Stockton, A. 2006, ApJS, 166, 89
Hamilton, D. & Keel, W. C. 1987, ApJ, 321, 211
Häring, N. & Rix, H.-W. 2004, ApJ, 604, L89
Heckman, T. M. 1980, A&A, 87, 152
Heckman, T. M., Kauffmann, G., Brinchmann, J., et al. 2004, ApJ, 613, 109
Henry, R. B. C. & Worthey, G. 1999, PASP, 111, 919
Ho, L. C., Filippenko, A. V., & Sargent, W. L. W. 1997, ApJS, 112, 315
Ho, L. C. & Ulvestad, J. S. 2001, ApJS, 133, 77
Holt, J., Tadhunter, C., Morganti, R., et al. 2006, MNRAS, 370, 1633
Holt, J., Tadhunter, C. N., & Morganti, R. 2003, MNRAS, 342, 227
Holt, J., Tadhunter, C. N., Morganti, R., & Emonts, B. H. C. 2011, MNRAS, 410, 1527
Hopkins, A. M., Connolly, A. J., Haarsma, D. B., & Cram, L. E. 2001, AJ, 122, 288
Hopkins, P. F., Bundy, K., Croton, D., et al. 2010, ApJ, 715, 202
Humphrey, A., Villar-Martín, M., Sánchez, S. F., et al. 2010, MNRAS, 408, L1
Husemann, B., Wisotzki, L., Sánchez, S. F., & Jahnke, K. 2008, A&A, 488, 145
Jahnke, K. & Macciò, A. V. 2011, ApJ, 734, 92
Jahnke, K. & Wisotzki, L. 2003, MNRAS, 346, 304
Jahnke, K., Wisotzki, L., Sánchez, S. F., et al. 2004, AN, 325, 128
Kaspi, S., Maoz, D., Netzer, H., et al. 2005, ApJ, 629, 61
Kaspi, S., Smith, P. S., Netzer, H., et al. 2000, ApJ, 533, 631
Kauffmann, G., Heckman, T. M., Tremonti, C., et al. 2003, MNRAS, 346, 1055
Kellermann, K. I., Sramek, R., Schmidt, M., Shaffer, D. B., & Green, R. 1989, AJ, 98, 1195
Kennicutt, Jr., R. C. 1998, ApJ, 498, 541
Kewley, L. J., Dopita, M. A., Sutherland, R. S., Heisler, C. A., & Trevena, J. 2001, ApJ, 556, 121
Kewley, L. J., Groves, B., Kauffmann, G., & Heckman, T. 2006, MNRAS, 372, 961
Khalatyan, A., Cattaneo, A., Schramm, M., et al. 2008, MNRAS, 387, 13
Kim, M., Ho, L. C., Peng, C. Y., et al. 2008, ApJ, 687, 767
Krist, J. 1995, in Astronomical Society of the Pacific Conference Series, Vol. 77, Astronomical Data Analysis Software and Systems IV, ed. R. A. Shaw, H. E. Payne, & J. J. E. Hayes, 349–+
Krug, H. B., Rupke, D. S. N., & Veilleux, S. 2010, ApJ, 708, 1145
Kukula, M. J., Dunlop, J. S., Hughes, D. H., & Rawlings, S. 1998, MNRAS, 297, 366
Lal, D. V. & Ho, L. C. 2010, AJ, 139, 1089
Lavalley, M., Isobe, T., & Feigelson, E. 1992, in Astronomical Society of the Pacific Conference Series, Vol. 25, Astronomical Data Analysis Software and Systems I, ed. D. M. Worrall, C. Biemesderfer, & J. Barnes, 245–+
Leipski, C. & Bennert, N. 2006, A&A, 448, 165
Leipski, C., Falcke, H., Bennert, N., & Hüttemeister, S. 2006, A&A, 455, 161
Letawe, G., Magain, P., Courbin, F., et al. 2007, MNRAS, 378, 83
Li, C., Kauffmann, G., Heckman, T. M., White, S. D. M., & Jing, Y. P. 2008, MNRAS, 385, 1915
Lim, J. & Ho, P. T. P. 1999, ApJ, 510, L7
Lipari, S., Sanchez, S. F., Bergmann, M., et al. 2009, MNRAS, 392, 1295
Magorrian, J., Tremaine, S., Richstone, D., et al. 1998, AJ, 115, 2285
Marziani, P., Zamanov, R. K., Sulentic, J. W., & Calvani, M. 2003, MNRAS, 345, 1133
McCarthy, P. J., Baum, S. A., & Spinrad, H. 1996, ApJS, 106, 281
McCarthy, P. J., Spinrad, H., & van Breugel, W. 1995, ApJS, 99, 27
McCarthy, P. J., van Breugel, W., Spinrad, H., & Djorgovski, S. 1987, ApJ, 321, L29
McLeod, K. K. & McLeod, B. A. 2001, ApJ, 546, 782
McLure, R. J., Kukula, M. J., Dunlop, J. S., et al. 1999, MNRAS, 308, 377
Miller, P., Rawlings, S., & Saunders, R. 1993, MNRAS, 263, 425
Moorwood, A., Cuby, J., & Lidman, C. 1998, The Messenger, 91, 9
Mulchaey, J. S., Wilson, A. S., & Tsvetanov, Z. 1996a, ApJS, 102, 309
Mulchaey, J. S., Wilson, A. S., & Tsvetanov, Z. 1996b, ApJ, 467, 197
Nagar, N. M., Wilson, A. S., Mulchaey, J. S., & Gallimore, J. F. 1999, ApJS, 120, 209
Nesvadba, N. P. H., Lehnert, M. D., Eisenhauer, F., et al. 2006, ApJ, 650, 693
Netzer, H., Shemmer, O., Maiolino, R., et al. 2004, ApJ, 614, 558
Nolan, L. A., Dunlop, J. S., Kukula, M. J., et al. 2001, MNRAS, 323, 308
Osterbrock, D. E. & Ferland, G. J. 2006, Astrophysics of gaseous nebulae and active galactic nuclei (2nd. ed. by D.E. Osterbrock and G.J. Ferland. Sausalito, CA: University Science Books, 2006)
Peacock, J. A. 1983, MNRAS, 202, 615
Peng, C. Y., Ho, L. C., Impey, C. D., & Rix, H.-W. 2002, AJ, 124, 266
Peterson, B. M., Ferrarese, L., Gilbert, K. M., et al. 2004, ApJ, 613, 682
Peterson, B. M. & Wandel, A. 2000, ApJ, 540, L13
Pettini, M. & Pagel, B. E. J. 2004, MNRAS, 348, L59
Press, W. H., Teukolsky, S. A., Vetterling, W. T., & Flannery, B. P. 1992, Numerical recipes in C. The art of scientific computing (Cambridge: University Press, —c1992, 2nd ed.)
Privon, G. C., O'Dea, C. P., Baum, S. A., et al. 2008, ApJS, 175, 423
Punsly, B. & Zhang, S. 2011, ArXiv e-prints
Pych, W. 2004, PASP, 116, 148
Rawlings, S. & Saunders, R. 1991, Nature, 349, 138
Roth, M. M., Kelz, A., Fechner, T., et al. 2005, PASP, 117, 620
Rupke, D. S., Veilleux, S., & Sanders, D. B. 2005, ApJS, 160, 115
Sánchez, S. F. 2006, AN, 327, 850
Sánchez, S. F., Aceituno, J., Thiele, U., Pérez-Ramírez, D., & Alves, J. 2007, PASP, 119, 1186
Schinnerer, E., Eckart, A., & Tacconi, L. J. 1998, ApJ, 500, 147
Schlegel, D. J., Finkbeiner, D. P., & Davis, M. 1998, ApJ, 500, 525
Schmidt, M. & Green, R. F. 1983, ApJ, 269, 352
Schmitt, H. R., Donley, J. L., Antonucci, R. R. J., Hutchings, J. B., & Kinney, A. L. 2003a, ApJS, 148, 327
Schmitt, H. R., Donley, J. L., Antonucci, R. R. J., et al. 2003b, ApJ, 597, 768
Schulze, A. & Wisotzki, L. 2010, A&A, 516, A87+
Schulze, A., Wisotzki, L., & Husemann, B. 2009, A&A, 507, 781
Sersic, J. L. 1968, Atlas de galaxias australes, ed. Sersic, J. L.
Stasińska, G., Vale Asari, N., Cid Fernandes, R., et al. 2008, MNRAS, 391, L29
Steinhardt, C. L. & Elvis, M. 2010, MNRAS, 402, 2637
Stockton, A. 1976, ApJ, 205, L113+
Stockton, A. & MacKenty, J. W. 1987, ApJ, 316, 584
Sulentic, J. W., Zwitter, T., Marziani, P., & Dultzin-Hacyan, D. 2000, ApJ, 536, L5
Sullivan, M., Mobasher, B., Chan, B., et al. 2001, ApJ, 558, 72
Tadhunter, C., Wills, K., Morganti, R., Oosterloo, T., & Dickson, R. 2001, MNRAS, 327, 227
Tremaine, S., Gebhardt, K., Bender, R., et al. 2002, ApJ, 574, 740
Tremonti, C. A., Heckman, T. M., Kauffmann, G., et al. 2004, ApJ, 613, 898
Tremonti, C. A., Moustakas, J., & Diamond-Stanic, A. M. 2007, ApJ, 663, L77
Unger, S. W., Pedlar, A., Axon, D. J., et al. 1987, MNRAS, 228, 671
Urry, C. M. & Padovani, P. 1995, PASP, 107, 803
Veilleux, S., Kim, D., Rupke, D. S. N., et al. 2009, ApJ, 701, 587
Veilleux, S. & Osterbrock, D. E. 1987, ApJS, 63, 295
Veilleux, S., Shopbell, P. L., & Miller, S. T. 2001, AJ, 121, 198
Vestergaard, M. 2002, ApJ, 571, 733
Vestergaard, M. & Peterson, B. M. 2006, ApJ, 641, 689
Villar-Martin, M., Tadhunter, C., & Clark, N. 1997, A&A, 323, 21
Villar-Martín, M., Tadhunter, C., Morganti, R., Axon, D., & Koekemoer, A. 1999, MNRAS, 307, 24
Villar-Martín, M., Tadhunter, C., Pérez, E., et al. 2010, MNRAS, 407, L6
Wampler, E. J., Burbidge, E. M., Baldwin, J. A., & Robinson, L. B. 1975, ApJ, 198, L49
Wild, V., Heckman, T., & Charlot, S. 2010, MNRAS, 405, 933
Wilson, A. S. & Tsvetanov, Z. I. 1994, AJ, 107, 1227
Wisotzki, L. 2000, A&A, 353, 861
Wisotzki, L., Christlieb, N., Bade, N., et al. 2000, A&A, 358, 77
Wold, I., Sheinis, A. I., Wolf, M. J., & Hooper, E. J. 2010, MNRAS, 1374
Wright, E. L. 2006, PASP, 118, 1711
Xu, C., Livio, M., & Baum, S. 1999, AJ, 118, 1169
Zakamska, N. L., Strauss, M. A., Krolik, J. H., et al. 2003, AJ, 126, 2125
Zamfir, S., Sulentic, J. W., & Marziani, P. 2008, MNRAS, 387, 856

Chapter 4

Integral field spectroscopy of nearby QSOs: Emission-line diagnostics, resolved gas-phase metallicities & the NLR size-luminosity relation⋆

B. Husemann[1], D. Nugroho[2], K. Jahnke[2], S. F. Sánchez[3], L. Wisotzki[1], D. Kupko[1], and M. Schramm[4]

[1] Astrophysikalisches Institut Potsdam, An der Sternwarte 16, 14482 Potsdam, Germany
[2] Max-Planck-Institut für Astronomie, Königsstuhl 17, D-69117 Heidelberg, Germany
[3] Centro Astronómico Hispano-Alemán, Calar Alto,(CSIC-MPG), C/Jesús Durbán Remón 2-2, E-04004 Almeria, Spain
[4] Department of Astronomy, Kyoto University, Kyoto 606-8502, Japan

ABSTRACT

We present VIMOS integral field spectroscopy of a flux-limited sample of 19 QSOs at low redshift ($z < 0.2$). These observations provide a spatially resolved spectroscopic follow-up of an extensive ground-based multi-colour imaging study of those objects. This work focuses on spatially resolved emission-line diagnostics to infer the physical properties of the ionised gas in the QSO host galaxies. With our dedicated software tool `QDeblend3D` we deblend the QSO and host galaxy light in the spatial and spectral dimension of the datacubes. Ionised gas is present in basically all QSO host galaxies irrespective of the host morphology, which originate from classical H II regions in more than 50% of the galaxies, whereas AGN ionised gas on several kpc scales is also present in ∼50% of our sample. We infer specific star formation rates in several disc-dominated AGN host galaxies that are in agreement with those of normal star forming galaxies, but some of our galaxies completely lack signature of star formation. Whether AGN feedback suppresses star formation in these systems or an intrinsically low gas content still remains an open question. On the other hand, ongoing major mergers clearly show enhanced star formation rates of up to $\sim 120\,M_\odot\,yr^{-1}$. In three objects we find tentative evidence for shock ionisation due to potential jet-cloud interactions, even though these QSOs are not classified as radio-loud. The gas-phase oxygen abundance gradients appear to be flatter than in inactive late-type spiral galaxies. We interpret this as a signature for radial gas flows, and we discuss possible drivers such as bar instabilities, galaxy interactions, and mergers. Interestingly, the oxygen abundances of the bulge-dominated QSO host galaxies (including one major merger) are systematically lower compared to disc-dominated hosts in our sample. We speculate that this can be attributed to metal dilution either as a result of minor mergers or as a particular evolutionary phase in the timeline of major mergers as recently suggested by numerical simulations. Complemented with additional data of higher and lower luminosity type 1 AGN, we study the NLR size-luminosity relation and find a strong correlation with the AGN continuum luminosity of the form $R_{\rm NLR} \propto L_{5100}^{0.52\pm0.06}$. A similar relation emerge when the integrated [O III] luminosity is used, but the scatter in the relation is significantly higher. We argue that NLR size is a better tracer for the bolometric AGN luminosity than the [O III] luminosity.

4.1. Introduction

Active Galactic Nuclei (AGN) are thought to be powered by gas accretion onto a supermassive Black Hole (BH) residing at the centre of galaxies. Luminous AGN are exclusively associated with the most massive galaxies above a stellar mass of $M_* > 10^{10}\,M_\odot$ (Kauffmann et al. 2003). The fraction of AGN among galaxies reach is maximum ∼20%, depending on the threshold AGN luminosity, at a stellar mass of around $10^{11}\,M_\odot$. Considering that all galaxies with a significant bulge component are suspected to host massive BHs, certain mechanisms need to be responsible for the triggering of a luminous AGN phase.

In particular for the most luminous AGN, i. e. Quasi-stellar objects (QSOs), gas-rich major mergers of galaxies have been quoted to be the main AGN triggering mechanism (e.g. Sanders et al. 1988a,b; Hutchings & Neff 1992; Canalizo & Stockton 2001). This scenario is appealing because those mergers are known to funnel enough gas to their nucleus to fuel QSO activity over its duty cycle. Nevertheless, no excess of major mergers were found for AGN hosts in direct comparison to quiescent galaxies (Dunlop et al. 2003; Sánchez et al. 2004b; Grogin et al. 2005; Tal et al. 2009; Cisternas et al. 2011). Whether the usual images are insufficiently deep remains an open question given the faint substructures reported in 4/5 elliptical QSO host from very deep observations Bennert et al. (2008). Considering a possible time delay between the onset of AGN activity and the peak of star formation (e.g. Emonts et al. 2006; Davies et al. 2007), the merger signatures could already be weak in their morphologies at the time an AGN can be recognised. Anyway, the fraction of AGN in close pairs of galaxies is not significantly higher compared to control samples of field galaxies (Barton et al. 2000; Alonso et al. 2007; Ellison et al. 2008; Li et al. 2008), and many lower luminosity AGN reside in disc-dominated galaxies that are not undergoing a major interaction (e.g. Hopkins & Hernquist 2009; Reichard et al. 2009). The metallicity of gas and stars takes a record of the past enrichment with heavy elements

⋆ This Chapter will be submitted to the journal *Astronomy & Astrophysics* within a few month time frame.

due to episodes of star formation and provide evidence for the past evolution of galaxies. Recent simulations have shown that galaxy interactions dilute the gas-phase metallicity in their nuclei (Montuori et al. 2010) and change the radial metallicity distribution (Rupke et al. 2010) due to radial gas mixing caused by gravitational torques. These may be used as independent diagnostics to identify recent interactions and to provide constraints on their timing.

Another interesting property of bulge-dominated host galaxies are their blue colours compared to inactive counterparts (Kauffmann et al. 2003; Jahnke et al. 2004b,c; Sánchez et al. 2004b; Zakamska et al. 2006; Schramm et al. 2008), which has been attributed to recent star formation. Since the fraction of AGN is the highest in the region of the colour-magnitude diagram between young star forming systems (the blue cloud) and old, mainly bulge-dominated, galaxies (the red sequence) (e.g. Nandra et al. 2007; Martin et al. 2007; Salim et al. 2007), AGN hosts might be in a particular transition phase. Star formation would have to cease along such an evolutionary path, either due to consumption of gas or feedback processes that actively quench star formation. While the consumption timescale may be too long (Kaviraj et al. 2010), AGN potentially support the required energy to shutdown star formation completely. Semi-analytic models were successful in reproducing the properties of the galaxy population across cosmic time more accurately than before, after some sort of AGN feedback was phenomenological included (e.g. Granato et al. 2004; Springel et al. 2005; Bower et al. 2006; Croton et al. 2006; Somerville et al. 2008; Cattaneo et al. 2009). It remains observationally difficult to quantify ongoing star formation in luminous QSOs in order to directly test this scenario. Analysing the [O II] line in the spectra of luminous QSOs, (Ho 2005) reported current star formation rate of only a few $M_\odot\,yr^{-1}$ which they attributed to a suppression of the star formation efficiency assuming that the molecular gas content of AGN hosts is typically high. Furthermore, Wild et al. (2010) found that the SFR in post-starburst AGN hosts decreased by 0.5 dex within a time frame of 500 Myr. However, star formation rate estimates based on infrared diagnostics indicate an enhancement of star formation (e.g. Schweitzer et al. 2006; Lacy et al. 2007).

One obvious impact of AGN on their hosts is the photoionisation of interstellar gas, the so-called Narrow-line Region (NLR), due to its hard ionising radiation field. The typical size of the NLR is <1 kpc, which can be well resolved from the ground in nearby Seyfert galaxies (e.g. Pogge 1988a,b; Storchi-Bergmann & Bonatto 1991; Storchi-Bergmann et al. 1992; Mulchaey et al. 1996). The NLR was mapped by Bennert et al. (2002) with narrow-band filters on board the Hubble Space Telescope (*HST*) for a small sample of 7 luminous QSOs. For these luminous QSOs the NLR sizes are larger than 1 kpc, and often referred to as an Extended Narrow Line Region (ENLR). Its dependence on the AGN luminosity can be well described by a power law. Bennert et al. (2002) inferred a power-law slope of $R_{\rm NLR} \propto L_{\rm [O\,III]}^{0.52\pm0.06}$, while Schmitt et al. (2003a) estimated a slope of $R_{\rm NLR} \propto L_{\rm [O\,III]}^{0.33\pm0.04}$ for a sample of 60 nearby Seyfert galaxies also observed with *HST*. An even flatter slope was recently inferred by Greene et al. (2011) of $R_{\rm NLR} \propto L_{\rm [O\,III]}^{0.22\pm0.04}$ from long-slit spectroscopy of luminous type 2 QSOs. From integral field spectroscopy for a sample of 31 QSOs, we already found in Chapter 3 that the *HST* narrow-band observations are quite shallow, leading to an underestimation of the NLR sizes by at least a factor of 2. Furthermore, we showed that the ENLR sizes of type 1 and type 2 QSO are consistent with each other, which basically rules out that both types obey different scaling relation as proposed by Bennert et al. (2006) due to projection effects. Thus, the issue of the slope of the NLR size-luminosity relation remains open, but is important to understand the nature of the coupling between the AGN radiation and its environment.

In this Chapter, we present IFS observations of a flux-limited sample of 19 low-redshift ($z < 0.2$) QSOs with intermediate luminosities. We focus on the spatially resolved characterisation of the ionised gas via standard emission-line diagnostics. H II regions are identified as signatures for recent star forming activity and estimate the corresponding specific star formation rates. The gas-phase oxygen abundance are studied to understand the origin of the gas and to distinguish between different possible AGN triggering mechanism. Furthermore, we investigate the NLR size-luminosity relation for type 1 AGN, and together with our QSO dataset presented in Chapter 3 estimate the power-law slope of the relation.

Throughout the Chapter we assume a cosmological model with $H_0 = 70\,{\rm km\,s^{-1}\,Mpc^{-1}}$, $\Omega_{\rm m} = 0.3$, and $\Omega_\Lambda = 0.7$.

4.2. The QSO sample

For our project we chose a statistically complete and flux-limited sample of 19 QSOs drawn from the Hamburg/ESO survey (HES, Reimers et al. 1996; Wisotzki et al. 1996, 2000). This sample contains all QSOs above a certain flux limit within an area of 611 deg^2 at $0.027 < z < 0.2$. The QSOs have total apparent magnitudes in the range of $13.7 < V_{\rm total} < 16.8$, and host magnitudes of $14.5 < V_{\rm host} < 18.0$ with corresponding host luminosities of $-25.6 < M_K < -23.2$ in the K band. It is a low-redshift subset of the sample defined by Köhler et al. (1997) to study the local QSO luminosity function. The main characteristics of our sample are summarised in Table 4.1 and described below in more detail.

An extensive set of ground-based multicolour *BVRIJHK* imaging observation for this sample is available and was analysed by Jahnke et al. (2004a), hereafter Ja04. Since the objects were selected purely on QSO luminosity, the sample is not biased towards a certain host morphology. The sample contains 9 bulge-dominated host galaxies, 8 disc-dominated host galaxies, and 2 obvious cases of ongoing major-mergers. A few objects have confirmed nearby companion galaxies of which some display signatures of ongoing interactions. High-resolution *HST* images of 9 objects (see Table 4.1) were obtained in different programs[1], some of which are unpublished so far. We retrieved all archival *HST* images from the Hubble Legacy Archive[2] and performed a deblending of the QSO and host components with `GALFIT` (Peng et al. 2002) using either a dedicated PSF star observation or, alternatively, a PSF model created with `TinyTim` (Krist 1995). The QSO-subtracted *HST* or ground-based images (mainly the V-band) of our targets are shown below in Fig. 4.7.

Based on the ground-based multi-colour images, stellar masses of these systems were estimated by modelling the broad-band spectral energy distribution with Bruzual & Charlot (2003) stellar population models to obtain proper mass-to-light ratios

[1] HST images from the following programs: "The nature of quasar host galaxies: combining ACS imaging and VLT Integral Field Spectroscopy" (Proposal 10238, PI: F. Courbin), "Subarcsecond structure in nearby AGN" (Proposal 5479, PI: M. Malkan), "WFC imaging of nearby bright Quasars" (Proposal 5434, PI: J. Bahcall), "High-resolution imaging of X-ray selected AGN" (Proposal 6361, PI: B. Boyle)

[2] Website of the Hubble Legacy Archive: http//hla.stsci.edu

Table 4.1. Overview of the sample characteristics

Object	z	m_V[a]	Morph.[b]	R_e[c] [kpc]	M_K[d]	$\log(M_*/M_\odot)$[e]	R[f]	$L_{1.4\,GHz}$[g] [W/Hz]	HST imaging[h]
HE 0952−1552	0.112	15.8	D	5.1	-25.5	11.18 ± 0.28	3.4	23.23	
HE 1019−1414	0.076	16.1	D	3.7	-24.1	10.77 ± 0.28	2.6	22.86	
HE 1020−1022	0.196	16.6	E	8.1	-25.8	11.45 ± 0.27	779.7	25.95	WFPC2/WF3 F606W
HE 1029−1401	0.085	13.7	E	3.1	-25.8	11.10 ± 0.38	0.6	23.43	WFPC2/WF3 F606W
HE 1043−1346	0.068	15.7	D	5.0	-24.9	10.88 ± 0.38	< 2.5	< 22.16	ACS/HRC F606W
HE 1110−1910	0.111	16.0	E	4.2	-24.8	10.81 ± 0.32	< 1.0	< 22.60	ACS/HRC F606W
HE 1201−2409	0.140	16.3	E	1.1	-25.3	10.96 ± 0.32	< 1.6	< 22.81	
HE 1228−1637	0.104	15.8	E	2.6	-24.6	10.79 ± 0.30	< 0.7	< 22.54	ACS/HRC F606W
HE 1237−2252	0.097	15.9	D	7.4	-25.4	11.14 ± 0.18	< 1.6	< 22.48	
HE 1239−2426	0.082	15.6	D	6.8	-25.2	11.15 ± 0.19	1.9	22.60	ACS/HRC F606W
HE 1254−0934	0.139	14.9	M	12.2	-25.2	11.19 ± 0.24	2.0	23.89	
HE 1300−1325	0.046	14.9	E	3.6	-24.8	10.75 ± 0.39	< 0.6	< 21.81	
HE 1310−1051	0.034	14.9	D	2.5	-23.2	10.21 ± 0.27	< 0.3	< 21.55	WFPC2/PC1 F606W
HE 1315−1028	0.099	16.8	D	6.1	-24.2	10.71 ± 0.31	< 2.0	< 22.49	
HE 1335−0847	0.080	16.3	E	3.7	-23.9	10.48 ± 0.31	< 1.9	< 22.30	
HE 1338−1423	0.041	13.7	D	10.0	-25.4	11.09 ± 0.32	0.5	22.29	
HE 1405−1545	0.196	16.2	M	6.9	-25.6	11.24 ± 0.38	< 0.9	< 23.12	
HE 1416−1256	0.129	16.4	E	4.9	-24.5	10.45 ± 0.39	5.9	22.95	WFPC2/PC1 F814W
HE 1434−1600	0.147	15.7	E	5.5	-25.7	11.10 ± 0.36	417.5	25.71	ACS/HRC F606W

Notes. [a] Total apparent V band magnitude. [b] Morphological classification of the QSO hosts: D – disc-dominated/late-type galaxies, B – bulge-dominated/early-type galaxies, and M – ongoing major mergers [c] Effective (half-light) radius of the QSO hosts as reported by Jah04 converted to our adopted cosmology. [d] k-corrected absolute K-band magnitudes of the QSO host as reported by Jah04. [e] Total stellar masses of the QSO hosts based on multi-color SED fits (Schramm et al. in prep.). [f] R parameter definied as the flux density ratio at 6 cm over that at 4400Å. [g] Continuum radio luminosity at 1.4 GHz. [h] Available HST imaging: WFPC2 – Wide Field Planetary Camera 2 with a sampling of either 0.1″with the Wide Field Chip (WFC) or 0.05″with the Planetary Camera (PC), ACS – Advanced Camera for Surveys with a sampling of 0.025″with its High Resolution Channel (HRC).

(Schramm et al. in prep.). The accuracy of these stellar mass estimates were estimated using a large suite of Monte-Carlo simulations based on the photometric errors and are typically not better than a factor of 2. We found a range in stellar masses of $10.2 < \log(M_*/M_\odot) < 11.5$. This stellar mass range is right at the peak of the AGN activity in the low-redshift galaxy population as inferred by Kauffmann et al. (2003). Thus, our QSO host galaxies correspond either to high-mass disc-dominated galaxies or to intermediate-mass bulge-dominated galaxies.

In order to characterise the radio properties of the sample we classified our objects into radio-loud, radio-intermediate and radio-quiet based on the R parameter (e.g. Kellermann et al. 1989), which is defined as the ratio of the flux density at 6 cm (5 GHz) over that at 4400Å (cf. Section 1.1.2 of the introduction). Follow-up observations for HES QSOs at 5 GHz with the Very Large Array (VLA) were only done for 7 QSOs of our sample. For the other objects we used the measurements and upper limits from the NRAO VLA Sky Survey (NVSS) at 1.4 GHz (Condon et al. 1998) as a surrogate for the radio flux at 5 GHz assuming a power-law radio spectral index of $\alpha_r = -0.5$ at the dividing line between steep and flat-spectrum radio source. Only two QSOs of our sample (∼10%), HE 1020−1022 and HE 1434−1600, are classified to be radio-loud QSOs ($R > 10$) as expected for optical selected QSO sample. The vast majority (12/19) of the QSOs within the sample are radio-quiet QSOs ($R < 1$), including all objects with an upper limit in R close to 1. Five QSOs exhibit an intermediate level of radio emission with R parameters in between $1 \leq R \leq 10$.

4.3. Observations and data reduction

4.3.1. VIMOS IFU observations

Integral field spectroscopy of all 19 objects in the sample was obtained with the IFU mode of the VIsible MultiObject Spectrograph (VIMOS, LeFevre et al. 2003) mounted on UT3 (Melipal) of the ESO Very Large Telescope in Chile. The observations were carried out in service mode in period 72 from the 18th December 2003 to the 28th January 2004 and in period 83 from 16th April 2009 and 19th May 2009 in dark time. We used the high resolution grisms (HR grisms) in order to obtain accurate kinematic information of emission and absorption lines as well as to detect and deblend kinematically different emission-line components. The spectral resolution ($\lambda/\Delta\lambda$) of the HR blue, HR orange, and HR red grisms are ∼2550, ∼2650 and ∼3100, respectively. Due to the limited wavelength coverage of the HR grisms, two different instrumental setups were often required to cover the important spectral regions around Hβ and Hα.

Depending on the apparent angular sizes of the QSO host galaxies we chose different magnifications of $0\farcs33 \times 0\farcs33$ or $0\farcs67 \times 0\farcs67$ per spaxel[3]. This yielded a field of view of $13'' \times 13''$ or $27'' \times 27''$ for the 1600 fibres arranged in a rectangular grid of 40×40 spaxels. The total integration time per instrumental setup between 900 s and 3150 s, split into at least 3 exposures. A dither pattern was applied to the exposure sequence to allow for the rejection of dead fibres. A short blank sky exposure of 90s or 300s length was obtained during each science exposure series. The median seeing of all observations

[3] spectral pixel, a single spatial resolution element containing a spectrum along the entire wavelength range

Table 4.2. VIMOS observational log.

Object	Obs. Date	Grism	Sampling	$t_{\rm total}$	$n_{\rm exp}$	Airmass	Seeing	Remarks
HE 0952−1552	2003–12–21	HR orange	0.″67	2700s	6	1.1	1.″2	
HE 1019−1414	2009–05–18	HR blue	0.″67	2000s	4	1.0	1.″2	
	2009–05–18	HR orange	0.″67	3000s	4	1.1	1.″3	
HE 1020−1022	2009–05–19	HR orange	0.″33	2000s	4	1.1	1.″0	(a)
	2009–05–13	HR red	0.″33	3000s	4	1.2	1.″3	(a)
HE 1029−1401	2003–12–17	HR blue	0.″67	900s	3	1.1	1.″2	
	2003–12–23	HR orange	0.″67	2700s	6	1.2	1.″3	
HE 1043−1346	2003–12–22	HR orange	0.″67	2700s	6	1.2	1.″3	
	2009–05–19	HR blue	0.″67	2000s	4	1.2	1.″3	
HE 1110−1910	2003–12–20	HR orange	0.″67	2700s	6	1.1	1.″2	
HE 1201−2408	2009–04–15	HR orange	0.″33	1500s	2	1.1	...	(b)
	2009–04–15	HR red	0.″33	1000s	2	1.0	...	(b)
HE 1228−1637	2003–12–30	HR orange	0.″67	3150s	7	1.2–1.6	1.″3	
HE 1237−2252	2003–12–31	HR orange	0.″67	2700s	6	1.6–2.3	1.″5	
HE 1239−2426	2003–12–28	HR blue	0.″67	900s	3	1.5	1.″4	
	2003–12–31	HR orange	0.″67	2700s	6	1.2–1.5	1.″3	
HE 1254−0934	2004–01–01	HR orange	0.″67	2700s	6	1.4–1.8	1.″3	
	2009–04–18	HR red	0.″67	2000s	4	1.2	1.″5	
HE 1300−1325	2009–04–22	HR blue	0.″67	2000s	4	1.2–1.5	1.″4	
	2009–04–25	HR orange	0.″67	3000s	4	1.2	1.″3	
HE 1310−1051	2009–04–22	HR blue	0.″67	2000s	4	1.2	1.″6	
	2009–04–25	HR orange	0.″67	3000s	4	1.3–1.5	1.″1	
HE 1315−1028	2004–01–17	HR orange	0.″67	3000s	4	1.3–1.7	1.″4	
HE 1335−0847	2009–04–24	HR blue	0.″33	2000s	4	1.3–1.6	...	
HE 1338−1423	2009–04–27	HR blue	0.″67	2000s	4	1.1	1.″3	
	2009–04–27	HR orange	0.″67	3000s	4	1.2–1.5	1.″3	
HE 1405−1545	2004–01–22	HR orange	0.″67	2700s	6	1.2–1.5	2.″3	
	2004–01–27	HR red	0.″67	900s	3	1.2	1.″5	
HE 1416−1256	2009–04–15	HR red	0.″33	2000s	4	1.3–1.5	1.″2	
	2009–04–18	HR orange	0.″33	3000s	4	1.1	1.″2	
HE 1434−1600	2009–04–17	HR orange	0.″33	1500s	2	1.2–1.5	...	(b)
	2009–04–18	HR orange	0.″33	1000s	2	1.2	...	(b)

Notes. (a) This object was rejected from the analysis due to an exceptionally bad spectrophotometry as explained in the text. (b) The QSO was positioned at the edge of the VIMOS FOV so that an absolute photometric calibration could not be performed.

was 1.″3 and the median airmass was 1.2. Details on the individual observations are given in Table 4.2.

The orientation and position of the VIMOS field of view with respect to each of the AGN host galaxies is shown in Fig. 4.7. Unfortunately, a few QSOs were not properly centred in the VIMOS field of view, which affected observations in the high magnification mode (0.″33 spaxels) more severely. Thus, for HE 1201−2408 and HE 1434−1600 only half of the host galaxies were actually covered. HE 1335−0847 was not covered at all with the HR orange grism setup. The observation of HE 1020−1022 suffered from poor photometric conditions resulting in an exceptionally bad spectrophotometry. The spectra of the HR orange and HR red observation did not match in the overlapping wavelength range, neither in slope nor in absolute calibration, so that we decided to rejected this object from any detailed analysis.

4.3.2. Data reduction

We used our own IFU reduction package `R3D` (Sánchez 2006) to perform all of the IFU related core reduction steps: Bias subtraction, visually checked fibre identification, fibre tracing, spectra extraction, wavelength calibration, fibre flatfielding and flux calibration. Several custom Python scripts were patched into the `R3D` reduction process to specifically handle the complex characteristics of VIMOS. We will therefore give a description of the different steps including our special treatment for VIMOS and demonstrate the gain of our approach, but also note some remaining limitations.

A master bias frame was created for each of the four independent CCDs by taking the median of 5 bias frames regularly taken each day as part of the standard calibration plan. These master bias frames were subsequently subtracted from all raw images. As automatic fibre identification often fails for VIMOS, we visually cross-matched the peak positions of the fibre profiles in the continuum lamp exposure along the cross-dispersion direction with a VIMOS fibre postion template. Because of several broken or vignetted fibres this procedure requires some experience to be successful. The peaks of the fibres were then traced along the dispersion axis. This process was rather robust except for the HR-blue observations where the tracing was lost for a few fibres at the blue end ($\lambda < 4300$Å) of the CCDs due to the low efficiency. We ignored that effect as the number of affected fibres was less than 100, and also because that spectral region is unimportant for our scientific analysis and suffers from low S/N anyway.

More important is the strong flexure of the instrument which also varies with the position of the telescope. Thus, the tracing of the fibre spectra in the continuum lamp exposure is not necessarily the same as that of raw science frames taken at different telescope positions. In order to estimate the offset in the tracing between the science frames and the continuum exposure,

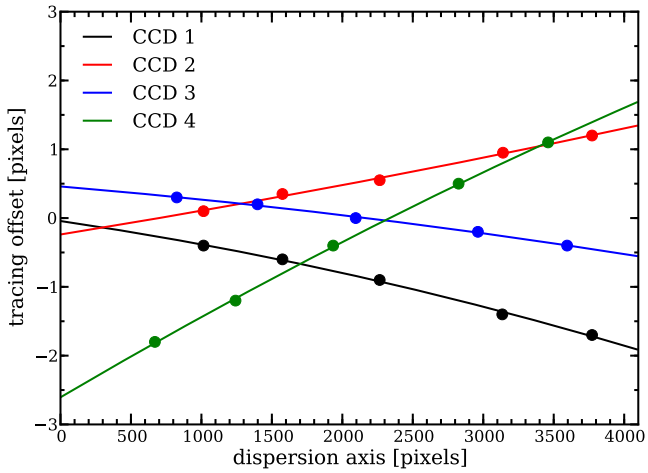

Fig. 4.1. Measured shifts in pixels between the fibre positions on the continuum exposure with respect to the science exposure of the 4 CCDs along the dispersion axis. The circles mark 5 measurements at bright sky lines distributed along the dispersion axis. The corresponding line in the same colour is a 2nd order Chebychev polynomial fit to the datapoints.

we measured the fibre positions directly in the science frame by co-adding the light of 200 pixels along the dispersion direction around 5–6 bright sky lines (or sky continuum) to gain in contrast. Afterwards we extrapolated the measured offsets at those few base points to the entire dispersion axis using a Chebychev polynomial of 2nd order (Fig. 4.1). We found offsets up to ±2.5 pixels in cross-dispersion for the observations of 2004 and only ±0.5 pixels for the observations in 2009 after an upgrade of the instrument. Similar offsets are also expected to occur in the dispersion direction, which can only be estimated from night sky emission lines. However, most of the sky lines were too faint in our data for an accurate measurement, so that no independent wavelength solution could be obtained directly from the target exposures. This limits the absolute wavelength calibration in the final science data to a precision of about half a pixel (~0.3Å) corresponding to ±20 km/s at maximum, which is still quite sufficient for our study.

Within VIMOS, 400 fibres are densely projected onto each CCD so that cross-talk is certainly an issue. R3D provides an iterative and fast algorithm to reduce the cross-talk via Gaussian profile fitting to each of the fibres and its nearest neighbours simultaneously. The median width of the fibre profiles are determined independently for each CCD and kept fixed for the extraction process. This procedure was tested and successfully applied to the data of the PINGS survey (Rosales-Ortega et al. 2010) conducted with the PPAK/PMAS IFU spectrograph at Calar Alto observatory. Further details about the extraction algorithm can be found in the R3D user guide[4].

Finally, the arc lamps were used to perform a wavelength calibration with R3D in a standard way and the data were resampled to a common wavelength solution for each instrumental setup. We used the continuum lamp exposures to create a fibreflat that corrects for the global differences in the fibre-to-fibre transmission. The straylight contribution was estimated and subtracted from the raw continuum exposures using CCD regions free of any fibre emission. By modelling the [O I] λ5577 night-sky line with a Gaussian profile in each fibre of the flat-field corrected blank sky fields we measured variation in the line flux of ±5% across the field with a characteristic pattern. This pattern corresponds most likely to an inhomogeneous light illumination of the continuum calibration frames itself. We note that those fluctuations in the fibre-to-fibre transmission are significantly smaller than reported for other VIMOS IFU observations, e.g. up to ±30% (Arribas et al. 2008), which is most likely explained by the fact that other pipelines do not take cross-talk into account properly. Another particular problem of VIMOS is that the width of the fibre profiles can be significantly broader in a few fibres, which cannot be handled by the current version of R3D and partially accounts for the inhomogeneities across the field.

Standard star observations were processed along the same steps outlined above. Since the stars were often obtained in different nights with respect to our targets, we generated a master sensitivity function by averaging the sensitivity curves of all standard stars (for a given instrumental setup) to perform a relative flux calibration of the science data.

We subsequently applied the following post-processing steps outwide the R3D package. Although dedicated sky exposure were taken, the exposure time of 90 sec for the 2009 observations were too short to achieve a sufficient S/N. In order to treat the data homogeneously, we therefore estimated the sky directly from each science exposure. A median sky spectrum was extracted from four spatial regions at the edges of the VIMOS field of view, which were free from host galaxy emission, and subsequently subtracted from each of the four quadrants separately. We measured the apparent position of the bright point-like QSO emission in each slice along the wavelength axis and resampled the individual slices to match a common QSO reference position using a Lanczos kernel. The different dithered science exposures were then registered with respect to the QSO centre and combined by taking the average excluding bad pixels/fibres. We established an absolute flux calibration by matching the total V-band photometry to the ground-based images (Jah04). The spectra were corrected for Galactic extinction assuming the attenuation law of Cardelli et al. (1989) together with the corresponding V band extinction (A_V) towards the sightline of each object measured by Schlegel et al. (1998). Finally, we removed the telluric absorption bands with a normalised absorption template generated from the standard star observations.

We also generated variance datacubes by propagating the pixel noise of the raw frames along the same reduction steps as the data itself. Because of a couple of resampling steps in the data reduction the final variances are necessarily underestimated. We thus compared the uncertainty given by the variance cube with the real noise in blank sky regions of the data and found a discrepancy of about a factor of 1.4–2.0. We multiplied this correction factor in quadrature to the variance cubes to empirically correct for this effect as good as possible. Additional systematic effects of the VIMOS instrument could however not be incorporated into the variance datacubes. First, VIMOS suffers from a strong fringing pattern with a peak-to-valley ration of ¿10% for wavelength greater than 8000Å. Given the low redshift for the majority of objects, this wavelength range is ususally not important for our analysis. Second, a few observations are affected by additional pickup noise in one of the four CCDs. Fortunately, the QSOs were centred on the other CCDs for those observation in most cases, so that we could ignore this systematic effect.

[4] The R3D manual can be downloaded from the project homepage at http://www.caha.es/sanchez/r3d/

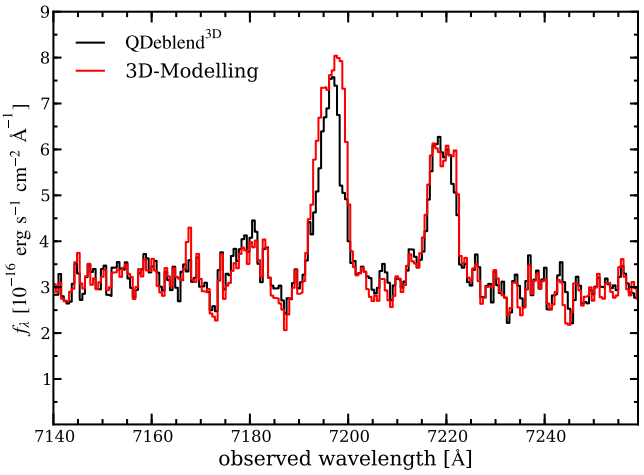

Fig. 4.2. Central co-added host spectra (3″ rectangular aperture) of HE 1237−2252 around the Hα line. The black and red line correspond to the host spectra after the QSO-host deblending with QDeblend^{3D} and the 3D Modelling technique, respectively.

4.4. Spectral QSO-host deblending in 3D

4.4.1. The method

Studying the properties of QSO host galaxies, and type 1 AGN hosts in general, requires a robust deblending of the nuclear and host galaxy light. In the case of 3D spectroscopy, this deblending needs to be done in the spatial *and* spectral dimension for which a dedicated algorithm is needed. In the course of this PhD thesis, we developed a software tool QDeblend^{3D} for this task[5], which is an improved version of the iterative algorithm initially presented by Christensen et al. (2006) to detect extended Lyα emission in IFU data of high-redshift QSOs. The basic concept of this method is that the spectrum in each spaxel is a superposition of the host galaxy spectrum at this position and of the QSO spectrum modulated in absolute flux according to the point-spread function (PSF) of the observation. Although IFU instruments usually do not capture stars simultaneously with the target due to their small field of view, type 1 AGN offer the opportunity to self-calibrate a PSF based on their broad emission lines, at least in a certain wavelength range, as presented by Jahnke et al. (2004c). A detailed description of the algorithm and the graphical user interface of QDeblend^{3D} is given in Appendix A, but we briefly outline the process here and specify the chosen setup of QDeblend^{3D} for these particular QSO observations.

A high S/N co-added QSO spectrum is extracted from a 3×3 spaxels region centred on the brightest QSO spaxels. The relative brightness of the broad nuclear emission line is measured against the local continuum, which is represented by a straight line through the median flux densities of the adjacent continuum regions on both sides of the broad line. A QSO cube is created by scaling the QSO spectrum to the accordingly measured broad line brightness of each spaxel and is subtracted from the observed one to construct a datacube with host galaxy emission only. However, the initially extracted QSO spectrum is inevitably contaminated by some host galaxy light. We therefore used the iterative scheme of QDeblend^{3D} to decontaminate the QSO spectrum based on the externally constrained 2D surface brightness profiles of the hosts (convolved with the reconstructed PSF of the observations). In four subsequent iterations, a host galaxy spectrum is extracted from a single spaxel wide annulus *around* the central QSO region (3×3 spaxels) from the QSO-subtracted datacube. That host spectrum is scaled to match the expected host galaxy surface brightness *within* the QSO region before it is subtracted from the initial QSO spectrum that serves for the next iteration. Although the FWHM of the PSF changes slowly with wavelength, we can only estimate PSFs at the observed wavelength of Hβ and Hα. We therefore split the datacubes in the case both lines were covered in a single observation. The separated datacubes are then individually processed and combined again at the end. The remaining PSF mismatch at wavelength far away from the Balmer lines certainly affect the recovered slope in the stellar continuum for those spaxels around the QSO position. However, we are focused on the diagnostic emission lines in this paper for which such a PSF mismatch is unimportant, because they are within 200Å from the Balmer lines.

An alternative method to deblend QSO and host emission is based on the analytic modelling of the surface brightness distribution that was developed to decompose broad-band imaging observations of QSOs and galaxies into their different components (e.g. Peng et al. 2002; Simard et al. 2002; Kuhlbrodt et al. 2004). The so-called 3D-Modelling technique extends this scheme by modelling each monochromatic slice of the datacube with an appropriate analytic model. Examples of this technique are the quadruple lensed QSO HE 0435−1223 (Wisotzki et al. 2003), the Seyfert 1 galaxy 3C 120 (Sánchez et al. 2004a; García-Lorenzo et al. 2005), the two broad-absorption line QSOs Mrk 231 (Lipari et al. 2009) and IRAS 04505−2958 (Lípari et al. 2009), and the QSO host of HE 1029−1401 (Husemann et al. 2010) which is also part of this sample. When we applied the 3D-Modelling technique to our sample, we realised that this technique was not optimal for a several objects in our sample. The adopted surface brightness distribution inferred from the broad-band image tracks the stellar continuum, but not necessarily that of the ionised gas. For example, in a galaxy with strong excess of ionised gas in the outer regions, the host model would overpredict the emission-line surface brightness at the centre and therefore underestimate the corresponding emission-lines in the QSO spectrum. As an example for this effect we compare the central host spectra recovered with both methods for HE 1237−2252 in Fig. 4.2. This particular object is a disc-dominated galaxy with strong extended Hα emission due to star formation. The Hα light distribution is modulated by rotational kinematics of the gas so that only a certain spatial region lights up in a given monochromatic slice according to the Doppler shift. This effect influences the results of the 3D-Modelling technique much more than QDeblend^{3D} and leads to a stronger ($> 20\%$) and significantly broadend Hα line at the galaxy centre. A similar effect was also reported for the deblending process in on-axis longslit spectroscopy (Jahnke et al. 2007).

4.4.2. Results and quality check

The decomposed spectrum of HE 0952−1552 is shown in Fig. 4.3 as an example for the results of the spectral 3D QSO-host deblending process. We extracted an integrated host galaxy spectrum by scaling a collapsed image of the entire host datacube to each slice of the cube. The QSO spectrum was taken from the pure QSO cube produced by QDeblend^{3D}. An overview of the deblended spectra can be found in Appendix C, except HE 1201−1201, HE 335−0847, HE 1416−1256 and HE 1434−1600 for which no stellar continuum emission of the

[5] available for download at http://sourceforge.net/projects/qdeblend/

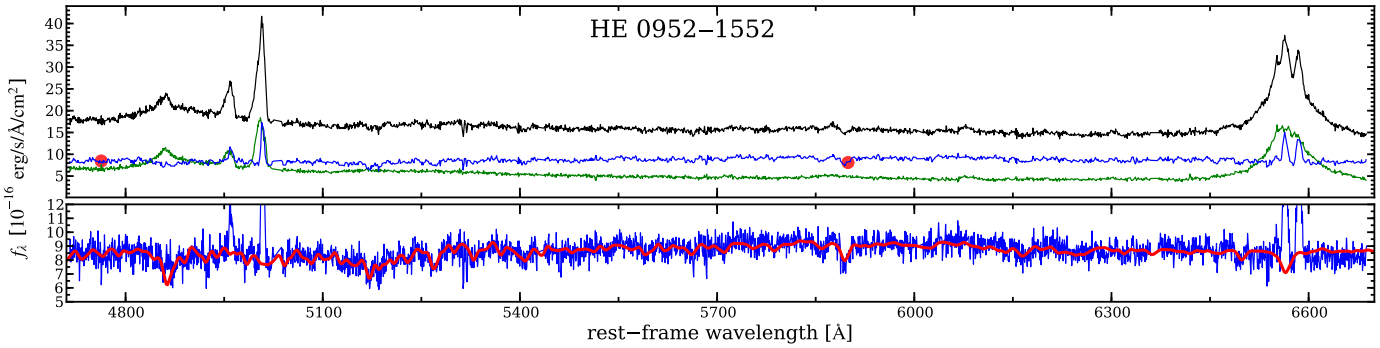

Fig. 4.3. Results of the spectral QSO-host deblending for HE 0952−1552. The black line correspond to the integrated spectrum, the green line to its QSO component and the blue line to its host galaxy component. All these three spectra are slightly smoothed by a median filter (5 spectral pixels) for display purposes. The bottom panel highlights the unsmoothed host galaxy continuum emission with the best-fit model spectrum (see Section 4.5.1 for details) overplotted as the red line.

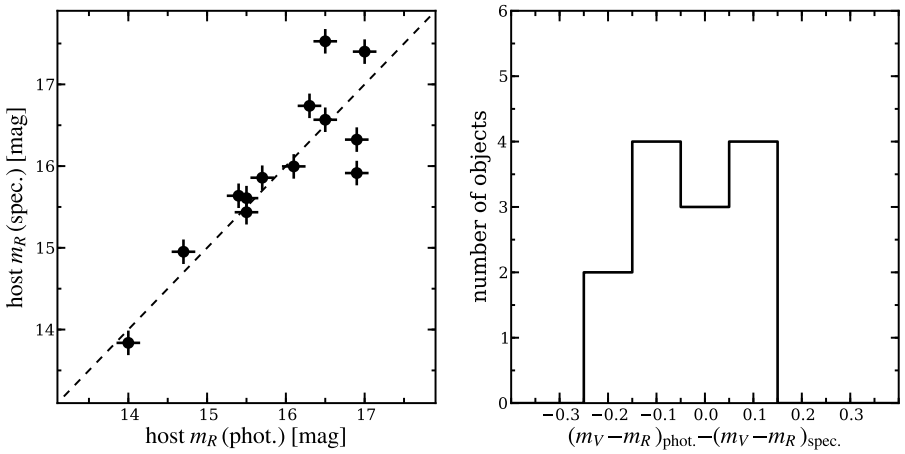

Fig. 4.4. Photometric comparison of our host spectra with the archival broad-band photometry of Jah04. *Left panel:* Synthetic R-band magnitudes of our deblended host spectra against the photometric ones. *Right panel:* Histogram of the $V - R$ colour difference between our spectroscopic and the archival photometric data.

host could be recovered. For the majority of our objects, various prominent stellar absorption lines are clearly visible in the continuum. We did not detect any remaining residuals of the broad emission lines in the host galaxy spectrum indicating a clean separation of host and QSO light with the adopted deblending algorithm.

In order to make a rough test on the quality of the host galaxy spectra, we compared the broad-band photometry after image decomposition with our spectroscopy data for a consistency check as shown in Fig. 4.4. We found that the V and R broad-band magnitudes computed from our host spectra are in good agreement with the photometric host magnitudes of the multicolour images (Jah04). A significant mismatch in the absolute photometry occurs mainly for the faintest host galaxies with $m_R \gtrsim 16.5$ where the S/N of the IFU apparently become critical for the QSO-host deblending in particular at high nucleus-to-host ratios. The $V - R$ colours are in very good agreement with the multicolour imaging data, with a colour difference of typically ±0.1 mag. This confirms that the shape of the underlying stellar continuum is not significantly contaminated by residual QSO continuum.

4.4.3. Monte-Carlo realisations

The deblending process is of course not free from random and systematic uncertainties. Certain wavelength regions covering either the QSO broad emission lines or their adjacent continuum were selected *manually* such that no residual broad line was visible in the host galaxy spectrum. Small changes in those selected wavelength regions may have a significant impact on the result. Thus, we tried to incorporate this effect in the analysis via Monte-Carlo simulations.

We generated 500 Monte-Carlo realisations for each observed datacube where we changed the flux in each pixel within the error distribution as inferred from the variance cube. The deblending process was then applied to each Monte-Carlo realisation exactly in the same way as the observed data except that the boundaries of the manually selected wavelength regions were randomly varied within ±10Å assuming a flat distribution. An additional constraint was that the new wavelength regions had a width of at least 2Å, otherwise new boundaries were randomly chosen to match this criterion.

Total host and QSO spectra were extracted and stored from the 500 deblended realisations, which we will use later to estimate the measurement errors of the integrated spectra. 50 datacubes of the Monte Carlo deblending process were fully kept for the analysis of the *spatially resolved* QSO host properties.

4.5. Emission-line measurements

4.5.1. Estimating the stellar continuum

Before we could actually measure and analyse the emission lines of the ionised gas, it was important to subtract the stellar continuum because the Balmer emission lines can be heavily blended with the corresponding stellar absorption lines. One possibility

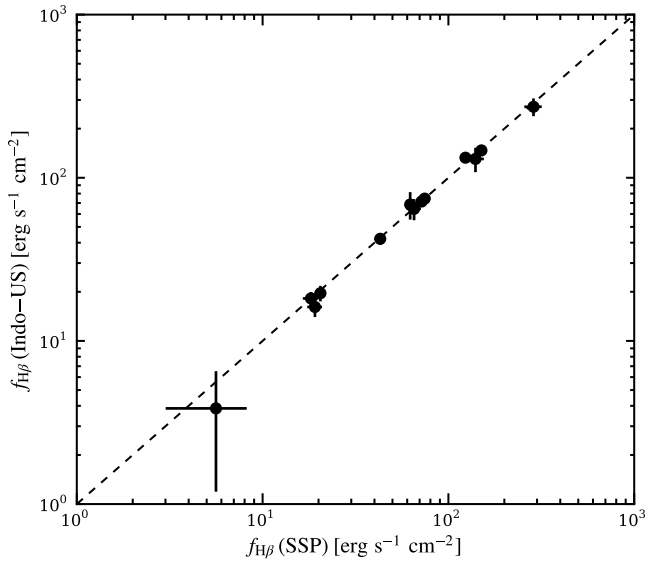

Fig. 4.5. Comparison of the continuum subtracted Hβ fluxes based on the continuum inferred either from the Indo-US stellar library or from the superposition of SSP models.

Table 4.3. Applied scheme for stellar continuum subtraction

Object	None	Integrated	Binned[(a)]
HE 0952−1552	–	–	×(16/53)
HE 1019−1414	–	×	–
HE 1029−1401	–	×	–
HE 1043−1346	–	–	×(18/59)
HE 1110−1910	–	×	–
HE 1201−2408	×	–	–
HE 1228−1637	–	×	–
HE 1237−2252	–	×	–
HE 1239−2426	–	–	×(18/53)
HE 1254−0934	–	–	×(7/40)
HE 1300−1325	–	–	×(50/79)
HE 1310−1051	–	–	×(15/49)
HE 1315−1028	–	×	–
HE 1335−0847	×	–	–
HE 1338−1423	–	–	×(66/113)
HE 1405−1545	–	×	–
HE 1416−1256	×	–	–
HE 1434−1600	×	–	–

Notes. [(a)] Bins with a resulting S/N in the continuum greater than 7 with respect to the total number of bins.

to estimate an appropriate stellar continuum spectrum is to find the best linear combination of a set of stellar template spectra. We used the spectral synthesis code STARLIGHT (Cid Fernandes et al. 2005) for this purpose which has frequently been used for the same task (e.g. Mateus et al. 2006; Rodrigues et al. 2008; Huang & Gu 2009; Cid Fernandes et al. 2010). While STARLIGHT is well documented we briefly summarise our handling of the code.

STARLIGHT models the observed spectrum O_λ with a model spectrum M_λ generated from the spectral base containing N spectra as

$$M_\lambda = \sum_{j=1}^{N} a_j B_{\lambda,j} \otimes G(v_*, \sigma_*) 10^{-0.4 A_\lambda} \,, \tag{4.1}$$

where $a_1, ..., a_N$ is the population vector $\boldsymbol{a}$ of the linear coefficients for the different base spectra $B_{\lambda,j}$. After normalising the base spectra at a certain wavelength, the spectra are convolved with a Gaussian kernel of width σ_* and displaced by v_* in order to match the kinematics of the observed and modelled spectrum. Finally, the modelled spectrum is reddened according to an extinction law $A_\lambda = A_V q_\lambda$. To find the "best" model spectrum, STARLIGHT searches for the minimum of

$$\chi^2 = \chi^2(\boldsymbol{a}, A_V, v_*, \sigma_*) = \sum_\lambda ((O_\lambda - M_\lambda)\, w_\lambda)^2 \qquad . \tag{4.2}$$

The weights w_λ are the inverse errors of the spectrum, but we doubled the weights for the spectral regions around the G-band and Mg I λ5166 absorption lines to improve the kinematical measurements and set the weights to zeros for any spectral region containing prominent emission line. STARLIGHT adopts a sophisticated scheme to minimise χ^2 using a mixture of simulated annealing, Metropolis and Markov Chain Monte Carlo techniques. The minimisation process is split up into several stages, among which suspicious pixels are excluded and irrelevant components of the base are discarded from the fitting.

For the base spectra we chose the high spectral resolution single stellar population library generated by González Delgado et al. (2005) from a library of synthetic stellar spectra (Martins et al. 2005). From that library we selected 39 different SSPs with ages of 1, 3, 5, 10, 25, 40, 100, 300, 600, 900, 2000, 5000 and 10000 Myr and metallicities $2Z_\odot$, $1Z_\odot$, and $0.2Z_\odot$. In order to cross-check the reliability of the results and to infer systematic errors due to the choice of the spectral bases we also used a set of 15 stellar spectra of stars ranging in spectral type from O to K from the Indo-U.S. library (Valdes et al. 2004) at a spectral resolution of ∼1Å.

The best-fitting superposition of SSP spectra to the individual integrated QSO host spectra are shown in the bottom panels of Fig. 4.3 and Fig. C.1. Although we performed a weighted integration over the entire host galaxy, the continuum originates mainly from the bright central region of the host close to the QSO position. We found a very good match between the observed and modelled continuum in most case considering that the QSO emission had to be removed.

In this work we focus on the emission lines. This requires a good model for the continuum, while an accurate determination of stellar population parameters is not important. Well known degeneracies of the stellar populations, like the age-metallicity degeneracy (Worthey 1994), usually reduces the ability to accurately recover the age of the stellar population (e.g. Cid Fernandes et al. 2004). We therefore need to check whether these degeneracies significantly affect the robustness of our emission line measurements. In Fig. 4.5 we compare the continuum subtracted Hβ fluxes of all our host spectra for our two independent continuum models based on the best-fit stellar population or stellar library synthesis models. We found that the Hβ fluxes do not significantly dependend on the chosen spectral base with a scatter of ≃0.05 dex. The emission lines are insensitive to the small changes in the continuum due to degeneracies mainly because the equivalent widths of the emission lines are rather high for our hosts. It suggests that emission-line diagnostics will be robust and independent of the chosen spectral base in our cases to first order.

A detailed analysis and interpretation of the stellar composition as inferred with STARLIGHT will be presented in the PhD thesis of Dading Nugroho, supervised by Knud Jahnke.

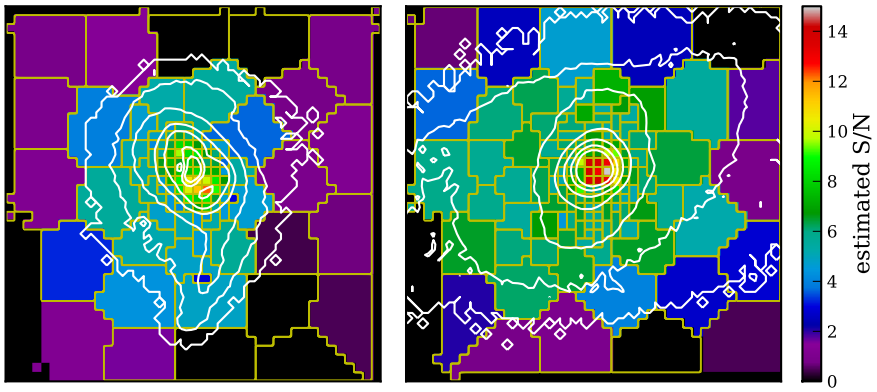

Fig. 4.6. Result of the Voronoi binning for the brightest host galaxies HE 1300−1325 (left panel) and HE 1338−1423 (right panel). The colour maps represent the estimated S/N of the host spectrum after binning of spaxels. The broad-band surface brightness distribution of the host is indicated by white contours.

For disc-dominated QSO hosts, the modelling of the stellar continuum could often be extended to a spatially resolved scheme. Because the S/N of the individual spaxels were in almost all cases still much below 10, we employed weighted Voronoi tesselations (Diehl & Statler 2006) , a generalisation of the Voronoi binning of Cappellari & Copin (2003), to perfrom an adaptive binning of the spaxels. Such an adaptive binning scheme was already applied successfully to the IFU data of the SAURON project (e.g. Emsellem et al. 2004; Sarzi et al. 2006; McDermid et al. 2006) and others (e.g. Gerssen et al. 2006; Chilingarian et al. 2007; Dumas et al. 2007; Pracy et al. 2009) for the same purpose. We estimated a S/N map directly from the data by measuring the mean and rms scatter in the rest-frame spectral window of 5500< λ <5700. This is a conservative S/N estimate due to presence of some weak absorption lines in that wavelength range. We chose a target S/N of 10 and a maximum number of 50 spaxels per bin for the weighted Voronoi algorithms. Due to the limitation in the number of binned spaxels we did not reach a S/N of 10 for all bins, but we thus avoided unintentional mixing of emission from physically unrelated regions. Two examples of the resulting S/N map after binning are shown in Fig. 4.6. After the binning, we again modelled the co-added stellar continuum of each bin with STARLIGHT as described above for the integrated spectra. Because the seeing often changed between the observations of different instrumental setups, the absolute continuum flux level for small bins (e.g. a single spaxel) may not necessarily be the same for the consecutive spectra. We therefore normalised the spectra of the two instrumental setups to match in the overlapping spectral region before combination.

Pure emission-line datacubes were subsequently created by subtracting the best-fit SSP continuum model either spatially resolved or based on the model of the integrated spectrum. The corresponding continuum model was scaled in absolute flux before subtraction to match that of each individual spaxel. When less than 5 bins had a S/N in the continuum greater than 7, we decided to use only the model of the integrated spectrum as a global continuum template spectrum for all spaxels instead of the spatially resolved models. For a few objects, mainly those observed with 0.″33 spatial resolution, no significant stellar continuum light could be recovered and no continuum was subtracted. Table 4.3 indicates which of this three schemes were applied to a specific object. We repeated the process for our 50 Monte Carlo realisation, previously constructed for the QSO-host deblending process, to generate 50 pure emission-line datacubes representing the additional uncertainties due to the continuum subtraction.

4.5.2. Narrow-band images

After removing the QSO emission and the underlying stellar continuum, we extracted 20Å wide narrow-band images (Fig. 4.7, left panel) from the datacubes centred on the strongest emission lines, Hα (or Hβ in the case of HE 1335−0847) and [O III] λ5007 (hereafter [O III]), to characterise the spatial distribution of the ionised gas. These images reveal the presence of extended ionised gas in almost all QSO host galaxies.

The Hα image of HE 1338−1423 shows strong residuals close to the nucleus. Apparently, the QSO-host deblending partially failed for the HR orange observation of this object. The broad Hα emission line of the QSO is rather narrow ($\sim$ 1600 km/s) and the extended [N II] $\lambda\lambda$6548, 6583 and Hα emission lines are quite bright for this nearby galaxy. In the deblending process it was thus impossible to define spectral windows covering parts of the broad Hα line without any contamination of extended emission, so that some oversubtraction occurred at those spaxels.

In comparison with the broad-band continuum images, in particular with the high-resolution HST images, we found that the Hα emission in most cases tracks very nicely the substructures in the morphology of the hosts. For example, the high surface brightness knots in the HST ACS F606W broad-band images of HE 1043−1346 and HE 1239−2426 seen along the spiral arm and close to the nucleus coincide with the observed pattern of strong Hα emission. Such regions presumably represent ongoing massive star forming regions in the host galaxies.

Furthermore, the distribution in the ionised gas, traced by the Hα and [O III] lines, is usually consistent with each other, which might already indicate that the ionisation mechanisms of the gas throughout the galaxy is the same. In a few galaxies the [O III] emission is rather weak or even undetected compared to Hα (e.g. HE 1239−2426) as typical for high metallicity H II regions or due to severe dust extinction. HE 0952−1552 and HE 1254−0934, on the other hand, display quite different light distributions in Hα and [O III] which presumably points at significant changes in the properties of the ISM across the galaxy.

4.5.3. Spectral analysis of specific regions

In order to investigate the physical conditions of the ISM in more detail, the fluxes of weaker emission lines, such as Hβ, [N II] $\lambda\lambda$6548, 6583 and [S II] $\lambda\lambda$6716, 6731, need to be measured. However, those lines were usually too weak to be detected in individual spaxels, except for a few objects, which calls for spatial binning of specific regions to increase the S/N. We manually defined several apertures (marked as black regions in

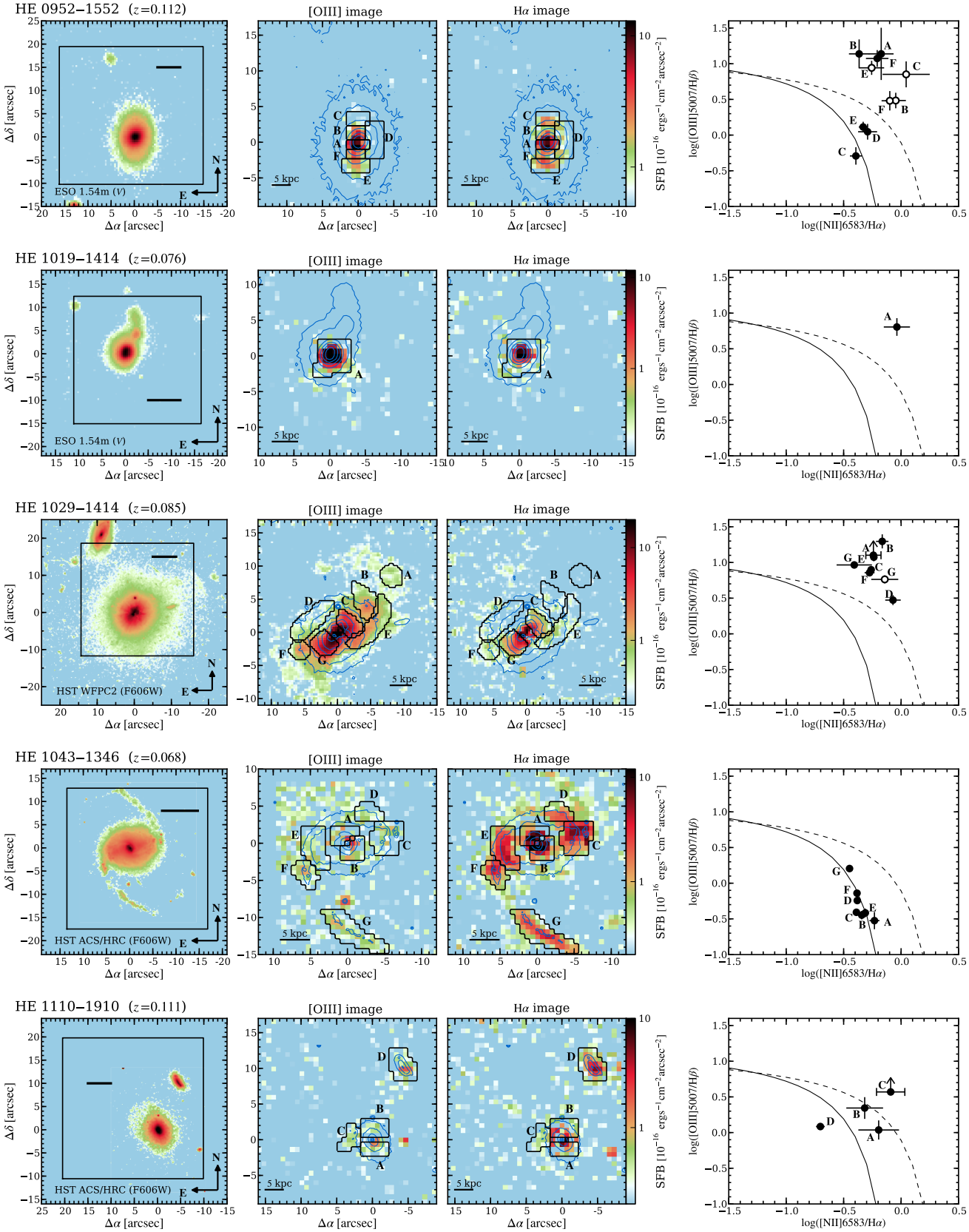

Fig. 4.7. Sample overview of the emission-line characteristics. *Left panel:* QSO subtracted broad-band images of the host galaxies with the VIMOS field of view indicated by the rectangle. The black scale bar correspond to 10 kpc at the redshift of the QSO. *Mid panel:* QSO and continuum subtracted [O III] and Hα narrow-band images in a logarithmic scaling. Apertures of specific regions are indicated by the black border lines and labelled alphabetically. Countours of the host SFB profile are overplotted in blue to aid direct comparison. *Right panel:* Standard BPT diagram for the individual regions that are labelled accordingly. A second kinematic system of emission-lines are indicated by the open symbols if present. Demarcation curves are shown as described in Fig. 4.9 in more detail.

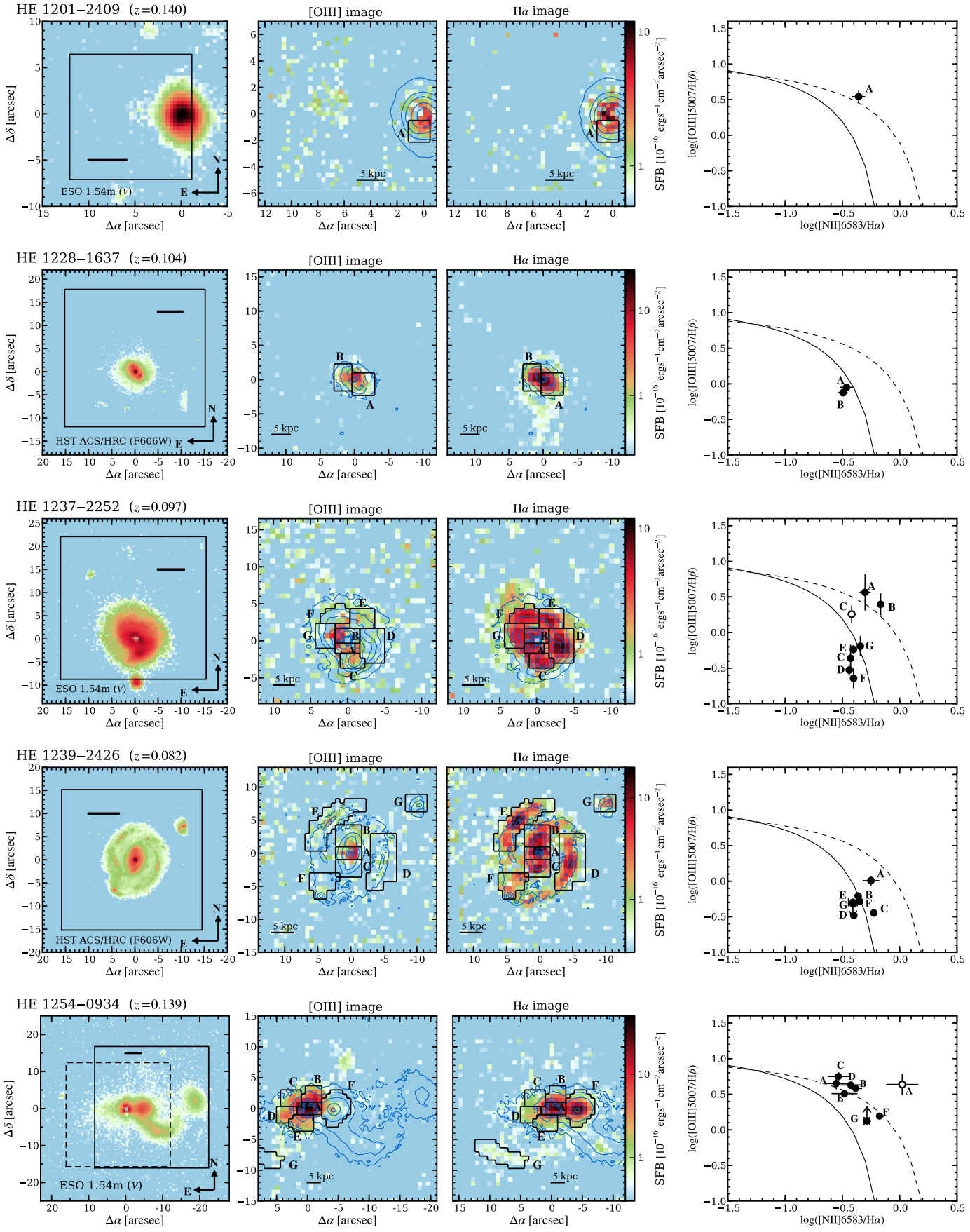

Fig. 4.7. Continued. In the case of HE 1254−0934, the HR orange (solid line) and the HR red (dashed line) observations have slightly different field of views with a substantial overlap.

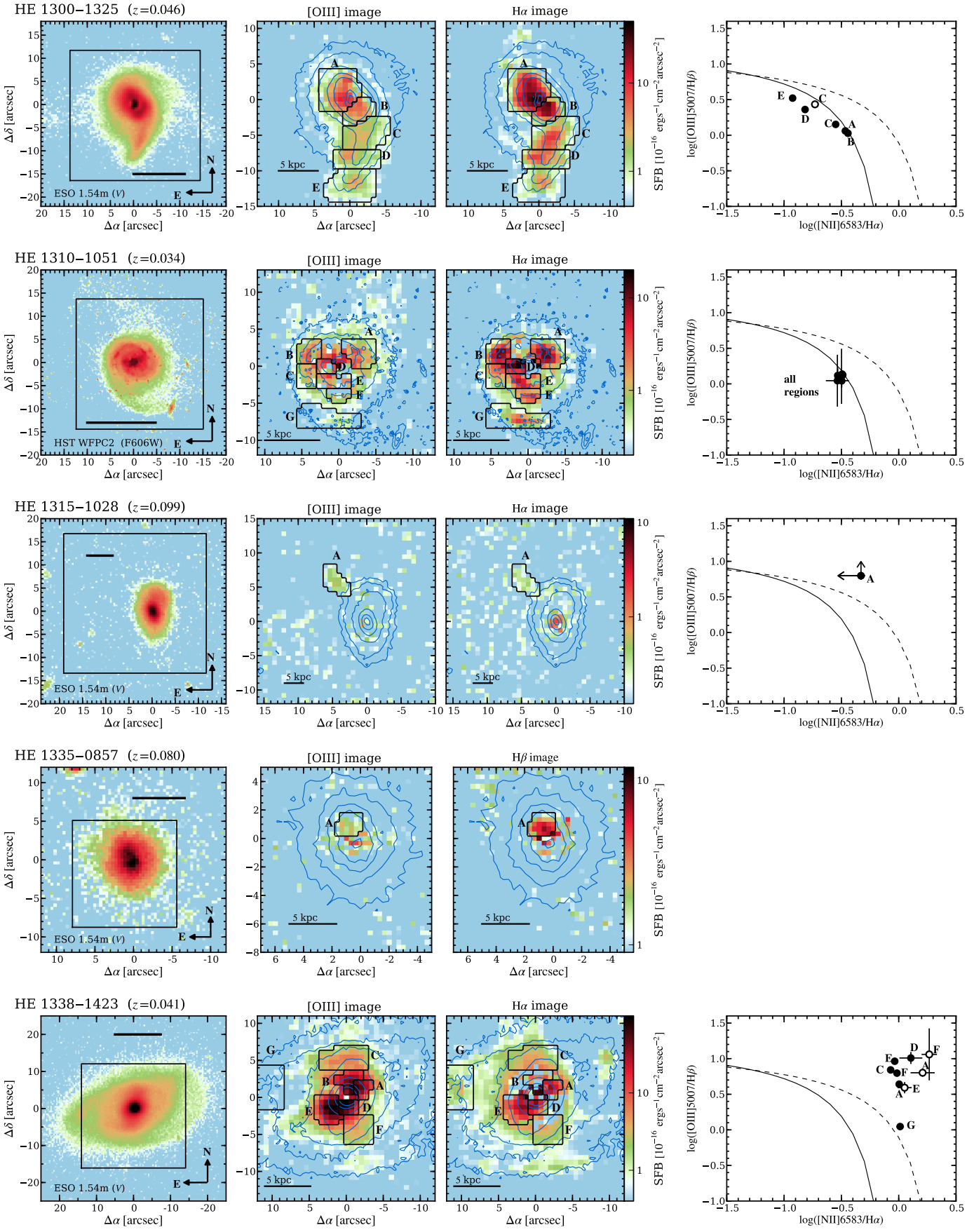

Fig. 4.7. continued.

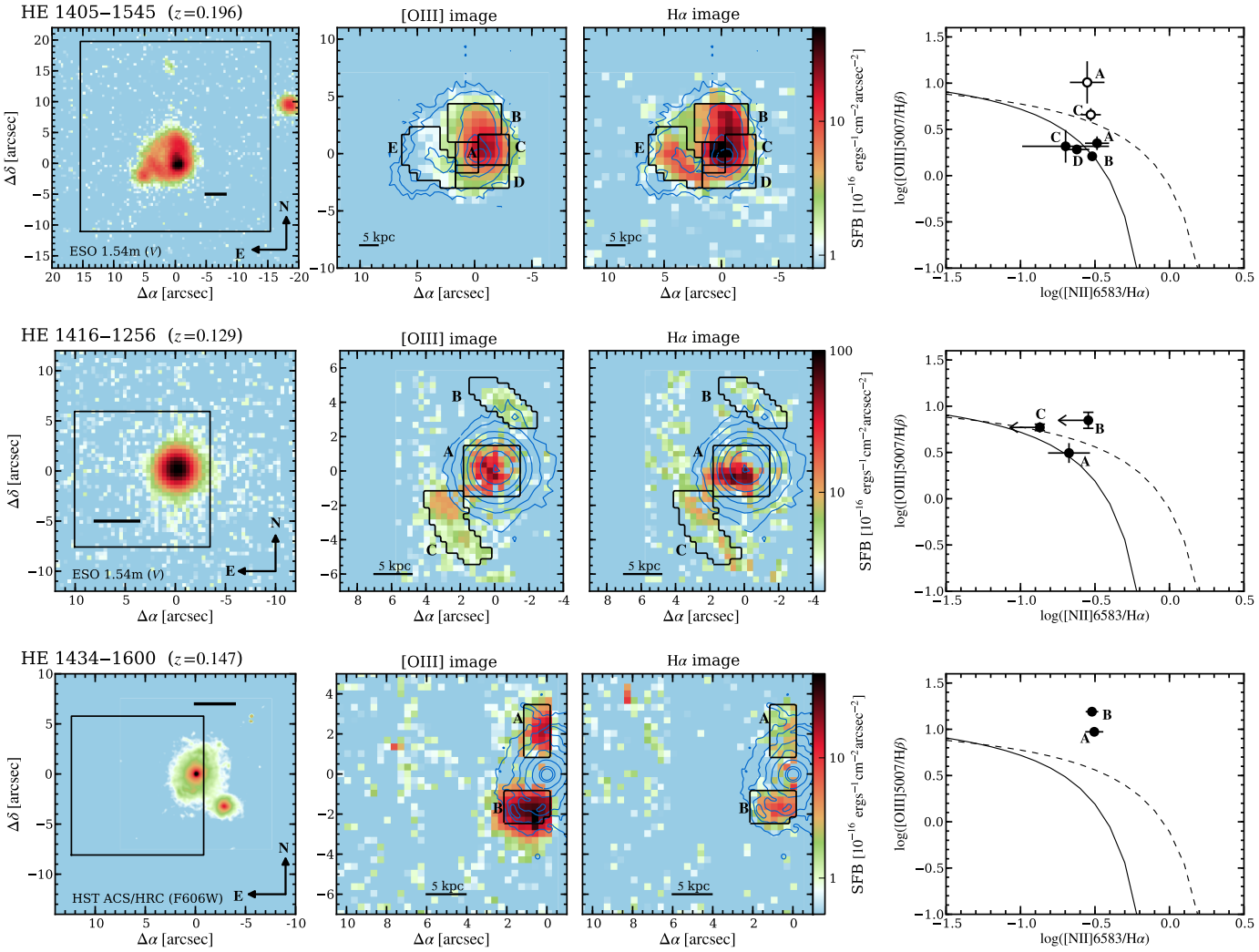

Fig. 4.7. Continued.

Fig. 4.7), each covering a physically connected region as judged from the Hα or [O III] light distribution.

We then modelled the emission-lines in the co-added spectrum of each aperture with simple Gaussians. Line ratios of the [O III] $\lambda\lambda$4960, 5007 and [N II] $\lambda\lambda$6548, 6583 doublets were fixed to their theoretical values. All emission lines, Hβ, [O III] $\lambda\lambda$4960, 5007, Hα, [N II] $\lambda\lambda$6548, 6583 and [S II] $\lambda\lambda$6716, 6731 were modelled simultaneously, and their line dispersions and redshifts were coupled to common values. This approach strongly reduced the number of free parameters and increased the accuracy of the model. To find the parameters of the best-fitting model we used a downhill simplex algorithms to search for the minimum χ^2.

With a spectral resolution of $\lambda/\Delta\lambda \sim 2500$, corresponding to a FWHM ~100 km/s, we were able to resolve emission line systems with different kinematic components. This is important to disentangle the emission of companion galaxies, within the same sightline to a host galaxy, or for detecting outflows/inflows associated with mergers, star formation, or AGN activity. In Fig. 4.8 we show two examples of the spectral emission line modelling that required two different emission line systems.

The measured emission line fluxes of Hβ, [O III], Hα, [N II], [S II]λ6716 and [S II]λ6731 are given in Table 4.4. We also provide measurements of the FWHM of the emission lines and the radial velocity with respect to the systemic velocity of the host galaxy for each defined spectral region. The quoted errors were derived from the 50 Monte-Carlo realisations of the datacubes analysed in the same way . In this way we included the random uncertainties of the QSO-host deblending and of the continuum subtraction into the error budget of the emission line measurements. We inferred 3σ upper limits for undetected Hβ, [O III] or [N II] lines based on the noise from the adjacent continuum and the width of the line constrained from the other detected lines.

4.6. Emission-line diagnostics

4.6.1. Separating H II regions from AGN ionisation

Emission line diagnostic diagrams are a powerful tool to constrain the ionising source of the ionised gas-phase of galaxies (e.g Baldwin et al. 1981; Veilleux & Osterbrock 1987). The most commonly used one is the [O III]λ5007/Hβ vs. [N II]λ6582/Hα diagram, often referred to as the BPT diagram. It involves only the brightest nebular emission lines in the rest-frame optical wavelength regime for which the line ratios are most insensitive to reddening.

Table 4.4. Results of the emission-line measurements

Object + Region		r [kpc]	Hβ	[O III] λ5007	Hα	[N II] λ6583	[S II] λ6716	[S II] λ6716	$v_{\rm rad}$	FWHM
					$[10^{-16}$ erg s^{-1} cm$^{-2}]$				[km s^{-1}]	[km s^{-1}]
HE 0952−1552	A	1.9	1.5 ± 1.2	20.4 ± 2.2	19.1 ± 3.0	12.8 ± 2.5	...	...	−21 ± 19	357 ± 30
	B	2.3	0.6 ± 0.3	7.6 ± 0.4	3.5 ± 0.3	1.5 ± 0.3	...	...	−76 ± 18	104 ± 12
			1.9 ± 0.4	5.8 ± 0.6	7.4 ± 1.1	6.6 ± 1.0	...	...	146 ± 20	295 ± 21
	C	6.3	1.1 ± 0.1	0.6 ± 0.2	5.4 ± 0.3	2.2 ± 0.2	...	...	194 ± 17	121 ± 11
			0.3 ± 0.1	2.0 ± 0.2	0.6 ± 0.2	0.7 ± 0.2	...	...	−38 ± 18	95 ± 25
	D	4.9	2.1 ± 0.3	2.3 ± 0.5	7.1 ± 0.8	3.6 ± 0.6	...	...	20 ± 18	343 ± 27
	E	6.4	1.2 ± 0.2	1.6 ± 0.2	6.6 ± 0.3	3.1 ± 0.2	...	...	−204 ± 17	121 ± 11
			0.7 ± 0.2	6.1 ± 0.3	2.6 ± 0.3	1.4 ± 0.3	...	...	8 ± 19	212 ± 10
	F	3.6	0.4 ± 0.1	4.6 ± 0.2	1.6 ± 0.2	1.0 ± 0.2	...	...	58 ± 19	188 ± 8
			0.6 ± 0.2	1.9 ± 0.3	3.3 ± 0.4	2.6 ± 0.3	...	...	−163 ± 19	222 ± 15
HE 1019−1414	A	1.6	23.5 ± 6.3	150.4 ± 14.8	55.1 ± 12.2	50.6 ± 7.1	...	...	−23 ± 25	314 ± 19
HE 1029−1401	A	18.8	< 0.4	5.4 ± 0.1	1.7 ± 0.1	1.0 ± 0.1	...	...	16 ± 15	86 ± 13
	B	9.6	0.9 ± 0.2	17.6 ± 0.3	3.8 ± 0.2	2.6 ± 0.3	...	...	−15 ± 14	135 ± 8
	C	2.9	6.5 ± 0.2	51.3 ± 0.3	19.6 ± 0.3	10.7 ± 0.3	4.2 ± 0.3	3.5 ± 0.3	−51 ± 13	157 ± 6
	D	6.9	2.6 ± 0.4	7.7 ± 0.5	4.4 ± 0.5	3.8 ± 0.4	...	...	7 ± 18	162 ± 19
	E	7.5	2.4 ± 0.3	29.0 ± 0.5	9.5 ± 0.4	5.5 ± 0.3	...	...	77 ± 14	145 ± 7
	F	9.8	1.1 ± 0.0	8.1 ± 0.1	3.4 ± 0.2	1.8 ± 0.2	...	...	108 ± 14	134 ± 7
	G	3.8	5.2 ± 0.4	47.7 ± 1.5	17.3 ± 3.1	6.8 ± 2.1	4.4 ± 1.1	4.1 ± 1.0	189 ± 13	86 ± 10
			4.7 ± 0.5	27.1 ± 1.6	13.2 ± 2.2	9.6 ± 2.0	2.6 ± 1.0	1.7 ± 0.8	112 ± 20	259 ± 9
HE 1043−1346	A	1.6	6.1 ± 0.6	1.8 ± 0.5	33.7 ± 2.0	19.7 ± 1.6	11.2 ± 0.8	6.9 ± 0.6	−160 ± 17	254 ± 11
	B	1.4	7.5 ± 0.7	2.7 ± 0.3	30.0 ± 1.1	13.6 ± 0.6	...	...	135 ± 16	216 ± 8
	C	7.5	7.2 ± 0.2	2.8 ± 0.1	31.2 ± 0.2	12.8 ± 0.1	5.3 ± 0.1	3.9 ± 0.1	40 ± 15	162 ± 5
	D	6.6	1.8 ± 0.1	1.0 ± 0.1	6.7 ± 0.1	2.8 ± 0.1	...	...	−71 ± 16	147 ± 6
	E	6.2	6.5 ± 0.4	2.5 ± 0.3	25.2 ± 0.3	12.3 ± 0.3	5.1 ± 0.2	3.7 ± 0.2	−66 ± 16	262 ± 5
	F	9.2	2.7 ± 0.1	2.0 ± 0.1	10.7 ± 0.1	4.4 ± 0.1	2.3 ± 0.1	1.6 ± 0.1	26 ± 18	104 ± 11
	G	16.3	3.8 ± 0.1	6.1 ± 0.2	20.7 ± 0.1	7.4 ± 0.1	4.4 ± 0.1	3.2 ± 0.1	118 ± 15	110 ± 9
HE 1110−1910	A	2.6	1.8 ± 0.4	2.0 ± 0.5	6.3 ± 1.7	4.0 ± 1.2	...	...	−149 ± 28	183 ± 48
	B	3.6	1.2 ± 0.4	2.7 ± 0.4	6.7 ± 1.4	3.2 ± 1.0	...	...	80 ± 26	164 ± 32
	C	6.1	< 0.6	2.4 ± 0.2	1.3 ± 0.2	1.0 ± 0.2	...	...	−26 ± 24	153 ± 27
	D	23.0	4.5 ± 0.3	5.5 ± 0.2	14.2 ± 0.3	2.8 ± 0.2	...	...	−326 ± 22	161 ± 7
HE 1201−2409	A	2.8	1.3 ± 0.3	4.6 ± 0.3	5.0 ± 0.3	2.2 ± 0.3	...	...	168 ± 11	130 ± 13
HE 1228−1637	A	2.3	25.2 ± 1.3	22.5 ± 1.2	84.9 ± 6.1	29.1 ± 3.4	...	...	−3 ± 20	181 ± 13
	B	2.6	20.9 ± 0.6	15.7 ± 0.6	64.8 ± 3.2	20.7 ± 1.7	...	...	−44 ± 19	148 ± 9
HE 1237−2252	A	2.2	0.7 ± 0.3	2.4 ± 0.8	7.0 ± 0.4	3.5 ± 0.3	...	...	107 ± 15	213 ± 15
	B	2.2	2.2 ± 0.5	5.4 ± 1.4	10.0 ± 0.4	6.8 ± 0.3	...	...	25 ± 15	239 ± 8
	C	5.3	1.3 ± 0.2	0.6 ± 0.2	6.5 ± 0.2	2.4 ± 0.2	...	...	150 ± 14	84 ± 12
			1.3 ± 0.3	2.4 ± 0.5	5.7 ± 0.2	2.2 ± 0.2	...	...	−131 ± 15	196 ± 10
	D	6.2	6.7 ± 0.2	2.0 ± 0.4	27.8 ± 0.3	10.1 ± 0.2	3.5 ± 0.1	1.9 ± 0.1	144 ± 13	120 ± 9
	E	6.1	3.4 ± 0.1	2.0 ± 0.3	13.3 ± 0.2	5.2 ± 0.1	2.5 ± 0.1	1.7 ± 0.1	29 ± 13	130 ± 8
	F	6.8	3.7 ± 0.2	0.8 ± 0.3	14.1 ± 0.2	5.6 ± 0.2	2.0 ± 0.2	1.6 ± 0.1	−64 ± 13	109 ± 8
	G	5.3	2.7 ± 0.2	1.7 ± 0.5	12.8 ± 0.3	5.8 ± 0.2	1.7 ± 0.1	1.6 ± 0.1	−22 ± 14	147 ± 7
HE 1239−2426	A	1.5	11.8 ± 1.5	12.0 ± 1.2	39.6 ± 4.3	22.2 ± 2.8	7.1 ± 0.5	6.5 ± 0.5	−34 ± 17	303 ± 21
	B	4.0	8.7 ± 0.5	5.4 ± 0.3	32.3 ± 1.0	14.0 ± 0.5	4.7 ± 0.2	4.2 ± 0.2	79 ± 16	175 ± 8
	C	3.6	6.2 ± 0.4	2.2 ± 0.2	24.4 ± 0.6	14.5 ± 0.7	3.9 ± 0.2	3.2 ± 0.1	−124 ± 16	134 ± 9
	D	8.0	9.7 ± 0.6	3.2 ± 0.3	45.4 ± 0.5	18.0 ± 0.4	6.2 ± 0.3	4.9 ± 0.3	13 ± 16	146 ± 7
	E	9.5	16.5 ± 0.4	7.9 ± 0.4	60.3 ± 0.7	23.7 ± 0.4	9.6 ± 0.3	9.7 ± 0.3	37 ± 16	186 ± 6
	F	9.5	4.0 ± 0.2	2.1 ± 0.1	13.9 ± 0.3	6.2 ± 0.2	3.3 ± 0.1	2.0 ± 0.1	−132 ± 16	79 ± 13
	G	19.9	1.6 ± 0.3	< 0.8	7.4 ± 0.3	2.9 ± 0.2	1.5 ± 0.2	0.8 ± 0.2	79 ± 17	114 ± 11
HE 1254−0934	A	2.7	24.6 ± 4.0	109.9 ± 10.3	83.0 ± 6.5	23.2 ± 4.8	15.4 ± 3.2	18.4 ± 2.8	−136 ± 23	351 ± 13
			14.5 ± 4.4	62.9 ± 10.0	31.2 ± 6.9	32.8 ± 7.7	7.6 ± 2.6	7.0 ± 2.8	−386 ± 83	977 ± 150
	B	4.8	11.3 ± 0.9	42.9 ± 1.5	22.3 ± 1.2	9.2 ± 1.1	6.7 ± 0.8	4.2 ± 0.3	−161 ± 21	457 ± 9
	C	6.3	4.7 ± 0.6	26.3 ± 0.8	12.6 ± 0.9	3.7 ± 0.7	...	...	−229 ± 22	584 ± 12
	D	7.9	5.3 ± 0.4	22.5 ± 0.6	13.3 ± 1.0	5.0 ± 0.9	...	...	−218 ± 25	690 ± 16
	E	5.3	9.3 ± 1.1	29.8 ± 1.5	19.0 ± 1.8	6.3 ± 1.5	...	...	−192 ± 23	626 ± 16
	F	10.5	11.7 ± 1.0	18.2 ± 0.8	128.0 ± 1.1	85.2 ± 1.0	32.7 ± 0.6	28.0 ± 0.6	−38 ± 19	427 ± 3
	H	24.7	< 0.6	0.8 ± 0.1	3.4 ± 0.1	1.8 ± 0.1	...	...	9 ± 20	92 ± 11
HE 1300−1325	A	1.8	80.6 ± 1.6	92.6 ± 4.3	302.7 ± 6.7	103.6 ± 4.6	71.1 ± 1.1	50.5 ± 0.8	110 ± 15	158 ± 8
	B	1.8	33.3 ± 0.6	35.5 ± 0.8	123.6 ± 1.4	44.6 ± 1.2	33.8 ± 0.8	24.0 ± 0.8	−114 ± 15	179 ± 6
	C	5.2	11.5 ± 0.2	16.2 ± 0.2	42.3 ± 0.3	11.9 ± 0.2	10.3 ± 0.1	6.8 ± 0.1	−111 ± 15	112 ± 10
			11.8 ± 0.2	32.2 ± 0.4	35.8 ± 0.2	6.7 ± 0.2	11.7 ± 0.1	7.4 ± 0.1	45 ± 15	103 ± 10
	D	7.7	13.7 ± 0.1	31.5 ± 0.1	54.5 ± 0.3	8.3 ± 0.1	13.1 ± 0.1	8.8 ± 0.1	93 ± 15	83 ± 13
	E	10.9	12.1 ± 0.2	40.3 ± 0.2	36.4 ± 0.2	4.3 ± 0.1	8.9 ± 0.1	6.2 ± 0.1	154 ± 15	78 ± 14
HE 1310−1051	A	2.1	17.5 ± 1.3	23.0 ± 5.4	63.1 ± 1.0	18.5 ± 0.5	8.0 ± 0.3	8.2 ± 0.3	30 ± 15	116 ± 10
	B	2.9	13.0 ± 0.4	16.0 ± 1.3	49.5 ± 0.4	14.8 ± 0.2	9.5 ± 0.2	6.8 ± 0.1	−99 ± 14	77 ± 15
	C	2.9	6.0 ± 0.3	8.2 ± 0.9	15.6 ± 0.3	5.0 ± 0.2	3.2 ± 0.1	2.6 ± 0.1	−73 ± 15	109 ± 11
	D	1.2	11.0 ± 2.2	12.2 ± 9.9	41.7 ± 5.0	12.2 ± 2.4	7.8 ± 0.9	6.0 ± 1.1	−88 ± 17	120 ± 24
	E	1.7	8.4 ± 2.1	10.7 ± 9.2	30.8 ± 1.1	9.8 ± 0.6	6.2 ± 0.7	4.3 ± 0.7	6 ± 16	126 ± 11
	F	2.8	3.3 ± 0.2	3.6 ± 0.8	13.6 ± 0.3	4.3 ± 0.1	3.2 ± 0.1	2.3 ± 0.1	48 ± 14	94 ± 13
	G	5.0	4.6 ± 0.2	6.2 ± 0.1	18.7 ± 0.2	6.1 ± 0.2	2.9 ± 0.2	2.3 ± 0.2	35 ± 14	101 ± 12
HE 1315−1028	A	13.4	< 0.7	4.7 ± 0.1	1.6 ± 0.1	< 0.7	...	...	−52 ± 23	98 ± 10

Table 4.4. Continued.

Object + Region		r [kpc]	Hβ	[O III] λ5007	Hα	[N II] λ6583	[S II] λ6716	[S II] λ6716	v_{rad} [km s^{-1}]	FWHM [km s^{-1}]
					[10^{-16} erg s^{-1} cm^{-2}]					
HE 1338−1423	A	2.1	18.3 ± 0.7	80.3 ± 1.6	47.8 ± 1.4	48.3 ± 1.3	26.4 ± 0.8	18.7 ± 1.1	145 ± 13	194 ± 7
			19.8 ± 2.4	125.3 ± 3.3	38.1 ± 8.4	61.5 ± 6.3	45.2 ± 1.3	36.3 ± 1.2	−121 ± 19	683 ± 7
	B	0.7	15.4 ± 1.5	69.3 ± 3.3	...	...	26.2 ± 1.6	16.7 ± 1.3	9 ± 14	179 ± 9
			21.2 ± 5.1	201.3 ± 8.3	...	...	42.8 ± 1.4	33.7 ± 1.4	−290 ± 20	448 ± 15
	C	4.4	11.0 ± 0.9	76.6 ± 1.7	40.2 ± 0.5	34.2 ± 0.3	9.8 ± 0.2	6.1 ± 0.2	7 ± 12	180 ± 6
	D	1.1	33.6 ± 6.5	343.2 ± 6.8	99.3 ± 20.6	126.8 ± 12.6	64.9 ± 2.0	54.1 ± 1.9	−48 ± 14	612 ± 9
	E	2.1	39.0 ± 1.9	358.6 ± 8.1	125.1 ± 4.5	115.4 ± 5.0	46.1 ± 2.5	37.4 ± 2.0	−104 ± 13	228 ± 6
			40.3 ± 7.2	157.5 ± 6.5	87.4 ± 10.4	98.4 ± 7.5	53.8 ± 2.9	31.3 ± 3.5	4 ± 24	706 ± 22
	F	4.1	6.9 ± 0.5	43.1 ± 1.1	16.3 ± 0.9	15.7 ± 0.4	5.9 ± 0.4	4.9 ± 0.4	19 ± 13	134 ± 9
			2.8 ± 2.3	31.8 ± 1.2	11.9 ± 0.3	22.0 ± 3.4	11.1 ± 0.9	8.4 ± 0.8	36 ± 29	852 ± 68
	G	8.7	6.5 ± 0.4	7.2 ± 0.5	30.2 ± 0.6	31.0 ± 2.3	16.4 ± 0.7	12.9 ± 0.5	−221 ± 16	204 ± 11
HE 1405−1545	A	3.0	16.5 ± 2.4	37.0 ± 3.2	94.9 ± 7.6	31.0 ± 5.2	...	...	82 ± 35	206 ± 18
			0.5 ± 0.2	5.3 ± 2.0	50.7 ± 6.0	14.2 ± 3.4	...	...	−79 ± 38	158 ± 22
	B	9.3	44.7 ± 0.8	72.4 ± 0.7	160.0 ± 1.7	48.5 ± 1.4	22.5 ± 0.8	17.9 ± 0.8	121 ± 31	157 ± 5
	C	4.6	9.9 ± 3.0	20.5 ± 5.5	27.1 ± 10.0	5.4 ± 3.1	...	...	−47 ± 45	165 ± 15
			15.2 ± 2.2	69.5 ± 5.2	98.0 ± 10.4	29.0 ± 3.3	...	...	114 ± 32	127 ± 10
	D	6.7	16.3 ± 1.4	31.3 ± 1.2	37.6 ± 2.2	9.0 ± 1.7	...	...	−26 ± 34	308 ± 9
HE 1416−1256	A	4.4	37.1 ± 6.2	115.7 ± 21.0	159.8 ± 17.4	33.8 ± 10.3	...	...	−9 ± 6	237 ± 22
	B	18.2	2.6 ± 0.5	18.6 ± 0.7	9.1 ± 0.7	< 2.6	...	...	−59 ± 3	128 ± 11
	C	19.0	9.4 ± 0.7	55.6 ± 1.4	42.4 ± 1.0	< 5.7	...	...	−36 ± 2	133 ± 7
HE 1434−1600	A	5.6	2.8 ± 0.3	26.5 ± 0.9	5.3 ± 0.3	1.7 ± 0.2	...	...	−30 ± 4	114 ± 8
	B	5.7	6.4 ± 0.4	99.1 ± 2.1	20.6 ± 0.4	6.2 ± 0.6	...	...	170 ± 5	98 ± 10

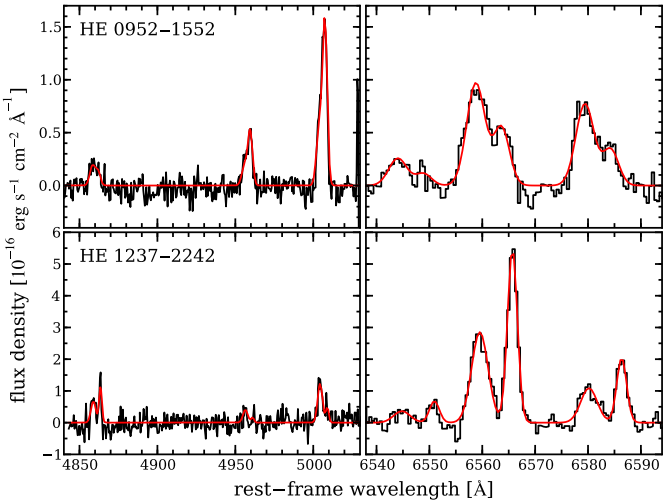

Fig. 4.8. Examples of the spectral modelling with two kinematically distinct emission-line systems. A spectrum of HE 0952−1552 (region F) is presented in the two top panels and a spectrum of HE 1237−2252 (region C) in the two bottom panels. The red line represents the best-fitting model consisting of Gaussians for the various emission lines that are kinematically coupled to represent two independent emission line systems.

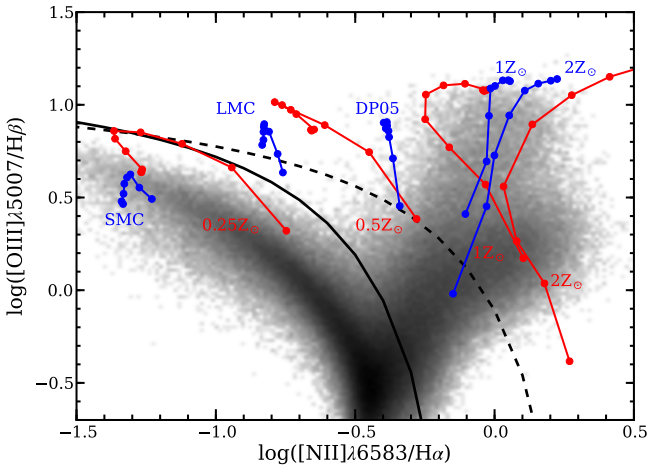

Fig. 4.9. Example of the standard BPT [O III]λ5007/Hβ vs. [N II]λ6583/Hα diagram constructed from more than 800 000 emission-line galaxies taken from the SDSS DR7 value-added MPA/JHU galaxy catalogue (grey scale). The Kauffmann et al. (2003) (black dashed line) and Kewley et al. (2001) (black solid line) demarcation curves are usually invoked to distinguish between star forming galaxies and AGN with an intermediate region in between. Tracks of the dusty radiation-pressure dominated photoionisation model by Groves et al. (2004) are shown in red for 4 different abundances in the range of $-3 < \log(U) < 0$ with $n_e = 100\,\mathrm{cm}^{-3}$ and an AGN spectral index of -1.4. Recent shock+precursor ionisation model tracks by Allen et al. (2008) are shown in blue for the abundances of the Small Magellanic Cloud (SMC), the Large Magellanic Cloud (LMC), of solar and super-solar metallicity, and the abundance set used by Dopita et al. (2005) (DP05). The shock velocity is increasing along each track from 300 km/s to 1000 km/s in steps of 100 km/s.

We show such a BPT diagram from more than 800 000 emission-line galaxies taken from the SDSS DR7 value-added MPA/JHU galaxy catalogue[6] (Fig. 4.9) in order to highlight the typical bimodal distribution of emission line ratios. As described in the Introduction, the branch on the left side of the diagram originates from H II regions powered by the ionising radiation of young OB stars in star forming regions, while the branch on the right side is usually attributed to ionisation by an AGN. Kewley et al. (2001) derived a boundary for the emission-line ratios up to which they could theoretically be produced by a massive starburst. An empirical boundary was drawn by Kauffmann et al. (2003) from the SDSS data to include all the galaxies in the apparent H II branch. These two demarcation curves have often been invoked to discriminate between pure star formation, dominant AGN photoionisation, and an intermediate region where both processes may significantly contribute to the ionisation.

[6] available at http://www.mpa-garching.mpg.de/SDSS/

However, line ratios in the intermediate region may also be produced entirely by a starburst, and line ratios in the AGN branch might also contain emission from H II regions as discussed by Cid Fernandes et al. (2010). In fact, region F of HE 1254−0934 is such an example which we will describe in detail later on. Besides AGN photoionisation, shocks generated by jet-cloud interactions and their precursors can be another source of ionisation that have been observed in AGN (e.g. Morganti et al. 1997; Clark et al. 1998; Villar-Martín et al. 1999; Moy & Rocca-Volmerange 2002; Rosario et al. 2010). Theoretical ionisation models for both processes can help to interpret the observed emission line ratios and to infer the dominant mechanisms. A few characteristic tracks of AGN dusty radiation-pressure photoionisation models as presented by Groves et al. (2004) and shock+precursor models by Allen et al. (2008) are shown in Fig. 4.9. For both processes the [O III]/Hβ ratio is increasing with ionisation parameter (U) or shock velocity, respectively, while the [N II]/Hα ratio is mainly linked to the metallicity of the gas. The expected line ratios of shock and photoionisation significantly overlap in several parts of this particular diagnostic diagram. Additional constrains, e.g. the FWHM of emission lines as a proxy for the shock velocity or the observed radio fluxes of the synchrotron radiation of the jet, will be required to judge whether shocks are likely to contribute to ionisation.

In Fig. 4.7 (right panel) we present the [O III]λ5007/Hβ vs. [N II]λ6583/Hα BPT diagrams for the objects in our sample. The diagnostic diagrams immediately reveal the quite diverse ionisation states of the ISM for the different host galaxies and even across a single galaxy.

For HE 1335−0847 the HR orange observation, covering the Hα and [N II] lines, is missing, so that we could not construct a BPT diagram for this object. Nevertheless, we obtained a low [O III]λ5007/Hβ line ratio of 0.3 (region A) which is consistent with an H II region only. In the case of HE 1315−1028, we found a faint extended emission-line region with no apparent counterpart in the continuum image. The ionisation source could not be unambiguously determined since only the [O III] and the Hα line could be detected leading to upper/lower limits in both line ratios. AGN ionisation or low-metallicity H II regions therefore remain possible scenarios.

We found clear evidence for ongoing star formation in 10 out of 18 host galaxies, marked by the presence of classical H II-like emission. In combination with the morphological classification, these numbers split up into 4/8 (50%) for bulge-dominated hosts, 5/8 (62.5%) for disc-dominated hosts and 1/2 (50%) for major-merger systems. If we assume that the emission-line ratios in the intermediate region of the BPT are at least partially caused by H II regions, the number of hosts with evidence for current star formation would increase by 3 objects including the second major-merger system. On the other hand, we found evidence for AGN photoionisation or shock ionisation by a jet also in 10 out of the 18 cases, which occurs in at least 3 hosts together with current star formation.

4.6.2. Dust-corrected star formation rates

Various common calibrations of the star formation rate (SFR) have been empirically determined based on the rest-frame UV luminosity, the radio luminosity at 1.4 GHz, the infrared luminosity, or the line luminosity of [O II] λ3727 or Hα. Here, we employed the Hα luminosity of H II regions to estimate the current SFR adopting the calibration of Kennicutt (1998),

$$\frac{\mathrm{SFR}}{\mathrm{M_\odot yr^{-1}}} = \frac{L(\mathrm{H}\alpha)}{1.26\times10^{41}\,\mathrm{erg\,s^{-1}}}\ . \tag{4.3}$$

Due to internal dust extinction, SFRs can be severely underestimated when based on the UV luminosity or the optical emission lines. In order to correct for this effect, we determined the reddening in the individual regions of the host galaxies from the observed Hα/Hβ Balmer decrement, theoretically predicted to be 2.86 at T_e = 10 000K (Osterbrock & Ferland 2006). Adopting a standard Milky way attenuation law for $A(\lambda)$ (Cardelli et al. 1989) with a mean value of R_V = 3.1, we computed the V band dust extinction (A_V) from the Balmer decrement as

$$A_V = \frac{\log\left(\mathrm{H}\alpha/\mathrm{H}\beta\right)_\mathrm{theo.} - \log\left(\mathrm{H}\alpha/\mathrm{H}\beta\right)_\mathrm{obs.}}{0.4(A(\mathrm{H}\alpha) - A(\mathrm{H}\beta))}\ . \tag{4.4}$$

In addition to the extinction in the individual regions, we also computed the variance weighted mean extinction (Table 4.5) from all regions of the host galaxy to allow a global comparison of the dust content between the different host galaxies and companions. We excluded HE 1110−1910, HE 1201−2409 and HE 1338−1423 as their estimated extinctions had an unacceptable large uncertainty. Since the Hα line could not be measured for HE 1335−0847 we only computed a lower limit to the SFR based on the Hβ luminosity assuming no extinction.

We found that the dust extinction is typically modest with $A_\mathrm{V} < 1.6$, but a very high extinction of $A_\mathrm{V} \sim 4.2$ was measured in the close companion/second nucleus (region F) of the ongoing major-merger system HE 1254−0934. A significant difference exists between the bulge and disc-dominated systems in general. The mean extinction for the bulge-dominated hosts ($\langle A_\mathrm{V}\rangle = 0.6$) is *on average only half* than that for the disc-dominated hosts ($\langle A_\mathrm{V}\rangle = 1.2$) in our sample.

The total Hα fluxes were measured by summing up all emission from H II-like regions (including the intermediate regions)

Table 4.5. Mean intrinsic extinctions

Object[a]	A_V[b]
HE 0952−1552	1.56 ± 0.25
HE 1029−1401	0.22 ± 0.09
HE 1043−1346	1.37 ± 0.06
HE 1110−1910 (c)	0.28 ± 0.21
HE 1228−1637	0.33 ± 0.15
HE 1237−2252	1.16 ± 0.08
HE 1237−2252 (c)	1.21 ± 0.75
HE 1239−2426	1.06 ± 0.07
HE 1239−2426 (c)	1.58 ± 0.28
HE 1254−0934	0.06 ± 0.20
HE 1254−0934 (F)	4.21 ± 0.27
HE 1300−1325	0.81 ± 0.04
HE 1300−1325 (c)	0.57 ± 0.03
HE 1310−1051	0.70 ± 0.08
HE 1405−1545	0.70 ± 0.06
HE 1416−1256	1.28 ± 0.67
HE 1434−1600	0.25 ± 0.19

Notes. [(a)] Companion galaxies are denoted with a (c) behind the name of the QSO host galaxy, otherwise the character in parenthesis correspond to specific region within the host galaxy. [(b)] Mean extinction averaged over all specific regions of the galaxies taking into account the individual uncertainties as weights.

Table 4.6. Extinction corrected Hα fluxes, luminosities, estimated SFRs and specific SFRs

Object[a]	$f(\mathrm{H}\alpha)^b$ $\left[10^{-16}\,\mathrm{erg\,cm^{-2}\,s^{-1}}\right]$	$f_{\mathrm{cor}}(\mathrm{H}\alpha)^c$ $\left[10^{-16}\,\mathrm{erg\,cm^{-2}\,s^{-1}}\right]$	$L_{\mathrm{cor}}(\mathrm{H}\alpha)^d$ $\left[\mathrm{erg\,s^{-1}}\right]$	SFR[e] $\left[\mathrm{M_\odot\,yr^{-1}}\right]$	log sSFR[f] $\left[\mathrm{yr^{-1}}\right]$
HE 0952−1552	19.0 ± 2.0	58 ± 17	41.25 ± 0.15	1.4 ± 0.4	−11.0 ± 0.3
HE 1043−1346	157.8 ± 8.3	491 ± 59	41.74 ± 0.05	4.3 ± 0.5	−10.2 ± 0.4
HE 1110−1910 (c)	14.3 ± 1.7	17 ± 3	40.74 ± 0.09	0.4 ± 0.1	...
HE 1228−1637	149.9 ± 17.5	203 ± 38	41.74 ± 0.09	4.3 ± 0.8	−10.2 ± 0.3
HE 1237−2252	74.5 ± 4.1	187 ± 19	41.64 ± 0.04	3.5 ± 0.3	−10.6 ± 0.2
HE 1237−2252 (c)	6.5 ± 0.8	23 ± 9	40.74 ± 0.22	0.4 ± 0.2	...
HE 1239−2426	215.9 ± 13.1	442 ± 45	41.87 ± 0.04	5.8 ± 0.6	−10.4 ± 0.2
HE 1239−2426 (c)	7.4 ± 1.0	23 ± 20	40.63 ± 0.39	0.3 ± 0.2	...
HE 1254−0934	128.0 ± 14.0	3025 ± 770	43.19 ± 0.12	123.9 ± 31.5	−9.1 ± 0.2
HE 1300−1325	601.0 ± 39.8	1115 ± 87	41.76 ± 0.03	4.6 ± 0.4	−10.1 ± 0.4
HE 1310−1051	214.1 ± 13.7	373 ± 1101	41.39 ± 0.47	1.9 ± 1.6	−9.9 ± 0.4
HE 1335−0847	> 24.0	> 24	> 40.58	> 0.3	> −11.0
HE 1405−1545	199.4 ± 17.5	529 ± 232	42.75 ± 0.26	45.2 ± 19.1	−9.6 ± 0.4
HE 1416−1256	151.7 ± 30.5	376 ± 291	42.26 ± 0.41	14.4 ± 8.6	−9.3 ± 0.4

Notes. [(a)] Companion galaxies are denoted with a (c) behind the name of the corresponding QSO. [(b)] Integrated Hα flux of all H II-like and intermediate region of a galaxy. [(c)] Extinction corrected Hα flux [(d)] Extinction corrected Hα luminosity [(e)] SFR estimated from the extinction corrected Hα luminosity following Kennicutt (1998). [(f)] Specific SFR were computed with the SED based stellar masses (see Table 4.1). No stellar mass estimates are currently available for the companion galaxies.

for each host galaxy. From the dust-corrected Hα luminosities we estimated the SFRs with Eq. 4.3 and computed the specific SFRs (sSFR $\equiv$ SFR/M_*) using SED-based estimates of M_* for our host galaxies. All values are listed in Table 4.6. Although the dust correction increases the uncertainty for the estimated SFRs significantly, the SFRs of our AGN host galaxies typically range between $1\,\mathrm{M_\odot\,yr^{-1}}$ and $10\,\mathrm{M_\odot\,yr^{-1}}$. However, we know that the SFR is correlated with stellar mass, so that the sSFR is almost constant for the bulk population of disc-dominated galaxies. The peak in the distribution was found at $\log(\mathrm{sSFR/yr^{-1}}) = -10.2 \pm 0.3$ for galaxies with stellar masses of $10.5 < \log(M_*/\mathrm{M_\odot}) < 11.3$ (Brinchmann et al. 2004). The specific SFRs of several disc-dominated AGN hosts with signatures for ongoing star formation are consistent with that value within the errors. On the other hand, in four of our disc-dominated galaxies, HE 0952−1552, HE 1019−1414, HE 1315−1028, and HE 1338−1423, the sSFR is low and H II regions are weak or even undetected. That we find no ongoing star formation in most of the bulge-dominated galaxies may not be surprising, since the sSFRs of inactive bulge-dominated galaxies are intrinsically wide-spread over 2 orders of magnitude with a much less pronounced peak around sSFR ~ -11 (Brinchmann et al. 2004).

Whether the low SFRs for a few objects are caused by AGN feedback or by an intrinsically low molecular gas content is something we cannot address with this dataset alone without information on the molecular gas content. Only HE 1310−1051 and HE 1338−1423 are part of a QSO sample observed with the IRAM 30m telescope to detect the molecular CO emission (Bertram et al. 2007), but only upper limits on the molecular gas mass could be inferred. We hope that the Atacama Large Millimeter Array (ALMA) will provide some of the required complementary information in the future. To reconstruct the recent SF history of the host galaxies is beyond the scope of this work. For example, it could be that the SFRs are currently declining and peaked prior to the luminous QSO phase as suggested by Schawinski et al. (2010a). Clearly, a more detailed analysis of this issue is needed to address these questions, which will be discussed in conjunction with the stellar populations of our QSO hosts in the companion PhD thesis by Dading Nugroho

We emphasise that the SF happens in a single region with a diameter of 5 kpc located ∼10 kpc to the east from the AGN. The emission-line ratios of this region F place it just below the Kewley et al. demarcation curve in the intermediate region of the BPT diagram that would usually be interpreted as a mix of an AGN and H II regions. A contamination by the neighbouring QSO can be excluded due to its large separation. The massive starburst implied by the Hα luminosity, however, is in agreement with line ratios close to the Kewley et al. (2001) maximum starburst curve. Furthermore, the high dust extinction in this region agrees very well with the estimated SFR considering the empirical relation between SFR and dust extinction (e.g. Hopkins et al. 2001; Sullivan et al. 2001). A faint arc-like structure is detected in Hα ∼30 kpc south-east of the QSO (Region G), which does not correspond to any structure in the ground-based continuum images. It remains open whether this feature is a signature of a galactic superwind (driven either by the starburst or AGN) or of star formation along a tidal arm.

4.6.3. Evidence for jet-cloud interactions and shock ionisation?

We identified three objects in which shock ionisation may contribute to the gas ionisation as revealed by the presence of broad extended emission lines. These three candidates are HE 0952−1552 (∼300 km/s FWHM), HE 1254−0934 (∼600 km/s FWHM) and HE 1338−1423 (400 km/s < FWHM < 900 km/s), for which the line ratios are consistent with the shock+precursor ionisation models.

Additionally, HE 0952−1552 and HE 1254−0934 display enhanced radio emission with $L_{1.4\mathrm{GHz}} > 10^{23}\,\mathrm{WHz^{-1}}$, that could be further evidence for a low-power radio-jet on kpc scales. However, we need to check whether SF, which also produces radio emission (e.g. Condon 1992), is able to account for the observed radio emission alone, in particular for HE 1254−0934 with its ongoing starburst. Here, we adopt the conversion of the 1.4 GHz luminosity to ongoing SFR,

$$\frac{\mathrm{SFR}}{\mathrm{M_\odot yr^{-1}}} = 5.52 \times 10^{-22} L_{1.4\mathrm{GHz}}\,, \tag{4.5}$$

as determined by Bell et al. (2003) valid only for $L_{1.4\mathrm{GHz}} > 6.4 \times 10^{21}\,\mathrm{WHz}^{-1}$. The estimated SFRs for HE 0952−1552 and HE 1254−0934 correspond to radio luminosities of $2.5 \times 10^{21}\,\mathrm{WHz}^{-1}$ and $2.3 \times 10^{23}\,\mathrm{WHz}^{-1}$, respectively. These radio luminosities are smaller by at least 0.5 dex than actually observed, so that unresolved radio emission from the AGN or of an extended jet need to contribute to the emission at least in these two sources.

HE 0952−1552 is an interesting object in this respect as the elongated and almost linear distribution of [O III] emission in North-South direction might indicate the orientation of a putative radio jet. Jahnke et al. (2007) already speculated about an outflow in this object based on the intriguing kinematics of the ionised gas seen in their long-slit spectra. On the other hand, regions C, D and E are confirmed to be star forming H II regions distributed in a rotating ring around the galaxy centre (see Appendix D for the kinematic maps). As the candidate jet-cloud interactions appear to happen within the ring of ongoing SF, a scenario of jet induced star formation could in principle be possible. However, since the exact orientation of the jet with respect to the plane of the star forming ring is unknown it appears more likely that this is simply a projection effect and the jet may in fact be oriented almost perpendicular to that plane.

HE 1338−1423 has a radio luminosity almost an order of magnitude lower compared to the other two candidates for jet-cloud interactions. It is one of the nearest objects in the sample so that we could resolve structures on 500 pc scales. Radio surveys of local Seyfert galaxies (e.g. Ho & Ulvestad 2001) found radio emission typically extended over ∼1–4 kpc even at integrated radio luminosities of $L_{1.4\,\mathrm{GHz}} < 10^{22}\,\mathrm{W\,Hz}^{-1}$. Unless the radio luminosity of HE 1338−1423 is severely contaminated by nuclear SF, the observed spatial scale of the extended broad emission lines would match with the typical sizes of extended radio emission in local Seyferts. In turn this means, that we would most likely be unable to spatially resolve the small-scale jet-cloud interactions directly in the other QSO hosts of the sample with a similar or lower radio luminosity because they are at least two times more distant.

In any case, follow-up high-resolution radio observations of our sample will be required to clearly identify extended low-power radio-jets and their spatial orientation with respect to the ionised gas.

4.7. Gas-phase metallicities

4.7.1. Estimating gas-phase oxygen abundances

H II regions

Element abundances of H II regions can be estimated from various empirically calibrated emission-line ratios of strong lines, the so-called strong-line method. Commonly used strong-line calibrations are the R_{23} index (e.g. Pagel et al. 1979; Edmunds & Pagel 1984; Dopita & Evans 1986; Pilyugin 2001; Pilyugin & Thuan 2005), the N2 index (Storchi-Bergmann et al. 1994; Denicoló et al. 2002; Pettini & Pagel 2004) and the O3N2 index (Alloin et al. 1979; Pettini & Pagel 2004). Since the [O II] λ3727 is not covered with the wavelength range of our observations, we cannot compute the R_{23} index. The N2 index is based only on the [N II] and Hα lines, but is not very sensitive at high metallicities. We thus decided to use the O3N2 index, defined as

$$12 + \log(\mathrm{O/H}) = 8.73 - 0.32 \log\left(\frac{[\mathrm{O\,III}]\lambda 5007/\mathrm{H}\beta}{[\mathrm{N\,II}]\lambda 6583/\mathrm{H}\alpha}\right) \quad (4.6)$$

by Pettini & Pagel (2004), as the best oxygen abundance calibrator for our available set of emission lines. The systematic uncertainty of ∼0.2 dex for this calibration is significantly larger than most of the other methods, because the ionisation parameter cannot be taken into account. On the other hand, it has the advantage of being single-valued in contrast to the R_{23} index.

All estimated oxygen abundances need to be used with care as every method has its strength and weaknesses, which are still heavily debated in the literature (e.g. Pagel et al. 1980; Kennicutt & Garnett 1996; Kewley & Dopita 2002; Pérez-Montero & Díaz 2005; Kewley & Ellison 2008). Comparing oxygen abundances obtained with different calibrations revealed large systematic offsets up to 0.5 dex in log(O/H) (Liang et al. 2006; Kewley & Ellison 2008). Transformations between the different calibrations, in particular with the O3N2 index, were therefore determined by Kewley & Ellison (2008). They compared the stellar mass-metallicity relation of galaxies for a variety of oxygen abundance calibrations and provided 4th order polynomial conversion functions between them. We decided to match our O3N2 oxygen abundance to the calibration adopted by Tremonti et al. (2004), who used the CLOUDY photoionisation code (Ferland 1996) to estimate oxygen abundances from a large set of emission lines observed in the SDSS spectra of star forming galaxies. This allows us to directly compare the oxygen abundances of our QSO hosts with the tight stellar mass-metallicity relation as presented by Tremonti et al. (2004).

AGN-ionised regions

Gas-phase element abundance calibrations for the AGN photoionised NLR are largely unexplored. Currently, only detailed photoionisation models can be used to quantitatively estimate the element abundance of the gas in that case. Storchi-Bergmann et al. (1998) computed the oxygen abundances for an artificial grid of line ratios with the photoionisation code CLOUDY using an empirical AGN spectrum as the ionising source. They estimated a calibration for the $[\mathrm{O\,III}]\lambda\lambda 4960, 5007/\mathrm{H}\beta$ ($\equiv x$) and $[\mathrm{N\,II}]\lambda\lambda 6548, 6583/\mathrm{H}\alpha$ ($\equiv y$) line ratios by fitting a two-dimensional polynomial of second-order to the resulting grid of oxygen abundances with an additional term representing the dependence on the electron density (n_e):

$$\begin{aligned} 12 + \log(\mathrm{O/H}) = {} & 8.34 + 0.212x - 0.012x^2 - 0.02y \\ & + 0.007xy - 0.002x^2y + 6.52 \times 10^{-4} y^2 \\ & + 2.27 \times 10^{-4} xy^2 + 8.87 \times 10^{-5} x^2 y^2 \\ & - 0.1 \log(n_\mathrm{e}/300)\,. \end{aligned} \quad (4.7)$$

We roughly estimated n_e from the density-sensitive [S II] $\lambda\lambda$6716, 6731 doublet line ratio (e.g. Osterbrock & Ferland 2006) for all regions in which those emission lines could be detected. A histogram of the line ratios for H II regions and NLRs is shown in Fig. 4.10. [S II] line ratios of 19 H II regions and only 6 NLRs could be obtained. The H II regions within our host galaxies show a clear peak roughly at a line ratio of ∼1.4 corresponding to $n_\mathrm{e} \sim 10 - 100\,\mathrm{cm}^{-3}$, close or even below the low-density limit. The NLR electron densities are within the range of $n_\mathrm{e} \sim 100 - 300\,\mathrm{cm}^{-3}$ and we adopted an electron density of $n_\mathrm{e} = 200\,\mathrm{cm}^{-3}$ for the calibration. We emphasise that a change of n_e by a factor of 2 would alter the oxygen abundance by 0.03 dex only.

Since the calibration of Storchi-Bergmann et al. (1998) was based on CLOUDY photoionisation models, we believe that these oxygen abundances are comparable to the ones based on H II

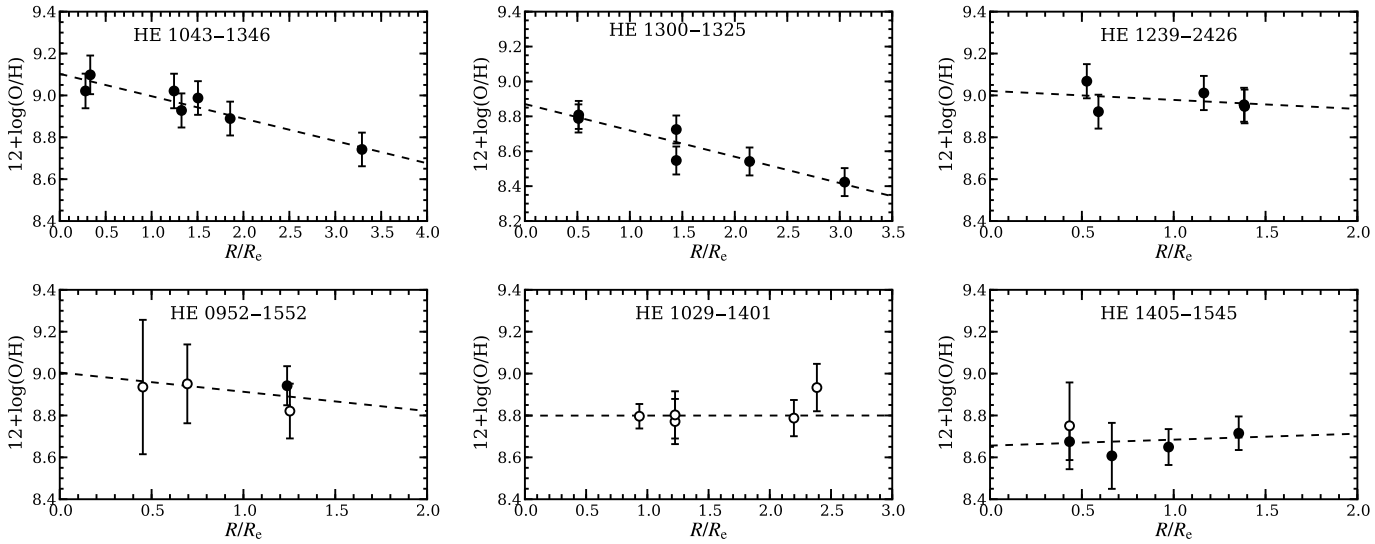

Fig. 4.11. Radial oxygen abundance distribution for those 6 host galaxies with an extended radial coverage. Filled symbols denote abundance estimates based on H II regions, while open symbols refer to abundances based on the NLR. A linear relation (dashed line) was fitted to the radial oxygen abundance distribution weighted by the individual measurement errors.

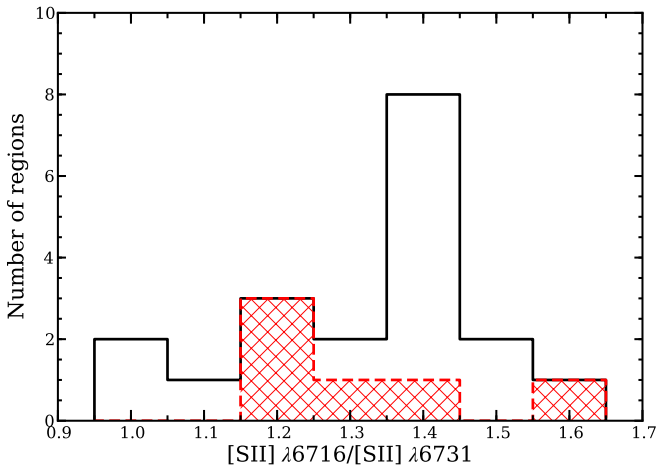

Fig. 4.10. Histogram of the measured [S II] line ratios. The black line corresponds to the line ratios of H II regions and the red shaded area to the ratios of the AGN ionised regions.

regions, after they were converted to the Tremonti et al. calibration. One remaining systematic uncertainty is introduced by the choice of the adopted AGN ionising spectrum. Storchi-Bergmann et al. (1998) already found that oxygen abundances were up to 0.5 dex larger when the AGN spectrum was approximated by a pure power-law function. Here, we empirically anchor the NLR oxygen abundances against those of H II regions in the host galaxies of HE 0952−1552 and HE 1405−1545 where both could be determined at a similar distance from the galaxy centre. We found a systematic difference of ≈0.2 dex between the oxygen abundances of the NLR and the H II regions in these two galaxies. Thus, all NLR oxygen abundance estimates were corrected by +0.2 dex in log(O/H).

4.7.2. Radial oxygen abundances gradients: Indication for radial gas flows?

In Fig. 4.11 we present the radial distribution of the oxygen abundances (with respect to R_e) for those 6 objects of our sample where the ionised gas regions were sufficiently spread over the host galaxy. Assuming an exponential decline of the oxygen abundance with radius parametrised as

$$12 + \log(\mathrm{O/H}) = \alpha \times \left(\frac{R}{R_e}\right) + \beta\,, \tag{4.8}$$

or

$$12 + \log(\mathrm{O/H}) = \alpha \times \left(\frac{R}{\mathrm{kpc}}\right) + \beta\,, \tag{4.9}$$

we estimated the slope α and zero-point β of the best-fitting model as reported in Table 4.7. The slope of the abundance gradient was either normalised to the effective radius R_e (Eq. 4.8) or based on physical units (Eq. 4.9).

We found only significant negative metallicity gradients in 2 out of the 6 QSO hosts, namely HE 1043−1346 and HE 1300−1325. HE 1043−1346 is a barred spiral galaxy with a prominent pair of spiral arms. The signature of an abundance gradient is the clearest in this object following remarkably well the assumed exponential decline. The steepest gradient was detected in the interacting galaxy HE 1300−1325. A sharp drop in the oxygen abundance occurs roughly at $1.5\,R_e$, where H II regions of the host galaxy and at the tip of a kinematical detached tidal feature (see Fig. D.1 in the Appendix) are superimposed along our line-of-sight. At larger radii the H II regions are solely located within the putative tidal structure. Thus, the overall radial abundance pattern for this galaxy might be considered as a superposition of a more shallow gradient for the central part of the host galaxy and an almost constant, low metallicity extended branch of external gas.

In the case of the other four host galaxies, HE 0952−1552, HE 1029−1401, HE 1029−1401 and HE 1405−1545, we detected no significant metallicity gradient. For the major-merger system, HE 1405−1545, the slope in the gradient might even

Table 4.7. Parameters of the best-fit oxygen abundance gradients

Object	α $\left[\text{dex } R_e^{-1}\right]$	α $\left[\text{dex kpc}^{-1}\right]$	β
HE 0952−1552	−0.09 ± 0.29	−0.02 ± 0.06	9.00 ± 0.33
HE 1029−1401	0.00 ± 0.03	0.00 ± 0.01	8.80 ± 0.07
HE 1043−1346	−0.10 ± 0.04	−0.02 ± 0.01	9.10 ± 0.07
HE 1239−2426	−0.04 ± 0.11	−0.006 ± 0.016	9.02 ± 0.12
HE 1300−1325	−0.15 ± 0.05	−0.04 ± 0.01	8.87 ± 0.08
HE 1405−1545	0.03 ± 0.14	0.004 ± 0.020	8.66 ± 0.14

be positive, but the uncertainties do not allow to make a strong claim. The averaged slope for the 6 host galaxy is $\langle\alpha\rangle = -0.06\,\text{dex}\,R_e^{-1}$ or $\langle\alpha\rangle = -0.008\,\text{dex kpc}^{-1}$.

Negative gas-phase metallicity gradients are a well known feature of undisturbed late-type galaxies and were found in numerous spectroscopic studies of the H II in nearby galaxies (McCall et al. 1985; Vila-Costas & Edmunds 1992; Zaritsky et al. 1994; Henry & Worthey 1999; Kennicutt et al. 2003; Magrini et al. 2007; Viironen et al. 2007). The gradients for prototypical isolated spiral galaxies, like NGC 300, M83, M101 and our own Milky Way, are significantly steeper with <-0.04 dex kpc^{-1} than the gradients of our QSO hosts. Several different explanation are certainly possible to explain the shallow abundance gradients given the variety of host galaxy morphologies in our sample. We now briefly discuss the most obvious ones.

One rather technical explanation might be that the abundance gradients are steeper close to the galaxy centre than in the outskirts (Magrini et al. 2007). This would cause a bias towards shallower slopes in our study, because we were only able to constrain the metallicity distribution for the *extended* part of the galaxies and not close to the centres. To explain the flatter metallicity gradients physically requires a radial mixing of the ISM on galaxy wide scale. One reasonable option would be gas migration from the outskirts towards the centre of barred galaxies along their bars. Several studies found that the gas-phase metallicity gradient in barred galaxies are flatter than in unbarred spirals (e.g. Vila-Costas & Edmunds 1992; Martin & Roy 1994). Indeed, the gradient of our barred spiral host galaxy HE 1043−1346 (−0.02 dex kpc^{-1}) is flatter than typical unbarred spirals but well consistent with the barred spiral population studied by Vila-Costas & Edmunds (1992).

Most of our AGN host galaxies do not have large-scale bars and would require another mechanism to radially drive gas inwards if that process is responsible for the flatter gradients. Recently, the evolution of the metallicity gradient in major galaxy interactions has reached increasing interest based on new numerical simulations (Rupke et al. 2010) and observations (Kewley et al. 2010). The simulations predicted a significantly flattened metallicity gradient between the first and second pericenter, which could observationally confirmed later on. A certain fraction of our galaxies are in early stages of galaxy interaction either with confirmed close-by (minor) companions (e.g. HE 1239−2426 and HE 1300−1325) or already in an advanced stage of a major merger (e.g. HE 1405−1545). The flat or possibly positive gradient in HE 1405−1545 fits well with the scenario outlined by the numerical simulation of Rupke et al. (2010). In the case of HE 1300−1325, we suggest that the low metallicity gas along the tidal feature corresponds to external gas currently being accreted by the galaxy.

Table 4.8. Gas-phase oxygen abundances at $1R_e$

Object	12 + log(O/H)	ionisation
HE 0952−1552	8.91 ± 0.08	NLR
HE 1029−1401	8.80 ± 0.05	NLR
HE 1043−1346	9.00 ± 0.04	H II
HE 1228−1637	8.84 ± 0.07	H II
HE 1237−2252	8.97 ± 0.07	H II
HE 1239−2426	9.03 ± 0.07	H II
HE 1300−1325	8.76 ± 0.06	H II
HE 1310−1051	8.75 ± 0.06	H II
HE 1405−1545	8.68 ± 0.05	H II
HE 1416−1256	8.55 ± 0.15	H II
HE 1434−1600	8.84 ± 0.06	NLR

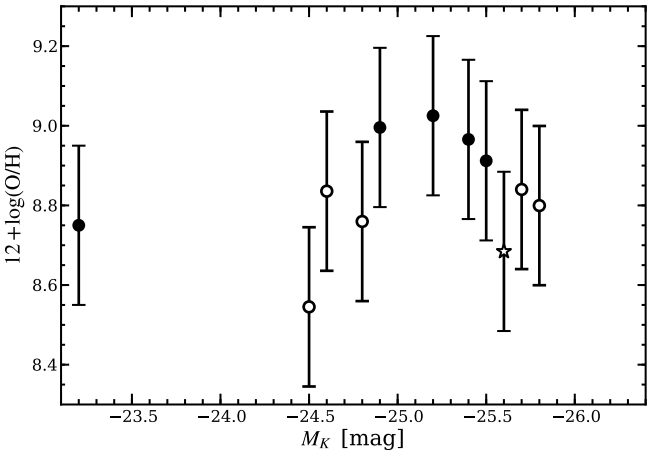

Fig. 4.12. Oxygen abundances at $1R_e$ against the absolute K-band magnitude. Filled circles denote disc-dominated hosts, opened circles indicate bulge-dominated hosts and the star symbol correspond to a major merger host. The systematic uncertainty of 0.2 dex for the oxygen abundance is assumed to dominate over the measurements errors in all cases.

4.7.3. Metal dilution in bulge-dominated QSO hosts?

The absolute values of the gas-phase oxygen abundances varies in the range of $8.6 < 12 + \log(\text{O/H}) < 9.1$ among the galaxies in our sample. In order to search for any systematic trend, we estimated the oxygen abundance at $1R_e$ for the majority of objects (Table 4.8). In most cases oxygen abundances could be measured from ionised gas region within $0.75R_e < R < 1.25R_e$ so that we computed their mean value as the representative value at $1R_e$. For the 6 objects with a metallicity gradient, we evaluated their radius-metallicity relation at $1R_e$.

In Fig. 4.12 we compare the oxygen abundances at $1R_e$ of our hosts with their absolute K band magnitudes as reported in Jah04. Since we compare the abundances in different galaxies, we assumed that their uncertainty is dominated by the systematics (~0.2 dex) of the adopted calibration rather than the measurements errors of the emission lines. In spite of the uncertainties we found that the bulge-dominated QSO hosts exhibit *systematically lower* oxygen abundances by about -0.2 dex than the disc-dominated hosts at comparable K band absolute magnitudes. The K-band luminosity has often been considered as a good proxy for the stellar mass of galaxies (e.g. Rix & Rieke 1993; Bell & de Jong 2001; Cole et al. 2001; Bell et al. 2003) due to the low variation of mass-to-light ratios compared to

other bands. In Fig. 4.13 we compare the metallicites against our stellar masses determined from the broad-band SED of the galaxies, which confirms our tentative impression that the bulge-dominated QSO hosts have a systematically lower oxygen abundance (at $1R_e$) at a given stellar mass. Interestingly, we found that almost all our disc-dominated hosts are still consistent with the global mass-metallicity relation of galaxies (Tremonti et al. 2004), but the bulge-dominated hosts, and the major merger in particular, are systematically below that relation. Letawe et al. (2007) also inferred the gas-phase metallicity for their sample of luminous QSOs and found typically low metallicities ($12 + \log(O/H) < 8.6$) for their hosts. They attributed the lowest metallicities to those host galaxies with distorted morphologies. However, their broad-band images were very shallow, so that a morphological classification might not be sufficiently robust to distinguish between undistorted and distorted galaxies, and to establish a causal connection of galaxy interactions with the low gas-phase metallicity.

The systematically lower oxygen abundance of the bulge-dominated QSO host galaxies with respect to their disc-dominated counterparts (at a given stellar mass) might be a new and common feature in addition to the well known blue colours that can be attributed to young stellar populations. The significance of our result is certainly reduced by the uncertainties of the oxygen abundances. However, such uncertainties should *randomly* affect the overall sample and not specifically galaxies with a certain morphology, except when there is a physical reason, e.g. the ionisation parameter for the H II regions depending on the host morphology. Thus, we think that the trend is real and points to a physical origin.

The gas-phase metallicities of inactive elliptical or bulge-dominated galaxies is not well explored. It is now known that more than 60% of the elliptical galaxies display detectable emission lines of a warm-ionised ISM (e.g. Trinchieri & di Serego Alighieri 1991; Goudfrooij et al. 1994; Macchetto et al. 1996; Sarzi et al. 2006). The gas is often concentrated at the nucleus and appears to be predominately ionised by post-AGB stars rather than recent or ongoing star formation. Metallicities of elliptical galaxies have been mainly obtained from the hot phase of the ISM and the stellar population (e.g. Trager et al. 2000). Only a few recent studies tried to infer the metallicity of the warm-ionised gas, concentrating on the galaxy centre. Annibali et al. (2010) found that the gas-phase oxygen abundances in a sample of 65 inactive bulge-dominated galaxies were systematically lower than the corresponding stellar abundances. They attributed this discrepancy either to a systematic mismatch between the gas-phase and stellar abundance calibrations or to the accretion of external gas, likely via minor mergers. In contrast, Athey & Bregman (2009) argued that the solar metallicity gas in elliptical galaxies is unlikely to be accreted from the environment, and they favoured mass loss of AGB stars as the origin of the gas.

It is therefore intriguing to find only the bulge-dominated QSO host galaxies and the major merger significantly below the mass-metallicity relation. Although we are not able to determine the metallicity at the galaxy centres due to the confusion with the QSO spectrum, the observed metallicity gradients are usually too shallow for the nuclear metallicities to be on the mass-metallicity relation. A general dilution of the element abundances may account for our observation that could be potentially induced by strong galaxy interactions, which were identified to be important processes affecting also the element abundances of the ISM at the galaxy centre. For example, Kewley et al. (2006) and Ellison et al. (2008) showed that galaxies with

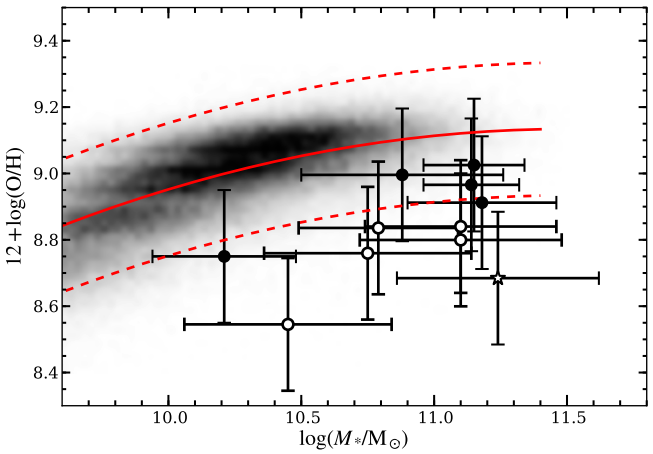

Fig. 4.13. Oxygen abundances at $1R_e$ against the total stellar mass of the hosts. Symbols are the same as in Fig. 4.12. The grey scale image correspond to a 2D histogram of the SDSS MPA/JHU galaxy catalogue as analysed by Tremonti et al. (2004). The red solid line represents the best-fit line to the SDSS data of with the dashed lines indicating roughly its 3σ uncertainty.

close companions have statistically lower central gas-phase oxygen abundances than isolated galaxies. Peeples et al. (2009) and Sol Alonso et al. (2010) found that the majority of extreme low-metallicity outliers from the mass-metallicity relation are distorted galaxies indicative of recent or ongoing interactions. Studying local LIRGs and ULRIGs, Rupke et al. (2008) found that the nuclear oxygen abundances were a factor of 2 lower than expected. Finally, Montuori et al. (2010) confirmed via numerical simulation of galaxy mergers that a dilution in the central metallicity is expected to occur after the first pericenter, at final coalescence and even during galaxy fly-bys.

That picture matches well with the situation for the ongoing major-merger system HE 1405−1545 which we find to be ∼0.4 dex below the mass-metallicity relation. The intriguing shells of gas around the bulge-dominated host galaxy HE 1416−1256 (Region B and C) could be a tentative indication for a recent (minor) merger event. The potential metal dilution in our morphologically undisturbed bulge-dominated systems may correspond to the second dilution peak at or shortly after the final coalescence stage of a recent major merger. An alternative possibility are recent accretion events that accumulate low-metallicity gas via minor mergers. This has not yet been extensively explored in numerical simulations. Kinematic studies of the ionised gas in inactive elliptical galaxies revealed that the kinematics of the gas is often decoupled from that of the stars, commonly interpreted a recent acquisition of external gas (e.g. Caon et al. 2000; Kannappan & Fabricant 2001; Sarzi et al. 2006). To study the kinematics of our host galaxies might thus help to identify whether gravitational interactions are ongoing, just happened or if the host galaxies can be considered as completely relaxed systems. In the course of this work, we derived the radial velocity fields and the dispersion maps from the ionised (Appendix D), but their analysis and discussion with respect to merger signatures is an essential part of the PhD thesis of Dading Nugroho.

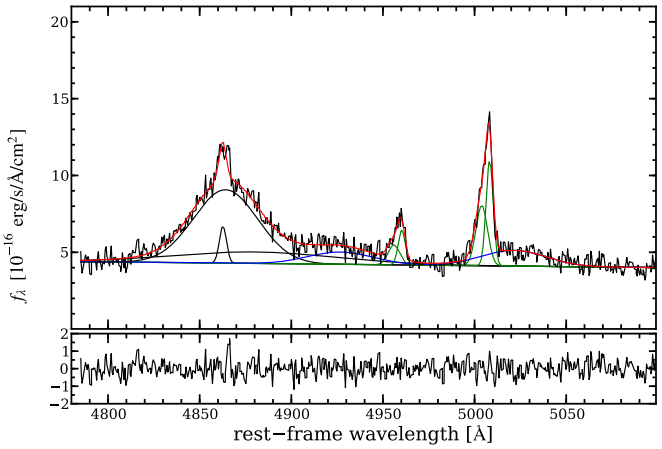

Fig. 4.14. Multi-component fit to the QSO spectrum of HE 1043−1346 in Hβ-[O III] spectral region. The best-fit model is indicated by the red solid line and the individual Gaussian components are plotted above the local linear continuum with the following colour coding: black – Hβ line, green – [O III] doublet lines, blue – Fe II doublet lines. The residuals of the model are shown in the panel underneath with a refined scaling.

4.8. NLR scaling relations

4.8.1. NLR sizes and QSO luminosities

We now turn our attention to the AGN-ionised gas, which represents the classical NLR. The [O III] line is the brightest of optical emission-line in case of AGN ionisation and we construed [O III] narrow-band image from the QSO-subtracted IFU datacubes to measure the characteristic size of the ENLRs. Here, we estimated the size in the same manner as in our previous study on the ENLR around luminous low-redshift QSOs observed with PMAS as presented in Chapter 3. All pixel below the 3σ background noise level of the narrow-band image were masked out as well as all previously confirmed H II regions. After this cleaning process, we measured the effective ENLR radius (r_e) as the flux or luminosity weighted radius computed over all unmasked pixels. We avoided to use the maximum extent of the ENLR, because the maximum projected size of the ENLR is sensitive to low surface brightness features, which depend on the depth of the observations (see section 3.7.2 in Chapter 3.

In several cases, the extended line emission was dominated by H IIso that no NLR could be resolved. We provide upper limits on their sizes in these cases based on the H II region with the smallest distance to the nucleus. Please note that we always refer to the *projected* radius, because the exact orientation of the ENLR is unconstrained from our data making a reasonable and homogeneous correction of the apparent radius impossible. We excluded the objects HE 1201−2409 and HE 1315−1028 from this analysis, as the nature of the ionised gas could not be determined in these cases. Furthermore, the ENLR of HE 1434−1600 is only partially covered by our observations so that we decided to exclude this object as well.

The deblended QSO datacubes provide high S/N spectra of the QSOs largely uncontaminated by host galaxy emission. For the purpose of the present investigation we measured the QSO continuum luminosity at 5100Å (L_{5100}) and the [O III] line emission. Similar to the analysis of the PMAS QSO spectra (see Appendix B), we modelled the spectral region around the broad Hβ line with a set of Gaussians for the narrow and broad emission lines plus an underlying local continuum. Two Gaussian were usually required to account for the asymmetry of the [O III] line. An example of the QSO spectral modelling is shown in Fig. 4.14 for illustration. The results for all of the QSO spectra and their parameters are presented in the Appendix B. The measured continuum luminosities L_{5100}, integrated [O III] luminosity (nucleus+ENLR) L([O III]) and ENLR size r_e, are provided in Table 4.9.

Table 4.9. The QSO luminosity at 5100Å, integrated [O III] luminosity and ENLR size.

Object	$\log L_{5100}$ $\left[\mathrm{erg\,s^{-1}}\right]$	$\log L$([O III]) $\left[\mathrm{erg\,s^{-1}}\right]$	r_e [kpc]
HE 0952−1552	44.09 ± 0.10	41.97 ± 0.11	3.5 ± 0.2
HE 1019−1414	43.50 ± 0.11	41.85 ± 0.12	1.5 ± 0.1
HE 1029−1401	44.88 ± 0.09	42.38 ± 0.19	5.5 ± 0.0
HE 1043−1346	44.88 ± 0.09	40.89 ± 0.12	<1.4
HE 1110−1910	44.21 ± 0.09	41.86 ± 0.10	4.2 ± 1.8
HE 1228−1637	44.21 ± 0.09	41.48 ± 0.10	<2.3
HE 1237−2252	43.90 ± 0.10	41.72 ± 0.13	3.4 ± 3.9
HE 1239−2426	43.90 ± 0.10	40.94 ± 0.13	<1.5
HE 1254−0934	44.84 ± 0.10	42.75 ± 0.10	7.6 ± 0.2
HE 1300−1325	44.84 ± 0.10	41.35 ± 0.10	<1.8
HE 1310−1051	44.84 ± 0.10	41.51 ± 0.11	<1.2
HE 1338−1423	43.86 ± 0.09	42.12 ± 0.11	2.2 ± 0.0
HE 1405−1545	44.41 ± 0.11	42.36 ± 0.17	5.3 ± 0.1
HE 1416−1256	44.15 ± 0.10	42.73 ± 0.11	4.4 ± 0.4

4.8.2. The size-luminosity relation

In Chapter 3 we studied the size of the ENLR for a sample of luminous QSOs, but the luminosity range was too narrow to infer a size-luminosity relation of the NLR. Our sample of type 1 AGN is now significantly expanded towards lower luminosities with this work, so that we are able to investigate the size-luminosity relation in more detail. Additionally, five Seyfert 1 galaxies (Fairall 265, Fairall 51, Mrk 915, NGC 3783, NGC 4593) were also observed with the VIMOS IFU, and analysed by D. Kupko in the course of his Master thesis, which further complement our sample. In Fig. 4.15 we compare the NLR sizes with the integrated [O III] luminosity (left panel) and the nuclear luminosity at 5100Å (right panel), which have both been considered as proxies for the intrinsic bolometric luminosity of AGN.

A correlation between the size of the NLR and the corresponding luminosity emerges in both cases. For a proper statistical analysis of these correlations, we wanted to take the censored data points into account. The Astronomy Survival Analysis package (ASURV, Lavalley et al. 1992) was specifically developed for this task and incorporates several statistical methods to deal with bi-variate censored data (Isobe et al. 1986). We computed the generalised Spearman's Rho correlation coefficient and found a significant correlation between the NLR size and the AGN continuum luminosity with a coefficient of 0.87 at a confidence level greater than 99.99%. A somewhat smaller correlation coefficient of 0.73 was computed for the correlation between the NLR size and the integrated [O III] luminosity at a confidence level of 99.99%.

A linear regression analysis using the Buckley-James method (Buckley & James 1979) yield a linear parametrisation

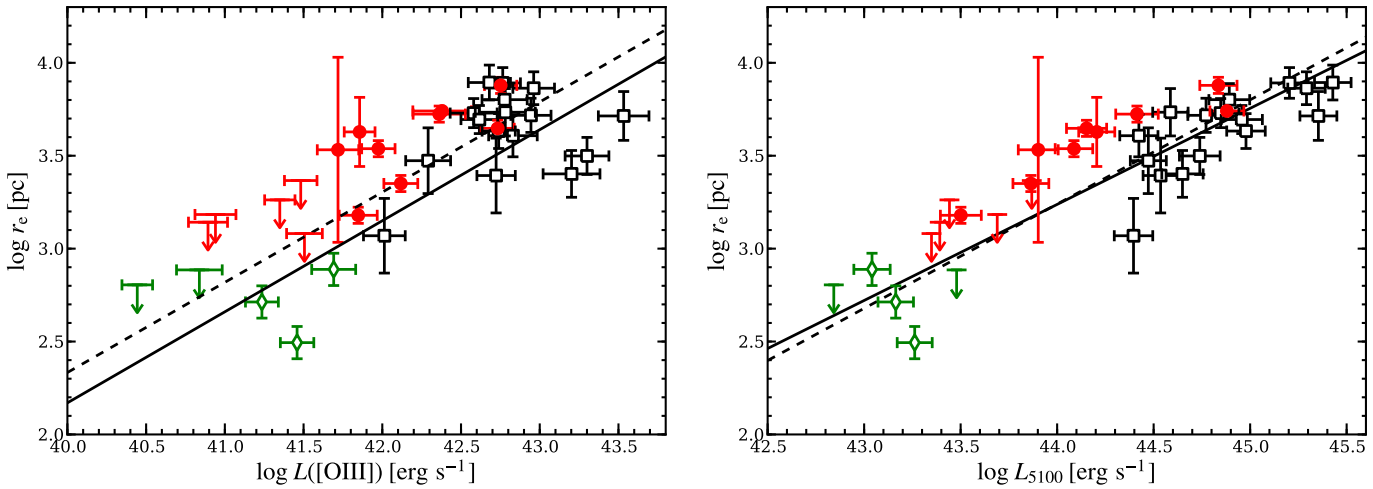

Fig. 4.15. Effective NLR size as a function of integrated [O III] luminosity (left panel) or AGN continuum luminosity at 5100Å (right panel). The data from this sample are shown as red filled circles. Additional measurements for more luminous QSOs (Chapter 3) and from 5 Seyfert 1 galaxies (provided by D. Kupko) are shown as black opened squares and green opened diamonds, respectively. Arrows indicate censored data with upper limits on the ENLR size. The solid line represent the linear relations inferred from the Buckely-James method and the dashed lines indicate the result of the orthogonal distance regression analysis ignoring censored data points.

for the NLR size of the form

$$\log r_e = (0.49 \pm 0.09) \times \log(L([\mathrm{O\,III}]) - (17.43 \pm 1.3)\,, \quad (4.10)$$

$$\log r_e = (0.52 \pm 0.06) \times \log(L_{5100})) - (19.5 \pm 2.23)\,, \quad (4.11)$$

for the integrated [O III] luminosity and the AGN continuum luminosity at 5100Å, respectively. Although the Buckely-James method takes censored data into account, it does not handle the uncertainties in the variables. Thus, we also applied the orthogonal distance regression method to our data, ignoring censored data points, which yield the following relations

$$\log r_e = (0.48 \pm 0.12) \times \log(L([\mathrm{O\,III}]) - (16.78 \pm 5.25)\,, \quad (4.12)$$

$$\log r_e = (0.56 \pm 0.09) \times \log(L_{5100}) - (21.45 \pm 3.86)\,. \quad (4.13)$$

Obviously, the correlation between the NLR size and the AGN continuum luminosity is much tighter than the correlation between the NLR size and the [O III] luminosity. In any case, the linear regression analysis recovers a slope consistent with ∼0.5.

4.8.3. Comparison with previous results and implications

The NLR size-luminosity relation has usually been approximated by a power law function, $\log(R_{\mathrm{NLR}}) = \alpha \log(L_{[\mathrm{O\,III}]}) + R_0$. We already discussed in Chapter 3 that the absolute zero-point R_0 of this relation is hardly comparable among the previous studies, because different definition of NLR size were used which are often sensitive to the depth of the data. We will thus restrict our discussion here to the slope α of the relation.

From our IFU data of more than 40 type 1 AGN covering 3 orders of magnitude in luminosity, we inferred a slope of $\alpha = 0.49 \pm 0.09$ for the NLR size-luminosity relation, which is in good agreement with the slope reported by Bennert et al. (2002). A value of $\alpha \sim 0.5$ can be theoretically explained by a constant ionisation parameter across the NLR. It is also the favoured scenario for the BLR size-luminosity relation, for which a slope of $\alpha = 0.52 \pm 0.06$ was measured (e.g. Bentz et al. 2009). Schmitt et al. (2003b) inferred a much flatter slope of $\alpha = 0.33 \pm 0.04$ for a sample of 60 nearby Seyfert galaxies. They argued that such a slope implies a Strömgren sphere like relation requiring a constant density of the ambient gas. Since the *HST* narrow-band images used by Bennert et al. (2002) and Schmitt et al. (2003b) do not allow to distinguish between [O III] emission from the NLR and H II regions, we supsect that the NLR size was overestimated at low [O III] luminosities due to a contamination with emission from star forming regions. This would lead to a flatter slope if the contamination is systematically higher at lower AGN luminosities. Bennert et al. (2006) proposed another physical explanation where the slopes are statistically different for type 1 and type 2 AGN, assuming an orientation-dependent projection of the NLR combined with the "receding torus" model (Lawrence 1991) of luminosity-dependent opening angles for the AGN ionisation cones. This explanation for the different slopes is no longer valid after we found in Chapter 3 that the NLR sizes of our type 1 QSOs agree with those of type 2 QSOs (Greene et al. 2011) at given [O III] luminosities. However, Greene et al. (2011) reported an even shallower slope of $\alpha = 0.22 \pm 0.04$, which they attribute to matter-bounded nebulae where the emission is limited by the gas density rather than the density of ionising AGN photons.

We suspect that most of confusion regarding the slope of the NLR size-luminosity relation is introduced by the use of the [O III] luminosity as a proxy for the intrinsic AGN bolometric luminosity. For the first time, we studied the NLR size-luminosity relation of type 1 AGN over a large luminosity range for which the the AGN continuum can be directly observed. We find that NLR size-luminosity relation is significantly tighter with respect to the continuum luminosity than the integrated [O III] luminosity. We recall that the correlation between the bolometric AGN luminosity and the [O III] luminosity was established over several orders of magnitude (e.g. Mulchaey et al. 1994; Zakamska et al. 2003; Heckman et al. 2005), but has a high scatter of >0.4 dex. The most recent assessments of the relation was performed by Punsly & Zhang (2011), who emphasised that emission lines of the BLR, like Hβ or Mg II are much better tracers for the bolometric luminosity. Netzer et al. (2006) reported that the [O III] over hard X-ray luminosity ratio is correlated with the X-ray luminosity itself, recently confirmed by Trouille & Barger

(2010). Furthermore, Greene et al. (2010) studied the BLR size-luminosity relation for different luminosities including the [O III] luminosity. They found that the [O III] luminosity had a higher scatter and possibly a different slope from the broad-line Hβ luminosity, in agreement with the results of Punsly & Zhang (2011). Thus, the [O III] luminosity may not be solely determined by the AGN bolometric luminosity. Whether the covering factor of the NLR is the most important additional parameter for the [O III] luminosity as proposed by Baskin & Laor (2005) remains open. If the $L_{[\mathrm{O\,III}]}/L_{5100}$ ratio systematically depends on additional parameter that also affect the apparent size of the NLR, the slope in the NLR size-luminosity relation would automatically be different.

Interestingly, our results suggest that the NLR size may be a more robust tracer of the bolometric luminosity of an AGN than the [O III] luminosity, with a scatter of 0.35 dex. The revised NLR size-luminosity relation may thus be used as an independent proxy for the bolometric luminosity of type 2 AGN, whenever the NLR size can be measured. There are however still a few caveats we need to point out. First, the unknown inclination of the NLR with respect to the observers sightline might enhance the scatter in the relation and can be a significant source of uncertainty. In the framework of the unifed model of AGN (Antonucci 1993), the NLR of type 2 AGN should appear more bicone-like and extended than type 1 ones due to the preferred orientation of the obscuring torus and associated ionisation cones for these two AGN classes. Such a clear distinction could not be made observationally (Schmitt et al. 2003b) and we also identified a few luminous QSOs with biconical ENLRs in the course of this PhD work (see Chapter 2 and Chapter 3).. This makes the bias in the relation due to the inclination difficult to quantify. More importantly, it could be that the NLR size-luminosity relation breaks down at very high AGN luminosities. Because the [O III] emission lines were frequently absent in spectra of luminous QSOs at high redshifts, Netzer et al. (2004) speculated that these QSO may have already lost their large, dynamically unbound, NLR or that a circumnuclear starburst may affect the emission-line spectrum so that the NLR would not be recognised. In Husemann et al. (2008) and Chapter 3, we emphasised that an ENLR was missing for almost 50% of QSOs in our sample, even though their continuum luminosity would predict a ENLR size of several kpc using the NLR scaling-relation derived in this work. Either the ENLR sizes are substantially smaller than expected for their QSOs or their ENLR luminosities are below the detection limit.

4.9. Summary and Conclusions

In this Chapter, we presented a comprehensive spatially resolved spectroscopic analysis of a well-defined sample of intermediate luminosity QSOs at low redshift ($z < 0.2$). It is the first step in the investigation of the QSO host properties with this rich dataset. The main aim of this work was to characterise the spatially resolved properties of the ionised gas for the host galaxies within our sample. The main results can be summarised as follows:

1. All QSO host galaxies contain at least some ionised gas, with a variety of ionisation mechanisms.
2. In more than 50% of the host galaxies, irrespective of the host galaxy morphology, we find ionised gas from classical H II regions indicating ongoing star formation activity. The specific star formation rates for a large number of our AGN host galaxies are consistent with those of the overall galaxy population, but a view disc-dominated galaxies are identified to have exceptionally low specific SFRs. Enhanced star formation activity among the hosts is almost always associated with major galaxy interactions, where major mergers form stars at a SFR of up to $120\,\mathrm{M}_\odot\,\mathrm{yr}^{-1}$.
3. The ionised gas in the rest of the sample is ionised entirely by the AGN. Of them, three object show possible signature of shock ionisation, potentially due to jet-cloud interactions, even though they are classified as radio-quiet QSOs. High spatial resolution radio observations are still required to confirm this hypothesis.
4. For a subsample of six QSO hosts we constructed radial oxygen abundance gradients which are flatter than expected for isolated spiral galaxies. We suggest that galaxy interactions or major/minor mergers are potential drivers for radial gas migration on galaxy wide scales. Bar instabilities should be the dominant mechanisms for barred galaxies, which are rare in our sample.
5. Bulge-dominated QSO hosts and a ongoing major merger exhibit systematically lower gas-phase oxygen abundances at $1R_\mathrm{e}$ by $\sim$0.2 dex compared to their disc-dominated counterparts in the sample, placing them below the mass-metallicity relation of galaxies. We suggest minor or major mergers as the most likely process that caused this metal dilution as supported by recent numerical simulations.
6. The size of the NLR correlates strongly with the intrinsic AGN luminosity as traced either by the AGN continuum luminosity at 5100Å or by the integrated [O III] luminosity. We find a relation of $R_\mathrm{NLR} \propto L_{5100}^{0.52\pm0.06}$ consistent with the slope of the BLR scaling relation. The scatter in the relation based on [O III] is significantly larger and we conclude that the [O III] luminosity does not solely depend on the AGN luminosity. We briefly discuss the possibility to use the NLR size-luminosity relation to determine the bolometric AGN luminosity of type 2 AGN and point out important caveats to keep in mind.

The properties of the ionised gas draw a quite diverse picture about the local population of QSO host galaxies. Ionisation from H II regions, AGN ionisation and shocks together with various signatures of galaxy interactions and secular evolution can be found in host galaxies of different morphological types. However, the AGN-ionised NLR in all our host galaxies follows a single size-luminosity relation. It means that at the high-luminosity end, a substantial fraction of the gas is ionised and heated by the AGN radiation on scales of the entire host galaxy. These luminous AGN might temporarily be able to quench star formation in the host galaxies depending on the covering fraction of the ionisation cones and the self-shielding of the molecular gas clouds. Other processes may be required to operate in the low-luminosity AGN to quench star formation. Since a large fraction of our QSO hosts have specific SFRs at the level of the normal galaxy population or above, we doubt that AGN feedback is a substantial or even a leading mechanism at least in the current phase of their evolution. However, we need to point out that our AGN sample cannot be directly compared with those usually studied from SDSS (e.g. Kauffmann et al. 2003; Schawinski et al. 2010b). For example, the stellar masses of our most massive bulge-dominated QSO host are 0.7 dex more massive than the ones in the sample of Schawinski et al. (2010b). Another major difference in the AGN samples is that we are focused on the more luminous type 1 AGN at low redshift. We therefore probe the high-luminosity end of the AGN luminosity function (Köhler et al. 1997; Schulze et al. 2009) and by design

miss the low-luminosity AGNs that dominate the AGN population at low redshift.

Furthermore, we emphasise that the gas-phase oxygen abundances may provide further indirect constraints on the importance of galaxy interaction, mergers and secular processes on the triggering of AGN activity. The discovery of generically low gas-phase metallicities in bulge-dominated galaxies and the rather flat slopes in their radial distribution indicates the importance of radial gas migration in QSO hosts possibly triggered by galaxy interactions. This process may also be responsible for intermittent phases of black hole growth. Numerical simulation already appeared to be quite successful in interpreting the properties of interacting systems, but a larger set of conditions would need to be simulated in order to match various possible scenarios with observations and to put the observed AGN phase in a timeline.

Acknowledgements. BH and LW acknowledge financial support by the DFG Priority Program 1177 "Witnesses of Cosmic History: Formation and evolution of black holes, galaxies and their environment", grant Wi 1369/22-1 and Wi 1369/22-2. SFS would like to thanks the 'Ministerio de Ciencia e Innovacion' project ICTS-2009-10, and the 'Junta de Andalucia' projects P08-FWM-04319 and FQM360. DN and KJ are funded through the DFG Emmy Noether-Program, grant JA 1114/3-1.

Funding for the SDSS and SDSS-II was provided by the Alfred P. Sloan Foundation, the Participating Institutions, the National Science Foundation, the U.S. Department of Energy, the National Aeronautics and Space Administration, the Japanese Monbukagakusho, the Max Planck Society, and the Higher Education Funding Council for England. The SDSS was managed by the Astrophysical Research Consortium for the Participating Institutions.

This research has made use of the NASA/IPAC Extragalactic Database (NED) which is operated by the Jet Propulsion Laboratory, California Institute of Technology, under contract with the National Aeronautics and Space Administration.

For the preparation of this paper we have made used of the cosmology calculator "CosmoCalc" (Wright 2006)

References

Allen, M. G., Groves, B. A., Dopita, M. A., Sutherland, R. S., & Kewley, L. J. 2008, ApJS, 178, 20
Alloin, D., Collin-Souffrin, S., Joly, M., & Vigroux, L. 1979, A&A, 78, 200
Alonso, M. S., Lambas, D. G., Tissera, P., & Coldwell, G. 2007, MNRAS, 375, 1017
Annibali, F., Bressan, A., Rampazzo, R., et al. 2010, A&A, 519, A40+
Antonucci, R. 1993, ARA&A, 31, 473
Arribas, S., Colina, L., Monreal-Ibero, A., et al. 2008, A&A, 479, 687
Athey, A. E. & Bregman, J. N. 2009, ApJ, 696, 681
Baldwin, J. A., Phillips, M. M., & Terlevich, R. 1981, PASP, 93, 5
Barton, E. J., Geller, M. J., & Kenyon, S. J. 2000, ApJ, 530, 660
Baskin, A. & Laor, A. 2005, MNRAS, 358, 1043
Bell, E. F. & de Jong, R. S. 2001, ApJ, 550, 212
Bell, E. F., McIntosh, D. H., Katz, N., & Weinberg, M. D. 2003, ApJS, 149, 289
Bennert, N., Canalizo, G., Jungwiert, B., et al. 2008, ApJ, 677, 846
Bennert, N., Falcke, H., Schulz, H., Wilson, A. S., & Wills, B. J. 2002, ApJ, 574, L105
Bennert, N., Jungwiert, B., Komossa, S., Haas, M., & Chini, R. 2006, New A Rev., 50, 708
Bentz, M. C., Peterson, B. M., Netzer, H., Pogge, R. W., & Vestergaard, M. 2009, ApJ, 697, 160
Bertram, T., Eckart, A., Fischer, S., et al. 2007, A&A, 470, 571
Bower, R. G., Benson, A. J., Malbon, R., et al. 2006, MNRAS, 370, 645
Brinchmann, J., Charlot, S., White, S. D. M., et al. 2004, MNRAS, 351, 1151
Bruzual, G. & Charlot, S. 2003, MNRAS, 344, 1000
Buckley, J. & James, I. 1979, Biometrika, 66, 429
Canalizo, G. & Stockton, A. 2001, ApJ, 555, 719
Caon, N., Macchetto, D., & Pastoriza, M. 2000, ApJS, 127, 39
Cappellari, M. & Copin, Y. 2003, MNRAS, 342, 345
Cardelli, J. A., Clayton, G. C., & Mathis, J. S. 1989, ApJ, 345, 245
Cattaneo, A., Faber, S. M., Binney, J., et al. 2009, Nature, 460, 213
Chilingarian, I. V., Prugniel, P., Sil'Chenko, O. K., & Afanasiev, V. L. 2007, MNRAS, 376, 1033
Christensen, L., Jahnke, K., Wisotzki, L., & Sánchez, S. F. 2006, A&A, 459, 717
Cid Fernandes, R., Gu, Q., Melnick, J., et al. 2004, MNRAS, 355, 273
Cid Fernandes, R., Mateus, A., Sodré, L., Stasińska, G., & Gomes, J. M. 2005, MNRAS, 358, 363
Cid Fernandes, R., Stasińska, G., Schlickmann, M. S., et al. 2010, MNRAS, 403, 1036
Cisternas, M., Jahnke, K., Inskip, K. J., et al. 2011, ApJ, 726, 57
Clark, N. E., Axon, D. J., Tadhunter, C. N., Robinson, A., & O'Brien, P. 1998, ApJ, 494, 546
Cole, S., Norberg, P., Baugh, C. M., et al. 2001, MNRAS, 326, 255
Condon, J. J. 1992, ARA&A, 30, 575
Condon, J. J., Cotton, W. D., Greisen, E. W., et al. 1998, AJ, 115, 1693
Croton, D. J., Springel, V., White, S. D. M., et al. 2006, MNRAS, 365, 11
Davies, R. I., Müller Sánchez, F., Genzel, R., et al. 2007, ApJ, 671, 1388
Denicoló, G., Terlevich, R., & Terlevich, E. 2002, MNRAS, 330, 69
Diehl, S. & Statler, T. S. 2006, MNRAS, 368, 497
Dopita, M. A. & Evans, I. N. 1986, ApJ, 307, 431
Dopita, M. A., Groves, B. A., Fischera, J., et al. 2005, ApJ, 619, 755
Dumas, G., Mundell, C. G., Emsellem, E., & Nagar, N. M. 2007, MNRAS, 379, 1249
Dunlop, J. S., McLure, R. J., Kukula, M. J., et al. 2003, MNRAS, 340, 1095
Edmunds, M. G. & Pagel, B. E. J. 1984, MNRAS, 211, 507
Ellison, S. L., Patton, D. R., Simard, L., & McConnachie, A. W. 2008, AJ, 135, 1877
Emonts, B. H. C., Morganti, R., Tadhunter, C. N., et al. 2006, A&A, 454, 125
Emsellem, E., Cappellari, M., Peletier, R. F., et al. 2004, MNRAS, 352, 721
Ferland, G. J. 1996, Hazy, A Brief Introduction to Cloudy 90, ed. Ferland, G. J.
García-Lorenzo, B., Sánchez, S. F., Mediavilla, E., González-Serrano, J. I., & Christensen, L. 2005, ApJ, 621, 146
Gerssen, J., Allington-Smith, J., Miller, B. W., Turner, J. E. H., & Walker, A. 2006, MNRAS, 365, 29
González Delgado, R. M., Cerviño, M., Martins, L. P., Leitherer, C., & Hauschildt, P. H. 2005, MNRAS, 357, 945
Goudfrooij, P., Hansen, L., Jorgensen, H. E., & Norgaard-Nielsen, H. U. 1994, A&AS, 105, 341
Granato, G. L., De Zotti, G., Silva, L., Bressan, A., & Danese, L. 2004, ApJ, 600, 580
Greene, J. E., Hood, C. E., Barth, A. J., et al. 2010, ApJ, 723, 409
Greene, J. E., Zakamska, N. L., Ho, L. C., & Barth, A. J. 2011, ArXiv e-prints
Grogin, N. A., Conselice, C. J., Chatzichristou, E., et al. 2005, ApJ, 627, L97
Groves, B. A., Dopita, M. A., & Sutherland, R. S. 2004, ApJS, 153, 9
Heckman, T. M., Ptak, A., Hornschemeier, A., & Kauffmann, G. 2005, ApJ, 634, 161
Henry, R. B. C. & Worthey, G. 1999, PASP, 111, 919
Ho, L. C. 2005, ApJ, 629, 680
Ho, L. C. & Ulvestad, J. S. 2001, ApJS, 133, 77
Hopkins, A. M., Connolly, A. J., Haarsma, D. B., & Cram, L. E. 2001, AJ, 122, 288
Hopkins, P. F. & Hernquist, L. 2009, ApJ, 694, 599
Huang, S. & Gu, Q.-S. 2009, ArXiv e-prints
Husemann, B., Sánchez, S. F., Wisotzki, L., et al. 2010, A&A, 519, A115+
Husemann, B., Wisotzki, L., Sánchez, S. F., & Jahnke, K. 2008, A&A, 488, 145
Hutchings, J. B. & Neff, S. G. 1992, AJ, 104, 1
Isobe, T., Feigelson, E. D., & Nelson, P. I. 1986, ApJ, 306, 490
Jahnke, K., Kuhlbrodt, B., & Wisotzki, L. 2004a, MNRAS, 352, 399
Jahnke, K., Sánchez, S. F., Wisotzki, L., et al. 2004b, ApJ, 614, 568
Jahnke, K., Wisotzki, L., Courbin, F., & Letawe, G. 2007, MNRAS, 378, 23
Jahnke, K., Wisotzki, L., Sánchez, S. F., et al. 2004c, AN, 325, 128
Kannappan, S. J. & Fabricant, D. G. 2001, AJ, 121, 140
Kauffmann, G., Heckman, T. M., Tremonti, C., et al. 2003, MNRAS, 346, 1055
Kaviraj, S., Schawinski, K., Silk, J., & Shabala, S. S. 2010, ArXiv e-prints
Kellermann, K. I., Sramek, R., Schmidt, M., Shaffer, D. B., & Green, R. 1989, AJ, 98, 1195
Kennicutt, Jr., R. C. 1998, ApJ, 498, 541
Kennicutt, Jr., R. C., Bresolin, F., & Garnett, D. R. 2003, ApJ, 591, 801
Kennicutt, Jr., R. C. & Garnett, D. R. 1996, ApJ, 456, 504
Kewley, L. J. & Dopita, M. A. 2002, ApJS, 142, 35
Kewley, L. J., Dopita, M. A., Sutherland, R. S., Heisler, C. A., & Trevena, J. 2001, ApJ, 556, 121
Kewley, L. J. & Ellison, S. L. 2008, ApJ, 681, 1183
Kewley, L. J., Groves, B., Kauffmann, G., & Heckman, T. 2006, MNRAS, 372, 961
Kewley, L. J., Rupke, D., Jabran Zahid, H., Geller, M. J., & Barton, E. J. 2010, ApJ, 721, L48
Köhler, T., Groote, D., Reimers, D., & Wisotzki, L. 1997, A&A, 325, 502
Krist, J. 1995, in Astronomical Society of the Pacific Conference Series, Vol. 77, Astronomical Data Analysis Software and Systems IV, ed. R. A. Shaw, H. E. Payne, & J. J. E. Hayes, 349–+
Kuhlbrodt, B., Wisotzki, L., & Jahnke, K. 2004, MNRAS, 349, 1027
Lacy, M., Sajina, A., Petric, A. O., et al. 2007, ApJ, 669, L61

Lavalley, M., Isobe, T., & Feigelson, E. 1992, in Astronomical Society of the Pacific Conference Series, Vol. 25, Astronomical Data Analysis Software and Systems I, ed. D. M. Worrall, C. Biemesderfer, & J. Barnes, 245–+
Lawrence, A. 1991, MNRAS, 252, 586
LeFevre, O., Saisse, M., Mancini, D., et al. 2003, in Society of Photo-Optical Instrumentation Engineers (SPIE) Conference Series, Vol. 4841, Society of Photo-Optical Instrumentation Engineers (SPIE) Conference Series, ed. M. Iye & A. F. M. Moorwood, 1670–1681
Letawe, G., Magain, P., Courbin, F., et al. 2007, MNRAS, 378, 83
Li, C., Kauffmann, G., Heckman, T. M., White, S. D. M., & Jing, Y. P. 2008, MNRAS, 385, 1915
Liang, Y. C., Yin, S. Y., Hammer, F., et al. 2006, ApJ, 652, 257
Lípari, S., Bergmann, M., Sanchez, S. F., et al. 2009, MNRAS, 398, 658
Lipari, S., Sanchez, S. F., Bergmann, M., et al. 2009, MNRAS, 392, 1295
Macchetto, F., Pastoriza, M., Caon, N., et al. 1996, A&AS, 120, 463
Magrini, L., Vílchez, J. M., Mampaso, A., Corradi, R. L. M., & Leisy, P. 2007, A&A, 470, 865
Martin, D. C., Wyder, T. K., Schiminovich, D., et al. 2007, ApJS, 173, 342
Martin, P. & Roy, J. 1994, ApJ, 424, 599
Martins, L. P., González Delgado, R. M., Leitherer, C., Cerviño, M., & Hauschildt, P. 2005, MNRAS, 358, 49
Mateus, A., Sodré, L., Cid Fernandes, R., et al. 2006, MNRAS, 370, 721
McCall, M. L., Rybski, P. M., & Shields, G. A. 1985, ApJS, 57, 1
McDermid, R. M., Emsellem, E., Shapiro, K. L., et al. 2006, MNRAS, 373, 906
Montuori, M., Di Matteo, P., Lehnert, M. D., Combes, F., & Semelin, B. 2010, A&A, 518, A56+
Morganti, R., Tadhunter, C. N., Dickson, R., & Shaw, M. 1997, A&A, 326, 130
Moy, E. & Rocca-Volmerange, B. 2002, A&A, 383, 46
Mulchaey, J. S., Koratkar, A., Ward, M. J., et al. 1994, ApJ, 436, 586
Mulchaey, J. S., Wilson, A. S., & Tsvetanov, Z. 1996, ApJS, 102, 309
Nandra, K., Georgakakis, A., Willmer, C. N. A., et al. 2007, ApJ, 660, L11
Netzer, H., Mainieri, V., Rosati, P., & Trakhtenbrot, B. 2006, A&A, 453, 525
Netzer, H., Shemmer, O., Maiolino, R., et al. 2004, ApJ, 614, 558
Osterbrock, D. E. & Ferland, G. J. 2006, Astrophysics of gaseous nebulae and active galactic nuclei (2nd. ed. by D.E. Osterbrock and G.J. Ferland. Sausalito, CA: University Science Books, 2006)
Pagel, B. E. J., Edmunds, M. G., Blackwell, D. E., Chun, M. S., & Smith, G. 1979, MNRAS, 189, 95
Pagel, B. E. J., Edmunds, M. G., & Smith, G. 1980, MNRAS, 193, 219
Peeples, M. S., Pogge, R. W., & Stanek, K. Z. 2009, ApJ, 695, 259
Peng, C. Y., Ho, L. C., Impey, C. D., & Rix, H.-W. 2002, AJ, 124, 266
Pérez-Montero, E. & Díaz, A. I. 2005, MNRAS, 361, 1063
Pettini, M. & Pagel, B. E. J. 2004, MNRAS, 348, L59
Pilyugin, L. S. 2001, A&A, 369, 594
Pilyugin, L. S. & Thuan, T. X. 2005, ApJ, 631, 231
Pogge, R. W. 1988a, ApJ, 328, 519
Pogge, R. W. 1988b, ApJ, 332, 702
Pracy, M. B., Kuntschner, H., Couch, W. J., et al. 2009, MNRAS, 396, 1349
Punsly, B. & Zhang, S. 2011, ArXiv e-prints
Reichard, T. A., Heckman, T. M., Rudnick, G., et al. 2009, ApJ, 691, 1005
Reimers, D., Koehler, T., & Wisotzki, L. 1996, A&AS, 115, 235
Rix, H. & Rieke, M. J. 1993, ApJ, 418, 123
Rodrigues, M., Hammer, F., Flores, H., et al. 2008, A&A, 492, 371
Rosales-Ortega, F. F., Kennicutt, R. C., Sánchez, S. F., et al. 2010, MNRAS, 405, 735
Rosario, D. J., Whittle, M., Nelson, C. H., & Wilson, A. S. 2010, ApJ, 711, L94
Rupke, D. S. N., Kewley, L. J., & Chien, L. 2010, ApJ, 723, 1255
Rupke, D. S. N., Veilleux, S., & Baker, A. J. 2008, ApJ, 674, 172
Salim, S., Rich, R. M., Charlot, S., et al. 2007, ApJS, 173, 267
Sánchez, S. F. 2006, AN, 327, 850
Sánchez, S. F., Garcia-Lorenzo, B., Mediavilla, E., González-Serrano, J. I., & Christensen, L. 2004a, ApJ, 615, 156
Sánchez, S. F., Jahnke, K., Wisotzki, L., et al. 2004b, ApJ, 614, 586
Sanders, D. B., Soifer, B. T., Elias, J. H., et al. 1988a, ApJ, 325, 74
Sanders, D. B., Soifer, B. T., Elias, J. H., Neugebauer, G., & Matthews, K. 1988b, ApJ, 328, L35
Sarzi, M., Falcón-Barroso, J., Davies, R. L., et al. 2006, MNRAS, 366, 1151
Schawinski, K., Dowlin, N., Thomas, D., Urry, C. M., & Edmondson, E. 2010a, ApJ, 714, L108
Schawinski, K., Urry, C. M., Virani, S., et al. 2010b, ApJ, 711, 284
Schlegel, D. J., Finkbeiner, D. P., & Davis, M. 1998, ApJ, 500, 525
Schmitt, H. R., Donley, J. L., Antonucci, R. R. J., Hutchings, J. B., & Kinney, A. L. 2003a, ApJS, 148, 327
Schmitt, H. R., Donley, J. L., Antonucci, R. R. J., et al. 2003b, ApJ, 597, 768
Schramm, M., Wisotzki, L., & Jahnke, K. 2008, A&A, 478, 311
Schulze, A., Wisotzki, L., & Husemann, B. 2009, A&A, 507, 781
Schweitzer, M., Lutz, D., Sturm, E., et al. 2006, ApJ, 649, 79
Simard, L., Willmer, C. N. A., Vogt, N. P., et al. 2002, ApJS, 142, 1
Sol Alonso, M., Michel-Dansac, L., & Lambas, D. G. 2010, A&A, 514, A57+
Somerville, R. S., Hopkins, P. F., Cox, T. J., Robertson, B. E., & Hernquist, L. 2008, MNRAS, 391, 481
Springel, V., Di Matteo, T., & Hernquist, L. 2005, ApJ, 620, L79
Storchi-Bergmann, T. & Bonatto, C. J. 1991, MNRAS, 250, 138
Storchi-Bergmann, T., Calzetti, D., & Kinney, A. L. 1994, ApJ, 429, 572
Storchi-Bergmann, T., Schmitt, H. R., Calzetti, D., & Kinney, A. L. 1998, AJ, 115, 909
Storchi-Bergmann, T., Wilson, A. S., & Baldwin, J. A. 1992, ApJ, 396, 45
Sullivan, M., Mobasher, B., Chan, B., et al. 2001, ApJ, 558, 72
Tal, T., van Dokkum, P. G., Nelan, J., & Bezanson, R. 2009, AJ, 138, 1417
Trager, S. C., Faber, S. M., Worthey, G., & González, J. J. 2000, AJ, 119, 1645
Tremonti, C. A., Heckman, T. M., Kauffmann, G., et al. 2004, ApJ, 613, 898
Trinchieri, G. & di Serego Alighieri, S. 1991, AJ, 101, 1647
Trouille, L. & Barger, A. J. 2010, ApJ, 722, 212
Valdes, F., Gupta, R., Rose, J. A., Singh, H. P., & Bell, D. J. 2004, ApJS, 152, 251
Veilleux, S. & Osterbrock, D. E. 1987, ApJS, 63, 295
Viironen, K., Delgado-Inglada, G., Mampaso, A., Magrini, L., & Corradi, R. L. M. 2007, MNRAS, 381, 1719
Vila-Costas, M. B. & Edmunds, M. G. 1992, MNRAS, 259, 121
Villar-Martín, M., Tadhunter, C., Morganti, R., Axon, D., & Koekemoer, A. 1999, MNRAS, 307, 24
Wild, V., Heckman, T., & Charlot, S. 2010, MNRAS, 405, 933
Wisotzki, L., Becker, T., Christensen, L., et al. 2003, A&A, 408, 455
Wisotzki, L., Christlieb, N., Bade, N., et al. 2000, A&A, 358, 77
Wisotzki, L., Koehler, T., Groote, D., & Reimers, D. 1996, A&AS, 115, 227
Worthey, G. 1994, ApJS, 95, 107
Wright, E. L. 2006, PASP, 118, 1711
Zakamska, N. L., Strauss, M. A., Krolik, J. H., et al. 2003, AJ, 126, 2125
Zakamska, N. L., Strauss, M. A., Krolik, J. H., et al. 2006, AJ, 132, 1496
Zaritsky, D., Kennicutt, Jr., R. C., & Huchra, J. P. 1994, ApJ, 420, 87

Chapter 5

The low-metallicity QSO HE 2158−0107: A phase of galaxy and BH growth due to cold gas accretion?⋆

Bernd Husemann[1], Lutz Wisotzki[1], Knud Jahnke[2], and Sebastian F. Sánchez[3]

[1] Astrophysikalisches Institut Potsdam, An der Sternwarte 16, 14482 Potsdam, Germany
[2] Max-Planck-Institut für Astronomie, Königsstuhl 17, D-69117 Heidelberg, Germany
[3] Centro Astronómico Hispano Alemán de Calar Alto (CSIC-MPIA), E-4004 Almería, Spain

ABSTRACT

The metallicities of Active Galactic Nuclei (AGN) are usually well above solar in their Narrow-Line Regions (NLR), often reaching up to several times solar in their Broad-Line Regions (BLR) independent of redshift. Low-metallicity AGN are rare objects which have so far always been associated with low-mass galaxies hosting low-mass black holes ($M_{\rm BH} \lesssim 10^6 {\rm M}_\odot$). In this Chapter we present integral field spectroscopy data of the low-metallicity QSO HE 2158−0107 at $z = 0.212$, where we find strong evidence for sub-solar NLR metallicities associated with a massive black hole ($M_{\rm BH} \sim 3 \times 10^8 {\rm M}_\odot$). This interesting QSO is surrounded by a large extended emission line region extending out to 30 kpc from the QSO in a tail-like geometry. We present optical and near-infrared images and investigate the properties of the host galaxy. The host of HE 2158−0107 is most likely a very compact bulge-dominated galaxies with a size of $r_{\rm e} \sim 1.4$ kpc. The multi-colour SED of the host is rather blue, indicative of a significant young or intermediate age stellar population formed within the last 1 Gyr. A 3σ upper limit of $L_{{\rm bulge},H} < 4.5 \times 10^{10} L_{\odot,H}$ for the H band luminosity and a corresponding stellar mass upper limit of $M_{\rm bulge} < 3.4 \times 10^{10} {\rm M}_\odot$ show that the host is offset from the local BH-bulge relations. This is independently supported by the kinematics of the gas. Although the stellar mass of the host galaxy is lower than expected, it cannot explain the extraordinarily low metallicity of the gas. An external origin is favoured and we speculate that cold gas accretion may be the most likely mechanism for this particular object. Since this process would occur rarely at low redshift for a galaxy of the this mass, we tentatively suggest HE 2158−0107 as a laboratory to study the growth of galaxies and BHs due to cold accretion in more detail at low redshift.

5.1. Introduction

Active Galactic Nuclei (AGN) are thought to be powered by the accretion of ambient gas onto a supermassive Black Hole (BH) in the centre of their host galaxies. Because AGN can reach high luminosities for the most massive BHs ($M_{\rm BH} \sim 10^{10} {\rm M}_\odot$), they can be observed as Quasi-Stellar Objects (QSOs) up to redshifts beyond $z > 6$ (Fan et al. 2003). The emission lines in the Broad Line Regions (BLR) and the Narrow Line Regions (NLR) of AGN can be used to infer gas metallicities (e.g. Hamann & Ferland 1993). QSOs are therefore considered as an import diagnostic for the metal enrichment and evolution of galaxies across cosmic time (e.g. Matteucci & Padovani 1993; Hamann & Ferland 1993, 1999). The metallicities in the BLR were found to be super solar, reaching $10 Z_\odot$ in some cases, and to be correlated with either the AGN luminosity, accretion rate, or BH mass (e.g. Hamann & Ferland 1993; Shemmer et al. 2004; Warner et al. 2004; Nagao et al. 2006; Matsuoka et al. 2011) showing almost no redshift evolution. This is usually interpreted in terms of vigorous star formation building up the most massive galaxies in which BHs reside and grow.

Because the BLR is confined to the very circumnuclear region on scales of $\lesssim$1 pc (e.g. Kaspi et al. 2000), it is not yet clear how the BLR metallicities are linked to the evolution of their host galaxies. The Narrow Line Region (NLR), on the other hand, is spatially extended on kpc scales (e.g. Bennert et al. 2002; Schmitt et al. 2003; Bennert et al. 2006a,b; Husemann et al. 2008) and is certainly more representative of the host galaxy properties. Emission-line ratios in nearby AGN are readily observable and their emission-line ratio have been calibrated to metal abundances via photoionisation models (e.g. Storchi-Bergmann et al. 1998; Groves et al. 2004). Systematic studies of obscured AGN by Groves et al. (2006) and Barth et al. (2008), based on spectroscopic data of the Sloan Digital Sky Survey (SDSS, York et al. 2000), revealed that AGN with NLR metallicities around solar and below are extremely rare and only found in low-mass galaxies hosting BHs with $M_{\rm BH} \lesssim 10^6 {\rm M}_\odot$. Only a few percent of all luminous AGN are found in host galaxies with stellar masses less than $10^{10} {\rm M}_\odot$ (e.g. Kauffmann et al. 2003). The BH mass-bulge mass relation Häring & Rix (2004) combined with the mass-metallicity relation of galaxies (e.g. Tremonti et al. 2004) thus naturally explains the rareness of low-metallicity AGN.

The QSO HE 2158−0107 at $z = 0.212$ was discovered by the Hamburg-ESO survey (HES, Wisotzki et al. 2000). A ra-

⋆ This Chapter is currently in press as an article in the journal *Astronomy and Astrophysics*: Husemann et al. A&A, in press, DOI 10.1051/0004-6361/201117596 reproduced with permission ©ESO. Please note that due to the referee process of the corresponding article in press some parts (including the title) of the present version in this PhD thesis differ from that of the journal article.

dio flux of 1.6 mJy was detected by the FIRST survey (Becker et al. 1995) for this QSOs. In relation to its optical brightness $m_B = 16.69$ the object is classified as a radio-quiet QSO. SDSS targeted this QSO due to its X-ray and radio properties as well and catalogued it as SDSS J220103.2-005300. It is also listed in the QSO catalogue of Véron-Cetty & Véron (2010), but not in the catalogue of Schneider et al. (2010). The public SDSS spectrum of this particular QSO is of rather poor quality. We already presented integral field spectroscopy for HE 2158−0107 in Chapter 3 as part of a larger sample of QSOs among which the objects stuck out by its exceptionally large nebula of ionised gas. In this paper we present evidence for HE 2158−0107 being a low-metallicity QSO for its high BH mass. We combine our spectrophotometry with archival optical and infrared photometry to explore the properties of this particular QSO in more detail.

Throughout this paper we assume a cosmological model with $H_0 = 70\,\mathrm{km\,s^{-1}\,Mpc^{-1}}$, $\Omega_\mathrm{m} = 0.3$, and $\Omega_\Lambda = 0.7$. The adopted cosmology corresponds to a physical scale of 3.45 kpc arcsec^{-1} at the redshift of HE 2158−0107 ($z = 0.212$). We will always use the AB system (Oke 1974) troughout this Chapter or explicitly refer to Vega magnitudes if required for the sake of comparison.

5.2. Observations and data reduction

5.2.1. Integral field spectroscopy

We observed HE 2158−0107 with the Potsdam Multi-Aperture Spectro-Photometer (PMAS, Roth et al. 2005) mounted on the 3.5 m telescope of the Calar Alto Observatory in the night of September 6th, 2002, as part of a larger sample of radio-quiet QSO host galaxy (see Chapter 3). Two exposures of 1800 sec each were obtained under photometric conditions at a seeing of 1.″1.

In the lens array configuration of PMAS we covered an 8″ × 8″ Field-Of-View (FOV) centred on the QSO. 256 individual spectra were obtained at a spatial sampling of 0.″5 × 0.″5. The low resolution V300 grism was positioned such that the Hβ and Hα emission-line could be covered in a single exposure. We determined a spectral resolution for this instrumental setup of $R \sim 900$ from a O I λ5577 night sky line width of 6.1 Å FWHM.

The reduction of the integral field data was done with the `R3D package` (Sánchez 2006). Here we just briefly outline the process as the details are described in Chapter 3 where the entire dataset is presented. We used the continuum and arc lamp calibration frames taken specifically for the target, at the same time and airmass, to trace and extract the 256 spectra on the CCD and to perform an absolute wavelength calibration. Twilight observation were obtained to construct a fibre flat-field to correct for the difference in fibre-to-fibre transmission. Photometric standard star observations allowed an absolute photometric calibration of the data including the correction for the atmospheric extinction at the Calar Alto site (Sánchez et al. 2007). A high S/N sky spectrum was extracted from a blank sky area *within* the PMAS FOV, which we subsequently subtracted from the entire datacube. After correcting for differential atmospheric refraction we spatially aligned the two exposures and co-added both to obtain the final datacube.

5.2.2. Near-Infrared and optical ground-based imaging

An *H* band image of HE 2158−0107 was acquired with the SOFI IR spectrograph and imaging camera (Moorwood et al. 1998) mounted on the New Technology Telescope of the La Silla Observatory (program 70.B-0418; PI: L. Wisotzki). Ten exposures were taken in the large field camera mode (0.″29 pixel^{-1}) that consists of 12 sub-integrations (NDIT) with exposure times of 5 sec (DIT) each, yielding a total integration time of 600 sec on the source. The seeing during the observation was 0.″8. We reduced these images with standard calibration frames using the public SOFI reduction pipeline provided by ESO. We measured an *H* band magnitude of 14.67 mag (Vega) for the QSO which is quite close to the value of 14.70 mag (Vega) reported by UKIDSS (Warren et al. 2007) and indicates a good photometric calibration of the image.

Table 5.1. Properties of the SDSS Stripe 82 images

Band	Seeing [″]	SFB limit [mag arcsec^{-2}]	A [mag]
u	1.4	26.88	0.38
g	1.2	27.54	0.28
r	1.1	27.60	0.20
i	1.0	26.94	0.15
z	1.0	25.60	0.10

Fortunately, HE 2158−0107 is in the footprint of the Supernova Survey as part of SDSS (Adelman-McCarthy et al. 2008, for DR7), which covered 270 deg^2 (a 2.5° wide scan along the celestial equator, generally called "Stripe 82") that were observed ∼80 times in the autumn of the years 1998–2007. We stacked the multiple epoch exposures in order to reach significantly deeper. This method was already applied to Stripe 82 data for precise photometry of galaxies (Gilbank et al. 2010) and to study details in the structure of nearby galaxies (Schawinski et al. 2010). Since observations of Stripe 82 were done under various ambient conditions, we co-added only the best 24 epochs with a seeing of <1.″3 and a limiting sky surface brightness of >20 mag arcsec^{-2} in the *r* band. The combined images effectively reach ∼5 times deeper (∼2 mag) compared to the individual SDSS images. Table 5.1 summarises the effective seeing and limiting surface brightness for the combined images as well as the Galactic extinction inferred from the Schlegel et al. (1998) extinction maps.

5.3. Black hole mass and NLR metallicity

5.3.1. QSO spectrum of HE 2158−0107

We first obtained the nuclear spectrum of HE 2158−0107 from the PMAS observation using a collapsed image of the datacube as a spatial weighting profile for the extraction. The resulting QSO spectrum with a S/N of about 100 per pixel in the continuum is shown in Fig. 5.1. Prominent broad Hβ and Hα emission lines are visible as well as narrow emission lines from the NLR. From the narrow [O III] λ5007 ([O III] hereafter) in the QSO spectrum we measured a redshift of $z = 0.2118$.

The synthetic *r* band magnitude of the spectrum is brighter by only 0.13 mag than the SDSS photometric *r* band magnitude, which might be caused by the intrinsic variability of QSOs and indicates a good absolute spectrophotometric calibration of the PMAS data. The Fe II complexes blue- and redward of Hβ (e.g. Boroson & Green 1992) are very weak and do not contribute significantly to the QSO pseudo-continuum. We find evidence for the presence of the Mg I λ5166 stellar absorption line at the corresponding rest-frame wavelength (see inset in Fig. 5.1). Thus, the QSO spectrum is contaminated by a small fraction of stellar light from the underlying host galaxy.

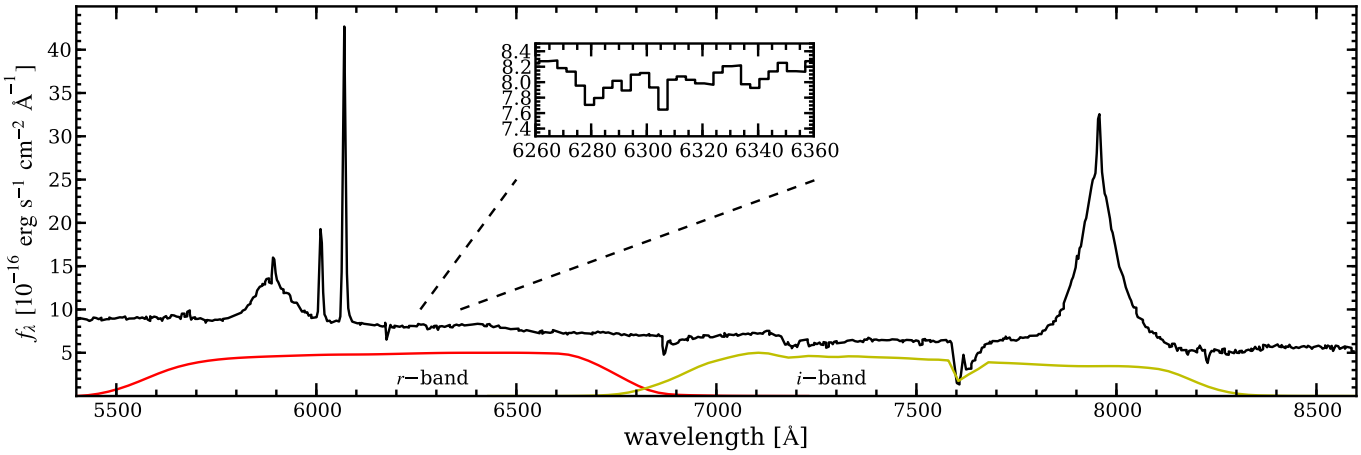

Fig. 5.1. Integrated QSO spectrum of HE 2158−0107 as observed with PMAS integral field spectrograph. The inset is a zoom into the wavelength region of the Mg I absorption line at the rest-frame of the QSO. The red and yellow curves below the QSO spectrum represent the arbitrarily scaled *r* and *i* band transmission curves, respectively.

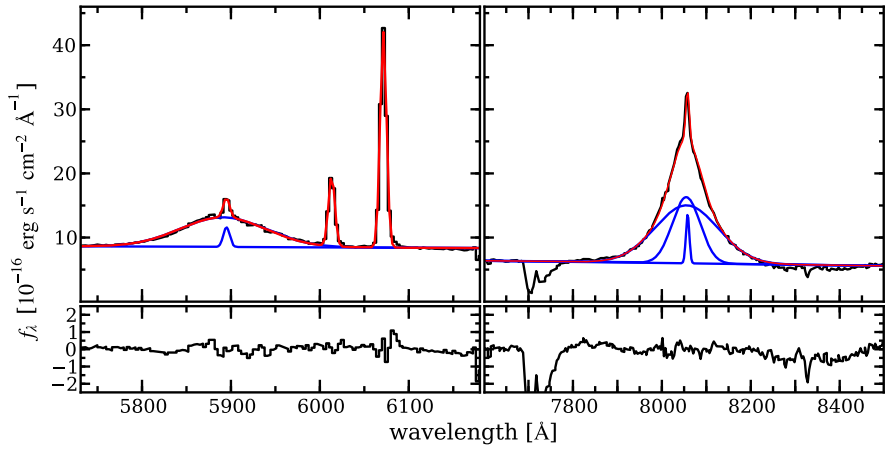

Fig. 5.2. Modelling of the broad Hβ (left panel) and Hα line (right panel). The red line represents the best-fit model to the data (black line) composed of individual Gaussians and a straight to approximate the local continuum. Individual Gaussian components for the Balmer lines are shown as blue lines above the continuum for a visual impression of their relative contribution. The residuals of the best-fit model are displayed in the panels below. Two telluric absorption bands of the Earth's atmosphere are visible at 7700–7800Å and 8250–8450Å.

5.3.2. Virial BH mass estimate

BH masses of QSOs can be estimated from their single epoch spectra via the so-called virial method (Peterson & Wandel 2000; Vestergaard 2002). The method combines the empirically derived size-luminosity relation for the BLR, determined via reverberation mapping (e.g. Kaspi et al. 2000; Peterson et al. 2004; Kaspi et al. 2005; Bentz et al. 2006, 2009), and assuming virialised motion of the BLR clouds that can be inferred from the broad line width.

We used the formula derived by Schulze & Wisotzki (2010),

$$M_{\rm BH} = 2.57 \times 10^7 \left(\frac{\sigma_{\rm H\beta}}{1000\,{\rm km\,s^{-1}}}\right)^2 \left(\frac{L_{5100}}{10^{44}{\rm erg\,s^{-1}}}\right)^{0.52} {\rm M}_\odot\,, \quad (5.1)$$

where $\sigma_{\rm H\beta}$ is the line dispersion of the broad Hβ line and L_{5100} is the continuum luminosity at 5100 Å. Equation (5.1) is derived from the empirical relation between the BLR size and the continuum luminosity as calibrated by Bentz et al. (2009) combined with the prescription by Collin et al. (2006) to infer the virial motions from $\sigma_{\rm H\beta}$ adopting a virial coefficient of 3.85. By modelling the QSO spectrum with multiple Gaussians for the emission lines and a straight line for the local continuum (Fig. 5.2, left panel), we measured an Hβ line dispersion of $\sigma_{\rm H\beta} = 2320 \pm 20\,{\rm km\,s^{-1}}$, excluding any NLR component, and a continuum luminosity of $\lambda L_\lambda(5100) = (8.0 \pm 0.3) \times 10^{44}\,{\rm erg\,s^{-1}}$. From those measurements we estimated a BH mass of $\log(M_{\rm BH}/{\rm M}_\odot) = 8.6 \pm 0.3$ for HE 2158−0107.

Greene & Ho (2005b) derived an alternative $M_{\rm BH}$ calibration based on the broad Hα line luminosity and width, which is less sensitive to host galaxy light contamination and also less susceptible to dust extinction,

$$M_{\rm BH} = 3.0 \times 10^6 \left(\frac{{\rm FWHM_{H\alpha}}}{1000\,{\rm km\,s^{-1}}}\right)^{2.06} \left(\frac{L_{\rm H\alpha}}{10^{42}\,{\rm erg\,s^{-1}}}\right)^{0.45} {\rm M}_\odot\,. \quad (5.2)$$

We modelled the Hα line with multiple Gaussian components (Fig. 5.2, right panel) and measured an Hα luminosity of $(3.6 \pm 0.4) \times 10^{43}\,{\rm erg\,s^{-1}}$ and a FWHM of $3860 \pm 70\,{\rm km\,s^{-1}}$ excluding the NLR narrow component. This yields a BH mass of $\log(M_{\rm BH}/{\rm M}_\odot) = 8.4 \pm 0.3$ with Eq. (5.2). Although the broad Hβ line could be well approximated by a single Gaussian component, the Hα model required two Gaussian components due to its extended wings that are not seen for Hβ. A difference in the line profiles is expected, because the FWHM of Hβ is systematically broader than Hα (e.g. Greene & Ho 2007; Schulze & Wisotzki 2010).

Both BH mass estimates differ only by 0.2 dex and are well consistent with each other assuming a canonical systematic uncertainty of ∼0.3 dex for virial $M_{\rm BH}$ estimates. This shows that a high-mass BH powers the QSO nucleus of HE 2158−0107. We adopt the average of both estimate, $\log(M_{\rm BH}/{\rm M}_\odot) = 8.5 \pm 0.3$, for the rest of this Chapter.

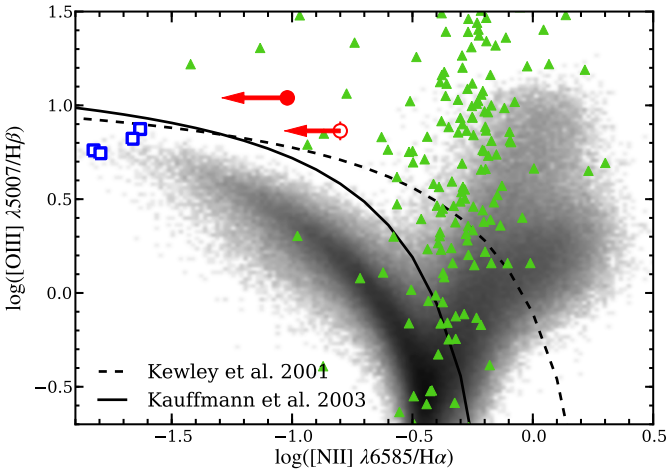

Fig. 5.3. Standard BPT emission-line ratio diagram for HE 2158−0107. The measured line ratios of the NLR (filled red circle) and the EELR (opened red circle) are shown for the $3\,\sigma$ limits on log([N II]/Hα) and the length of the arrows are such that their tip corresponds to the $1\,\sigma$ limit. The distribution of emission-line ratios for ∼40000 randomly selected SDSS galaxies are indicated by the grey scale for comparison. Triangle symbols indicate the NLR line ratio for a sample of AGN with low BH masses (Greene & Ho 2005b) and blue opened squares represent four candidate low-metallicity AGN in dwarf galaxies as reported by Izotov & Thuan (2008) and Izotov et al. (2010).

5.3.3. Evidence for an exceptionally low NLR gas-phase metallicity

The estimated BH mass for HE 2158−0107 implies an expected bulge mass of $\log(M_{\rm bulge}/{\rm M}_\odot) = 11.3 \pm 0.3$ for its host adopting the empirical $M_{\rm BH}$-$M_{\rm bulge}$ relation of Häring & Rix (2004). If the host galaxy has a substantial disc, the total mass of the system would even be higher, depending on the bulge-to-disc ratio. Galaxies with such a high stellar mass have generally gas-phase metallicities that are super solar. The mean mass-metallicity relation by (Tremonti et al. 2004) gives $\log({\rm O/H}) - 12 = 9.13 \pm 0.2$ at our estimated stellar mass. In the case of the AGN photoionised NLR region, the [N II]/Hα line ratio is a good tracer for the gas-phase metallicity as calibrated with state of the art photoionisation codes (e.g. Storchi-Bergmann et al. 1998; Groves et al. 2004, 2006).

The QSO spectrum of HE 2158−0107 displays prominent narrow emission lines from the NLR and we included also Gaussian components for the narrow [N II] $\lambda\lambda$6548, 6583 emission line doublet to the model of the Hα line (see Fig. 5.2). However, the presence of any [N II] λ6583 ([N II] herafter) is not really clear. It is likely that the [N II] line is actually below our detection limit considering the low spectral resolution and the blending with the underlying broad Hα line. In order to determine a realistic detection limit for the [N II] line, we performed Monte-Carlo simulation as described in Appendix F. From those simulations we determine a robust 3σ upper limit of $\log([{\rm N\,II}]/{\rm H}\alpha) < -1.0$ ($\log([{\rm N\,II}]/{\rm H}\alpha) < -1.2$ at $1\,\sigma$). The location of the NLR of HE 2158−0107 in the log([O III]/Hβ) vs. log([N II]/Hα) diagram, the so-called BPT diagnostic diagram (Baldwin et al. 1981), is shown in Fig. 5.3. The line ratios place the NLR in the domain of AGN ionisation above the Kewley et al. (2001) and Kauffmann et al. (2003) demarcation curves as expected, but are significantly offset from the local population of AGN towards a much lower [N II]/Hα line ratio. With the abundance calibrations of Storchi-Bergmann et al. (1998) we infer an upper limit of $\log({\rm O/H}) - 12 < 8.4$ for the oxygen abundance in the NLR of HE 2158−0107 based on the [O III]/Hβ and [N II]/Hα line ratios and assuming a canonical electron density for the NLR of $n_{\rm e} \sim 1000\,{\rm cm}^{-3}$. This oxygen abundance corresponds to $Z < 0.5 Z_\odot$ and also agrees with the gas-phase metallicity of the Groves et al. (2006) photoionisation models.

That the exceptionally low [N II]/Hα line ratio is not caused by the blending with the broad Hα line is further supported by line ratios of an Extended Emission Line Region (EELR) that we resolved around the QSO (Fig. 5.4). We employed our software tool `QDeblend`^{3D} for the deblending of the QSO and extended emission using an iterative algorithm improving the technique introduced by Christensen et al. (2006). Details on the algorithm can be found in the `QDeblend`^{3D} manual[1], and its application to the PMAS IFU observation are described in Chapter 3 more detailed. Briefly, a high S/N QSO spectrum from the central spaxel was subtracted from all other spaxels after being scaled to match the broad Balmer lines. Three iterations were performed to empirically decontaminate the QSO spectrum from its host contribution using 8 spaxels surrounding the central QSO spaxel. We extracted a co-added spectrum from a high surface brightness region South-East of the QSO as indicated in Fig. 5.4. No broad emission lines are left in the extended spectrum after we applied our QSO-host deblending proccess, so that the blending of broad and narrow lines is not a problem for the EELR spectrum. The [N II] doublet is still undetected in this spectrum and we determined a 3σ upper limit of [N II]/Hα< −0.8 ([N II]/Hα< −0.94 at 1σ) using the same type of simulation method applied for the QSO spectrum (see Appendix F). The emission-line ratios of the EELR are close to the unresolved NLR in the BPT diagram (Fig. 5.3). It is likely that the AGN is the main ionisation source for the extended emission as well. However, due to the 0.15 dex lower [O III]/Hβ line ratio and the upper limit in [N II]/Hα, we cannot strictly rule out excitation by young massive stars from emission-line diagnostics alone. In either case, the limit on the [N II]/Hα line ratio implies that the gas-phase metallicity must be low over a region of several kpc, suggesting that the low metallicity gas is not confined to the circumnuclear region.

Only very few other AGN with similarly low oxygen abundances in the NLR gas are known to date. Groves et al. (2006) found only 40 low-metallicity AGN among 23 000 Seyfert 2 galaxies, all of which are in low-mass galaxies. Only two of them actually have gas-phase metallicities lower than HE 2158−0107. Greene & Ho (2005b) constructed a sample of low BH mass AGN ($M_{\rm BH} < 2 \times 10^6 {\rm M}_\odot$) and measured the line ratios of the NLR which are shown in Fig. 5.3 for comparison. They also found only 2 AGN with $\log({\rm H}\alpha/[{\rm N\,II}]) < -1.0$ in their NLR. Finally, 4 low-metallicity AGN candidates with $\log({\rm H}\alpha/[{\rm N\,II}]) \sim -1.6$ were reported by Izotov & Thuan (2008) and Izotov et al. (2010), all residing in dwarf galaxies with BH masses in the range of the Greene & Ho sample. In contrast to the other AGN considered so far, those candidate AGN display emission-line ratios in the NLR that are well consistent with classical H II regions powered by massive stars. Therefore, they should be considered as a completely different class of objects.

HE 2158−0107 is the first low-metallicity AGN, to our knowledge, that is associated with a high-luminosity QSO and a high BH mass. Our limiting gas-phase oxygen abundance is 0.7 dex lower than expected for the stellar mass predicted by the BH mass-bulge mass relation. Either the host of HE 2158−0107

[1] http://sourceforge.net/projects/qdeblend/

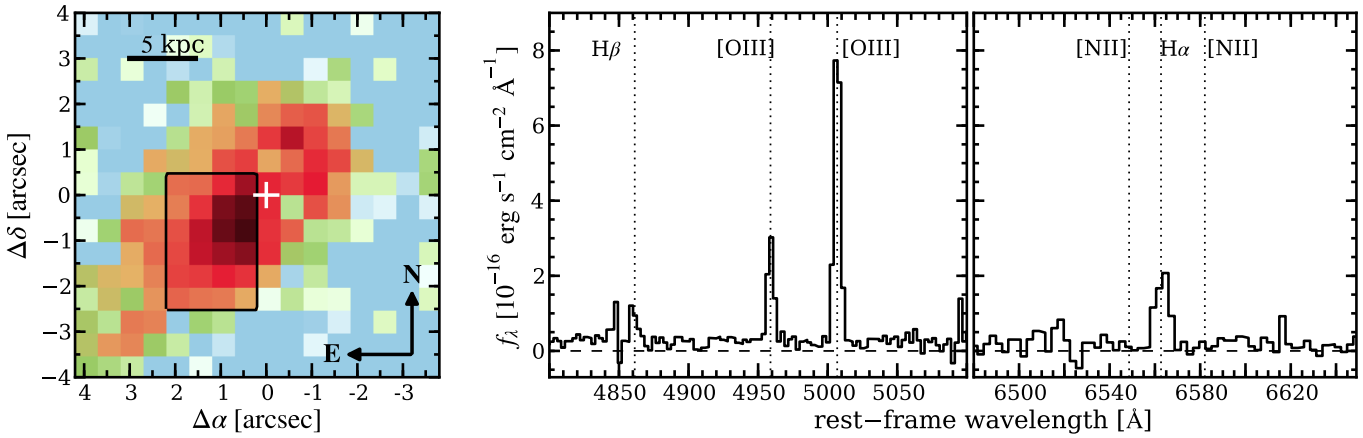

Fig. 5.4. [O III] light distribution and EELR spectrum for HE 2158−0107. *Left panel:* Nucleus-subtracted 40Å wide [O III] narrow-band image as extracted from our PMAS datacube. The position of the QSO is highlighted by the white cross. A black box indicates the boundary for the extraction of a co-added spectrum. *Right panel:* Co-added spectrum of the EELR region as defined in the left panel. The expected wavelengths of various emission-lines are indicated by the vertical dotted lines.

is an extremely rare outlier from the mass-metallicity relation of galaxies, or it is strongly offset from the BH mass-bulge mass relation, or even both. We explore the latter aspect in the next section.

5.4. The multi-colour SED of HE 21584−0107 and its bulge mass

In order to directly constrain the bulge mass and to test whether the host galaxy of HE 2158−0107 is significantly offset from the BH mass-bulge mass relation, we analysed the optical and infrared broad-band images to reconstruct the multi-colour Spectral Energy Distribution (SED) of the host. To do this, the emission of the QSO and the host need to be decomposed, which requires a good characterisation of the Point Spread Function (PSF) in each band.

Two bright stars are close to HE 2158−0107, brighter than the QSO by 2 mag and 1 mag in the r band, respectively. We empirically determined the PSF for each observation from these two stars. Their distances to the QSO of 62″ and 76″ already caused subtle PSF variations with respect to the PSF at the position of the QSO. These variations are particularly strong for the SOFI image taken with the large field objective due to coma (Moorwood et al. 1998). To overcome the limitations imposed by the field variations we analysed their PSF residuals from another star only 18″ away from the QSO, which has a similar r band magnitude. We used the residuals within a radius of 2″ to make an empirical corrections to our two PSF stars. Since all the stars in the SDSS field are at least 0.5 mag fainter than the QSO in the u band, we were not able to construct a useful PSF in this band and excluded it from our analysis.

5.4.1. Results of the QSO-host decomposition

We employed `GALFIT v3.0.2` (Peng et al. 2002, 2010) to decompose the host galaxy and the point-like QSO of HE 2158−0107 by modelling the observed two-dimensional surface brightness (SFB) distribution in the SDSS and SOFI broad-band images with an appropriate model. We considered two different models. Model 1 consists of a PSF only to check whether any detectable signal from the host remains in the residuals even when the QSO contribution is oversubtracted. Model 2 is composed of a de Vaucouleur profile for the presumably bulge-dominated host and a PSF component for the QSO. After trying other models as well, the host turned out to be so faint that we fixed the SFB model of the host to the de Vaucouleur profile to increase the robustness of the `GALFIT` model and the recovered host galaxy magnitudes (e.g. Kim et al. 2008). Although other SFB models for the host galaxy including a disc component might be possible, we emphasise that those models would inevitably lead to a *fainter* bulge component. Hence, our approach provides a robust upper limit for the bulge luminosity.

In Fig. 5.5 we present the results of the QSO-host decomposition. In all cases, except the H band, we resolve the underlying host galaxy and recover the structural properties for our assumed host model. Interestingly, the r and i band host images reveal an extended tail in the light distribution, towards the South-East, that matches with the EELR seen in our PMAS data. We find that the ellipticity ($e \equiv 1 - b/a$) and effective radius r_e of the best-fit de Vaucouleur profile are larger in the r and i bands than the g and z bands. This is expected if line emission of the EELR significantly contributes to the signal of these particular bands (see Fig. 5.1). In order to estimate the emission-line contribution of the EELR to the r and i bands, we synthesised a pure emission-line spectrum for the EELR based on its [O III] flux of $(150 \pm 30) \times 10^{-16}$ erg s^{-1} cm^{-2} within an aperture of 3″ centred on the QSO and the observed line ratios. From the synthetic EELR spectrum we determined an emission-line brightness in the r and i bands of 20.5 ± 0.2 mag and 21.6 ± 0.2 mag, respectively. This corresponds to a substantial emission-line contribution of 18 ± 7% within the central 3″ of the r band and a rest-frame [O III] equivalent width (EW) of EW([O III]) = 170 ± 70 Å given the large width of the r band filter.

Due to the apparently large nucleus-to-host ratio of >10 in the z-band and the small apparent size of the host, it is furthermore import to estimate the systematic errors and to clean the structural parameters and magnitudes from systematic effects. We performed a suite of Monte-Carlo simulations for various nucleus-to-host ratios and five different effective radii for each band. We used one empirical PSF to generate 200 mock images for a given set of parameters and analysed the image subsequently with the other empirical PSF. Detailed information about these simulations are given in Appendix F.

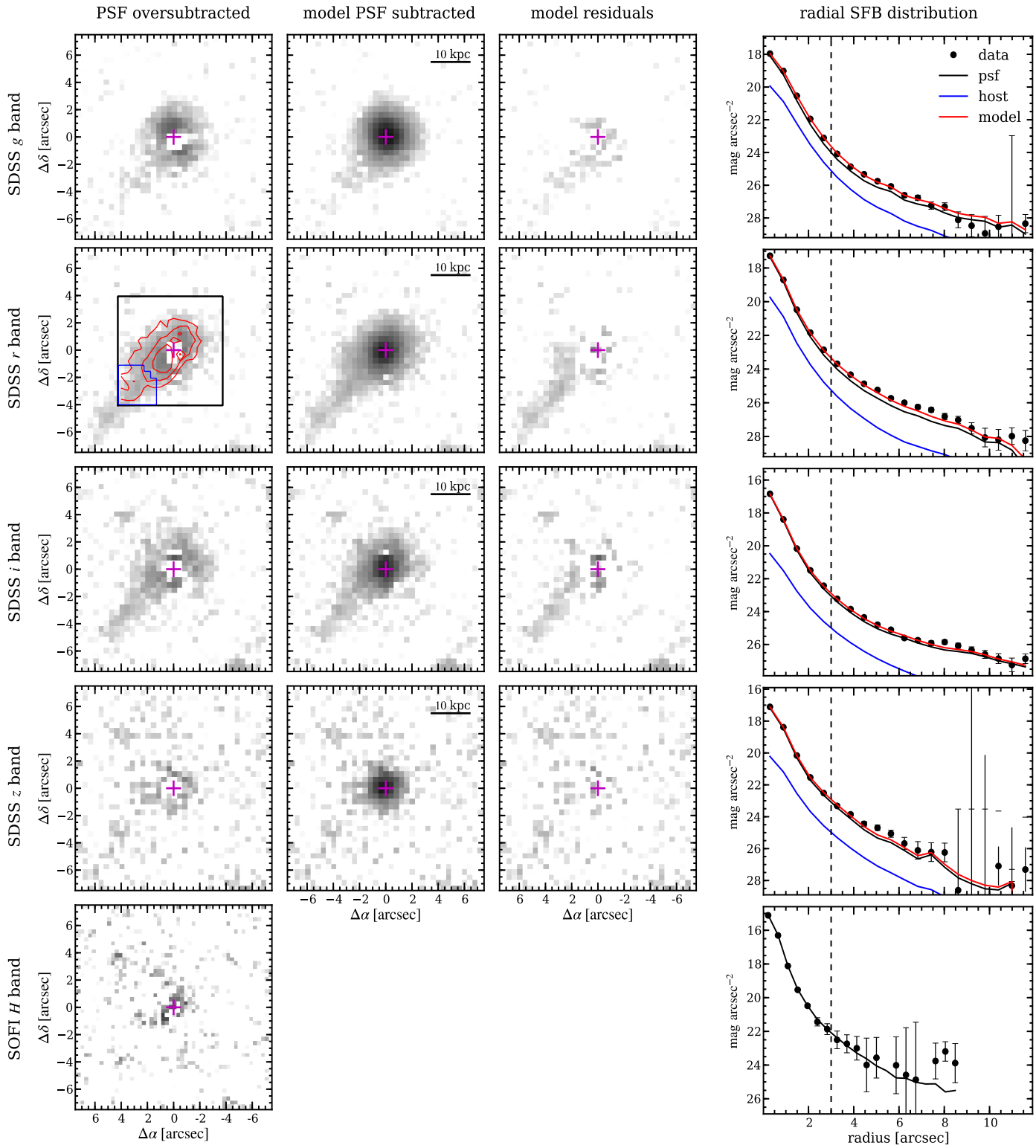

Fig. 5.5. Host galaxy images of HE 2158−0107 after 2D QSO-host decomposition with GALFIT. The first column represents the PSF (over)subtracted host images of the best-fit model including a point source only. The PSF subtracted host images and residuals of the best-fit model, including a point source *and* a de Vaucouleurs profile for the host, are shown in the second and third column, respectively. The radial surface brightness profiles of the data, best-fit model, and their components are presented in the fourth column to highlight the low contrast between nucleus and host. The orientation and position of the PMAS FOV with respect to the QSO is indicated by the black rectangle in the *r* band image and the corresponding PMAS [O III] narrow-band image by the red countours. A certain area covering the tail geometry is defined by the blue boundary within the PMAS FOV as analysed in Sect. 5.4.5

Table 5.2. QSO-host decomposition results corrected for systematics

Passband	$m_{\rm QSO}$ [mag]	$m_{\rm host}$ [mag]	$r_{\rm e}$ [″]	b/a	PA [°]	$m_{\rm host}$ (< 3″) [mag]
SDSS r	16.18 ± 0.01	18.53 ± 0.04	0.52 ± 0.03	0.59	47	18.65 ± 0.04
SDSS i	15.79 ± 0.01	18.71 ± 0.05	0.58 ± 0.06	0.63	40	18.91 ± 0.05
SDSS z	15.99 ± 0.02	18.78 ± 0.11	0.40 ± 0.10	0.90	24	18.89 ± 0.11

The GALFIT results of the best-fit models are listed in Table 5.2 after correcting them for Galactic extinction and for the systematic biases recovered by the simulation. We determined a 3σ upper limit for the host magnitude of $m_{\rm host} > 18.19$ mag in the H band from our simulation. We rejected the g band from our analysis because the decomposition is possibly unreliable due to an intrinsic PSF mismatch between the stars and the QSO in this band. The SEDs of the QSO and stars are so different in the blue part of the spectrum that the "effective" PSF seen in the g band may be dominated by the seeing at shorter wavelengths for the QSO and the seeing at longer wavelengths for the stars. This effect would lead to a slight underestimation of the PSF width based on the stars, which matches with the exceptionally low effective radius of $r_{\rm e} \sim 0\farcs2$ for this band compared to the others.

5.4.2. An SED-based stellar mass estimate

After taking into account the systematics of the two-dimensional QSO-host decomposition, the emission-line contribution, and the foreground Galactic extinction in the different bands, we show the SED of the host galaxy from the *rizH* photometry in Fig. 5.6. Even after subtracting the EELR contribution from the SED, the shape of the SED appears to be very blue. Scattered light of the QSO due to large amounts of dust within the host could significantly contribute to the apparent host light in rest-frame blue and UV bands (e.g. Tadhunter et al. 1992; Zakamska et al. 2006). We thus looked at the *GALEX* UV images of the Medium Imaging Survey for HE 2158−0107. They are consistent with a point source without any asymmetry that would indicate large scale scattered emission. Since the low gas-phase metallicity implies a low dust content anyway, we think that a young stellar population as often found in bulge-dominated QSO hosts (e.g. Kauffmann et al. 2003; Jahnke et al. 2004; Sánchez et al. 2004) accounts for the blue colour.

In order to constrain the stellar population, we modelled the SED with a grid of SSP model spectra from Bruzual & Charlot (2003) with ages in the range of 5 Myr to 17 Gyr and $0.2Z_\odot$, $0.4Z_\odot$, $1Z_\odot$ and $2Z_\odot$ metallicities. A χ^2 test was applied to check which SSPs models were consistent with the photometry at a 95% confidence level. We incorporated the upper limit in the H band by assuming a value of half the limit and a 3σ error matching with the 3σ limit. Given the few photometric data points and their considerable errors we find that formally all SSPs with ages younger than 1 Gyr are consistent with the data. The best-fit SSP of solar metallicity has an age of 100 Myr. From all matching SSP models we constrain a minimum stellar mass of $M_{\rm bulge} > 3.0 \times 10^8_\odot$.

Although the light of the host is apparently dominated by young stars, the mass of the system could still be dominated by an underlying old stellar population. Thus, we determined how much stellar mass in an old 11 Gyr SSP can be *added* to the stellar mass of the young SSP, so that the composite model still obeys the 3σ upper limit of $L_{{\rm bulge},H} < 4.5 \times 10^{10} {\rm L}_{\odot,H}$ in the H band. From all possible combinations we infer a maximum total stellar mass for the host galaxy of $M_{\rm bulge} < 3.4 \times 10^{10}_\odot$. Because the lower mass limit is unphysically low we will ignore it for all our considerations and refer only to the upper limit.

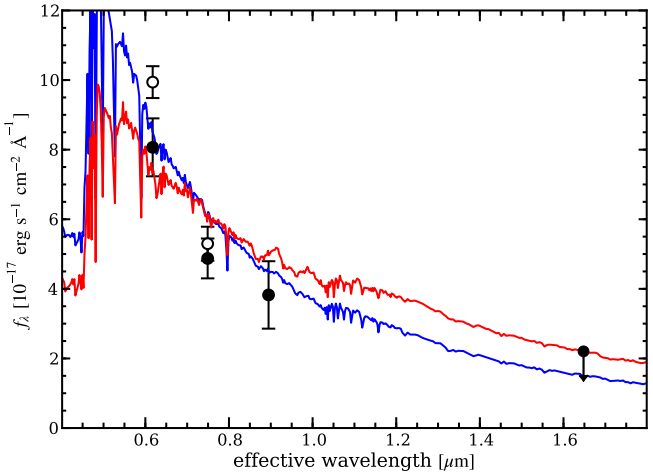

Fig. 5.6. The host SED of HE 2158−0107 within a circular aperture of 3″. Open and filled symbols correspond to the SED with and without the contribution of the emission lines in the r and i band. The best-fit 100 Myr SSP model (blue line) and composite 100 Myr+11 Gyr SSP model (red line) taken from the Bruzual & Charlot (2003) spectra library are shown for comparison.

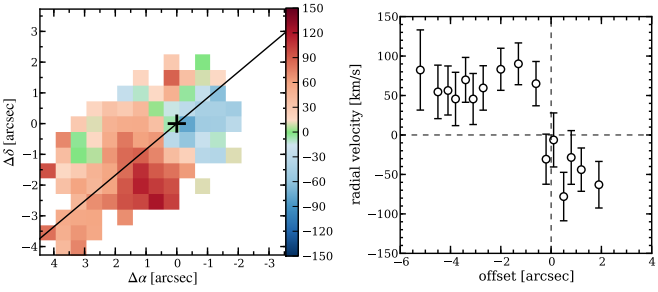

Fig. 5.7. Velocity field of the [O III] EELR around HE 2158−0107. *Left panel:* Radial velocity map inferred from the [O III] emission line Doppler shift with respect to the rest-frame of the QSO. The black and red solid line represent roughly the apparent kinematic major and minor axis. *Right panel:* Radial velocity curves extracted from velocity map along the kinematic major (black symbols) and minor axis (red symbols).

5.4.3. Additional mass constraints from the gas kinematics

In Fig. 5.7 we present the [O III] velocity field of the EELR which we derived by modelling the [O III] doublet lines in each spaxel of the nucleus-subtracted datacube with Gaussian profiles. We

constructed a synthetic longslit curves from the velocity map along the apparent kinematic from all spaxels within ±0.″5 away from that kinematic major axis. The radial Doppler motion of the gas was estimated using the redshift of the spatially unresolved [O III] line as the reference for the QSO rest-frame. From the velocity curve along the major axis we infer a maximum radial velocity of $v_r = 80 \pm 20\,\mathrm{km\,s^{-1}}$ at a radius of 2″ from the nucleus.

Assuming that the velocity field is due to a dynamically cold rotating gas disc within the bulge of the host, we infer a dynamical mass within a radius $R = 7\,\mathrm{kpc}$ (2″) of

$$M_{\mathrm{dyn}} = \frac{R\,v_r^2}{G\sin(i)} \approx \frac{1.6\times10^{10}\mathrm{M}_\odot}{\sin(i)}\,, \tag{5.3}$$

where i is the inclination of the gas disc with respect to our line-of-sight, and G is the gravitational constant. Since the host galaxy has no prominent stellar disc we use the axis ratio of the EELR $b/a = 0.59$ to estimate an inclination of $i = 54°$ assuming an intrinsically circular gas disc. With these rough assumption we determine a best guess dynamical mass of $M_{\mathrm{dyn}} = 2\times10^{10}\mathrm{M}_\odot$, which agrees with our limiting stellar mass from the SED. However, the enclosed dynamical mass depends linearly on the radius. We argue that 7 kpc is a rather conservative assumption for the dynamical mass of the bulge considering its effective radius of $r_{\mathrm{e}} \sim 1.4\,\mathrm{kpc}$ in the z band.

We also tried to estimate the velocity dispersion σ_* of the bulge. Although we cannot directly determine σ_* from the PMAS spectrum of the QSO, Nelson & Whittle (1996) found that in Seyfert galaxies, the dispersion of the [O III] emission line in an unresolved NLR is correlated with σ_*. Thus, Nelson (2000) suggested that $\sigma_{[\mathrm{O\,III}]}$ may be used as a surrogate for σ_*. The [O III] line in the unresolved NLR of HE 2158−0107 can be described by a single Gaussian profile with a line dispersion of $\sigma_{[\mathrm{O\,III}]} = 128 \pm 11\,\mathrm{km\,s^{-1}}$ after subtracting the instrumental ressolution in quadrature. This is only about half of the expected stellar velocity dispersion ($\sigma_* = 245 \pm 44\,\mathrm{km\,s^{-1}}$) from the M_{BH}-σ_* relation (e.g. Gültekin et al. 2009) at the BH mass of HE 2158−0107 ($\log(M_{\mathrm{BH}}/\mathrm{M}_\odot) = 8.5\pm0.3$). The discrepancy remains high even when we account for a potential intrinsic offset $\Delta\sigma = \log(\sigma_*) - \log(\sigma_{[\mathrm{O\,III}]}) = 0.11$ dex as recently found by Ho (2009). Either a significant rotational component contributes to the unresolved NLR kinematics, which would support the EELR gas disc scenario, or M_{bulge} is significantly lower than expected given its BH mass.

5.4.4. Is HE 2158−0107 an outlier from the BH-bulge relations?

Above we collected several independent estimates for the bulge properties of the QSO host. Figure 5.8 highlights the position of HE 2158−0107 in comparison to the M_{BH}-$L_{\mathrm{bulge},H}$ relation of Marconi & Hunt (2003) (left panel), the M_{BH}-M_{bulge} relation of Häring & Rix (2004), and the M_{BH}-σ_* relation studied by Gültekin et al. (2009). We find that this QSO host is offset from the local scaling relations *in all three cases*.

The bulge luminosity $L_{\mathrm{bulge},H}$ is smaller by more than 0.6 dex than the value indicated by the relation. One advantage of the H band is that the K correction (e.g. Oke & Sandage 1968; Hogg et al. 2002) is almost negligible (e.g. Mannucci et al. 2001; Chilingarian et al. 2010) up to $z \sim 0.5$ and largely independent of the galaxy type. We therefore do not expect that this is caused by systematic effect due to the redsift of object. Since we adopted a robust 3σ upper limit for $L_{\mathrm{bulge},H}$, the offset from the relation may even be substantially larger.

It is clear that our estimate for M_{bulge} from the SED is tied to the upper limit in $L_{\mathrm{bulge},H}$ and thus appears similarly offset from the M_{BH}-M_{bulge} relation (middle panel of Fig. 5.8). However, the estimated dynamical mass from the extended gas kinematics is in agreement with the limiting stellar mass, but emphasize a considerable uncertainty of that estimate given the numerous assumption made. Furthermore, the small apparent size of the bulge measured in the z band supports the notion of an undermassive bulge with $M_{\mathrm{bulge}} = (1.4 \pm 0.6)\times10^{10}\mathrm{M}_\odot$ based on the empirical size-mass relation of bulge-dominated galaxies (Shen et al. 2003, 2007). It suggests that the bulge of HE 2158−0107 could be significantly away from M_{BH}-M_{bulge} relation. Deeper high-spatial resolution photometry in the infrared and optical emission-line free bands are however required to accurately determine the SED of the host galaxy and to pin down the bulge luminosity and mass.

The offset in the BH mass-bulge relations appears to be most conspicuous in σ_*. However, the robustness of $\sigma_{[\mathrm{O\,III}]}$ as a surrogate for σ_* is strongly debated as the scatter in the relation is much higher for $\sigma_{[\mathrm{O\,III}]}$ than for σ_* (Shields et al. 2003; Boroson 2005; Greene & Ho 2005a). One major concern is that the circumnuclear gas kinematics probed by the high ionisation [O III] line may significantly affected by AGN outflows or jet-cloud interactions (e.g. Greene & Ho 2005a; Komossa & Xu 2007; Ho 2009).

Each measurement has some drawbacks and would certainly be considered inconclusive individually. Here, we emphasise that *all* the independent results agree with each other and point into the same direction. Nevertheless, the offset of HE 2158−0107 from the M_{BH}-bulge relations is still formally consistent with the intrinsic scatter of the scaling relations except for the velocity dispersion. So far we can refer to HE 2158−0107 only as a candidate outlier from the M_{BH}-bulge relations. The fact that the QSO spectrum is particularly suited to directly measure the *stellar* velocity dispersion from a high S/N spectrum provides a good opportunity to verify and pin down the offset in the future.

5.4.5. The origin of the low-metallicity gas

While there is strong evidence for a significantly lower mass of the host than what would be expected from the M_{BH}, the mass is still too high to reasonably explain the low metallicity of the gas in the NLR and EELR. The mass-metallicity relation decreases only by 0.2 dex from $10^{11}\mathrm{M}_\odot$ to $10^{10}\mathrm{M}_\odot$ in stellar mass. We suggest that the large EELR with its intriguing tail-like geometry is the key to explain the puzzling properties of HE 2158−0107.

The [O III] light distribution extends beyond the PMAS field of view, but we can follow the structure in the Stripe 82 r and i band images out to 30 kpc projected distance from the host galaxy. We determined the emission-line contribution to the broad-band images from a small area at the South-East part of the EELR (see Fig. 5.5), which is still covered by PMAS field of view but not contaminated by host galaxy light. We constructed a synthetic emission-line spectrum for that area of the tail including the [O III], Hβ and Hα lines based on the observed [O III] flux, assuming an [O III]/Hβ line ratio of 7 and a Balmer decrement of 2.86. Furthermore, we assumed an average [O II]/[O III] line ratio of the order of 1/3 (e.g. Villar-Martín et al. 2008) to roughly predict the emission-line contamination in the g band. The surface brightness of the tail are reported in Table 5.3 for the SDSS photometry and the synthetic emission line spectrum. The corresponding SED is shown in Fig. 5.9. We find that the emission lines actually account for 57% of the flux in the r band

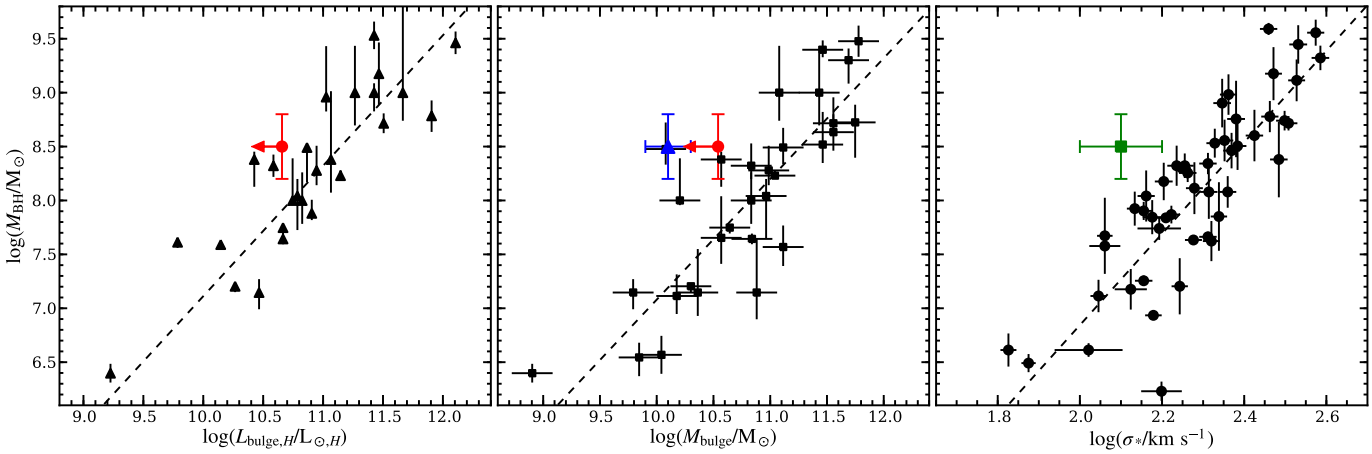

Fig. 5.8. *Left panel:* M_{BH}-L_{bulge} relation for the H band. The black triangles are measurements from Marconi & Hunt (2003) for local galaxies and the dashed line is their best-fit relation. Our 3σ upper limit on $L_{H,bulge}$ for HE 2158−0107 is shown as the red symbol. *Middle panel:* M_{BH}-M_{bulge} mass relation. The black squares correspond to the measurements of Häring & Rix (2004) with their best-fit relation shown as the dashed line. An SED based 3σ upper limit for the stellar mass of the HE 2158−0107 is indicated by the red circle. An independent estimate based on the bulge size in the z-band using the size-mass relation by Shen et al. (2003) is shown as the blue triangle. *Right panel:* M_{BH}-σ_* relation for local galaxies with dynamical M_{BH} measurements. Measurements by Gültekin et al. (2009) are shown as black round symbols and the dashed line indicate their best-fit relation. We used the line dispersion of the [O III] line (green square) in the unresolved NLR of HE 2158−0107 as a surrogate for σ_*, following the suggestion by Nelson (2000).

Table 5.3. Photometry of the extended tail

Band	SDSS image [mag arcsec^{-2}]	Line Spectrum [mag arcsec^{-2}]
g	25.01 ± 0.07	26.50 ± 0.20
r	24.17 ± 0.03	24.78 ± 0.16
i	24.23 ± 0.06	25.71 ± 0.20
z	24.50 ± 0.26	...
H	> 24.42	...

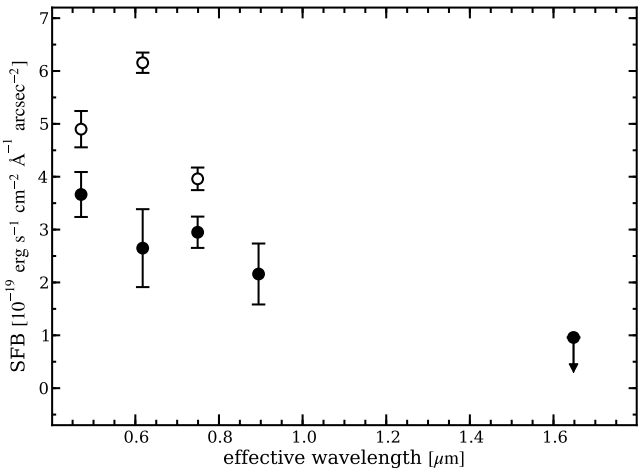

Fig. 5.9. SED of the extended tail close to HE 2158−0107. The surface brightness of a certain region centre on the extended tail (cf. Fig. 5.5) is shown at the effective wavelength of the corresponding passband. The initial surface brightnesses are indicated as the open symbols wheres as the filled symbols denote the true continuum surface brightness after subtraction of the emission-line contribution.

whereas the Hα line account for 25% of the i band flux. The emission lines are clearly dominating the r band flux, but an underlying continuum must also be present with a corresponding [O III] rest-frame EW of EW([O III]) = 1120 ± 500 Å. Such a high EW for the [O III] line was only observed in the integrated light of 2 out of 256 type 2 QSOs (Zakamska et al. 2003). If the EELR should be powered by star formation, only blue compact dwarf galaxies reach such high equivalent widths in the [O III] line (e.g. Thuan & Izotov 2005).

One explanation for this intriguing feature dominated by gaseous emission may be that it is a tidal tail due to a recent galaxy interaction. This scenario would be attractive for HE 2158−0107, as significantly diluted central gas-phase metallicities are observed and theoretically predicted for major mergers due to inflowing low-metallicity gas from large radii (Rupke et al. 2010; Montuori et al. 2010). However, this process can effectively funnel low-metallicity gas towards the galaxy nucleus, we find no signatures for a recent or ongoing major merger from the stellar light distribution at our spatial resolution of 1 kpc/pixel. Pointing to a different stage of galaxy interactions, Villar-Martín et al. (2010) recently reported the detection of a gas-rich tidal bridge of 180 kpc between a type 2 QSO (z = 0.399) and a companion galaxy. The gas along that bridge is ionised due to ongoing star formation, but the QSO is capable of ionising the gas in its vicinity up to ∼35 kpc distance. The EW of the [O III] emission and the associated low gas-phase metallicity along the tidal bridge of that interacting system are consistent with the EELR properties of HE 2158−0107. However, we cannot not identify a potential companion galaxy around HE 2158−0107 that could be responsible for such a tail.

To put constraints on the mass of a potential interacting companion we estimated the ionised gas mass from the emission line luminosity of the entire EELR. Following the prescription given in Osterbrock & Ferland (2006) and assuming Case B recombination, a low-density limit and a gas temperature of

$T \approx 10,000$ K for ionised nebulae, the ionised gas mass is given by

$$M_{\rm ion} \approx \left(\frac{100\,{\rm cm}^{-3}}{n_{\rm e}}\right)\left(\frac{L_{\rm H\beta}}{10^{41}\,{\rm erg\,s}^{-1}}\right)10^{7}{\rm M}_{\odot}\,, \quad (5.4)$$

where $n_{\rm e}$ is the electron density of the gas. Since $n_{\rm e}$ cannot be estimated from our data, we assumed a density of the order of $100\,{\rm cm}^{-3}$ for the extended emission on kpc scales (cf. Stockton et al. 2002). The [O III] luminosity of the entire EELR is $L_{[\rm O\,III]} = 2.1\times10^{42}{\rm erg\,s}^{-1}$, which corresponds to an Hβ luminosity of $L_{\rm H\beta} = 3\times10^{41}{\rm erg\,s}^{-1}$ assuming an average [O III]/Hβ ratio of 7 throughout the entire EELR. Under these assumptions we estimate an ionised gas mass of roughly $M_{\rm ion} \approx 3\times10^{7}{\rm M}_{\odot}$. This is not a large amount of ionised gas even though cold molecular and neutral gas may add more than an order of magnitude of mass to this. A tidally disrupted small gas-rich companion would thus be sufficient to account for the observed ionised gas mass and the low metallicity of the gas.

Given the large number of low mass satellites in cosmological simulations, the frequency of minor merger events is high and may be generically important to trigger nuclear activity (e.g. Cisternas et al. 2011). However, a low NLR metallicity such as detected for HE 2158−0107 has never been reported for luminous QSOs, which suggests that a minor merger is an unlikely scenario for this particular QSOs. A more appealing option would be smooth accretion of pristine gas in a "code mode" from a filament in the cosmic web (Kereš et al. 2005, 2009). This mode of accretion is different from the standard picture of galaxy formation where gas is heated to the virial temperature according to the gravitational potential of the galaxy before it is accreted. This is usually called the "hot mode" of accretion, where the gas is shock-heated before it can cool down again and condenses onto the galaxy. If the gas density is high enough, such as in dense filaments of the cosmic web, the cooling time scale is short enough that the gas is never heated to virial temperatures and is directly accreted onto the galaxy.

5.5. Discussion and Conclusions

Combining PMAS integral field spectroscopy and multi-colour broad band images, we were able to recover a lot of interesting properties of the luminous QSO HE 2158−0107. We find strong evidence for an unusual sub-solar metallicity of its NLR. Only very few AGN are currently known to have such low NLR metallicities, and all of them are low mass system with much lower BH masses than the value found for HE 2158−0107, $\log(M_{\rm BH}/{\rm M}_{\odot}) = 8.5\pm0.3$. This QSO clearly is a highly unusual object at least at low redshift.

Another interesting property of this QSO is that its host appears to be offset from basically all known BH-bulge relations established for local inactive galaxies. The stellar mass and *H* band luminosity, inferred from the SED of the bulge-dominated host, are both 0.6 dex lower than expected, which is independently supported by the kinematics of the ionised gas. Clearly, the offset for a single object can always be explained by chance given the intrinsic scatter of the relation, but the low stellar mass estimated from the size-mass relation of galaxies and the low velocity dispersion of the nuclear gas suggest that HE 2158−0107 could be an outlier from the local $M_{\rm BH}$-bulge relations. We tentatively note that the estimated offset from the relation matches, by order of magnitude, with the systematic offsets recently found at higher redshifts (e.g. Peng et al. 2006; Treu et al. 2007; Schramm et al. 2008; Merloni et al. 2010). Jahnke & Macciò (2011) recently studied with numerical simulations how the BH mass-bulge relations may get established over cosmic time. They found that merging of galaxies in a ΛCDM universe alone is sufficient to produce a tight relation at $z = 0$, even if the BH and bulge masses are initially uncorrelated. In fact, the local relation would have a much lower scatter than actually observed if no additional physical processes operate to *increase* the scatter. Thus, it is important to understand the physical mechanisms that lead to the observed scatter in the BH mass-bulge relations. Whether HE 2158−0107 is currently offset from the relation due to such a process or event that influences the relative growth of BH and bulges remains an open question.

If the low-metallicity gas is causally connected to the higher-than-expected $M_{\rm BH}/M_{\rm bulge}$ ratio is a key question. A striking feature of HE 2158−0107 is its large Extended Emission Line Region (EELR) with a tail-like geometry extending out to 30 kpc from the QSO. EELRs are common around radio-loud QSOs and are well-studied. However, it is still controversial whether they are produces by tidal debris from interacting galaxies, inflated by galactic superwinds, or whether they may also represent smoothly accreted cold gas from the environment (e.g. Stockton & MacKenty 1987; Fabian et al. 1987; Kereš et al. 2005; Stockton et al. 2006; Fu & Stockton 2009). In the case of our radio-quiet QSO, a galactic superwind can be excluded with high confidence, because the EELR kinematics are rather quiescent and a large scale radio jet is absent. Given the low ionised gas mass, the low gas-phase metallicity and lack of major merger signatures, we favour minor mergers or smooth cold gas accretion as the origin for the EELR of HE 2158−0107. The scenario of smooth cold gas accretion would be very attractive because the pristine gas would naturally account for the low gas-phase metallicity. Additionally, numerical simulations have shown that a hot accretion mode rather than the cold mode dominates for high-mass systems ($M_{\rm gal} = 10^{11}{\rm M}_{\odot}$) at $z \sim 0$ (e.g. Kereš et al. 2005, 2009) which might also explain the rareness of objects like HE 2158−0107 in the local universe.

HE 2158−0107 displays many unique properties for an object at low redshift. Taking all our evidences together we tentatively speculate whether this QSO might currently experience a particular evolutionary phase that usually happens much more frequently at higher redshift. A fundmental difference in the BH and bulge growth could occur when a BH is stochastically fed by an intrinsic gas reservoir of its host in contrast to a process where large amounts of gas are dumped onto the galaxy on a short timescale. HE 2158−0107 might therefore be an ideal laboratory at low redshift to study the growth of galaxies and their associated BHs via smooth cold gas accretion, a much more important process for the evolution of massive galaxies at higher redshifts.

References

Adelman-McCarthy, J. K., Agüeros, M. A., Allam, S. S., et al. 2008, ApJS, 175, 297
Baldwin, J. A., Phillips, M. M., & Terlevich, R. 1981, PASP, 93, 5
Barth, A. J., Greene, J. E., & Ho, L. C. 2008, AJ, 136, 1179
Becker, R. H., White, R. L., & Helfand, D. J. 1995, ApJ, 450, 559
Bennert, N., Falcke, H., Schulz, H., Wilson, A. S., & Wills, B. J. 2002, ApJ, 574, L105
Bennert, N., Jungwiert, B., Komossa, S., Haas, M., & Chini, R. 2006a, A&A, 459, 55
Bennert, N., Jungwiert, B., Komossa, S., Haas, M., & Chini, R. 2006b, A&A, 456, 953
Bentz, M. C., Peterson, B. M., Netzer, H., Pogge, R. W., & Vestergaard, M. 2009, ApJ, 697, 160

Bentz, M. C., Peterson, B. M., Pogge, R. W., Vestergaard, M., & Onken, C. A. 2006, ApJ, 644, 133
Boroson, T. 2005, AJ, 130, 381
Boroson, T. A. & Green, R. F. 1992, ApJS, 80, 109
Bruzual, G. & Charlot, S. 2003, MNRAS, 344, 1000
Chilingarian, I. V., Melchior, A., & Zolotukhin, I. Y. 2010, MNRAS, 405, 1409
Christensen, L., Jahnke, K., Wisotzki, L., & Sánchez, S. F. 2006, A&A, 459, 717
Cisternas, M., Jahnke, K., Inskip, K. J., et al. 2011, ApJ, 726, 57
Collin, S., Kawaguchi, T., Peterson, B. M., & Vestergaard, M. 2006, A&A, 456, 75
Fabian, A. C., Crawford, C. S., Johnstone, R. M., & Thomas, P. A. 1987, MNRAS, 228, 963
Fan, X., Strauss, M. A., Schneider, D. P., et al. 2003, AJ, 125, 1649
Fu, H. & Stockton, A. 2009, ApJ, 690, 953
Gilbank, D. G., Baldry, I. K., Balogh, M. L., Glazebrook, K., & Bower, R. G. 2010, MNRAS, 405, 2594
Greene, J. E. & Ho, L. C. 2005a, ApJ, 627, 721
Greene, J. E. & Ho, L. C. 2005b, ApJ, 630, 122
Greene, J. E. & Ho, L. C. 2007, ApJ, 670, 92
Groves, B. A., Dopita, M. A., & Sutherland, R. S. 2004, ApJS, 153, 9
Groves, B. A., Heckman, T. M., & Kauffmann, G. 2006, MNRAS, 371, 1559
Gültekin, K., Richstone, D. O., Gebhardt, K., et al. 2009, ApJ, 698, 198
Hamann, F. & Ferland, G. 1993, ApJ, 418, 11
Hamann, F. & Ferland, G. 1999, ARA&A, 37, 487
Häring, N. & Rix, H.-W. 2004, ApJ, 604, L89
Ho, L. C. 2009, ApJ, 699, 638
Hogg, D. W., Baldry, I. K., Blanton, M. R., & Eisenstein, D. J. 2002, ArXiv Astrophysics e-prints
Husemann, B., Wisotzki, L., Sánchez, S. F., & Jahnke, K. 2008, A&A, 488, 145
Izotov, Y. I., Guseva, N. G., Fricke, K. J., et al. 2010, A&A, 517, A90+
Izotov, Y. I. & Thuan, T. X. 2008, ApJ, 687, 133
Jahnke, K., Kuhlbrodt, B., & Wisotzki, L. 2004, MNRAS, 352, 399
Jahnke, K. & Macciò, A. V. 2011, ApJ, 734, 92
Kaspi, S., Maoz, D., Netzer, H., et al. 2005, ApJ, 629, 61
Kaspi, S., Smith, P. S., Netzer, H., et al. 2000, ApJ, 533, 631
Kauffmann, G., Heckman, T. M., Tremonti, C., et al. 2003, MNRAS, 346, 1055
Kereš, D., Katz, N., Fardal, M., Davé, R., & Weinberg, D. H. 2009, MNRAS, 395, 160
Kereš, D., Katz, N., Weinberg, D. H., & Davé, R. 2005, MNRAS, 363, 2
Kewley, L. J., Dopita, M. A., Sutherland, R. S., Heisler, C. A., & Trevena, J. 2001, ApJ, 556, 121
Kim, M., Ho, L. C., Peng, C. Y., Barth, A. J., & Im, M. 2008, ApJS, 179, 283
Komossa, S. & Xu, D. 2007, ApJ, 667, L33
Mannucci, F., Basile, F., Poggianti, B. M., et al. 2001, MNRAS, 326, 745
Marconi, A. & Hunt, L. K. 2003, ApJ, 589, L21
Matsuoka, K., Nagao, T., Marconi, A., Maiolino, R., & Taniguchi, Y. 2011, A&A, 527, A100+
Matteucci, F. & Padovani, P. 1993, ApJ, 419, 485
Merloni, A., Bongiorno, A., Bolzonella, M., et al. 2010, ApJ, 708, 137
Montuori, M., Di Matteo, P., Lehnert, M. D., Combes, F., & Semelin, B. 2010, A&A, 518, A56+
Moorwood, A., Cuby, J., & Lidman, C. 1998, The Messenger, 91, 9
Nagao, T., Marconi, A., & Maiolino, R. 2006, A&A, 447, 157
Nelson, C. H. 2000, ApJ, 544, L91
Nelson, C. H. & Whittle, M. 1996, ApJ, 465, 96
Oke, J. B. 1974, ApJS, 27, 21
Oke, J. B. & Sandage, A. 1968, ApJ, 154, 21
Osterbrock, D. E. & Ferland, G. J. 2006, Astrophysics of gaseous nebulae and active galactic nuclei (2nd. ed. by D.E. Osterbrock and G.J. Ferland. Sausalito, CA: University Science Books, 2006)
Peng, C. Y., Ho, L. C., Impey, C. D., & Rix, H. 2010, AJ, 139, 2097
Peng, C. Y., Ho, L. C., Impey, C. D., & Rix, H.-W. 2002, AJ, 124, 266
Peng, C. Y., Impey, C. D., Rix, H.-W., et al. 2006, ApJ, 649, 616
Peterson, B. M., Ferrarese, L., Gilbert, K. M., et al. 2004, ApJ, 613, 682
Peterson, B. M. & Wandel, A. 2000, ApJ, 540, L13
Roth, M. M., Kelz, A., Fechner, T., et al. 2005, PASP, 117, 620
Rupke, D. S. N., Kewley, L. J., & Chien, L. 2010, ApJ, 723, 1255
Sánchez, S. F. 2006, AN, 327, 850
Sánchez, S. F., Aceituno, J., Thiele, U., Pérez-Ramírez, D., & Alves, J. 2007, PASP, 119, 1186
Sánchez, S. F., Jahnke, K., Wisotzki, L., et al. 2004, ApJ, 614, 586
Schawinski, K., Dowlin, N., Thomas, D., Urry, C. M., & Edmondson, E. 2010, ApJ, 714, L108
Schlegel, D. J., Finkbeiner, D. P., & Davis, M. 1998, ApJ, 500, 525
Schmitt, H. R., Donley, J. L., Antonucci, R. R. J., et al. 2003, ApJ, 597, 768
Schneider, D. P., Richards, G. T., Hall, P. B., et al. 2010, AJ, 139, 2360
Schramm, M., Wisotzki, L., & Jahnke, K. 2008, A&A, 478, 311
Schulze, A. & Wisotzki, L. 2010, A&A, 516, A87+
Shemmer, O., Netzer, H., Maiolino, R., et al. 2004, ApJ, 614, 547
Shen, B. S., Mo, H. J., White, S. D. M., et al. 2007, MNRAS, 379, 400
Shen, S., Mo, H. J., White, S. D. M., et al. 2003, MNRAS, 343, 978
Shields, G. A., Gebhardt, K., Salviander, S., et al. 2003, ApJ, 583, 124
Stockton, A., Fu, H., Henry, J. P., & Canalizo, G. 2006, ApJ, 638, 635
Stockton, A. & MacKenty, J. W. 1987, ApJ, 316, 584
Stockton, A., MacKenty, J. W., Hu, E. M., & Kim, T.-S. 2002, ApJ, 572, 735
Storchi-Bergmann, T., Schmitt, H. R., Calzetti, D., & Kinney, A. L. 1998, AJ, 115, 909
Tadhunter, C. N., Scarrott, S. M., Draper, P., & Rolph, C. 1992, MNRAS, 256, 53P
Thuan, T. X. & Izotov, Y. I. 2005, ApJS, 161, 240
Tremonti, C. A., Heckman, T. M., Kauffmann, G., et al. 2004, ApJ, 613, 898
Treu, T., Woo, J., Malkan, M. A., & Blandford, R. D. 2007, ApJ, 667, 117
Véron-Cetty, M. & Véron, P. 2010, A&A, 518, A10+
Vestergaard, M. 2002, ApJ, 571, 733
Villar-Martín, M., Humphrey, A., Martínez-Sansigre, A., et al. 2008, MNRAS, 390, 218
Villar-Martín, M., Tadhunter, C., Pérez, E., et al. 2010, MNRAS, 407, L6
Warner, C., Hamann, F., & Dietrich, M. 2004, ApJ, 608, 136
Warren, S. J., Hambly, N. C., Dye, S., et al. 2007, MNRAS, 375, 213
Wisotzki, L., Christlieb, N., Bade, N., et al. 2000, A&A, 358, 77
York, D. G., Adelman, J., Anderson, Jr., J. E., et al. 2000, AJ, 120, 1579
Zakamska, N. L., Strauss, M. A., Krolik, J. H., et al. 2003, AJ, 126, 2125
Zakamska, N. L., Strauss, M. A., Krolik, J. H., et al. 2006, AJ, 132, 1496

Chapter 6

Conclusions and Outlook

6.1. Summary of results

6.1.1. IFU observations of QSOs

In this thesis we presented the use of the novel technique of integral field spectroscopy to systematically study the host galaxy properties of Quasi-Stellar Objects (QSOs). With the integral field units (IFUs) PMAS (Calar Alto) and VIMOS (ESO-VLT) we have collected observations of ∼50 luminous, low-redshift ($z < 0.3$) type 1 QSOs, which represents the largest dataset of its kind to date. With their combined spatial and spectral coverage these IFU observations are not hampered by the limited spatial sampling of conventional long-slit or even single-fibre spectroscopy. The size of the sample allowed us to study the properties of QSOs as a population, but we also could focus on individual objects, gaining new insights into astrophysical processes that would have been difficult to achieve with other observing techniques.

Since our QSOs are type 1 Active Galactic Nuclei (AGN) for which the central engines are not obscured by gas and dust, we had to deal with the blending of the bright emission of the nuclei and that of the underlying host galaxies. Building up on previous ideas for IFU deblending techniques (Sánchez et al. 2004; Jahnke et al. 2004; Christensen et al. 2006), we developed an efficient algorithm for the deblending of these two components in IFU data using the broad emission lines of the QSO to estimate Point Spread Function (PSF). We recently released a graphical user interface to control the algorithm, called `QDeblend`^{3D}, as a tool for the entire astronomical community to make the analysis QSOs with IFU data easier than today.

6.1.2. Scaling relations for the narrow-line region

One of the main goals of this thesis has been to provide an independent re-assessment of the size-luminosity relation of the AGN narrow-line region (NLR). Previous studies of the NLR size-luminosity relation, mainly using Hubble Space Telescope (*HST*) narrow-band images, reported controversial results for the relation in the last ten years. With the advantage of IFUs to simultaneous cover the spatial and spectral dimensions we have robustly separated the true AGN-excited narrow-line regions from star forming H II regions, which has been a severe problem for previous studies.

We have shown in Chapter 3 that *HST* based narrow-band images suffer from a very low sensitivity and underestimate the size of the true NLR by significant factors compared to our IFU observations, which reach almost an order of magnitude deeper. Furthermore, several different definitions were used in the literature to characterise the NLR size, which we systematically compared for the first time to assess their merits. We find that different size definitions are in agreement with each other, apart from a systematic offset by design, within a scatter of ∼30%. However, there a some indications that the depth of the data systematically influences the measured size more severly for some particular NLR size definitions. Dedicated simulations are need to follow-up on this issue and to check the dependence on the depth for each size definition individually.

Our best-fit NLR size-luminosity relation has a power-law slope of $R_{\rm NLR} \propto L_{[\rm O\,III]}^{0.49\pm0.09}$, which agrees with the result by Bennert et al. (2002) and is consistent with the scenario of a constant ionisation parameter throughout the NLR. Comparing to NLR sizes for luminous type 2 QSOs recently measured by Greene et al. (2011), we found that NLR sizes of type 1 and type 2 QSOs are similar, ∼10 kpc at $L_{[\rm O\,III]} \sim 5 \times 10^{42} \rm erg\,s^{-1}$, in contradiction to previous observations that suggested different NLR scaling relation for type 1 and type 2 AGN (Schmitt et al. 2003). Additionally, we show for the first time that the NLR size-luminosity relation is much tighter for L_{5100} than $L_{[\rm O\,III]}$ which has probably been an intrinsic source of uncertainty for small samples. Whether the NLR size is further limited by the size of host galaxy at higher QSO luminosities still remains an open question, since the NLR for the most luminous QSO in our sample just reached the size of their hosts.

On the other hand, we could not detect any signature for extended NLRs around a certain population of QSOs, although their sizes would be expected to be several kpc given their high luminosity. Netzer et al. (2004) studied the rest-frame optical spectra of high-redshift QSOs that often lack even an unresolved NLR. They proposed that the gas of the NLR might have already been expelled from those galaxy. These types of QSOs exhibit narrow Hβ lines and strong Fe II emission similar to the properties of those QSOs in our sample that also lack an extended NLR. This is certainly connected to a particular physical process, but we could not identify outflows around those QSOs which does not support the scenario outline by Netzer et al. (2004). Comparing the radio luminosities with the limiting or measured [O III] luminosities of the extended NLR we showed that almost all our radio-quiet QSOs with a luminous NLR are also associated with enhanced radio emission, while objects without an extended NLR are preferentially undetected in the radio. We speculate that low-power radio jets in radio-quiet QSOs might actively increase the covering factor of gas clouds to the AGN radiation due to the expansion and fragmentation of dense gas clouds as the jet developts and grow beyond the nucleus. This may have important consequences also for the various models of AGN feedback, as the covering factor is an

important parameter for the efficiency of that process (Hopkins & Elvis 2010).

6.1.3. Star formation in QSO hosts

To detect ongoing star formation in QSO hosts via their optical emission lines have always being difficult due to the severe contamination with emission from the nucleus. With our QSO-host deblending technique for IFU observations we could for the first time map out H II regions over the entire host galaxies to systematically investigate signatures for ongoing star formation activity in QSO hosts.

We demonstrated that the specific star formation rates in several disc-dominated host galaxies are consistent with those of normal star forming galaxies, while others display no detectable star formation activity. It remains an open question whether star formation has been actively suppressed in those particular host by the AGN, or whether the gas content is intrinsically low. Deep observations to detect the signal from molecular and neutral gas will be required to convincingly argue about AGN related quenching of star formation.

6.1.4. No evidence for ubiquitous outflow signatures

At the time the PhD project was started, AGN feedback had become popular, in particular due to the work of Di Matteo et al. (2005) and Croton et al. (2006). Severe outflows driven by the AGN, capable to remove most of the gas from the system, have often been invoked to explain the required truncation of star formation to produce a "red and dead" galaxy. Our IFU observations do not support that scenario as the ionised gas kinematics in most of our QSOs have been identified to be gravitationally driven (Chapter 3).

On the other hand, in a few cases we did discover evidence for non-gravitational motions and outflows of gas, which we tentatively attribute to an interaction of low-power radio jets with their ambient medium. It is unquestionable that AGN can have a strong impact on their host galaxies, but whether this is a short phase within the duty cycle of all AGN, or whether it occurs only in certain AGN when certain physical conditions are fulfilled, needs to be investigated in the future.

Together with other very recent studies (Krug et al. 2010; Greene et al. 2011) our observations provide evidence that the importance of AGN feedback may have been overrated in theoretical works, at least at low redshifts. Understanding the evolution of galaxies remain a challange. Many other processes, like starburst-driven superwinds or gravitational heating, might in the sum be more important ingredients than the proposed AGN feedback scenarios alone.

6.1.5. The gas-phase metallicity as a signature for galaxy interactions and gas accretion

From recent observations of major mergers and dedicated numerical simulation it has become clear that strong galaxy interactions lead to radial gas flows modulating the distribution of metals and can be used as a new diagnostic tool. With our unique IFU dataset we were able to study for the first time the gas-phase metallicity gradients in QSO hosts (Chapter 4). For all objects where this analysis was possible, the metallicity gradients are always flatter than inactive disc-dominated galaxies

By comparing the gas-phase metallicities of disc- and bulge-dominated QSO hosts, we discovered that the metallicity of bulge-dominated hosts is systematically lower than their disc-dominated counterparts, measured at one effective radius. This interesting phenomenon might be attributed to major merger processes by which the bulge-dominated hosts were formed. However, most of our bulge-dominated hosts do not show signatures of recent major merger events indicating that they should have happened several 100 Myr ago. We argued that the accretion of external low metallicity gas due to minor mergers or smooth gas accretion from the intergalactic medium in the "cold mode" are more likely scenarios to explain the observed properties, as we highlighted by very detailed investigations of two QSOs in Chapter 2 and Chatper 5.

HE 1029−1401 is the brightest QSO in the southern sky and with a redshift of only $z = 0.086$ it offers the unique opportunity to map out the host properties of a luminous QSO a high spatial scales. With our new VIMOS IFU observations we detected large amounts of AGN-ionised gas inside the host galaxy with solar metallicity, two times lower than expected for a massive bulge-dominated host. The velocity field of the ionised gas in this objects indicates the presence of a kinematically cold gas disc, but we also found large scale perturbations that were previously missed in long-slit observations of this object (Letawe et al. 2007). The low gas metallicity combined with the kinematic distortion make a strong case for a tidally disrupted minor companion galaxy as the origin for the gas, which is possibly also causing the QSO activity.

Another exciting discovery has been that the QSO HE 2158−0107 ($z = 0.218$) is the most metal poor luminous QSO ever observed, representing a unique object among several thousands of low-redshift AGN. The QSO host is also offset from the BH mass-bulge scaling relations towards a higher $M_{\rm BH}/M_{\rm bulge}$ ratio. The stellar mass of the host is however still too high to plausibly explain the low metallicity with an intrinsic gas reservoir. The presence of large (30 kpc) extended ionised gas with a tail-like geometry reported in Chapter 5 supports our interpretation of an ongoing accretion event with pristine external gas in a "cold mode" of accretion. This process happens infrequently for massive galaxies at low redshift, but is much more likely to occur at earlier epochs of the universe. HE 2158−0107 might therefore be an ideal laboratory at low redshift to study the growth of galaxies and their associated BHs via smooth cold gas accretion, a much more important process for the evolution of massive galaxies at higher redshifts.

6.2. Future Prospects

6.2.1. A large Integral Field Survey of galaxies: CALIFA

One major limitation of most IFU studies has been their small sample size. We obtained IFU observations for a large sample of ∼50 QSOs, which already is a substantial improvement. However, even this sample contains only small numbers of objects with similar physical properties, given the large variety of host luminosities, stellar masses, morphologies and environments. Furthermore, we still lack dedicated IFU control samples that are required to statistically test certain hypothesis. Larger IFU surveys, like SAURON (de Zeeuw et al. 2002), provided observations with a high scientific impact. A new era will be soon reached with the upcoming Calar Alto Legacy Integral Field Area (CALIFA) survey, designed to observe 600 galaxies ($0.005 < z < 0.03$) representative of the local galaxy population with the PPAK IFU at Calar Alto observatory over the next 3 years. The instrument has a large field of view ($65'' \times 72''$)

that covers the entire galaxies and a large spectral coverage from 3700Å to 7000Å providing a panchromatic view of all galaxies.

With the enormous amount of information recorded for each galaxy, the possible science cases are manyfold. As part of the CALIFA collaboration our group is assigned to lead the study of AGN hosts within the project. Since CALIFA will automatically provide matching control samples of normal star-forming galaxies, we will focus on a comparison study of AGN and star forming galaxies, which was the key to achieve milestone results from SDSS (e.g. Kauffmann et al. 2003). With the results of this thesis in mind, we want to statistically test some of our hypothesis to identify their importance for the evolution of galaxies:

(i) Are the gas-phase metallicities systematically flatter in AGN hosts, indicative for radial gas flow to the centre?

(ii) Do bulge-dominated AGN hosts contain significantly lower metallicity gas, which would be a signature for external gas accretion?

(iii) Is star formation actively suppressed by the AGN?

6.2.2. Stellar populations of QSO hosts at $0.2 < z < 0.5$

With our VIMOS data we were only able to detect the stellar continuum in the hosts at the lowest redshifts $z < 0.08$ of our sample. This is technically limited by the low spatial resolution and quantum efficiency of current IFU instruments. It is thus difficult to investigate the recent assembly history of AGN hosts already at small redshifts.

The Multi Unit Spectroscopic Explorer (MUSE) will be a unique IFU instrument equipped with cutting edge technology with which such a study might be possible even for QSO hosts at intermediate redshifts ($0.2 < z < 0.5$). The instrument is currently being build as a second generation instruments for the ESO VLT to be commissioned at the end of 2012. It will be one of the largest and most efficient IFUs in the world, covering a continuous $1' \times 1'$ field of view with a sampling of $0\farcs2 \times 0\farcs2$ per spaxel. The covered wavelength range is 4800–9300Å at medium spectral resolution ($R \sim 2800$) and instruments throughput of ~35% at 7500Å. A new ground-layer AO system will provide four Laser Guide Stars positioned around the field of view to achieve an enhanced seeing even at optical wavelength (~$0\farcs4$). With its large field of view, MUSE will be the first instrument to obtain stars together with the target QSO in the same exposure. This will solve the problem of accurate PSF estimation for the entire wavelength range that we currently struggled with our data.

A 2D analysis of the stellar populations in QSO hosts at redshifts $0.2 < z < 0.5$ will thus be possible for the first time at $\sim$ 1 kpc resolution. Additionally, the environment of the hosts can be investigated including nearby companion galaxies and their gas. New observational contrains for the triggering of AGN activity via minor interaction with galaxies will then be possible and their importance for the growth of galaxies across cosmic times.

6.2.3. Ionised gas around high-redshift QSOs

In this work we focused on QSOs in the low-redshift universe ($z < 0.3$), but the number density of luminous QSOs is significantly higher at earlier epochs, coincident with the major episode of galaxy growth. In order to understand the importance of the AGN feedback mechanism, the relation with their host need to be studied at those epochs more closely. The rest-frame optical emission lines are redshifted in the near-infrared bands at $z \sim 1-2$, where they are still observable from the ground.

For example Nesvadba et al. (2006) studied with the near-infrared IFU SINFONI the severe interaction of a radio-jet with the ionised ambient medium in a radio-loud AGN host. The released superwind in this object is able to remove most of the gas from the system, which can be considered as smoking gun evidence for AGN feedback. However, a systematic study of the ionised gas using their rest-frame optical emission lines has not yet been performed for high-redshift radio-quiet QSOs to verify the universality of such AGN feedback mechanisms. It is also still open if the NLR size for the most luminous QSOs at that redshift is significantly smaller than expected from the extrapolated size-luminosity relation, which might be due to the expulsion of the gas from the host galaxy as claimed by Netzer et al. (2004).

Our group already used the SINFONI IFU as a light bucket even under bad seeing conditions to obtain NIR spectra of luminous QSOs at redshift $z \sim 2$ centred on the Hβ line. The major aim was to estimate BH masses for the QSO population based on the optical calibrations in relation to previous estimates using rest-frame UV lines. However, the seeing for a few objects may be sufficient to exploit with our developed deblending techniques if any significant extended emission can be detected. We intend to propose a follow-up study with SINFONI for the most promising objects using adaptive optics to achieve a much higher spatial resolution to recover the detail properties of these ionised nebulae.

6.2.4. The impact of radio jets on the ISM of radio-quiet QSO hosts

One outcome of this work has been that radio jets of radio-quiet QSOs may be partially responsible for the presence of extended NLR regions and its kinematics due to jet-cloud interactions. Only the integrated radio luminosities have been measured for all our objects. High spatial resolution radio imaging to map its distribution on subarcsecond scales were obtained only for just a few of our QSOs. This prohibited a systematic investigation of the connection between impact of radio jets on the ISM of the AGN hosts. We still do not know whether high-velocity clouds and regions of turbulent gas kinematics are directly related to expanding low-power radio jets, or AGN or star-burst driven winds.

We therefore plan to obtain radio follow-up observations of all QSOs in our sample with the LOw Frequency ARray (LOFAR). The telescope has recently started its operations with antennae and receivers distributed across Europe that can be interferometrically linked to achieve subarcsecond resolution at unprecedented depth in the frequency range 10–90 MHz and 110–250 MHz. At these frequencies we will catch the low-energy electrons which possibly dominate the synchrotron emission of low-power radio jets. Those may be missed at higher frequencies which have so far been extensively studied with the Very Large Array (VLA) for radio-loud and radio-quiet QSOs.

6.2.5. The neutral and molecular gas content in QSO hosts

The seed of all star formation is the cold molecular and neutral gas. The evolution of galaxies in terms of their star formation history is primarily dependent on the cold gas content and the star formation efficiency as a function of time. AGN may influence that process either by heating and destructing the molec-

ular gas to suppress star formation, or by the expulsion of a significant fraction of cold gas that truncates star formation almost completely. Thus, a low specific star formation rate in AGN hosts does not necessarily imply that AGN have suppressed star formation, the cold gas content could also be intrinsically low. On the other hand, the absence of strong outflow signature in the ionised gas does not mean that AGN are unable to truncate star formation, if the outflows primarily comprise molecular and neutral gas.

The importance of the cold gas phase in the interpretation of the properties of galaxies is reflected by the initiation of several legacy surveys. The Galex Arecibo SDSS Survey (GASS, Catinella et al. 2010) uses the large 300 m Arecibo radio dish to obtain the H I content of ~1000 galaxies ($0.025 < z < 0.05$). Its complement COLD GASS (Saintonge et al. 2011) undertakes a survey with IRAM 30 m telescope of the molecular gas content for those galaxies via the detection of CO lines. However, current radio and sub-mm telescopes are limited by sensitivity and spatial resolution to low-redshift galaxies and would not be able to resolve or detect the emission in more distant QSO hosts.

New observational capabilities will soon be available with the completion of the ESO Atacama Large Millimeter Array (ALMA) forseen in 2013. In its final stage the interferometric array will consist of 66 antennae with a diameter of 25 m operating from 0.3 mm to 3.6 mm with a maximum baseline of up to 15 km to achieve an angular resolution of $0\farcs1$. We plan to use this facility to study the molecular gas content of QSO hosts. This will enable to study the cold gas kinematics and, together with optical IFU observation of the ionised gas, to infer the star formation efficiency. Both can be used to conclusively test whether AGN feedback process are one of the leading mechanisms for the transition of galaxies for the blue cold to the red sequence.

References

Bennert, N., Falcke, H., Schulz, H., Wilson, A. S., & Wills, B. J. 2002, ApJ, 574, L105
Catinella, B., Schiminovich, D., Kauffmann, G., et al. 2010, MNRAS, 403, 683
Christensen, L., Jahnke, K., Wisotzki, L., & Sánchez, S. F. 2006, A&A, 459, 717
Croton, D. J., Springel, V., White, S. D. M., et al. 2006, MNRAS, 365, 11
de Zeeuw, P. T., Bureau, M., Emsellem, E., et al. 2002, MNRAS, 329, 513
Di Matteo, T., Springel, V., & Hernquist, L. 2005, Nature, 433, 604
Greene, J. E., Zakamska, N. L., Ho, L. C., & Barth, A. J. 2011, ArXiv e-prints
Hopkins, P. F. & Elvis, M. 2010, MNRAS, 401, 7
Jahnke, K., Wisotzki, L., Sánchez, S. F., et al. 2004, AN, 325, 128
Kauffmann, G., Heckman, T. M., Tremonti, C., et al. 2003, MNRAS, 346, 1055
Krug, H. B., Rupke, D. S. N., & Veilleux, S. 2010, ApJ, 708, 1145
Letawe, G., Magain, P., Courbin, F., et al. 2007, MNRAS, 378, 83
Nesvadba, N. P. H., Lehnert, M. D., Eisenhauer, F., et al. 2006, ApJ, 650, 693
Netzer, H., Shemmer, O., Maiolino, R., et al. 2004, ApJ, 614, 558
Saintonge, A., Kauffmann, G., Kramer, C., et al. 2011, ArXiv e-prints
Sánchez, S. F., Garcia-Lorenzo, B., Mediavilla, E., González-Serrano, J. I., & Christensen, L. 2004, ApJ, 615, 156
Schmitt, H. R., Donley, J. L., Antonucci, R. R. J., et al. 2003, ApJ, 597, 768

Appendix A

Deblending of AGN and hosts emission in IFU data: QDeblend^{3D}

ABSTRACT

To decompose the bright emission of a QSOs and the emission of its host galaxy is already a difficult task for broad-band images. This even more difficult for IFU datacubes. We developed a software tool, called QDeblend^{3D}, specifically for IFU data and provide a graphical user interface for the community to handle that task more easily. Here, we describe the algorithm with the aid of instructive figures and try to point out its strengths as well as its limitations.

A.1. Description of the algorithm

A.1.1. Background

For the study of QSO host galaxies, 2D analytic modelling of broad-band photometric observations with dedicated software packages, such as GALFIT (Peng et al. 2002, 2010) or GIM2D (Simard et al. 2002), has enabled us to properly deblend the QSO and host galaxy emission to infer their properties independently. However, spectroscopic observation are required to gain further insight into the properties and distribution of the ISM, dust content, kinematics, element abundances, etc. Techniques to deblend the QSO and host galaxy contribution in longslit spectra have already been developed (Jahnke et al. 2007; Letawe et al. 2007), but longslit spectroscopy can only cover a certain part of the host galaxy. In order to get a more complete picture, integral field units (IFUs) offer exciting new perspectives but also require the development of new techniques to cope with the data.

A.1.2. Basics of the algorithm

At the core of our QDeblend^{3D} software tool, we used an improved iterative algorithm that was initiated by Christensen et al. (2006). The basic concept is to treat the spaxels (x, y) of the IFU datacube as a set of independent spectra $f(x, y, \lambda)$. The spectral shape of a point source is the same in each spaxel (in the absence of atmospheric dispersion), whereas the brightness is a function of position with scale factors $s(x, y)$ according to the Point Spread Function (PSF) of the observations. In the following we assume that the scale factors are normalised to one at the QSO position $(x, y) = (x_{\rm cent}, y_{\rm cent})$.

While broad-band imaging studies typically use stars simultaneously observed within the field of the target to obtain an empirical PSF, current IFUs usually do not capture stars with the target due to their relatively small FOV of a few arcseconds. In the case of a broad-line AGN, scale factors for each spaxel can fortunately be estimated from the strength of the broad emission lines with respect to the adjacent continuum as presented by Jahnke et al. (2004) to reconstruct the scale factors $s(x, y)$ at the wavelength of the chosen broad emission line (see Fig. A.1 for illustration).

On the other hand, the underlying continuum and line emission of the host may be spatially resolved and follow different distributions, $h(x, y)$ and $l(x, y)$, which contribute both to the spectra of the IFU datacube:

$$f(x, y, \lambda) = s(x, y) f_{\rm QSO}(\lambda) + h(x, y) f_{\rm cont}(\lambda) + l(x, y) f_{\rm lines}(\lambda) \quad \text{(A.1)}$$

For simplicity we assume for the time being that the spectral shapes of the host spectrum and the emission line spectrum does not change in a datacube. We will relax and discuss this assumption later on.

Since we can easily construct the scale factors $s(x, y)$ from the data itself, only the QSO spectrum $f_{\rm QSO}(\lambda)$ needs to be determined to separate $f(x, y, \lambda)$ in a QSO and host galaxy term for each spaxel (x,y). But how can we obtain a pure QSO spectrum without any contamination from resolved host emission? The spectrum at the QSO position, e.g. the brightest spaxel, should contain an almost pure S/N QSO spectrum

$$f(x_{\rm cent}, y_{\rm cent}, \lambda) \approx s(x_{\rm cent}, y_{\rm cent}) f_{\rm QSO}(\lambda) \, . \quad \text{(A.2)}$$

under the condition that

$$s(x_{\rm cent}, y_{\rm cent}) f_{\rm QSO}(\lambda) \gg h(x_{\rm cent}, y_{\rm cent}) f_{\rm cont}(\lambda) + l(x_{\rm cent}, y_{\rm cent}) f_{\rm lines}(\lambda) \quad . \quad \text{(A.3)}$$

This condition is certainly not fullfilled for low or intermediate luminosity QSOs so that the measured template QSO spectrum $f_{\rm QSO,temp}(\lambda) \equiv f(x_{\rm cent}, y_{\rm cent}, \lambda)$ will be inevitably contaminated by a significant fraction of host galaxy emission. Thus, the residual datacube

$$f_{\rm residual}(x, y, \lambda) = f(x, y, \lambda) - s(x, y) f_{\rm QSO,temp}(\lambda) \quad \text{(A.4)}$$

will be subject to an oversubtraction of the QSO component around the QSO position.

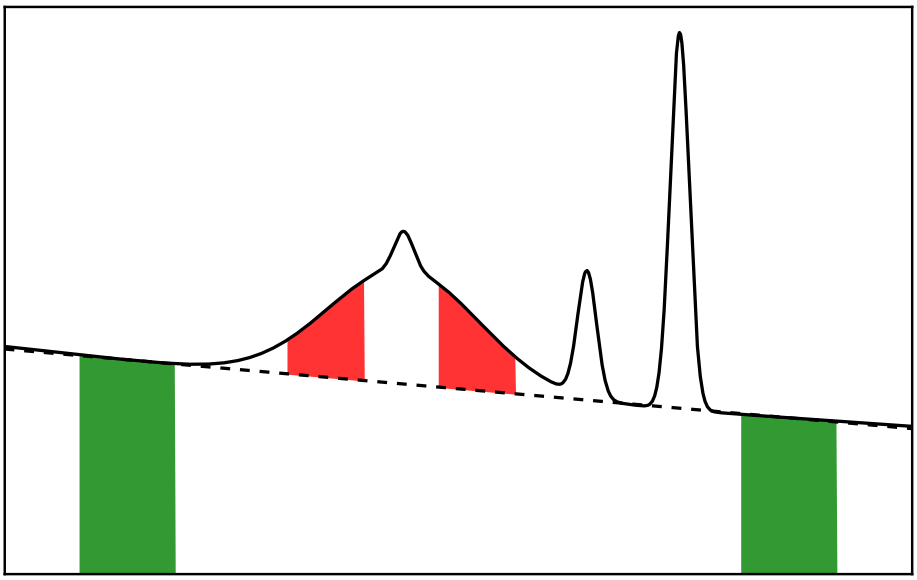

Fig. A.1. Sketch of the broad line measurement in the case of Hβ spectral region. Two adjacent continuum windows (green shaded areas) are defined to estimate a linear approximation of the local continuum (dashed line). To avoid contamination by a narrow Hβ component one or two spectral windows at the Hβ wings are selected and the flux is measured within these regions above the local continuum (red shaded areas).

A.1.3. The Iterative Scheme

Our solution is an iterative scheme to reduce the host contamination of the QSO spectrum in an empirical way as good as possible. When we subtract the scaled QSO spectrum $s(x,y)f_{\rm QSO,temp}(\lambda)$ from each spaxel in the datacube during the initial iteration. The signal in the central spaxel of the residual datacube will then be $f(x_{\rm cent}, y_{\rm cent}, \lambda) = 0$ by design. Since the host galaxy emission is spatially extended, their normalised scale factors will be higher than that of the QSO $h(x,y) > s(x,y)$ and $l(x,y) > s(x,y)$ for all spaxels around the centre. Some level of host galaxy emission will therefore remain in the residual datacube around the QSO position. We define a certain region around the one used to construct the QSO spectrum, i.e. 8 spaxels around the central one or any other selection of spaxels that appears best suited, to extract a host galaxy spectrum ($f_{\rm host}$) from the residual datacube. The idea is now to decontaminate the QSO spectrum $f_{\rm QSO,temp}(\lambda)$ iteratively by subtracting the extracted host spectrum from the QSO spectrum

$$f_{\rm host}(\lambda) = \frac{h(x_{\rm cent}, y_{\rm cent})}{\sum_{(x,y)\in(X,Y)} h(x,y)} \sum_{(x,y)\in(X,Y)} f_{\rm residual}(x,y,\lambda)\ . \tag{A.5}$$

Here, we have made the implicit assumption that host continuum and line emission follow the same light distribution $h(x,y) = l(x,y)$, which is not necessarily true, but in most cases only $h(x,y)$ can be constrained externally from broad-band images with an analytic profile. If no external information is available at all, the flux of the host galaxy spectrum needs to be extrapolated based on other assumption as discussed in the next paragraph.

In each of the subsequent iterations a cleaned QSO spectrum is created via $f_{\rm QSO,iter}(\lambda) = f_{\rm QSO,temp}(\lambda) - f_{\rm host}(\lambda)$ and subtracted from the initial datacube. After a few iterations (3-4) the QSO spectrum usually converges to a stable solution. We provide an illustration of the iterative process in Fig. A.2, which also outlines the basic steps that can be summarised as follows:

1. Extraction of $f_{\rm QSO,temp}(\lambda)$ from the IFU datacube (e.g. the spectrum of the brightest spaxel or a co-added spectrum over a few central spaxels).
2. Determination of $s(x,y)$ based on the broad emission lines above the continuum.
3. Subtraction of $s(x,y)f_{\rm QSO,temp}(\lambda)$ from the initial datacube.
4. Reconstruction of $f_{\rm host}(\lambda)$ by co-adding several spaxel from $f_{\rm residual}(x,y,\lambda)$ and assuming some analytic distribution for $h(x,y)$ and/or $l(x,y)$.
5. Decontamination of $f_{\rm QSO,temp}(\lambda)$ with $f_{\rm host}(\lambda)$.
6. Iterate steps 2-5 until the QSO spectrum converges.

A.1.4. Limitation and Advantages

In the previous section we assumed, mainly for mathematical clarity, that the spectral shape of $f_{\rm cont}(\lambda)$ and $f_{\rm lines}(\lambda)$ do not change in the entire datacube. This is certainly not true, but the algorithm actually does not use this very strict assumption. An identical spectral shape is only assumed around a small region around the QSO nucleus corresponding to the galaxy centre. The physical size of that region, however, strongly depends on the spatial resolution of the observations and the redshift of the galaxy.

On the other hand, this is already much better compared to the 3D Deblending technique (Sánchez et al. 2004), which performs a 2D analytic modelling of each monochromatic IFU image to deblend the QSO and host spectrum. By design this method assumes implicitly that the shape of $f_{\rm host}(\lambda)$ is constant over the entire field of view, which certainly affects the deblended spectra.

In the case of low S/N data the spatial regions to extract $f_{\rm QSO,temp}(\lambda)$ and $f_{\rm host}(\lambda)$ can be enlarged compared to the best solution outlined above. This has the disadvantage of limiting the ability to decontaminate the QSO spectrum leading to oversubtraction effects. The user must find a compromise depending on the specific situation.

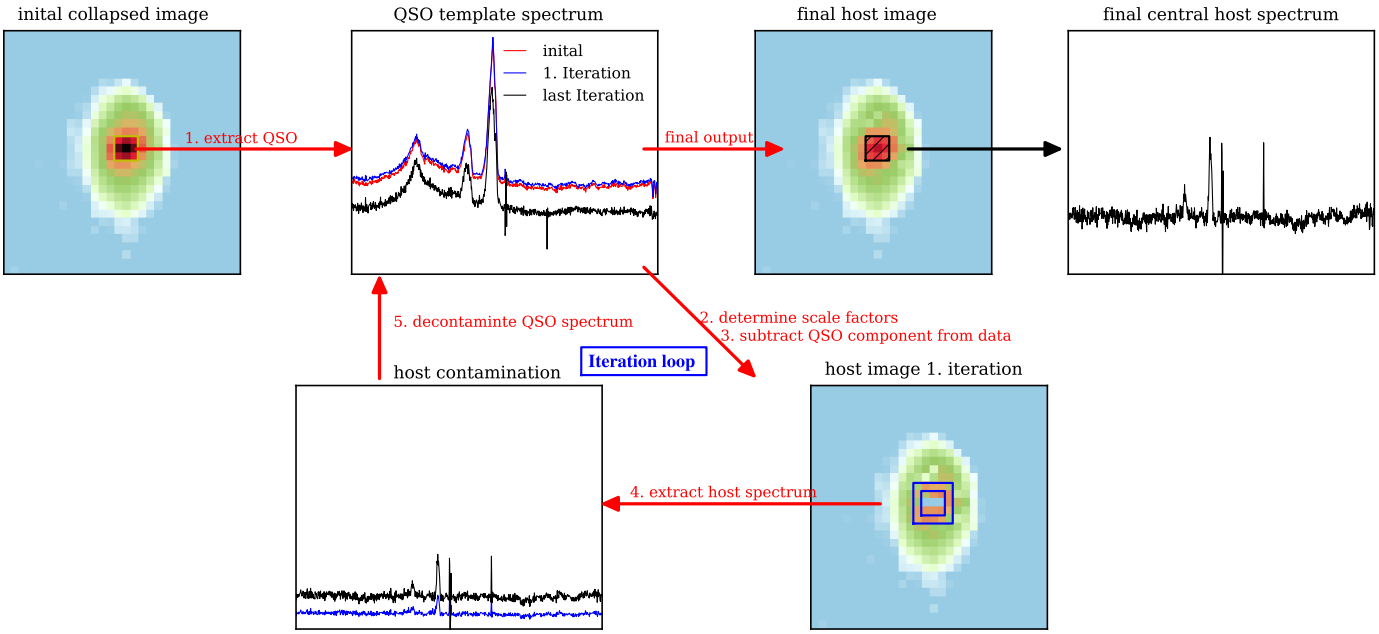

Fig. A.2. Illustration of the iterative deblending process used by QDeblend^{3D}.

The deblending results will certainly depend on the assumed surface brightness distribution $h(x, y)$ of the host. Unfortunately, this cannot be self-consistently determined within the algorithm and needs to be determined externally, e.g. using high resolution broad-band images or via reasonable assumptions. Several options can be considered to set $h(x, y)$:

- An analytic surface brightness model based on broad-band imaging or other (probably the best option)
- A constant surface brightness $h(x, y) = 1$ in the central galaxy region of concern (reduces oversubtraction)
- $\frac{h(x_{\rm cent}, y_{\rm cent})}{\sum_{(x,y)\in(X,Y)} h(x,y)}$ is manually set to a certain value, i.e, so that no stellar absorption line remain in the deblended QSO spectrum.

The adopted scheme will depend on the AGN sample and the science, but it should be chosen to be consistent for the whole sample even though it might not be the optimal solution in all cases.

Another limitation of the algorithm is that the atmospheric dispersion, in particular the wavelength dependence of seeing, is not taken into account, because the PSF $s(x, y)$ can only be determined self-consistently from the data at the wavelength of broad lines. Several broad lines might be covered in the wavelength range of the spectrum, but the S/N may not be high enough to reconstruct the PSF with a sufficient accuracy for all of them. It is therefore recommended to restrict the deblending to a certain wavelength range centred on the broad line or to split up the data into several subcubes when more than one broad line can be used for the deblending. Only when a PSF star is in the FOV of the IFU one would be able to use a proper PSF for each wavelength. This will be possible with next generation instruments such as MUSE at the Very Large Telescope.

A.2. The Graphical User Interface of QDeblend^{3D}

In Fig. A.3 we show the main graphical window of the QDeblend^{3D} user interface, which is the core of the program to set the required parameters interactively and to immediately check the quality of the results. The main window is split up into two areas, on the left side, the `Deblending Control Widget` where the user sets the required parameters for the deblending, and on the right side, the `Cube Viewer Widget` to visualise the input data *and* deblending result at the same time. This part is similar to `E3D` (Sánchez 2004), but with the possibility to compare the spaxels of two datacubes at a given position. Furthermore, spectral windows and spatial regions can be selected and used in the deblending process. We hope that this little tool, available at http://sourceforge.net/projects/qdeblend/, will be useful for the community and may help to reduce reluctance of obtaining spatially resolved spectroscopy for unobscured type 1 QSOs due to the technical difficulties.

References

Christensen, L., Jahnke, K., Wisotzki, L., & Sánchez, S. F. 2006, A&A, 459, 717
Jahnke, K., Wisotzki, L., Courbin, F., & Letawe, G. 2007, MNRAS, 378, 23
Jahnke, K., Wisotzki, L., Sánchez, S. F., et al. 2004, AN, 325, 128
Letawe, G., Magain, P., Courbin, F., et al. 2007, MNRAS, 378, 83
Peng, C. Y., Ho, L. C., Impey, C. D., & Rix, H. 2010, AJ, 139, 2097
Peng, C. Y., Ho, L. C., Impey, C. D., & Rix, H.-W. 2002, AJ, 124, 266

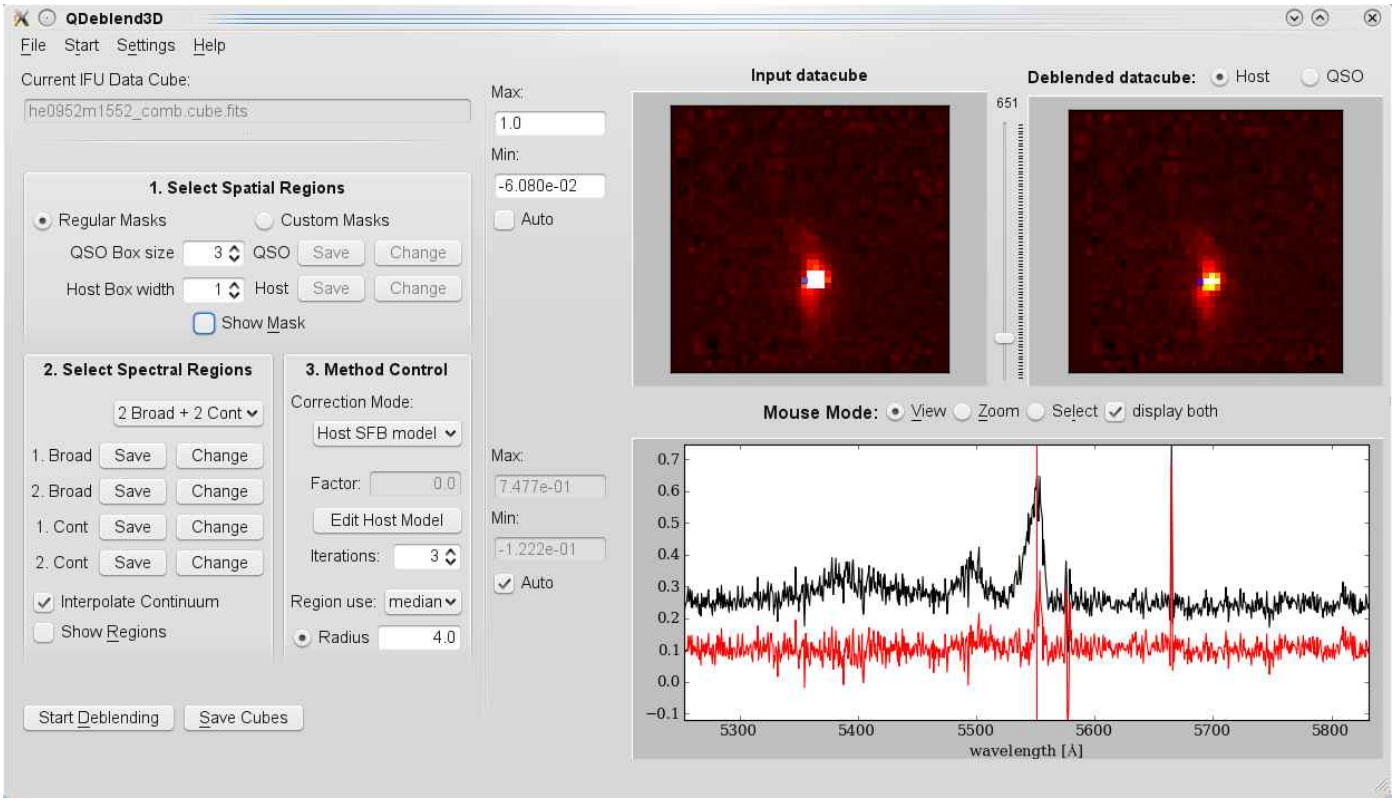

Fig. A.3. The main window of the QDeblend^{3D} graphical user interface.

Sánchez, S. F. 2004, Astronomische Nachrichten, 325, 167
Sánchez, S. F., Garcia-Lorenzo, B., Mediavilla, E., González-Serrano, J. I., & Christensen, L. 2004, ApJ, 615, 156
Simard, L., Willmer, C. N. A., Vogt, N. P., et al. 2002, ApJS, 142, 1

Appendix B

Analysis of QSOs spectra

ABSTRACT

To estimate BH masses and Eddington ratios from single-epoch spectra of type 1 AGN has become a standard tool. Here we describe our approach to analyse the QSO spectra and the adopted calibration to compute the BH masses and Eddington ratios for the whole sample presented in the thesis. In direct comparison with the low-resolution QSO spectra of the Hamburg/ESO survey, we infer the observational uncertainty and possible systematic effects on the estimated BH masses. We find that the HES spectra slightly overestimate the AGN continuum due to host contamination. As the BH mass depends weakly on the continuum luminosity this does not produce a significant offset in the derived BH masses for HES spectra. The uncertainty in the BH mass is of the order of 0.2 dex for measurements based on the line dispersion of Hβ and slightly higher for BH masses based on the its FWHM. Furthermore, we show that L_{5100} is much better correlated with $L_{\rm bol}$ than $L_{\rm [O\,III]}$ and provide scaling relations. Interestingly, we find that all QSOs with a detected ENLR tend to be more luminous in [O III] at a given bolometric luminosity than objects without an ENLR.

B.1. Modelling of the broad-line AGN spectra

To estimate physical parameters of the AGN, we first need to extract several information from its spectrum. The spectral region around Hβ is the most intensively investigated part of the spectra for low-redshift AGN ($z < 0.5$). Although Hα is significantly brighter than Hβ it is often affected by telluric absorption troughs at these redshifts and the host contribution to the observed continuum around Hα is much higher than at shorter wavelength. On the other hand, Fe II emission lines can be quite strong in the spectra of AGN leading to a prominent pseudo-continuum of Fe II complexes redward and blueward of Hβ. Most studies used template Fe II spectra to subtract the pseudo-continuum from the spectra before modelling the broad Hβ and the neighbouring forbidden [O III] emission-line doublet (e.g. Boroson & Green 1992; Brotherton 1996; Marziani et al. 2003; Shen et al. 2008).

Two template Fe II spectra have been used in the literature which were empirically (Boroson & Green 1992) or theoretically (Véron-Cetty et al. 2004) created based on high S/N observations of the QSOs I Zw 1. The PMAS spectrum of I Zw 1 is shown in the left panel of Fig. B.1 and the two archival Fe II template spectra generated from I Zw 1 are presented in the right panel. The broad lines of I Zw 1 have a FWHM of less than 2000 km s^{-1}, a archetypal Narrow-Line Seyfert 1 (NLS1) galaxy, in which most of the Fe II lines are resolved. We found that the two Fe II template spectra are significantly different from each other. Possible explanations are that the underlying power-law continuum of the AGN was modelled differently, the physical conditions are not completely understood to predict the Fe II line strengths for the synthetic spectra, or the intrinsic profile of the empirically subtracted emission lines could not be properly inferred. Anyway, the dominant Fe II emission adjacent to Hβ and [O III] originates from the well resolved Fe II $\lambda\lambda$4924, 5018 doublet as revealed by both template spectra. To avoid additional uncertainties due to the choice of the Fe II template, we followed a more simple approach and incorporate this particular doublet into our emission-line model for that region without requiring the need for a dedicated iron template.

Various line profiles have been used in the literature to model the broad Balmer lines: Blue and red-sided power-law functions (Nagao et al. 2006), Lorentzian functions (Véron-Cetty et al. 2001, 2004), Gauss-Hermite functions (Salviander et al. 2007; McGill et al. 2008; Hu et al. 2008) and most commonly a superposition of Gaussian profiles (e.g. Brotherton et al. 1994; Laor et al. 1994; Sulentic et al. 2002; Véron-Cetty et al. 2006). We chose to use Gaussian components to model the line profiles of the broad and narrow emission lines. Our model consists of up to 3 Gaussian components for the Hβ line, up to 2 Gaussian components for the profile of the [O III] and Fe II doublets and a straight line to approximate the local continuum. The two lines of a doublet are coupled as a system in line width, radial velocity and line ratio (a factor of 3 for [O III] $\lambda\lambda$4960, 5007 and 1.29 for Fe II $\lambda\lambda$4924, 5018), which significantly increases the robustness of our model and reduces the number of free parameters. If a narrow Hβ component is present on top of a broad Hβ profile, we couple its kinematic parameters with that of the narrow [O III] component as these lines originate both from the NLR. In cases where the Fe II lines were broad and its width could hardly be constrained against the background continuum, we coupled the line width and radial velocity to that of the broad Hβ line. We obtained the best-fit parameters of our model by minimising the χ^2 of the residual using the Nelder-Mead downhill simplex algorithm of `scipy`. The best-fit models are shown in Fig B.2 for all QSO objects discussed in this thesis.

From the best-fit model we determined several important parameters of which we list the continuum flux and luminosity at 5100Å, and the broad Hβ line widths in Table B.1. The continuum flux at 5100 Å was determined from the best-fit local continuum model. From the model of the Hβ lines, we excluded any narrow component that we coupled with the narrow [O III] line to determine the FWHM (FWHM$_{\rm H\beta}$) and line dispersion ($\sigma_{\rm H\beta}$) of the broad component only. Other parameters will be listed, but those are important to estimate the BH mass and Eddington ratio.

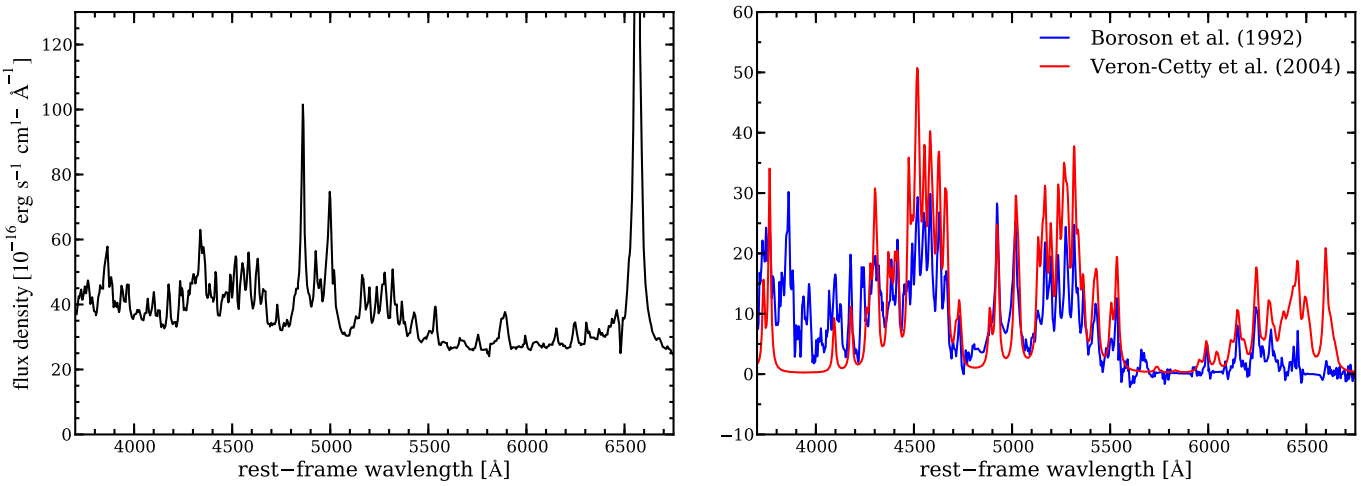

Fig. B.1. *Left panel*: PMAS spectrum of the Narrow-Line Seyfert 1 galaxy I Zw 1. *Right panel*: Comparison of the empirical and theoretical Fe II template by Boroson & Green (1992) and Véron-Cetty et al. (2004), respectively, based on I Zw 1.

B.2. BH masses and Eddington ratios from single-epoch AGN spectra

To infer the BH mass and Eddington ratio for an AGN from its single-epoch spectra, the assumption of virial motion of BLR gas clouds is needed as well as an estimate for the size of the BLR region. The virial product

$$\mathrm{VP} \equiv v_{\mathrm{line}}^2 R_{\mathrm{BLR}} G^{-1} \tag{B.1}$$

for the BLR can be used to estimate the BH mass adopting a certain virial coefficient f_{vir},

$$M_{\mathrm{BH}} = f_{\mathrm{vir}} \times \mathrm{VP} \quad . \tag{B.2}$$

On the other hand, f_{vir} depends on the geometry and kinematics of the BLR, which is still not sufficiently constrained and can be a substantial source of uncertainty (Krolik 2001). A virial coefficient of $f_{\mathrm{vir}} = 3/4$ is often assumed in the case of a spherically symmetric BLR (e.g. Wandel et al. 1999; Kaspi et al. 2000). Most commonly, f_{vir} was empirically constrained from a sample of AGN by matching the estimated BH masses with the expectations from the M_{BH}-σ_* relation (e.g. Onken et al. 2004; Collin et al. 2006; Woo et al. 2010). For low-redshift QSOs the FWHM of the broad Hβ line has mainly been used over the last ten years as a measure for v_{line}, but Peterson et al. (2004) proposed that the line dispersion $\sigma_{\mathrm{H}\beta}$ is a more robust estimator of v_{line}. This issue was investigated in more detail by Collin et al. (2006). They found that a single virial coefficient $f_{\mathrm{vir}} = 3.85$ is sufficient to match the BH masses of the entire sample with the M_{BH}-σ_* correlation if $\sigma_{\mathrm{H}\beta}$ was used to estimate M_{BH}. If $\mathrm{FWHM}_{\mathrm{H}\beta}$ is used instead, they showed that f_{vir} depends on the line profile of Hβ (i.e. $\mathrm{FWHM}_{\mathrm{H}\beta}/\sigma_{\mathrm{H}\beta}$) to achieve a similarly good match. A VP based on $\sigma_{\mathrm{H}\beta}$ should therefore be a more unbiased estimator for the BH mass.

The size of the BLR can be estimated from the correlation between continuum AGN luminosity and R_{BLR} (e.g. Kaspi et al. 2000, 2005; Bentz et al. 2006). R_{BLR} was directly measured for a sample of ∼30 AGN via the reverberation mapping technique (Blandford & McKee 1982; Peterson & Wandel 2000). One of the most recent calibrations for the BLR radius-luminosity relation were determined by Bentz et al. (2009) for the continuum luminosity at 5100Å (rest-frame),

$$\log\left(\frac{R_{\mathrm{BLR}}}{\mathrm{lt-days}}\right) = 1.54 + 0.519 \log\left(\frac{L_{5100}}{10^{44}\,\mathrm{erg\,s^{-1}}}\right) \quad , \tag{B.3}$$

who subtracted the stellar contribution from the QSO continuum based on *HST* photometry. If the stellar light contamination is not properly taken into account, the slope of the relation would be much steeper with a slope of 0.665 (Kaspi et al. 2005).

Combining equations B.1 and B.2 with B.3 for $\sigma_{\mathrm{H}\beta}$ and adopting the associated virial coefficient $f_{\mathrm{vir}} = 3.85$, we get a BH mass calibration of the form

$$\log\left(\frac{M_{\mathrm{BH},\sigma}}{\mathrm{M}_\odot}\right) = 2\left(\frac{\sigma_{\mathrm{H}\beta}}{1000\,\mathrm{km\,s^{-1}}}\right) + 0.52\left(\frac{L_{5100}}{10^{44}\,\mathrm{erg\,s^{-1}}}\right) + 4.41 \quad . \tag{B.4}$$

Since BH masses based on $\mathrm{FWHM}_{\mathrm{H}\beta}$ are still quite common in the literature we also estimate M_{BH} for this line width adopting a virial coefficient of $f_{\mathrm{vir}} = 3/4$ for a spherical symmetric BLR geometry (e.g. Krolik 2001),

$$\log\left(\frac{M_{\mathrm{BH,FWHM}}}{\mathrm{M}_\odot}\right) = 2\left(\frac{\mathrm{FWHM}_{\mathrm{H}\beta}}{1000\,\mathrm{km\,s^{-1}}}\right) + 0.52\left(\frac{L_{5100}}{10^{44}\,\mathrm{erg\,s^{-1}}}\right) + 3.95 \quad . \tag{B.5}$$

The Eddington luminosity of the BH can be computed from M_{BH} as

$$\log\left(\frac{L_{\mathrm{Edd}}}{\mathrm{erg\,s^{-1}}}\right) = \log\left(\frac{4\pi G M_{\mathrm{BH}} m_{\mathrm{p}} c}{\sigma_T}\right) = \log\left(\frac{M_{\mathrm{BH}}}{10^7 \mathrm{M}_\odot}\right) + 45.1 \tag{B.6}$$

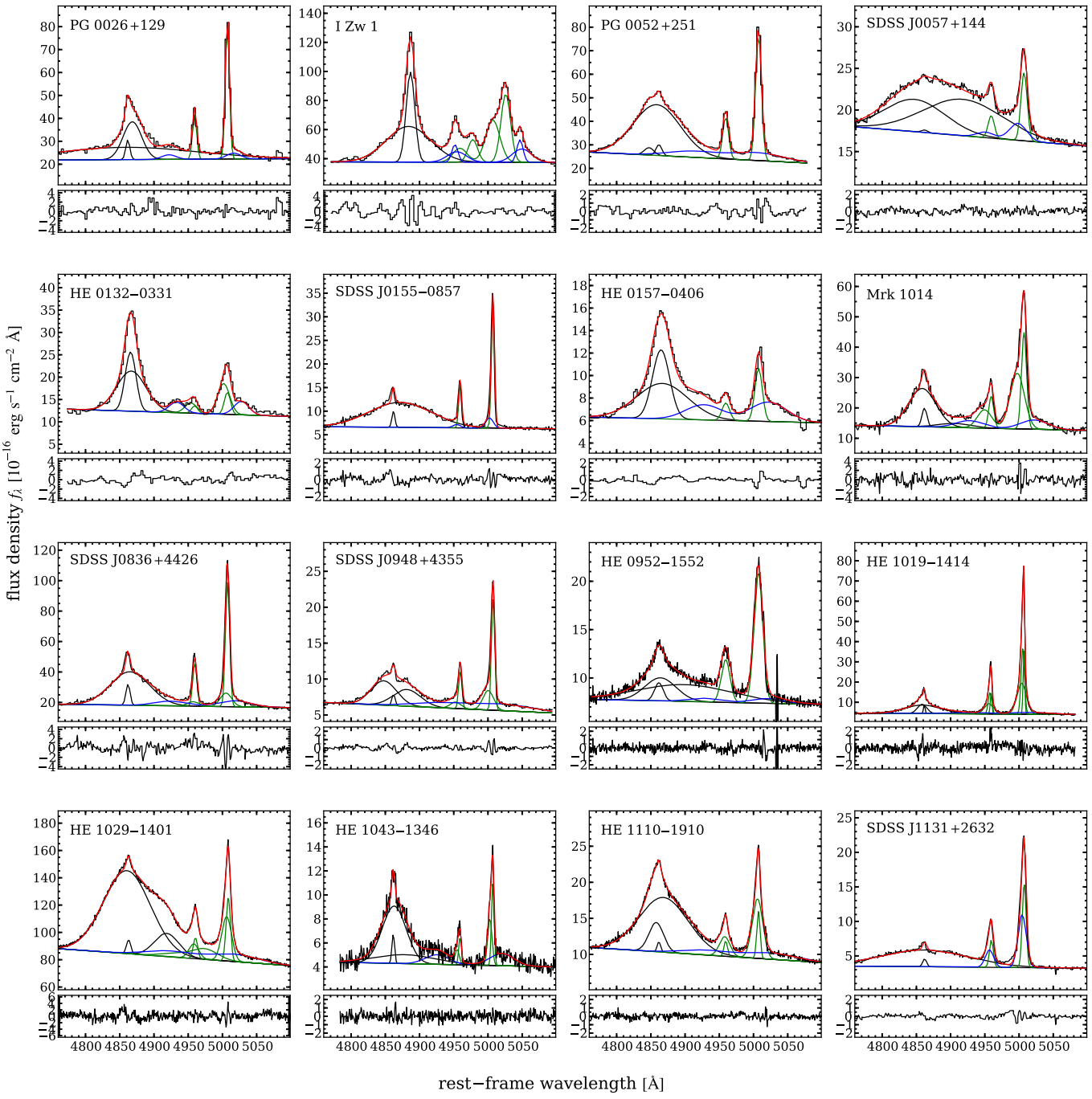

Fig. B.2. Modelling of the QSO spectra in the Hβ-[O III] spectral region. The QSO spectra (solid line) and best-fit models (red line) for all objects in the sample are presented. The different Gaussian components for the Hβ line (black lines), the [O III] doublet (green lines) and the Fe II doublet (blue lines) are plotted above the local continuum. The residual of the models are shown below each spectrum.

where m_p is the Proton mass, G is the gravitational constant and σ_T is the Thomson cross-section. To compute the Eddington ratio $\lambda \equiv L_{bol}/L_{Edd}$, the bolometric luminosity needs to be estimated from the optical luminosity with an appropriate bolometric correction. An often used bolometric correction based on the AGN continuum luminosity L_{5100} is

$$L_{bol} = 9 \times L_{5100} \quad , \tag{B.7}$$

as proposed by Kaspi et al. (2000). Consistently, a mean value for the bolometric correction factor of 10.3 ± 2.1 was directly inferred by Richards et al. (2006) from QSO SEDs. Furthermore, the bolometric correction may be luminosity dependend (Marconi et al. 2004; Hopkins et al. 2007), but we decided to still use a constant correction factor (Eq. B.7).

The distributions of M_{BH} and λ for our sample are shown in Fig. B.3 based on FWHM$_{H\beta}$ and $\sigma_{H\beta}$ as described above. The distributions are significantly different from each other with sample means and standard deviations of $\langle \log M_{BH,\sigma} \rangle = 8.26 \pm 0.47$

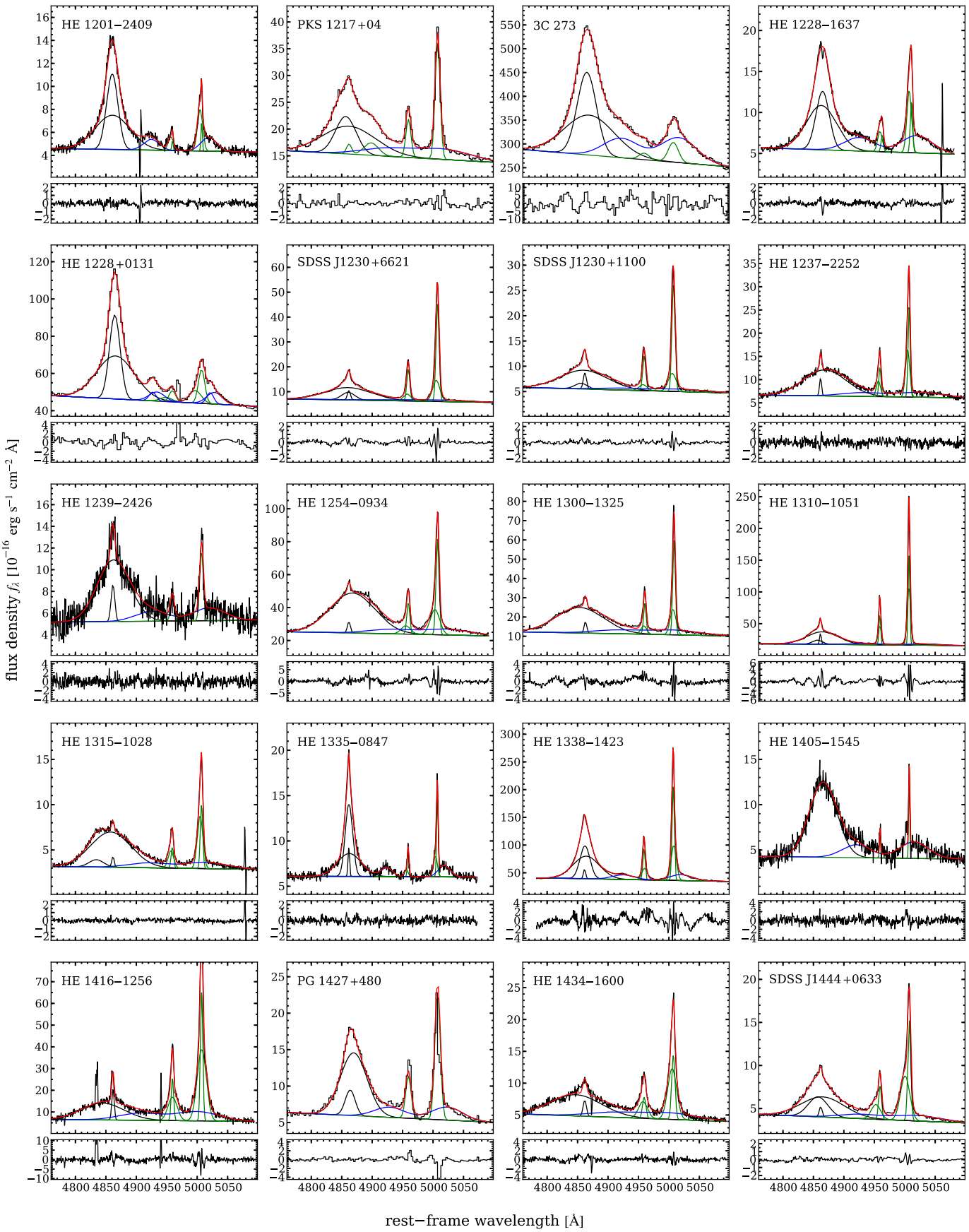

Fig. B.2. Continued.

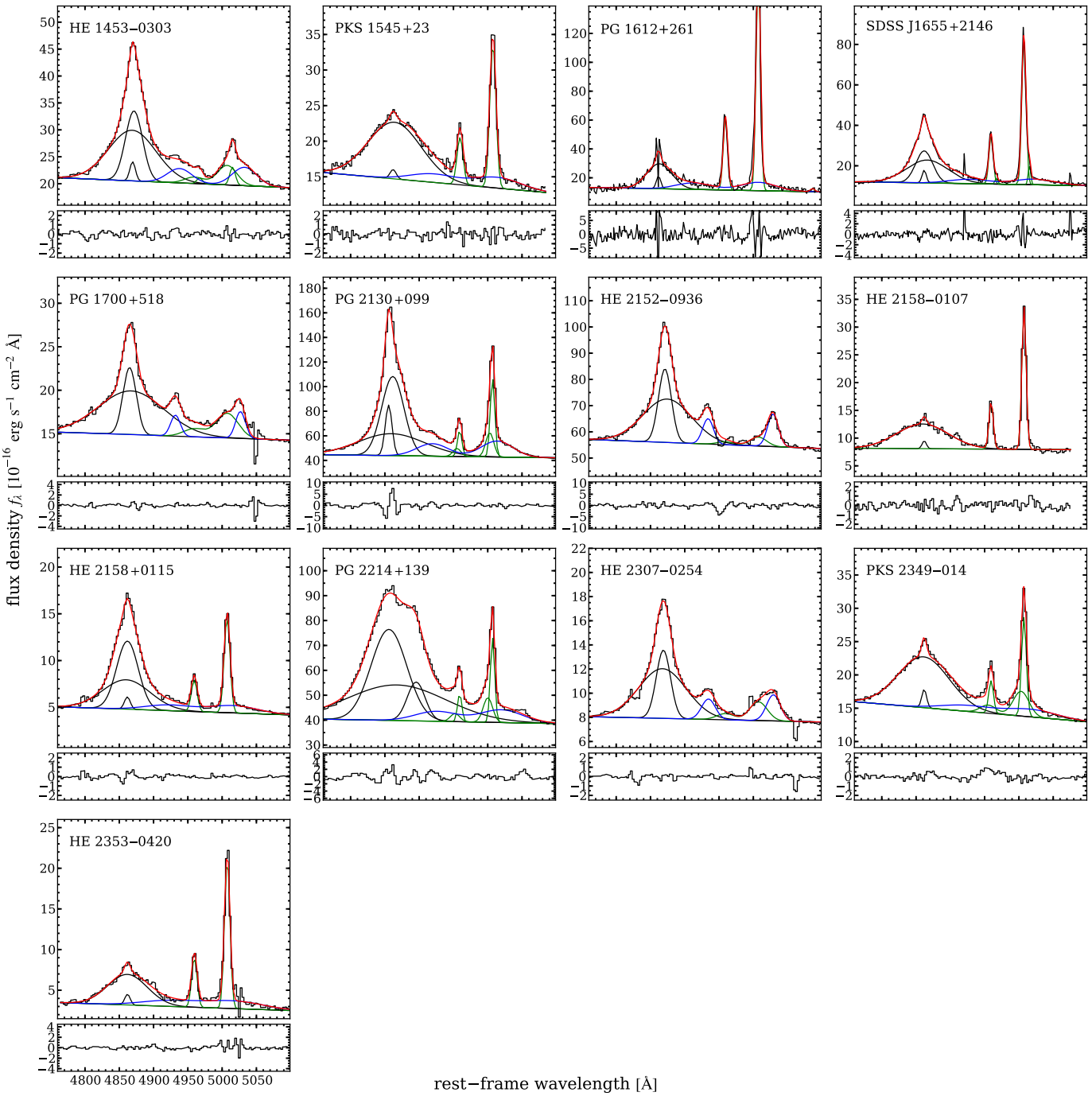

Fig. B.2. Continued.

and $\langle \log M_{\rm BH,FWHM} \rangle = 8.04 \pm 0.54$, respectively. A similar offset by ∼0.2 dex is also found for the Eddington ratios λ and we note that several objects would accrete at super Eddington rate using $M_{\rm BH,FWHM}$, while those AGN are absent in the distribution based on $M_{\rm BH,\sigma}$. This is in qualitative agreement with the results of Schulze & Wisotzki (2010), who studied a large sample of local type 1 AGN including Seyfert type objects, but we inferred a larger offset in the mean of the $M_{\rm BH}$ and λ distributions. Since $M_{\rm BH,\sigma}$ is expected to be more robust we have always used this BH mass estimate throughout the thesis.

B.3. Uncertainty of measurements and possible observational systematics

Spectra were obtained with follow-up observations for all objects of our VIMOS sample as part of the Hamburg/ESO survey, which were recently analysed by Schulze et al. (2009). The spectral resolution of these spectra is low ($R \sim 400$), almost a magnitude lower than our VIMOS spectra ($R \sim 2500$). As these completely independent QSO spectra were analysed in the same way, we can directly compare the results to estimate measurement errors and identify possible observational systematics.

Table B.1. AGN parameters derived from the QSO spectrum

Object	f_{5100} $\left[10^{-16}\,\frac{\mathrm{erg}}{\mathrm{s\,cm^2}}\right]$	$\log L_{5100}$ [erg s^{-1}]	FWHM$_{H\beta}$ [km s^{-1}]	$\sigma_{H\beta}$ [km s^{-1}]	$\log(M_{BH,\sigma})$ [$M_\odot$]	$\log\lambda_\sigma$	$\log(M_{BH,FWHM})$ [$M_\odot$]	$\log\lambda_{FWHM}$
PMAS observations								
PG 0026+129	27.5 ± 6.7	44.96 ± 0.11	2430 ± 28	3471 ± 18	8.98	−1.18	7.96	−0.16
I Zw 1	45.8 ± 11.3	44.31 ± 0.11	1111 ± 12	1652 ± 10	8.00	−0.85	6.95	0.21
PG 0052+251	25.1 ± 5.8	44.98 ± 0.10	4604 ± 24	2088 ± 8	8.55	−0.73	8.53	−0.70
SDSS J0057+1446	18.6 ± 4.2	44.95 ± 0.10	10506 ± 159	4143 ± 39	9.13	−1.34	9.23	−1.43
HE 0132−0441	12.6 ± 2.9	44.69 ± 0.10	1487 ± 21	960 ± 47	7.73	−0.20	7.40	0.14
HE 0157−0406	6.2 ± 1.3	44.72 ± 0.09	5493 ± 174	2333 ± 77	8.52	−0.95	8.55	−0.98
SDSS J0155−0857	6.7 ± 1.4	44.47 ± 0.09	6650 ± 87	2824 ± 35	8.55	−1.24	8.59	−1.26
Mrk 1014	13.7 ± 3.0	44.77 ± 0.09	3002 ± 25	1549 ± 16	8.19	−0.57	8.05	−0.43
SDSS J0846+4426	17.9 ± 3.9	45.35 ± 0.10	4169 ± 128	1771 ± 56	8.60	−0.41	8.64	−0.43
SDSS J0948+4335	5.4 ± 1.2	44.72 ± 0.09	4060 ± 61	1571 ± 30	8.17	−0.61	8.28	−0.72
SDSS J1131+2623	3.4 ± 0.7	44.59 ± 0.09	9370 ± 328	3957 ± 128	8.90	−1.48	8.94	−1.51
PKS 1217+023	14.6 ± 3.2	45.20 ± 0.10	4300 ± 178	2272 ± 686	8.74	−0.70	8.59	−0.53
3C 273	272.7 ± 59.2	46.04 ± 0.09	2852 ± 7	1999 ± 7	9.06	−0.18	8.66	0.23
SDSS J1230+1100	5.1 ± 1.1	44.73 ± 0.10	4439 ± 129	2307 ± 30	8.51	−0.94	8.37	−0.79
HE 1228+0131	44.5 ± 9.7	44.95 ± 0.09	1671 ± 11	1572 ± 38	8.29	−0.50	7.63	0.17
SDSS J1230+6621	5.9 ± 1.2	44.54 ± 0.09	3297 ± 93	2190 ± 22	8.36	−0.99	8.01	−0.62
PG 1427+480	5.3 ± 1.1	44.67 ± 0.09	2455 ± 68	1268 ± 105	7.96	−0.45	7.82	−0.30
SDSS J1444+0633	5.9 ± 1.2	44.54 ± 0.09	3297 ± 93	2190 ± 22	8.36	−0.99	8.01	−0.62
HE 1453−0303	27.4 ± 7.9	45.31 ± 0.12	2513 ± 43	1795 ± 27	8.59	−0.44	8.18	−0.01
PKS 1545+21	14.1 ± 3.1	45.29 ± 0.10	5644 ± 38	2397 ± 15	8.83	−0.70	8.87	−0.73
PG 1612+261	21.2 ± 5.1	44.74 ± 0.11	2770 ± 26	1177 ± 11	7.93	−0.35	7.96	−0.37
SDSS J1655+2146	12.0 ± 3.0	44.65 ± 0.11	2483 ± 37	1576 ± 27	8.14	−0.65	7.82	−0.32
PG 1700+518	15.6 ± 3.4	45.43 ± 0.09	2067 ± 41	2600 ± 53	8.98	−0.71	8.07	0.21
PG 2130+099	48.3 ± 11.1	44.40 ± 0.10	2727 ± 10	2144 ± 17	8.27	−1.04	7.77	−0.53
HE 2152−0936	60.7 ± 13.8	45.59 ± 0.10	1877 ± 13	1853 ± 16	8.76	−0.34	8.07	0.37
HE 2158−0107	9.6 ± 2.3	44.89 ± 0.11	5486 ± 45	2325 ± 19	8.60	−0.87	8.64	−0.89
HE 2158+0115	4.8 ± 1.1	44.21 ± 0.10	2739 ± 33	1637 ± 42	7.94	−0.89	7.68	−0.62
PG 2214+139	48.3 ± 12.1	44.44 ± 0.11	5506 ± 23	3190 ± 77	8.64	−1.36	8.40	−1.12
HE 2307−0254	8.6 ± 1.9	44.89 ± 0.10	2172 ± 27	1823 ± 32	8.39	−0.66	7.83	−0.09
PKS 2349−014	14.0 ± 3.0	44.85 ± 0.09	4041 ± 83	2265 ± 25	8.55	−0.87	8.35	−0.65
HE 2353−0420	2.7 ± 0.6	44.42 ± 0.10	4176 ± 40	1774 ± 17	8.12	−0.86	8.16	−0.88
VIMOS observations								
HE 0952−1552	7.3 ± 0.2	44.09 ± 0.10	2991 ± 125	3650 ± 215	8.58	−1.60	7.69	−0.75
HE 1019−1414	3.9 ± 0.2	43.50 ± 0.11	3782 ± 153	1606 ± 70	7.56	−1.17	7.59	−1.24
HE 1029−1401	75.7 ± 0.2	44.88 ± 0.09	6135 ± 82	2327 ± 27	8.59	−0.83	8.73	−1.00
HE 1043−1346	4.0 ± 0.2	43.39 ± 0.11	2766 ± 73	1796 ± 346	7.60	−1.32	7.26	−1.02
HE 1110−1910	8.9 ± 0.1	44.21 ± 0.09	3637 ± 37	2082 ± 12	8.15	−1.06	7.92	−0.87
HE 1201−2409	4.3 ± 0.1	44.09 ± 0.10	1734 ± 28	1417 ± 65	7.76	−0.78	7.22	−0.28
HE 1228−1637	4.9 ± 0.1	43.87 ± 0.10	2135 ± 13	1290 ± 13	7.56	−0.80	7.29	−0.57
HE 1237−2252	6.1 ± 0.2	43.90 ± 0.10	5105 ± 51	2166 ± 20	8.03	−1.24	8.06	−1.31
HE 1239−2426	5.3 ± 0.4	43.69 ± 0.12	3855 ± 167	1637 ± 72	7.67	−1.10	7.71	−1.17
HE 1254−0934	22.8 ± 0.5	44.84 ± 0.10	5344 ± 26	2270 ± 11	8.55	−0.83	8.58	−0.90
HE 1300−1325	10.2 ± 0.2	43.44 ± 0.09	5674 ± 35	2409 ± 15	7.88	−1.55	7.91	−1.62
HE 1310−1051	15.5 ± 0.6	43.35 ± 0.10	3055 ± 229	1526 ± 16	7.44	−1.20	7.33	−1.13
HE 1315−1028	2.9 ± 0.1	43.59 ± 0.10	4816 ± 33	2009 ± 24	7.80	−1.32	7.85	−1.41
HE 1335−0847	6.0 ± 0.2	43.72 ± 0.10	1049 ± 36	917 ± 53	7.19	−0.58	6.59	−0.02
HE 1338−1423	34.4 ± 0.5	43.86 ± 0.09	1635 ± 19	1119 ± 20	7.43	−0.68	7.05	−0.34
HE 1405−1545	4.0 ± 0.2	44.41 ± 0.11	3304 ± 53	1403 ± 20	7.91	−0.61	7.95	−0.68
HE 1416−1256	5.6 ± 0.2	44.15 ± 0.10	5086 ± 90	2160 ± 39	8.15	−1.11	8.19	−1.18
HE 1434−1600	4.0 ± 0.1	44.11 ± 0.10	6068 ± 126	2577 ± 59	8.29	−1.29	8.32	−1.36

Firstly, we compare the line width of the broad Hβ line in Fig. B.4. The scatter in the FWHM measurements are 0.15 dex, slightly larger than for $\sigma_{H\beta}$ with 0.09 dex, but both agree with each other in the mean. We note that $\sigma_{H\beta}$ becomes systematically higher in the HES spectra than the VIMOS spectra at large width. The origin of this effect, if it is not a statistical coincidence, remains unknown. We identified two apparent outliers from the one-to-one correlation, which are assigned to the objects HE 0952−1552 and HE 1043−1346. A comparison of the HES and VIMOS spectra is presented in Fig. B.5. The discrepancy in the Hβ line width for HE 0952−1552 is related to the broad wings of the line which cannot be well resolved against the continuum in the HES spectra, so that we infer a significantly larger line dispersion. In the case of HE 1043−1346, we think that the strong emission of the star formation increased the apparent strength of the narrow component of Hβ in the HES spectra. Although the narrow component should not taken into account for the FWHM of Hβ this happened for the HES spectrum so that FWHM measured from our VIMOS

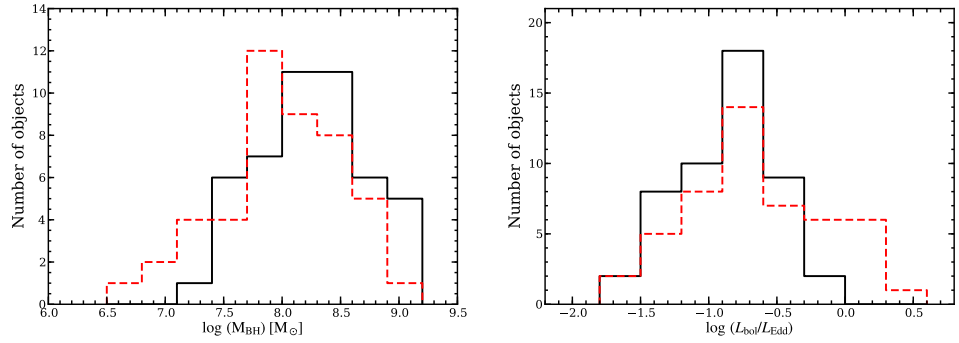

Fig. B.3. Distribution of BH masses (left panel) and Eddington ratios (right panel) for our entire sample. $M_{\rm BH}$ and $L_{\rm bol}/L_{\rm Edd}$ were estimated based either on the broad Hβ line dispersion (solid black line) or on the FWHM of the broad Hβ line (dashed red line).

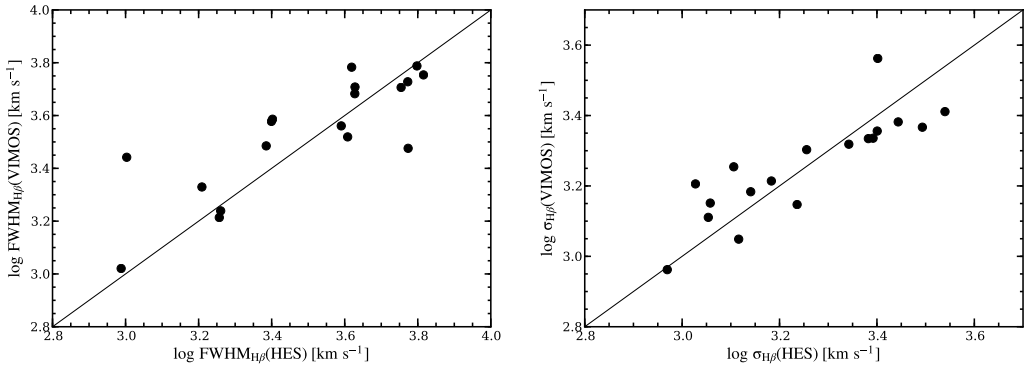

Fig. B.4. Comparison of the broad Hβ width as measured from our VIMOS spectra and slitsless HES spectra. The FWHM of Hβ is shown in the left panel and the line dispersion σ of Hβ is shown in the right panel. The solid line indicates the one-to-one relation.

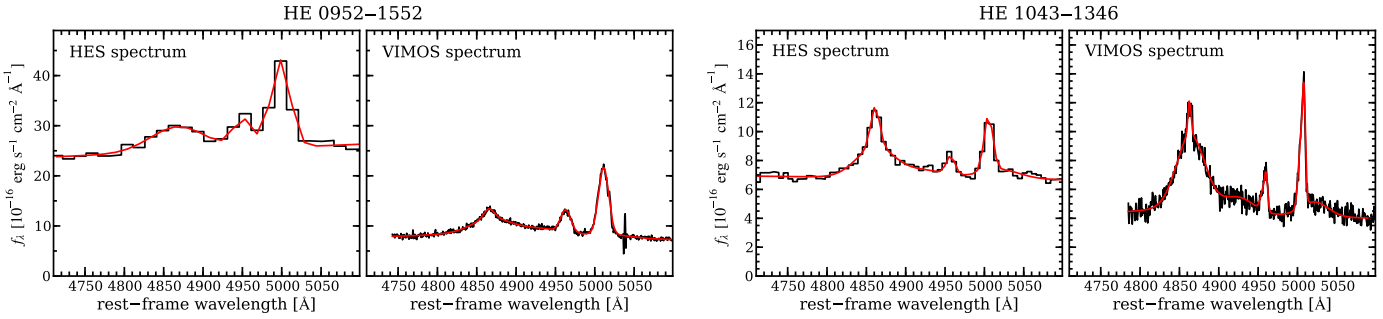

Fig. B.5. Comparison of HES and VIMOS spectra for the two QSOs, HE 0952−1552 and HE 1043−1346. The red line is a model to the data shown as the black line.

spectra is significantly larger. These "mistakes" introduced by the low resolution of the HES spectra are apparently not very frequent and should therefore not systematically affect the results reported by Schulze & Wisotzki (2010) on the BH mass function.

Secondly, we compare the continuum luminosities (L_{5100}) and total Hβ luminosity ($L_{\rm H\beta}$) in Fig. B.6. The continuum luminosities are systematically higher for the HES spectra by 0.15 dex in the mean, which is much more pronounced at low AGN luminosities. This effect is somewhat expected, because the host continuum contribution to the AGN could not be properly subtracted from the HES spectra, but was possible for our IFU data with the aid of the available broad-band images. We can rule out that the variability of the AGN significantly contribute to the offset since no systematic offset is found in $L_{\rm H\beta}$. The overall scatter in both observables is 0.2 dex.

Thirdly, we compare the two BH mass estimates, $M_{\rm BH,\sigma}$ and $M_{\rm BH,FWHM}$, for both datasets in Fig. B.7. We find that $M_{\rm BH,\sigma}$ is only 0.05 dex higher in the mean for the HES spectra, while a higher offset of 0.16 dex is recovered for $M_{\rm BH,FWHM}$ with a scatter of 0.19 dex and 0.26 dex respectively. This is further evidence for $M_{\rm BH,\sigma}$ to be more robust at least from the observational point of view. The offset for $M_{\rm BH,\sigma}$ can be explained by the systematic offset in the continuum luminosity.

Although the observational uncertainty from our measurements is much less than a factor of 2, the systematic uncertainties due to the geometry and physics of the broad-line region could be much higher. For example, it is not yet clear whether the broad-line width is inclination dependent (e.g. Jarvis & McLure 2006; Collin et al. 2006) or radiation pressure is an important ingredient in the physics of the BLR (see Marconi et al. (2008) and Netzer (2009) for an ongoing discussion).

B.4. Bolometric correction based on emission lines

Alternative bolometric corrections are important in cases where the AGN continuum is significantly contaminated by host galaxy light or when the AGN continuum is unobservable like in type 2 AGN. AGN emission lines are not affected by host contamination

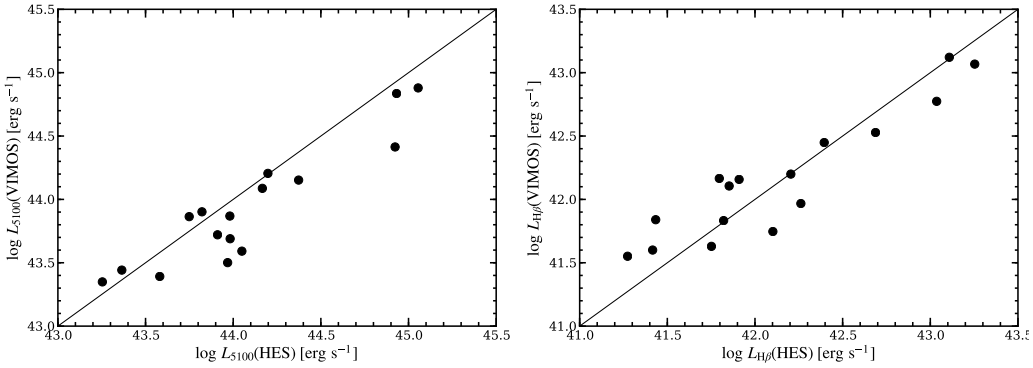

Fig. B.6. QSO continuum luminosities at 5100Å (left panel) and total Hβ luminosities (right panel) are compared for our VIMOS spectra against the slitless HES spectra. The solid line indicates the one-to-one relation.

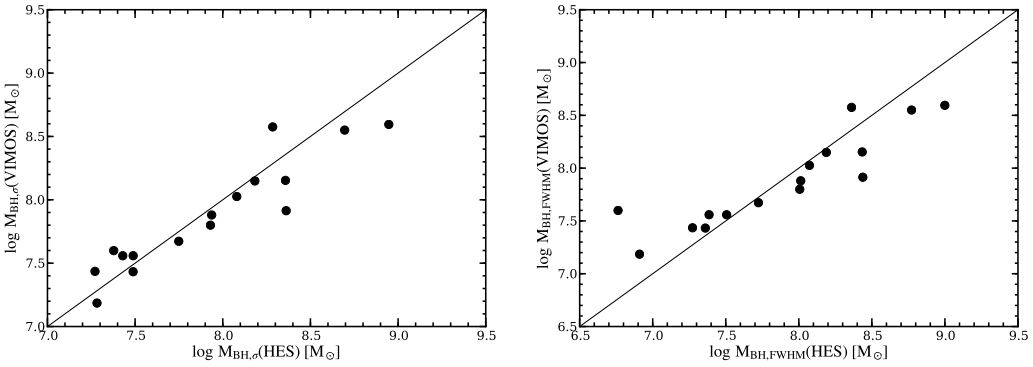

Fig. B.7. Comparison of $M_{\mathrm{BH},\sigma}$ (left panel) and $M_{\mathrm{BH,FWHM}}$ (right panel) for the HES and VIMOS measurements. The solid line indicates the one-to-one relation.

and the luminosity of the broad Hβ line or the [O III] line are often employed for a bolometric luminosity (e.g. Heckman et al. 2004; Greene & Ho 2005). In Fig. B.8 we compare the luminosity of both emission lines with our bolometric luminosity estimated with Equation B.7 from the continuum luminosity for all objects in our sample. $L_{H\beta}$ is almost perfectly correlated with L_{bol} given its high Spearman rank correlation coefficient ($\varrho = 0.96, P = 10^{-27}$) with a scatter of only 0.1 dex. A correlation is also detected for $L_{[\mathrm{OIII}]}$ ($\varrho = 0.72, P = 10^{-6}$), but the scatter is significantly larger (0.4 dex). This is in agreement with the most recent systematic study on bolometric corrections by Punsly & Zhang (2011) based on type 1 AGN with $0.04 < z < 0.08$ from SDSS DR7. Our best-fit linear relations,

$$\log\left(\frac{L_{\mathrm{bol}}}{\mathrm{erg\,s^{-1}}}\right) = 1.0\log\left(\frac{L_{H\beta}}{\mathrm{erg\,s^{-1}}}\right) + 2.2 \qquad \text{and} \tag{B.8}$$

$$\log\left(\frac{L_{\mathrm{bol}}}{\mathrm{erg\,s^{-1}}}\right) = 0.80\log\left(\frac{L_{[\mathrm{OIII}]}}{\mathrm{erg\,s^{-1}}}\right) + 12.1 \qquad , \tag{B.9}$$

are significantly steeper than those reported by Punsly & Zhang (2011). They could not determine the host contribution to the observed continuum for these AGN, so that they most likely overestimated the AGN continuum luminosity. This happens preferentially at low AGN luminosities which skew their relation towards a flatter slopes. Furthermore, we note that our QSOs with a detected ENLR tend to have higher [O III] luminosities at a given bolometric luminosity compared to objects without an ENLR. This may introduce a certain selection bias for luminous type 2 QSOs with respect to their ENLR properties as they are selected based on their [O III] luminosity.

References

Bentz, M. C., Peterson, B. M., Netzer, H., Pogge, R. W., & Vestergaard, M. 2009, ApJ, 697, 160
Bentz, M. C., Peterson, B. M., Pogge, R. W., Vestergaard, M., & Onken, C. A. 2006, ApJ, 644, 133
Blandford, R. D. & McKee, C. F. 1982, ApJ, 255, 419
Boroson, T. A. & Green, R. F. 1992, ApJS, 80, 109
Brotherton, M. S. 1996, ApJS, 102, 1
Brotherton, M. S., Wills, B. J., Francis, P. J., & Steidel, C. C. 1994, ApJ, 430, 495
Collin, S., Kawaguchi, T., Peterson, B. M., & Vestergaard, M. 2006, A&A, 456, 75
Greene, J. E. & Ho, L. C. 2005, ApJ, 630, 122
Heckman, T. M., Kauffmann, G., Brinchmann, J., et al. 2004, ApJ, 613, 109
Hopkins, P. F., Richards, G. T., & Hernquist, L. 2007, ApJ, 654, 731
Hu, C., Wang, J., Ho, L. C., et al. 2008, ApJ, 687, 78
Jarvis, M. J. & McLure, R. J. 2006, MNRAS, 369, 182
Kaspi, S., Maoz, D., Netzer, H., et al. 2005, ApJ, 629, 61
Kaspi, S., Smith, P. S., Netzer, H., et al. 2000, ApJ, 533, 631
Krolik, J. H. 2001, ApJ, 551, 72

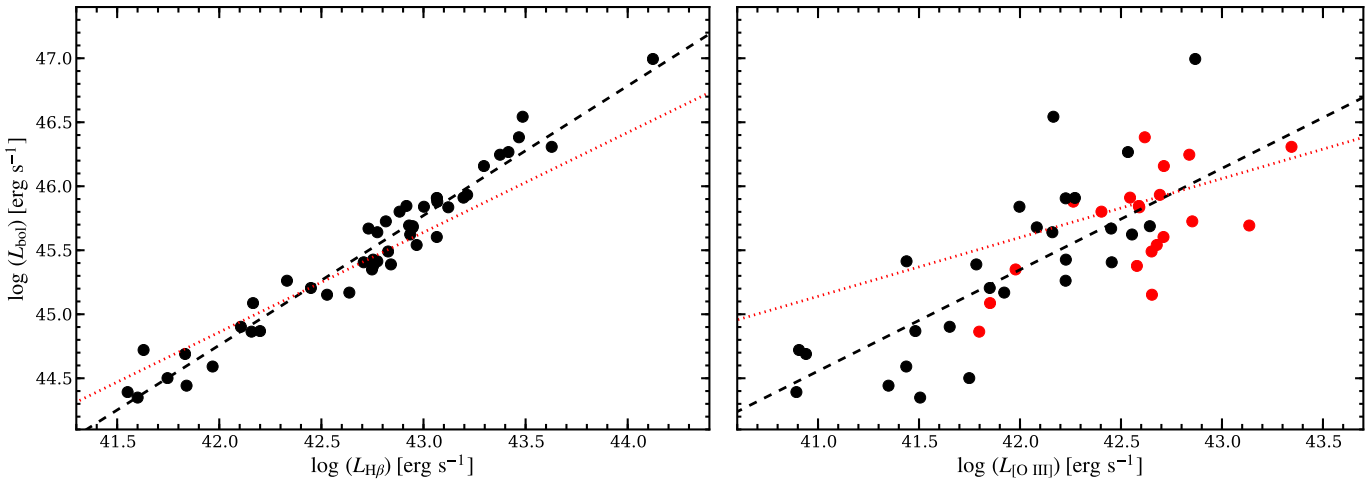

Fig. B.8. AGN bolometric luminosity as a function of the broad Hβ line luminosity (left panel) and [O III] line luminosity (right panel) for our full QSO sample. The dashed black line is our best-fit linear relation through the data. Linear relation provided by Punsly & Zhang (2011) were converted to our bolometric correction and are shown as the red dotted lines. All QSOs with a detected ENLR are highlighted as red symbols in the left panel.

Laor, A., Bahcall, J. N., Jannuzi, B. T., et al. 1994, ApJ, 420, 110
Marconi, A., Axon, D. J., Maiolino, R., et al. 2008, ApJ, 678, 693
Marconi, A., Risaliti, G., Gilli, R., et al. 2004, MNRAS, 351, 169
Marziani, P., Sulentic, J. W., Zamanov, R., et al. 2003, ApJS, 145, 199
McGill, K. L., Woo, J.-H., Treu, T., & Malkan, M. A. 2008, ApJ, 673, 703
Nagao, T., Marconi, A., & Maiolino, R. 2006, A&A, 447, 157
Netzer, H. 2009, ApJ, 695, 793
Onken, C. A., Ferrarese, L., Merritt, D., et al. 2004, ApJ, 615, 645
Peterson, B. M., Ferrarese, L., Gilbert, K. M., et al. 2004, ApJ, 613, 682
Peterson, B. M. & Wandel, A. 2000, ApJ, 540, L13
Punsly, B. & Zhang, S. 2011, ArXiv e-prints
Richards, G. T., Lacy, M., Storrie-Lombardi, L. J., et al. 2006, ApJS, 166, 470
Salviander, S., Shields, G. A., Gebhardt, K., & Bonning, E. W. 2007, ApJ, 662, 131
Schulze, A. & Wisotzki, L. 2010, A&A, 516, A87+
Schulze, A., Wisotzki, L., & Husemann, B. 2009, A&A, 507, 781
Shen, Y., Greene, J. E., Strauss, M. A., Richards, G. T., & Schneider, D. P. 2008, ApJ, 680, 169
Sulentic, J. W., Marziani, P., Zamanov, R., et al. 2002, ApJ, 566, L71
Véron-Cetty, M., Joly, M., & Véron, P. 2004, A&A, 417, 515
Véron-Cetty, M.-P., Joly, M., Véron, P., et al. 2006, A&A, 451, 851
Véron-Cetty, M.-P., Véron, P., & Gonçalves, A. C. 2001, A&A, 372, 730
Wandel, A., Peterson, B. M., & Malkan, M. A. 1999, ApJ, 526, 579
Woo, J., Treu, T., Barth, A. J., et al. 2010, ApJ, 716, 269

Appendix C

Results of the spectral QSO-host deblending for the QSOs observed with VIMOS

ABSTRACT

We present here the results of the spectral QSO-host deblending process for 13 QSOs from the sample presented in Chapter 3 for which a decent signal of the underyling host could be detected and modelled with STARLIGHT.

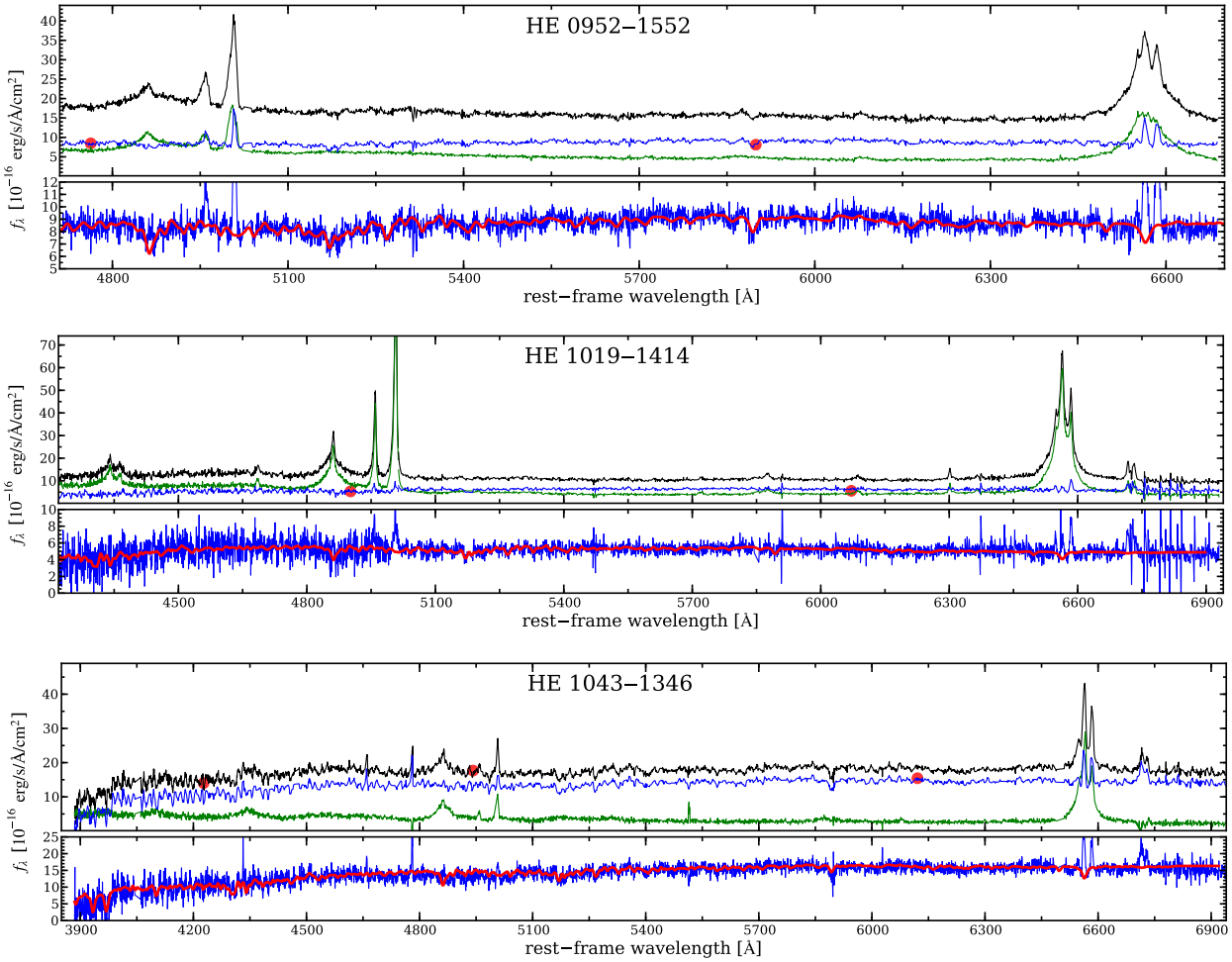

Fig. C.1. Results of the spectral debelending of QSO and host emission for the individual objects. Shown are the integrated spectrum (black line), the QSO component (red line) and the galaxy component (blue line) for each object with sufficient S/n. These spectra are slightly smoothed by a median filter (5 spectral pixels) for display purposes. The unsmoothed galaxy spectrum (blue line) is presented overplotted with the best-fit model spectrum (red line) below.

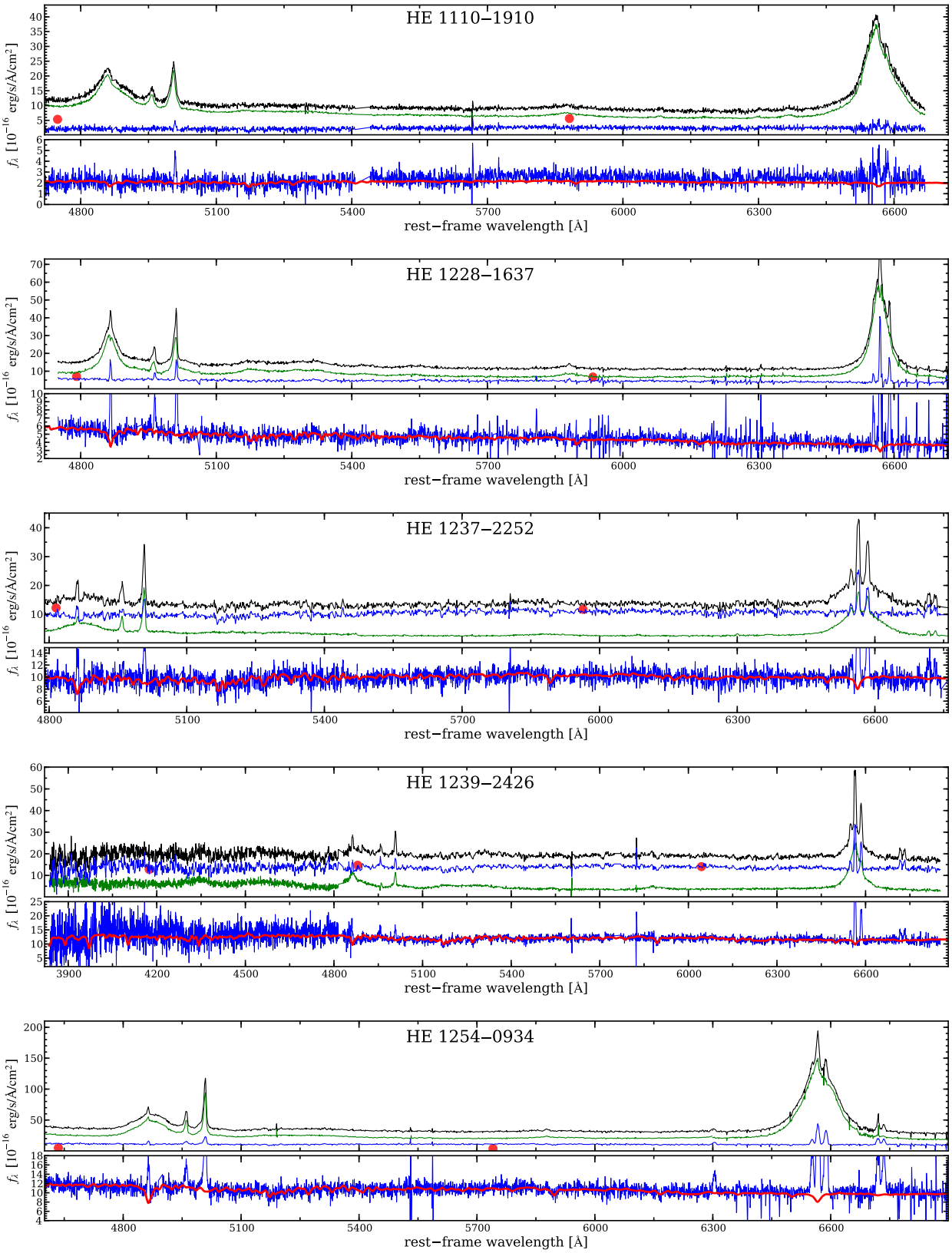

Fig. C.1. *continued*

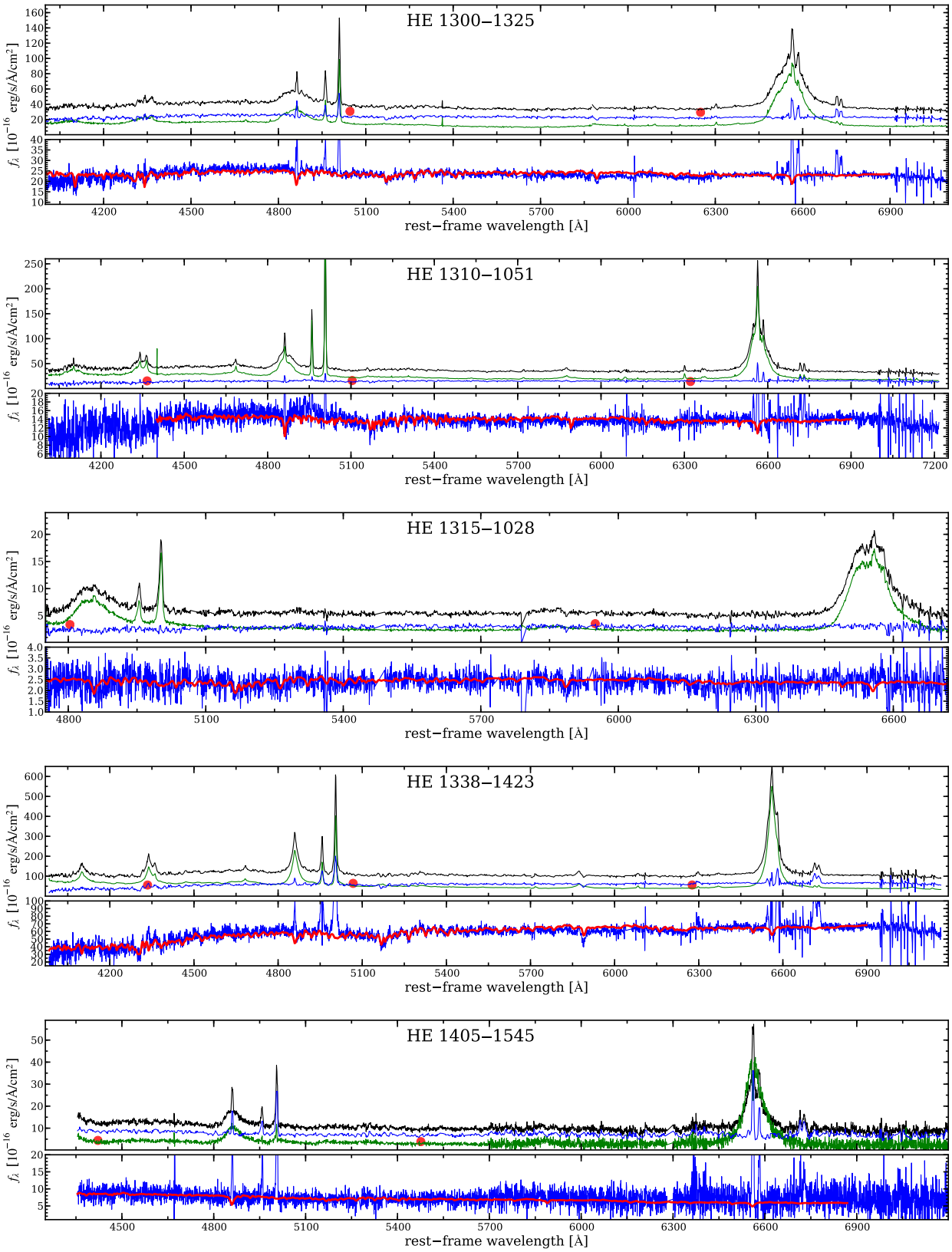

Fig. C.1. *continued*

Appendix D

Gas and stellar kinematics of QSO hosts in the VIMOS sample

ABSTRACT

As a byproduct of our analysis, we derived also the gas kinematics from the IFU observations for all QSO hosts in the VIMOS sample, and even stellar kinematics for the nearest objects. Although the interpretation of the kinematics is part of Dading Nugroho's PhD thesis, the construction of the kinematic maps from the data was our contribution to the collaborative work and are presented in this Appendix. We briefly comment on individual objects, but similar to the kinematic results for the QSO host in our PMAS sample we do not find evidence for gas outflows in the majority of cases.

D.1. Kinematic maps

We constructed radial velocity maps for the ionised gas component by modelling all the major emission lines Hβ, [O III], Hα, [N II] and [S II], if present, *simultaneously* with a Gaussian profile coupled in radial velocity and intrinsic line dispersion. With this approach we achieve a high accuracy in the radial velocity of the order of $\sim$10 km s^{-1} dominated by the uncertainty in the intrinsic wavelength calibration of the data. Due to the relatively high spectral resolution of VIMOS, we were able to kinematically separate different emission-line components in the host galaxies of HE 1237−2252, HE 1300−1325. The measured velocity dispersion $\sigma_{\rm obs}$ was corrected for the instrumental dispersion ($\sigma_{\rm instr}$ $\sim$45 km s^{-1}) to obtain the intrinsic velocity dispersion $\sigma_{\rm intr}$ via $\sigma_{\rm intr} = \sqrt{\sigma^2_{\rm obs} - \sigma^2_{\rm instr}}$.

For the brightest host galaxies, HE 1043−1346, HE 1237−2252, HE 1300−1325, HE 1310−1051, and HE 1338−1423, the S/N of the stellar continuum is sufficiently high to measure the radial velocity and velocity dispersion for the stellar component, spatially binned using Voronoi Tesselation. Because we modelled the continuum for those objects with `STARLIGHT`, as described in Chapter 4, the kinematics of the stellar component were an automatic byproduct of this analysis. The stellar velocity dispersion was similarly corrected for the instrumental dispersion as the gaseous velocity dispersion.

We masked out all spaxels with an uncertainty in the radial velocity greater than 30 km s^{-1} and 60 km s^{-1} for the gaseous and stellar component, respectively, because we consider them to be unreliable. In Fig. D.1 we present the resulting kinematic maps for the sample.

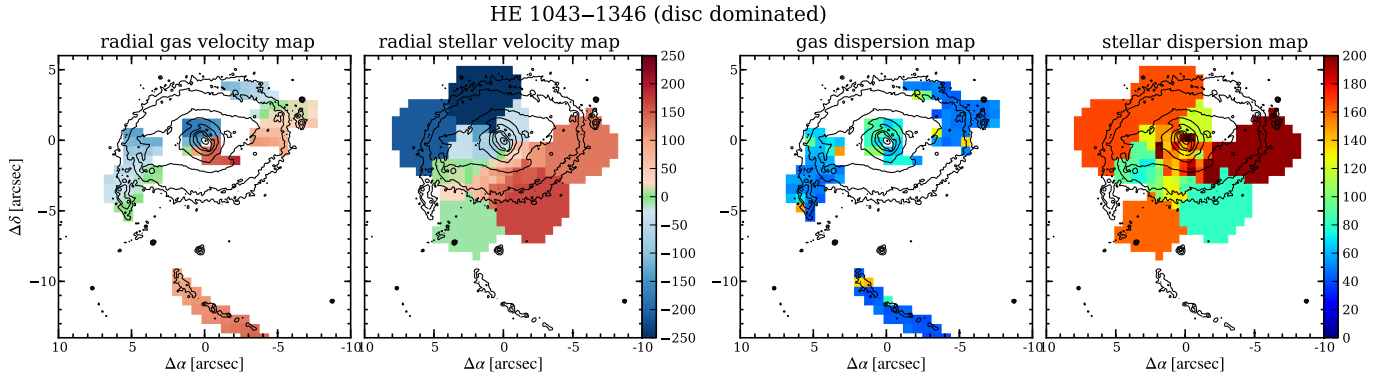

Fig. D.1. Kinematic map for our QSO hosts. Depending on the object stellar kinematics are presented together with the gaseous kinematics. The velocity fields are presented in the left panels while the velocity dispersion are shown on the right panels. All values are in km s^{-1}. Countours of broad-band surface brightness are overplotted to guide the eye.

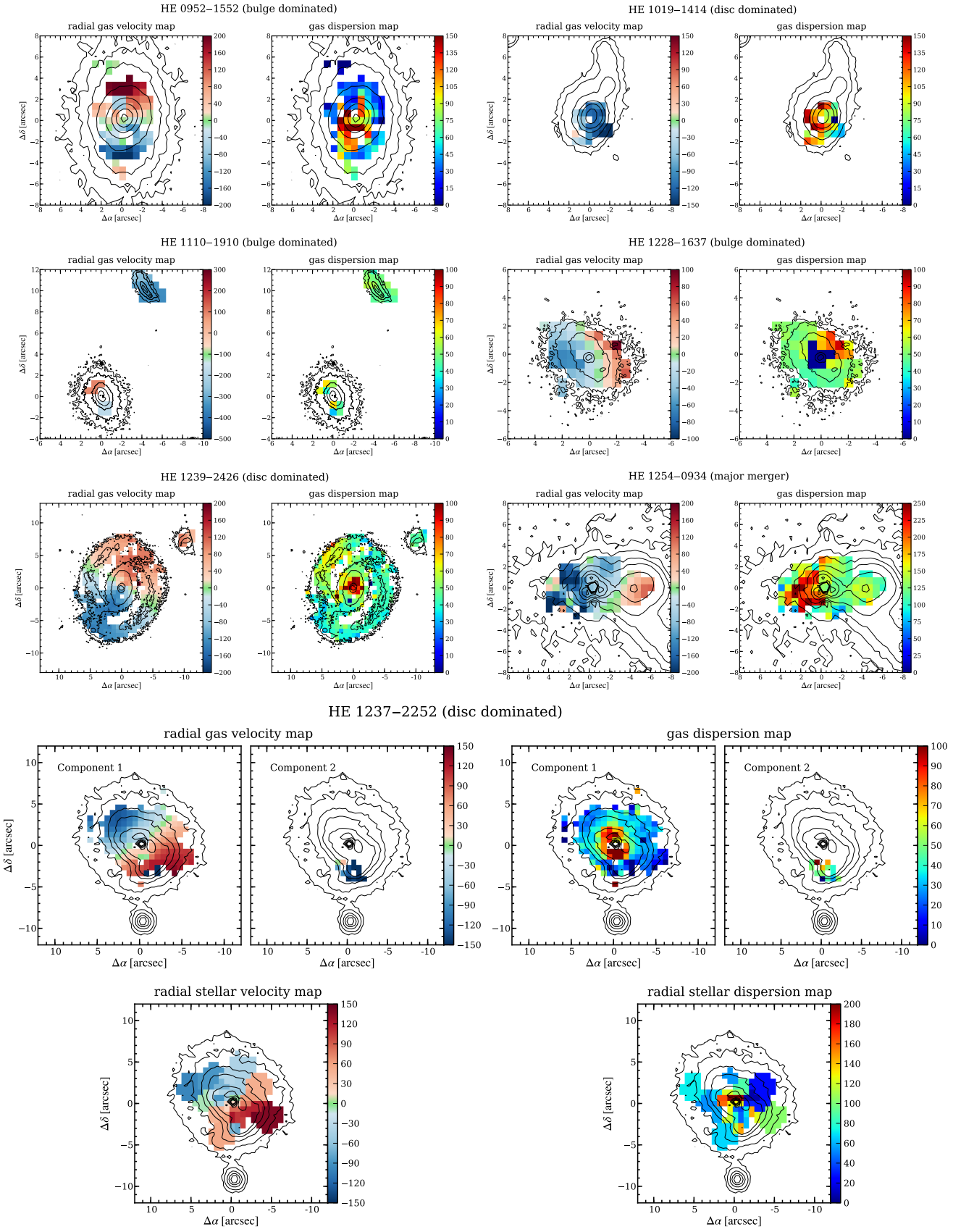

Fig. D.1. Continued.

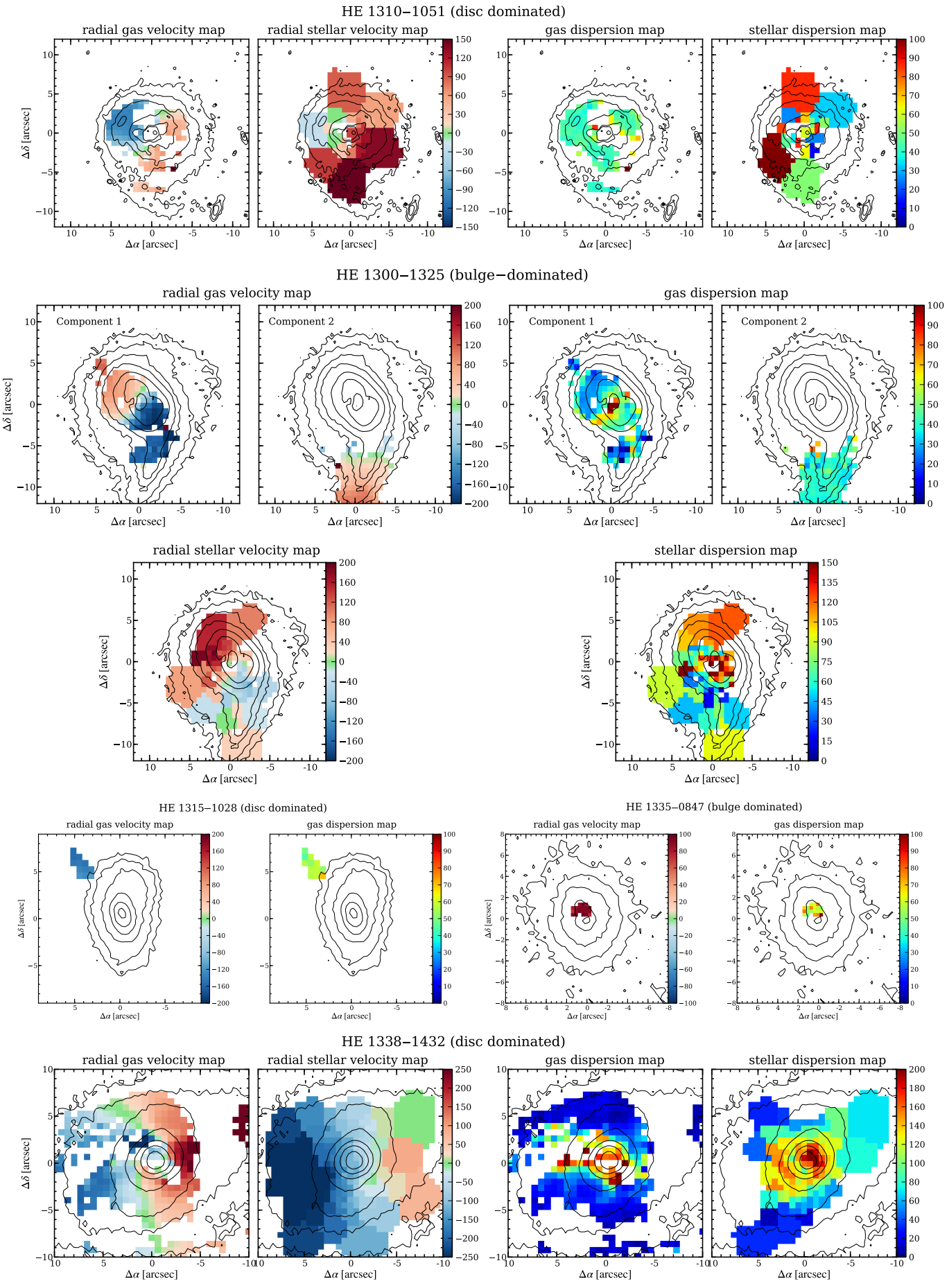

Fig. D.1. Continued.

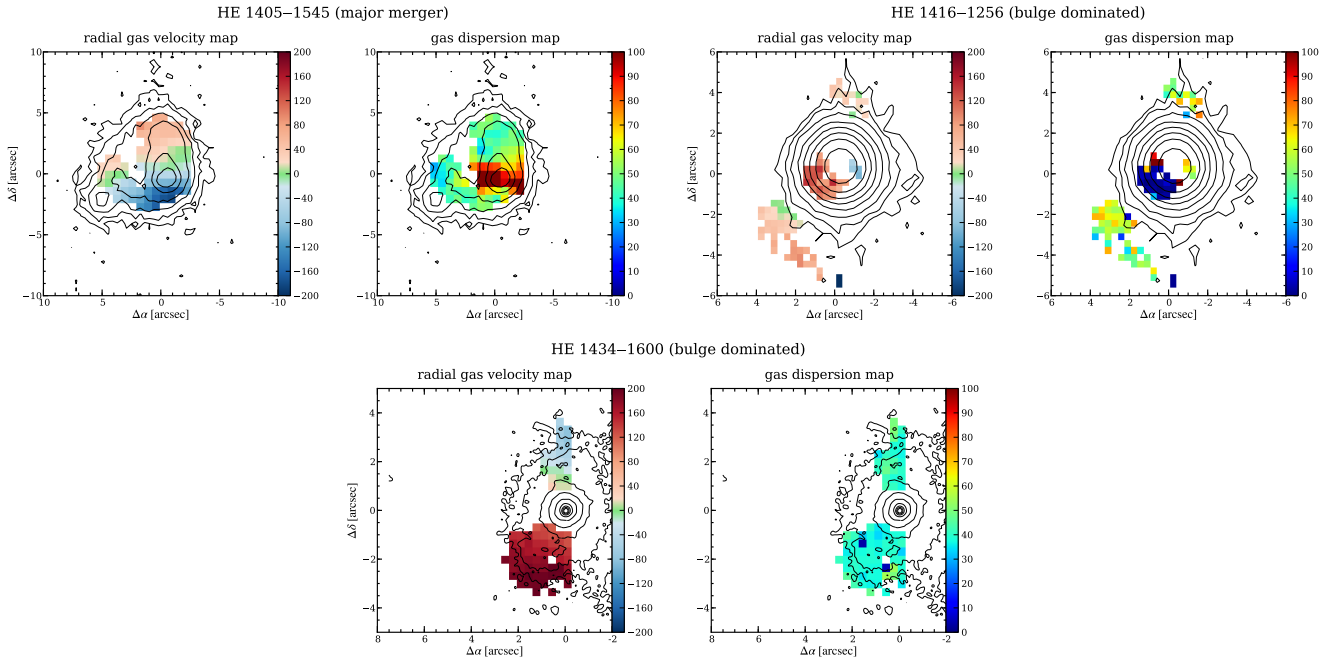

Fig. D.1. Continued.

D.2. Comments on individual objects

D.2.1. HE 0952−1552

Although this QSO host galaxy has been classified as a bulge-dominated galaxy, we detect significant emission from H II regions and AGN-ionised gas. The presented velocity field highlights mainly the kinematics of the H II regions which follows a clear rotational pattern. However the measurements are affected by the blending with emission lines of the extended AGN-ionised gas along the same line of sight. The morphology and kinematics of the AGN-ionised gas indicate a possible jet-cloud interaction. These regions have a significantly higher velocity dispersion. A deblending of these line should also be possible, although the S/N is not sufficient to do this for each spaxel individually.

D.2.2. HE 1019−1414

Although the galaxy is apparently interacting with another galaxy, ionised gas is only detected around the centre to measure the gaseous velocity field. However, we do not detect any significant radial velocity, or velocity dispersion gradient across the ionised gas region, which may indicate that the emission is almost point like. No valueable kinematic information can be obtained from this object.

D.2.3. HE 1043−1346

A clear rotational pattern is found in the gas and stellar velocity field as expected for such an undisturbed disc galaxy. The ionised emission around the QSO is dominated by massive star forming regions for which the radial velocity in the gas is higher on both the red- and blue-shifted side with respect to the stellar velocity field in that region. We speculate whether the kinematic axis of the circumnuclear gas disc has a lower inclination with respect to the axis primary disc of the galaxy. The gas velocity dispersion in the disc is low $\sigma << v_r$ as expected for rotational-dominated kinematics. On the other hand, the stellar velocity dispersion is substantial higher, which can be partially explained by the large bins covering a substantial part of the galaxy. The rise of the stellar velocity dispersion towards the centre is most likely a real feature, suggesting either a significant bulge component or the superposition of the kinematics of young stars formed in the circumnuclear disc and those of the major disc component.

D.2.4. HE 1110−1910

Emission lines are weak in this bulge-dominated galaxy, but two spots of emission indicate a significant velocity gradient in the ionised gas of the order of $300\,\mathrm{km\,s^{-1}}$. Given the low velocity dispersion, the gas is either rotational dominated or might represent a bipolar directional outflow without a significant dispersion component. The nearby companion is at the same redshift and its morphology supports the notation of an ongoing interaction. A gradient in its velocity field is present likely to be of rotational motion as the galaxy is almost oriented edge-on with respect to our line of sight.

D.2.5. HE 1228−1637

The radial gaseous velocity field shows a velocity gradient of about $\pm 80\mathrm{km\,s^{-1}}$, but does not look like a pure rotational pattern. Given that it is morphologically a bulge-dominated galaxy this may not be expected, but the gas is also kinematically cold. Only in the region with the greatest Hα flux, i.e. strongest star formation, the dispersion increases as an indication for a highly disturbed medium possibly due to shocks.

D.2.6. HE 1237−2252

A disc-dominated galaxy with a minor companion superimposed along our line-of-sight, which we were able to kinematically decouple. The primary galaxy displays the same rotational pattern in the gas as well as in the stellar velocity field. Apparently, its kinematic is not much affected by the gravitation of the nearby minor galaxy. The velocity dispersion increases towards the centre and changes from a kinematically cold to hot mode, which we interpret as an indication for a substantial bulge component in this disc galaxy.

D.2.7. HE 1239−2426

Grand-design spiral galaxy with a particularly well-defined gaseous rotational velocity field. Its velocity dispersion increases towards to bulge as expected, but also in the North-East spiral arm with the strong star formation signal of the galaxy. Similar to HE 1228−1637, we interpret this as evidence for a turbulent medium driven by shocks. A minor disc-dominated companion galaxy is confirmed to be at the same redshift, with a possible signature of weak rotation.

D.2.8. HE 1254−0934

Complex ionised gas kinematics are recovered for this major merger host galaxy. The velocity dispersion is high (¿$100\,\mathrm{km\,s^{-1}}$) throughout the entire region, indicating a turbulent medium. One explanation for this might be the feedback from supernovae at

the starburst region and jet or outflows from the AGN close to the nucleus. The velocity field is complex and does not reveal any signature for ordered motion.

D.2.9. HE 1300−1325

The radial gas velocity field of this galaxy confirms that the prominent structure in the broad-band image is a tidal tail and not a spiral arm, since it is kinematically detached from the rotational gas motion of the host galaxy. Thus, the morphological classification of a bulge-dominated galaxy is not violated. The stellar kinematics also show signatures of rotational motion, but much less pronounced than seen in the gas. Either the gas was recently accreted from the environment or the superposition of stellar population at the position of the tidal tail hampers the determination of the stellar velocity field. The clear interaction signatures and the high stellar velocity dispersion, not only along the tidal tail, support more the first scenario of externally accreted gas.

D.2.10. HE 1310−1051

Only the *HST* image revealed the interaction minor companion South-West of the galaxy followed by a large tidal stream of stars. The gas kinematics are kinematically cold and follow a rotational pattern, whereas the stellar velocity field is less pronounced. Whether this is introduced due to the large bins required to accumulate enough signal for the stellar continuum is unknown.

D.2.11. HE 1315−1028

Ionised gas is only found outside the main body of the host galaxy without a counterpart in the broad-band images. The only thing we can say about the kinematics of this region is that it is blue-shifted with respect to the host by $\sim 150\mathrm{km\,s^{-1}}$ and is kinematically cold.

D.2.12. HE 1335−0837

Only a single star forming region is detected in this bulge-dominated galaxy located 1″ North of the nucleus and redshifted by about $\sim 100\mathrm{km\,s^{-1}}$ with respect to the QSO emission lines.

D.2.13. HE 1338−1423

One of the nearest QSO with a disc-dominated host galaxy, for which the stellar kinematics could be measured with the highest accuracy. The stellar and gaseous velocity field display a clear rotational pattern as expected. The apparent offset between the two are possible cause by a mistake for the systematic which we could not identify before finishing the thesis. The velocity dispersion around the nucleus is high for the stars and also for the gas. Various broad emission lines in the extended ionised gas are found while inspecting those spaxels. The emission line profile at those regions would require several components to be accurately modelled, so that it is difficult to create proper kinematic maps for these regions. We tentatively note that the stellar light is dominated by intermediate or old stellar populations, so that this process would be interesting to study in terms of AGN feedback processes in the future.

D.2.14. HE 1405−1545

The gaseous velocity field of this apparently ongoing major-merger host shows that the system is rotating around its centre of mass, which is not coincident with the QSO position. The high gas velocity dispersion close to the QSO is due to kinematically decoupled emission lines that we could only model in the co-added light of this region, but not in individual spaxel for which we had to use a single Gaussian. We speculate that this is evidence for outflowing material ejected along the path of the lowest resistance which is the steepest gradient in matter density.

D.2.15. HE 1416−1256

Two intriguing shells of gas are detected on both sides of the bulge-dominated host galaxy. Due to the low S/N for individual spaxels it is difficult to infer clear kinematic maps for these structures. Only close to the nucleus a significant velocity gradient could be detected which might be attributed to rotational motion, but the shells appear to have almost the same radial velocity. The nature of these gas structure therefore remains open.

D.2.16. HE 1434−1600

Longslit spectroscopy for this radio-loud elliptical galaxy was already presented for this object. They recovered a velocity curve that did not match with a simple rotational model with two almost flat curves on the blue and redshifted side of the nucleus. The reason for this is probably very simple. Our data show that the emission originates from two distinct structures on both sides of the nucleus which match with the very sharp high surface brightness structure in the broad-band *HST* images. In ground-based images or spectroscopy these regions appear spatially extended due to the seeing but are physically not very extended in radial direction from the nucleus. These structures possibly represent the bow shock of an outflow or the shell of an expanding bubble of material.

Appendix E

Kinematics of the nuclear [O III] λ5007 line

ABSTRACT

The narrow [O III] λ5007 is the brightest forbidden line in the rest-frame optical spectra of QSOs and is commonly used to estimate their systemic redshifts. The [O III] line width was shown to correlate with the stellar velocity dispersion of the bulge, and therefore used to study the BH mass-bulge relations up to high redshifts. The [O III] line is mainly emitted from regions that are AGN ionised and are thus particular susceptible to non-gravitational motions due to AGN outflows and interaction with radio jets, so that it appears often blueshifted with respect to lower ionisation lines. Here we study the kinematics of the [O III] line in the QSO spectra for our combined PMAS and VIMOS sample. Based on the extended gaseous velocity fields and the stellar absorption lines, we find that the [O III] line is a good measure for $z_{\rm sys}$ at least for QSO with FWHM$_{\rm H\beta} > 2500\,{\rm km\,s^{-1}}$. The tip of H$\beta$ might be a better estimate of $z_{\rm sys}$ for all other QSOs, but extended ionised gas was only detected for one QSO of that class. Without a-priori knowledge about the previous studies concerning the [O III] line width, we find that $\sigma_{\rm [O\,III]}$ would be uncorrelated with σ_*, indirectly tested via the $M_{\rm BH}$-σ_* relation. We detect a couple of outliers from the presumed relation, which are all accreting close or above the Eddington limit. Previous reported trends of increasing gaseous velocity dispersion with Eddington ratio are not confirmed, possibly due to the low number of objects. Interestingly, we detected a few bulge-dominated galaxies with kinematically cold extended gas, that is found to be decoupled from the circumnuclear gas kinematics without no systematic shift of their location in the $M_{\rm BH}$ - $\sigma_{\rm g}$ plane. We measured the stellar velocity dispersion for only 4 bulge-dominated systems and found that they are on or slightly above the local $M_{\rm BH}$ - σ_* relation.

E.1. Blueshifted [O III] line in QSO spectra

The [O III] λ5007 line of QSOs is typically used to estimate their systemic redshifts, because it is the strongest narrow line and not blended with a broad Balmer line, like the [N II] λ6584 line for instance. Since the seminal work of Heckman et al. (1981) it is well known that the [O III] line can be blueshifted (>100 km s^{-1}) with respect to other estimators of the systemic redshift. Eracleous & Halpern (2004) and Boroson (2005) used lower ionisation lines, e.g. [N II] or [S II] for a systematic study of this effect. They found that the strength of the blueshift is closely related to the Eddington ratio λ, although some objects were also detected by Boroson (2005) with negligible [O III] blueshifts at high Eddington ratio.

As a byproduct of our modelling of the QSO spectra (see Appendix B) we also obtained information about the [O III] line, like its redshift and line width, which we list in Table E.1. Additionally, we measured the redshift for the tip of Hβ directly from the QSO spectra. Letawe et al. (2007) proposed that the tip of Hβ might be a better proxy for the systemic redshift based on resolved gas kinematics of 5 QSO hosts. In order to reach subpixel precision for the Hβ peak, we modelled the 5-10 spectral data points, depending on the spectral resolution, around the Hβ maximum with a Gaussian.

In Fig. E.1 we compare the rest-frame radial velocity difference between the core of the [O III] line and the tip of Hβ, which we defined as

$$\Delta v = (c\, z_{\rm [O\,III]} - c\, z_{\rm H\beta})/(1 + z_{\rm H\beta}) \quad , \tag{E.1}$$

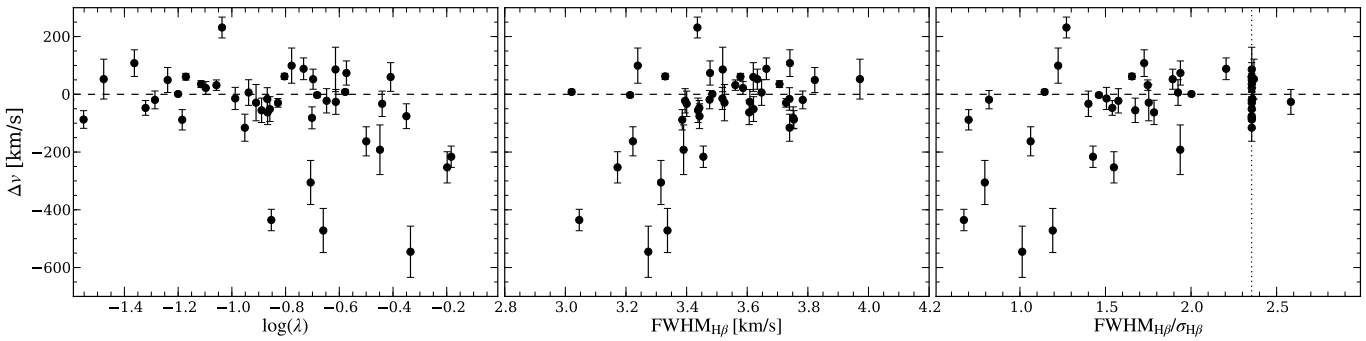

Fig. E.1. Comparison of the [O III] and Hβ rest-frame radial velocity offset Δv with other QSO parameters. This velocity offset is shown against the Eddington ratio λ (left panel), the FWHM of the broad Hβ line (middle panel) and the shape of the broad Hβ line profile FWHM$_{\rm H\beta}/\sigma_{\rm H\beta}$ (right panel). The zero velocity offset is highlighted by the dashed line throughout the three panels. In the right panel, a vertical dotted line indicates the FWHM$_{\rm H\beta}/\sigma_{\rm H\beta}$ ratio for a pure Gaussian line profile.

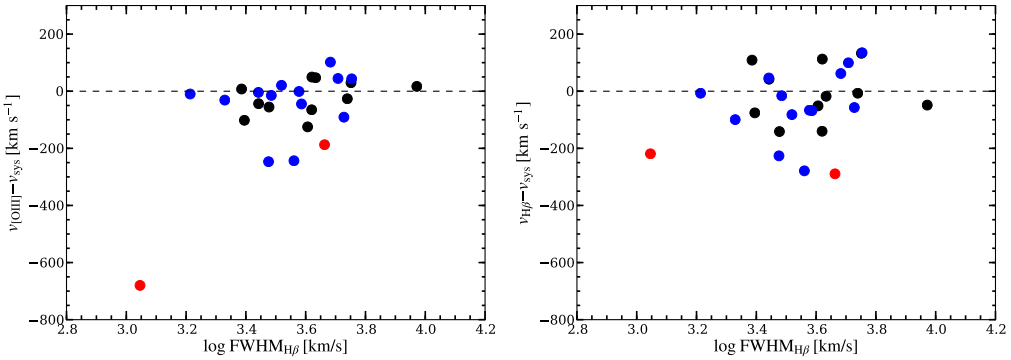

Fig. E.2. Radial velocity offset of the nuclear [O III] line (left panel) and the tip of the broad Hβ line (right panel) with respect to the independent systemic redshift of the host as a function of the Hβ FWHM. The black, red and blue symbols indicate systemic redshift measurements based on the resolved [O III] kinematics, the resolved Hα kinematics and absorption lines in the stellar continuum, respectively.

against λ, FWHM$_{H\beta}$ and the shape of Hβ line profile described as FWHM$_{H\beta}/\sigma_{H\beta}$. Large blueshifted [O III] lines with $\Delta v < -200\,\mathrm{km\,s^{-1}}$ are only present for QSOs with high Eddington ratio in the range of $-1.0 < \log\lambda < 0.0$, so that a trend of an increasing [O III] blueshift together with λ emerged. The extreme blueshifted [O III] lines at high Eddington ratios are usually interpreted as potential signatures for AGN outflows considering that no extreme redshifted lines have been detected. A similar trend is also seen for a decreasing FWHM$_{H\beta}$. The highest blueshifted objects are only detected at FWHM$_{H\beta} < 2500\,\mathrm{km\,s^{-1}}$. This was highlighted by Aoki et al. (2005), who discovered the two largest blueshifts of [O III] ($\Delta v < 800\mathrm{km\,s^{-1}}$) known to date are found in QSOs with similarly narrow Hβ lines. Those trends are in general agreement with results reported by Boroson (2005). Since the Eddington ratio depends on FWHM$_{H\beta}$ via the BH mass at a given continuum luminosity, low mass BH can have rather narrow Hβ lines even at low Eddington ratios $\lambda < -1.0$ if its AGN luminosity is low. This possibly explains the few objects with $\Delta v \approx 0\,\mathrm{km\,s^{-1}}$ for narrower Hβ lines that are not present in the plot along λ. We further emphasise that the shape of the Hβ line profile is connected with the blueshift of the [O III] as well. QSOs for which Hβ significantly deviates from a Gaussian profile towards a Lorentzian shape (FWHM$_{H\beta}/\sigma_{H\beta} < 1.6$) have a higher probability for having a significantly blueshifted [O III] line.

E.2. Systemic redshift from gas and stellar kinematics

The peak of the Hβ line in the QSO spectra might also not correspond to the "true" systemic redshift, so that we try to infer the systemic redshift *independently* from the spatially resolved gas kinematics in the spirit of Letawe et al. (2007) or even from stellar absorption lines. We determined the systemic redshift from the velocity fields of the ionised gas by fitting a straight line to the gradient in the velocity curve along the kinematic major axis as described in section 3.6. For the VIMOS QSOs we adopted the systemtic redshift of the stellar absorption lines that we measured as a byproduct of the stellar continuum modelling with `STARLIGHT` for many objects.

In Fig. E.2 we present the measured radial velocity offsets $v_{[O\,III]}-v_{sys}$ and $v_{H\beta}-v_{sys}$ for our QSOs. The velocity offsets are within $\pm 200\,\mathrm{km\,s^{-1}}$ for the majority of objects in both cases. The mean value of the velocity offsets for QSOs with FWHM$_{H\beta} > 2500\,\mathrm{km\,s^{-1}}$ are $\langle v_{[O\,III]}-v_{sys}\rangle = -38\pm88$ and $\langle v_{H\beta}-v_{sys}\rangle = -39\pm118$. Thus, the H$\beta$ as well as the [O III] line can be a good proxy for the systemic redshift of the host galaxy in the QSO spectra for objects with FWHM$_{H\beta} > 2500\,\mathrm{km\,s^{-1}}$. The uncertainty for the tip of the Hβ line is higher, because its redshift cannot be measured with the same precision as the redshift of the narrow [O III] line. From the objects with a highly blueshifted [O III] line in the QSO spectrum, we could only infer the systemic redshift for I Zw 1 from the extended gas kinematics. The tip of Hβ is a much better estimate for z_{sys} for this object. We need to point out a potential observational bias, because extended ionised gas preferentially detected around QSOs with a broad Hβ line. The [O III] line is usually quite strong in those objects and probably follows the kinematics of the extended gas.

Overall, we can recommend to use the tip of the broad Hβ line as a proxy for the systemic redshift as initially suggested by Letawe et al. (2007). Unfortunately, we could not test this for all objects of our sample. In particular those objects lack of extended ionised gas for which the blueshift of their [O III] lines is potentially the highest. An unbiased test is thus not possible. The reason for the lack of extended ionised gas in those objects is still unknown and may be related to systematic differences in the properties of the QSOs. If the extremely blueshifted [O III] lines in QSO spectra are really signatures of gas outflows driven by the AGN (e.g Zamanov & Marziani 2002; Aoki et al. 2005), an outflow is probably confined to the circumnuclear region on scales much less than 1 kpc.

E.3. Testing the use of the [O III] line width as a proxy for σ_*

Nelson & Whittle (1996) studied a sample of nearby type 2 AGN and found that the width of the nuclear [O III] lines is correlated with the velocity dispersion of stars (σ_*) in the bulge of their host galaxies. Subsequently, Nelson (2000) proposed to use the dispersion of the gas (σ_g) defined as σ_g = FWHM$_{[O\,III]}$/2.354 as a proxy for σ_* and did not find a systematic offset from the M_{BH} - σ_* relation for a local sample of type 1 AGN. This technique was applied to a sample of QSOs up to $z < 3.3$ for which no significant evolution in the M_{BH} - σ_* relation was found (Shields et al. 2003). However, the scatter in the M_{BH} - σ_g relation based on [O III] is substantially larger compared to σ_* (e.g. Nelson & Whittle 1996; Boroson 2003; Onken et al. 2004; Woo et al. 2006). The major concern is that the kinematics of the [O III] line may be significantly affected by non-gravitational motions due to an interaction with a radio jet or an AGN driven outflow. Here, we try to further study the use of the [O III] line as a proxy for σ_* with our QSO

Table E.1. Properties of the nuclear [O III] line

Object	f([O III]) $\left[10^{-16}\frac{\mathrm{erg}}{\mathrm{s\,cm^2}}\right]$	$\sigma_{[\mathrm{O\,III}],\mathrm{na}}$ km s^{-1}	$\sigma_{[\mathrm{O\,III}],\mathrm{br}}$ km s^{-1}	$\sigma_{[\mathrm{O\,III}],\mathrm{full}}$ km s^{-1}	FWHM$_{[\mathrm{O\,III}],\mathrm{full}}$ km s^{-1}	$cz_{[\mathrm{O\,III}]}$ km s^{-1}	$cz_{\mathrm{H}\beta\,\mathrm{tip}}$ km s^{-1}
PMAS observations							
PG 0026+129	622 ± 127	111 ± 15	...	111 ± 14	258 ± 37	43465 ± 30	43566 ± 27
I Zw 1	2048 ± 426	389 ± 6	600 ± 7	755 ± 4	1831 ± 12	17572 ± 33	18033 ± 22
PG 0052+251	765 ± 155	216 ± 8	...	216 ± 7	507 ± 17	46174 ± 30	46072 ± 31
SDSS J0057+1446	230 ± 62	267 ± 6	550 ± 90	439 ± 26	676 ± 11	51320 ± 44	...
HE 0132−0441	221 ± 81	228 ± 20	434 ± 54	431 ± 10	911 ± 25	46511 ± 56	46803 ± 28
HE 0157−0406	88 ± 20	312 ± 11	...	312 ± 10	733 ± 26	65007 ± 36	65147 ± 44
SDSS J0155−0857	227 ± 57	115 ± 7	323 ± 26	204 ± 12	283 ± 16	49324 ± 42	49266 ± 28
Mrk 1014	979 ± 206	211 ± 4	621 ± 5	582 ± 3	711 ± 8	48831 ± 41	48746 ± 26
SDSS J0846+4426	1119 ± 281	171 ± 7	498 ± 129	287 ± 58	431 ± 12	76257 ± 43	76182 ± 45
SDSS J0948+4335	185 ± 42	129 ± 5	455 ± 22	356 ± 16	337 ± 12	68038 ± 43	68071 ± 31
SDSS J1131+2623	265 ± 87	158 ± 18	356 ± 36	301 ± 15	509 ± 11	73140 ± 53	73075 ± 67
PKS 1217+023	297 ± 61	213 ± 7	...	213 ± 6	501 ± 17	72044 ± 31	71979 ± 30
3C 273	1083 ± 251	...	477 ± 13	477 ± 13	1116 ± 33	47123 ± 35	47373 ± 25
SDSS J1230+1100	263 ± 60	140 ± 5	385 ± 24	248 ± 11	366 ± 12	70875 ± 42	70867 ± 35
HE 1228+0131	477 ± 124	277 ± 19	575 ± 51	526 ± 39	814 ± 25	35009 ± 51	35190 ± 24
SDSS J1230+6621	465 ± 100	134 ± 6	354 ± 7	242 ± 4	360 ± 11	55419 ± 41	55436 ± 20
PG 1427+480	252 ± 56	236 ± 11	...	236 ± 12	554 ± 24	66028 ± 37	66262 ± 98
SDSS J1444+0633	465 ± 100	134 ± 6	354 ± 7	242 ± 4	360 ± 11	55419 ± 41	55436 ± 20
HE 1453−0303	281 ± 75	205 ± 30	833 ± 33	770 ± 23	1205 ± 77	61574 ± 45	61613 ± 28
PKS 1545+21	320 ± 66	238 ± 6	...	238 ± 7	559 ± 14	79251 ± 31	79354 ± 37
PG 1612+261	3036 ± 627	138 ± 5	351 ± 3	223 ± 4	357 ± 12	39155 ± 40	39241 ± 27
SDSS J1655+2146	811 ± 171	169 ± 5	101 ± 12	208 ± 4	405 ± 11	45809 ± 42	45835 ± 25
PG 1700+518	158 ± 37	...	938 ± 29	938 ± 31	2209 ± 76	86131 ± 87	86524 ± 46
PG 2130+099	1002 ± 217	127 ± 15	315 ± 11	243 ± 9	393 ± 28	18835 ± 31	18589 ± 22
HE 2152−0936	139 ± 36	...	708 ± 85	708 ± 77	1667 ± 187	56976 ± 102	57625 ± 27
HE 2158−0107	295 ± 60	128 ± 11	...	128 ± 11	301 ± 28	63742 ± 30	63762 ± 36
HE 2158+0115	144 ± 30	213 ± 8	...	213 ± 8	500 ± 19	44055 ± 32	44119 ± 36
PG 2214+139	586 ± 131	113 ± 18	380 ± 14	321 ± 11	365 ± 29	19645 ± 32	19530 ± 38
HE 2307−0254	69 ± 17	...	756 ± 33	757 ± 35	1781 ± 87	65831 ± 80	66406 ± 47
PKS 2349−014	301 ± 68	158 ± 12	673 ± 43	483 ± 26	467 ± 21	52106 ± 33	52179 ± 37
HE 2353−0420	246 ± 50	199 ± 8	...	199 ± 6	467 ± 18	68383 ± 31	68446 ± 43
VIMOS observations							
HE 0952−1552	238 ± 6	382 ± 3	...	382 ± 4	899 ± 9	32357 ± 6	32378 ± 38
HE 1019−1414	382 ± 21	59 ± 9	403 ± 15	299 ± 6	328 ± 9	23175 ± 8	23110 ± 14
HE 1029−1401	1014 ± 141	182 ± 24	415 ± 47	1456 ± 893	446 ± 58	25596 ± 15	25663 ± 135
HE 1043−1346	69 ± 6	109 ± 8	186 ± 21	199 ± 10	399 ± 26	20475 ± 12	20525 ± 29
HE 1110−1910	222 ± 5	141 ± 5	460 ± 6	418 ± 4	617 ± 10	33400 ± 6	33365 ± 23
HE 1201−2409	52 ± 4	53 ± 12	256 ± 20	243 ± 17	447 ± 23	40996 ± 12	40883 ± 72
HE 1228−1637	113 ± 4	109 ± 5	224 ± 5	223 ± 3	525 ± 7	30860 ± 8	30791 ± 13
HE 1237−2252	191 ± 8	98 ± 3	201 ± 6	176 ± 3	304 ± 4	28936 ± 6	28991 ± 13
HE 1239−2426	52 ± 5	180 ± 21	...	180 ± 21	423 ± 58	24580 ± 19	24556 ± 21
HE 1254−0934	753 ± 17	144 ± 2	462 ± 22	350 ± 15	396 ± 5	41771 ± 5	41805 ± 20
HE 1300−1325	438 ± 10	120 ± 2	283 ± 6	205 ± 3	327 ± 4	13964 ± 4	14055 ± 35
HE 1310−1051	1175 ± 72	72 ± 5	166 ± 5	134 ± 2	228 ± 6	10301 ± 4	10300 ± 9
HE 1315−1028	112 ± 4	115 ± 4	270 ± 4	239 ± 3	408 ± 6	29427 ± 5	29387 ± 781
HE 1335−0847	51 ± 5	68 ± 7	179 ± 30	154 ± 17	188 ± 12	24076 ± 7	24067 ± 12
HE 1338−1423	1570 ± 48	105 ± 3	262 ± 9	197 ± 4	303 ± 5	12415 ± 4	12417 ± 11
HE 1405−1545	26 ± 2	46 ± 6	...	46 ± 6	109 ± 15	58036 ± 8	57933 ± 95
HE 1416−1256	1030 ± 21	113 ± 3	445 ± 7	372 ± 5	376 ± 6	38645 ± 5	38605 ± 16
HE 1434−1600	247 ± 10	160 ± 9	438 ± 15	377 ± 9	553 ± 14	43350 ± 9	43372 ± 38

sample. This will mainly be done via an indirect comparison with the M_{BH} - σ_{g} relation. Spatially resolved kinematics and directly measured stellar velocity dispersions for a few QSOs allow us however to explore new aspects.

E.3.1. The M_{BH} - σ_{g} relation

In Fig. E.3 we compare M_{BH} with σ_g of the [O III] line width in the QSO spectra. Four different panels are shown for the combination of the two different M_{BH} estimates based either on the FWHM or line dispersion of Hβ and the two indicators for the [O III] line width, the FWHM of the full line or the line dispersion of the narrow line core. When we compare our results with those

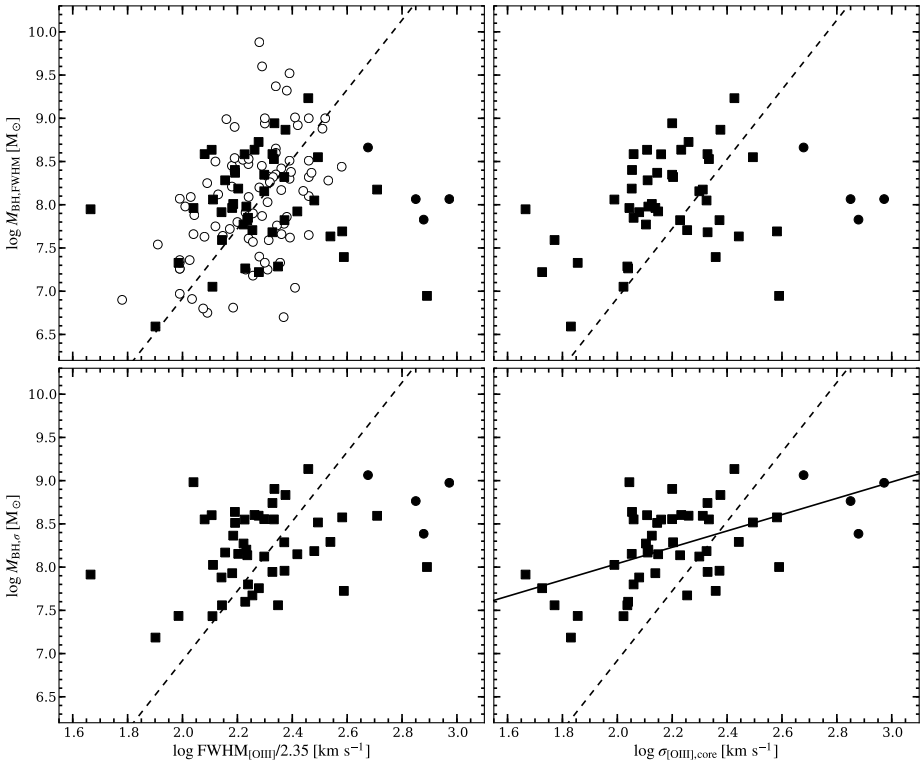

Fig. E.3. BH mass against the width of [O III] line as a proxy for σ_*. The FWHM of the broad Hβ line was used to compute M_{BH} for both upper panels following Eq. B.5, while $\sigma_{H\beta}$ was used for both bottom panels following Eq. B.4. In the left panels FWHM of the full [O III] line was taken as a proxy for σ_*, while the dispersion of the [O III] line core was used in the right panels. Objects for which the [O III] line was only modelled with a signal Gaussian are shown as round symbols. The M_{BH} - σ_* relation of Tremaine et al. (2002) is indicated by the black dashed line for comparison. The initial measurements by Shields et al. (2003) for their QSO sample restricted to $z < 1.0$ are shown as black open circles in the upper left panel. A linear fit to our data is indicated by the solid black line in the lower right panel.

presented by Shields et al. (2003), we find that both distributions are in good agreement with each other, except for 6 outliers with FWHM$_{[O\,III]} > 900\,km\,s^{-1}$, and scatter around the $M_{BH} - \sigma_*$ relation of Tremaine et al. (2002),

$$\log\left(\frac{M_{BH}}{M_\odot}\right) = 8.13 + 4.02\left(\frac{\sigma_*}{200\,km\,s^{-1}}\right) \quad . \tag{E.2}$$

The properties of the outliers are similar to narrow-line Seyfert 1 (NLS1) galaxies characterised by FWHM$_{H\beta} < 2000\,km\,s^{-1}$ and strong Fe II emission. This type of QSOs was missing in the compilation of Shields et al. (2003), because the [O III] line width were not measured for the objects at that time.

After excluding those 6 outliers, we performed a 2D Kolomogorov-Smirnov test (Fasano & Franceschini 1987; Press et al. 1992) on our data set and the sample of Shields et al. (2003). The probability that the difference between the two samples originate from random variations is only 0.45. Thus, the two samples are consistent with being drawn from the same parent population. However, the Spearman rank correlation coefficient for the entire sample is only $\varrho = 0.09$ with a probability for no correlation of $P = 0.51$. Even when we deblend the [O III] line into two components, a narrow core and a broad blue-shifted wing, using a double Gaussian model as recommended by Komossa & Xu (2007), the correlation coefficient increases only mildly ($\varrho = 0.29, P = 0.04$). One potential problem is that we are not able to deblend the [O III] line into two components for all objects, in particular the weak and broad [O III] lines of the NLS1 type objects. Komossa & Xu (2007) found that the [O III] emission lines were blueshifted in the NLS1 objects by more than 75 km/s with respect to [S II]. They argued that the gas kinematics recovered by the [O III] line are rather dominated by outflows than virial motions to reject those objects from the relation. Given that the rejection of objects based on this criterion is somewhat arbitrary and not possible without a detection of [S II], the general use of the [O III] line width as a surrogate for σ_* comes into question.

When we compare the [O III] line width with $M_{BH,\sigma}$, the result do change significantly. It can be seen from Fig. E.3 that the majority of objects would then clearly move *above* the reference $M_{BH} - \sigma_*$ for $\sigma_{[OIII],core}$ and that the extreme outliers move significantly towards the relation. The Spearman rank correlation coefficient in that case is $\varrho = 0.53$ with $P = 10^{-4}$. The relation implied by our data without rejecting any object is shown in Fig. E.3 and has the form of

$$\log\left(\frac{M_{BH,\sigma}}{M_\odot}\right) = 6.15 + 0.94\log\left(\frac{\sigma_{[OIII],core}}{km\,s^{-1}}\right) \quad , \tag{E.3}$$

which is much flatter than the $M_{BH} - \sigma_*$ of Tremaine et al. (2002).

With this analysis we want to emphasise that the relation between σ_* and σ_g is certainly more complex than previously thought. Whether both are causally correlated and not only by chance is not clear from our sample. Whether AGN outflows are the prime process that affects the kinematics of the gas is unclear, but it will be difficult to objectively identify those object anyway to use σ_g completely unbiased as a tracer for σ_*.

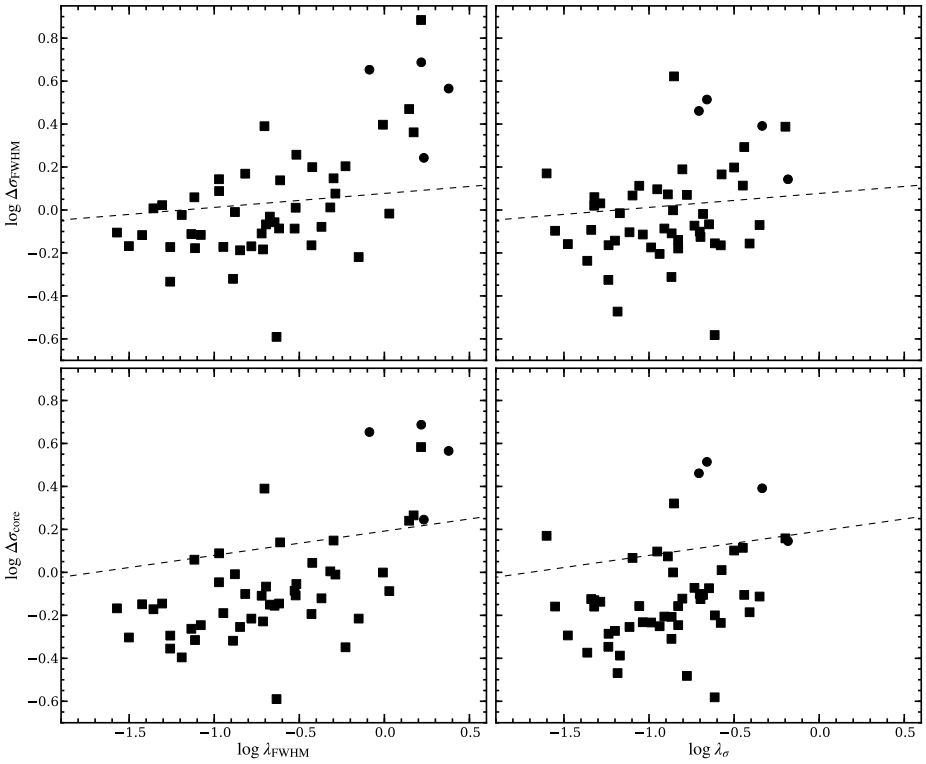

Fig. E.4. The ratio of the gaseous to excepted stellar velocity dispersion $\Delta\sigma = \log\sigma_g - \log\sigma_*$ against Eddington ratio λ. We estimated σ_* from the M_{BH} - σ_* relation of Tremaine et al. (2002), where M_{BH} was based on $FWHM_{H\beta}$ (left panels) or $\sigma_{H\beta}$ (right panels). σ_g was taken as the FWHM of the full [O III] line in the upper panels and as the dispersion of the [O III] line core in the lower panels. Objects for which the [O III] line could only be modelled with a single Gaussian are shown as round symbols. The black dashed line indicates the relation reported by Greene & Ho (2005) derived from SDSS for comparison.

E.3.2. The dependence on Eddington ratio

To test any dependence on the Eddington ratio we defined $\Delta\sigma_{core} = \log(\sigma_{[O\,III],core}) - \log(\sigma_*)$ and $\Delta\sigma_{FWHM} = \log(FWHM_{[O\,III]}/2.354) - \log(\sigma_*)$, where σ_* was estimated with Eq. E.2 for a given BH mass. In Fig. E.4 we compare $\Delta\sigma_{core}$ and $\Delta\sigma_{FWHM}$ with the Eddington ratios λ_σ and λ_{FWHM}, based on the FWHM and line dispersion of the broad Hβ line, respectively. We find that the distributions of $\Delta\sigma_{core}$ and $\Delta\sigma_{FWHM}$ appear to be bimodal in comparison with λ_{FWHM}. Objects with super-Eddington rates are separate from the bulk of the other objects scattering around $\Delta\sigma \sim 0$. However, this clear separation vanished for λ_σ.

Greene & Ho (2005) and Ho (2009) investigated how the ratio of the gaseous to the stellar velocity dispersion depend on λ for a large sample of obscured AGN. They reported significant positive correlations of the form

$$\Delta\sigma_{core} = (0.113 \pm 0.005)\log\lambda + (0.192 \pm 0.008) \quad , \tag{E.4}$$

and

$$\Delta\sigma_{FWHM} = (0.065 \pm 0.002)\log\lambda + (0.077 \pm 0.004) \quad . \tag{E.5}$$

They interpreted this trend as a signature for non-gravitational gas motions driven by the AGN.

Their relation for $\Delta\sigma_{FWHM}$ appears to be in good agreement with our measurement except for the super-Eddington objects, whereas their $\Delta\sigma_{core}$ relation is systematically higher than for our objects. The method of Greene & Ho (2005) to study the [O III] kinematics of type 2 AGN is however different from our approach. We estimated σ_* indirectly from M_{BH}, which we inferred directly from our QSO spectra as well as λ. Contrary, Greene & Ho (2005) measured σ_* directly from the stellar continuum as the central engine is obscured, but need to estimate M_{BH} with the scaling relation (Eq. E.2) as well as the λ using $L_{[O\,III]}$ as a proxy for L_{bol}. Both ways are certainly not optimal as they rely on secondary calibration which have a much higher uncertainty and possibly subject to unknown systematic effects. For example, it is obvious that the choice of the M_{BH} calibration has a systematic impact on the results.

E.3.3. Resolved gas kinematics and σ_* for bulge-dominated systems

So far, we only analysed and discussed the measurements from our QSO spectra which could also be done with a much larger sample of QSOs observed with SDSS. With the IFU observations we can provide additional information for some of our QSO hosts, either the spatially resolved gas kinematics, or even the stellar velocity dispersion determined with STARLIGHT from the stellar continuum for several objects in the VIMOS sample. Here we focus on morphologically classified bulge-dominated hosts as their kinematics should not be affected by a prominent stellar disc component and assumed as an isothermal sphere to first order.

In the left panel of Fig. E.5 we compare the velocity dispersion of the ionised gas on kpc scales ($\sigma_{g,extended}$) with the [O III] line dispersion in the QSO spectrum ($\sigma_{g,QSO}$) for all bulge-dominated host galaxies with EELRs. We already discussed the kinematics of the EELRs in Chapter 3 and in Appendix D, where we identified 5 bulge-dominated systems with *kinematically cold* extended gas discs contrary to our expectations of isothermal spheres. We find that $\sigma_{g,extended}$ is significantly lower than $\sigma_{g,QSO}$ for these objects, while the other bulge-dominated hosts display consistent extended and central velocity dispersions. This suggests that an

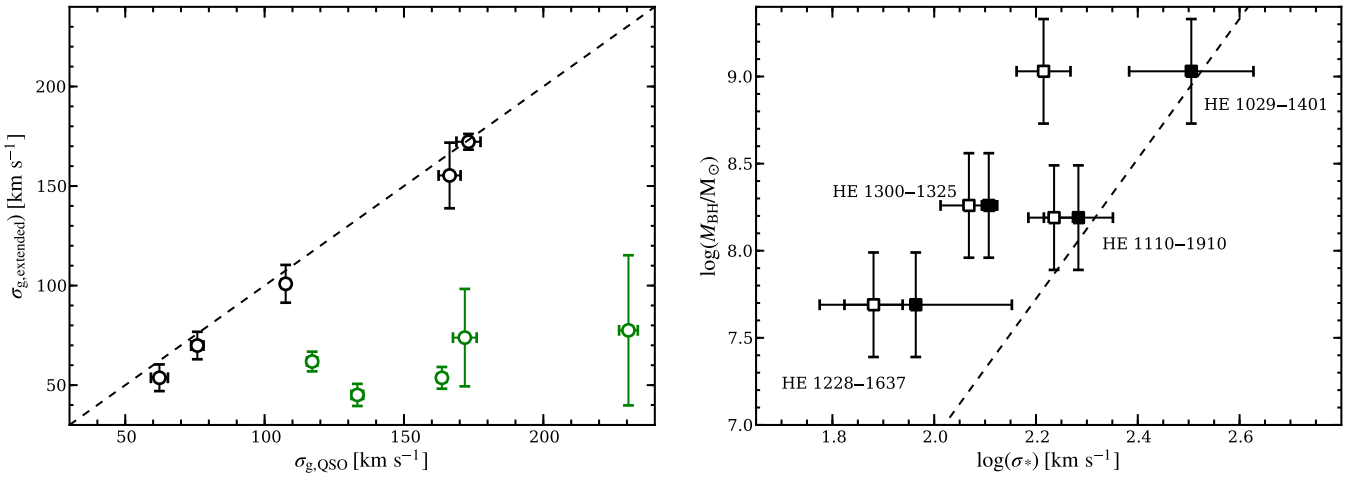

Fig. E.5. *Left panel:* Extended ionised gas velocity dispersion ($\sigma_{g,extended}$) against the [O III] core line dispersion of the QSO ($\sigma_{g,QSO}$) for morphologically bulge-dominated galaxies. Objects with a rotational-like pattern in the EELR velocity field are shown as green open symbols, while all other objects are denoted by the black open symbols. The dashed line indicates the one to one relation. *Right panel:* BH mass against the stellar velocity dispersion for the few bulge-dominated systems with σ_* measurements from the stellar continuum (filled symbols). For comparison we also plot the velocity dispersion of the nuclear [O III] line $\sigma_{g,QSO}$ for these objects (open symbols). The solid black line is the M_{BH} - σ_* relation of Tremaine et al. (2002) shown as a reference.

kinematically cold rotating gas disc in bulge-dominated systems may be decoupled from the gas kinematics in the bulge on scales of $\ll 1$ kpc. This is supported by the fact that $\Delta\sigma_{[O\,III]}$ is not significantly different for objects with or without a kinematically cold EELR.

Unfortunately, we could directly determine σ_* for only 4 bulge-dominated hosts, which are compared with M_{BH} in the right panel of Fig. E.5. We find that HE 1029−1401 and HE 1110−1910 are on the M_{BH} - σ_* relation within their errors, but σ_* of HE 1228−1637 and HE 1300−1325 is slightly smaller by 0.2 dex with respect to M_{BH}. Duet to the low number of objects and the intrinsic scatter in the M_{BH} - σ_* relation, this offset for two objects is not significant. On the other hand, $\sigma_{[O\,III],core}$ is systematically smaller than σ_* by about $\langle\Delta\sigma\rangle = -0.12$ dex in the mean. This is still much less than the discrepancy in the central and extended velocity dispersion found for those EELRs that are kinematically cold.

References

Aoki, K., Kawaguchi, T., & Ohta, K. 2005, ApJ, 618, 601
Boroson, T. 2005, AJ, 130, 381
Boroson, T. A. 2003, ApJ, 585, 647
Eracleous, M. & Halpern, J. P. 2004, ApJS, 150, 181
Fasano, G. & Franceschini, A. 1987, MNRAS, 225, 155
Greene, J. E. & Ho, L. C. 2005, ApJ, 627, 721
Heckman, T. M., Miley, G. K., van Breugel, W. J. M., & Butcher, H. R. 1981, ApJ, 247, 403
Ho, L. C. 2009, ApJ, 699, 638
Komossa, S. & Xu, D. 2007, ApJ, 667, L33
Letawe, G., Magain, P., Courbin, F., et al. 2007, MNRAS, 378, 83
Nelson, C. H. 2000, ApJ, 544, L91
Nelson, C. H. & Whittle, M. 1996, ApJ, 465, 96
Onken, C. A., Ferrarese, L., Merritt, D., et al. 2004, ApJ, 615, 645
Press, W. H., Teukolsky, S. A., Vetterling, W. T., & Flannery, B. P. 1992, Numerical recipes in C. The art of scientific computing (Cambridge: University Press, —c1992, 2nd ed.)
Shields, G. A., Gebhardt, K., Salviander, S., et al. 2003, ApJ, 583, 124
Tremaine, S., Gebhardt, K., Bender, R., et al. 2002, ApJ, 574, 740
Woo, J., Treu, T., Malkan, M. A., & Blandford, R. D. 2006, ApJ, 645, 900
Zamanov, R. & Marziani, P. 2002, ApJ, 571, L77

Appendix F

Systematic effects and detection limits recovered with simulations

ABSTRACT

For our analysis of the object HE 2158−0107 we had to compute several upper limits for emission lines and host magnitudes. Furthermore, we need to study the systematics of the QSO-host deblending process of broad-band images. Here we briefly present our adopted methodology and the corresponding results.

F.1. Systematics of the QSO-host decomposition for HE 2158−0107

The two-dimensional QSO-host decomposition is a complex process which is not free of systematic effects, especially in the high contrast regime. Here we present Monte Carlo simulation designed to investigate these systematic effects specifically for HE 2158−0107. We infer realistic errors for each band and obtain a robust upper limit for the host brightness in the H band. We created a suite of mock images for each band with a fixed QSO magnitude corresponding to the observation. The surface brightness (SFB) distribution of the underlying host galaxy was set to a de Vaucouleur law, the effective radii r_e were set to 0.″32, 0.″44, 0.″55, 0.″67 or 0.″79, and the host magnitudes varied within a reasonable range in steps of 0.3 mag. We produced 200 mock images for each set of parameters from the two-dimensional grid in parameter space. The host orientations and the axis ratios (b/a) we randomly chosen where b/a was restricted to a range of 0.5–1.0. The simulated images were convolved with the first of the available two PSF stars and the Gaussian noise pattern of the observed images was added before the images were analysed with `GALFIT` using the other PSF star.

The results of the Monte-Carlo simulations, shown in Fig. F.1, reveal that each band is subject to different systematic effects. Obviously, the r band is the deepest image of the four with the highest S/N introducing no discernable systematics. For the i band image, we found that r_e increases strongly with the nucleus-to-host ratio, so that the r_e was significantly overestimated. We think that this could be caused by an exceptionally strong PSF mismatch between the two PSFs for this band. The recovered r_e in the z and H bands displays only little variation with host magnitude, but appears to be slightly offset from the true input value.

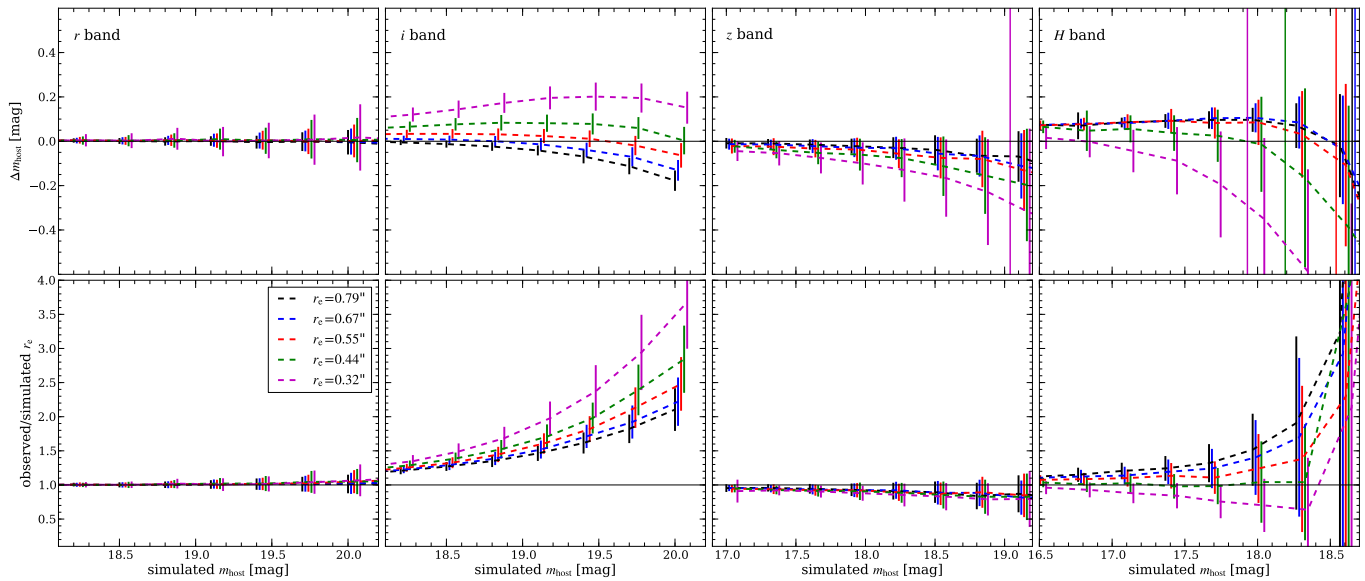

Fig. F.1. Results of Monte Carlo simulations to estimate the systematic uncertainties of the 2D decomposition with `GALFIT` for HE 2158−0107. The upper panels present the difference in simulated and observed host magnitudes (Δm_{host}) as a function of the simulated host magnitude for 5 different effective radii assuming a de Vaucouleurs surface brightness profile. Detection limits for the different effective radii are indicated by the solid vertical lines in their corresponding colour. The lower panels show the ratio of the observed over the simulated effective radii as a function of the simulated host brightness.

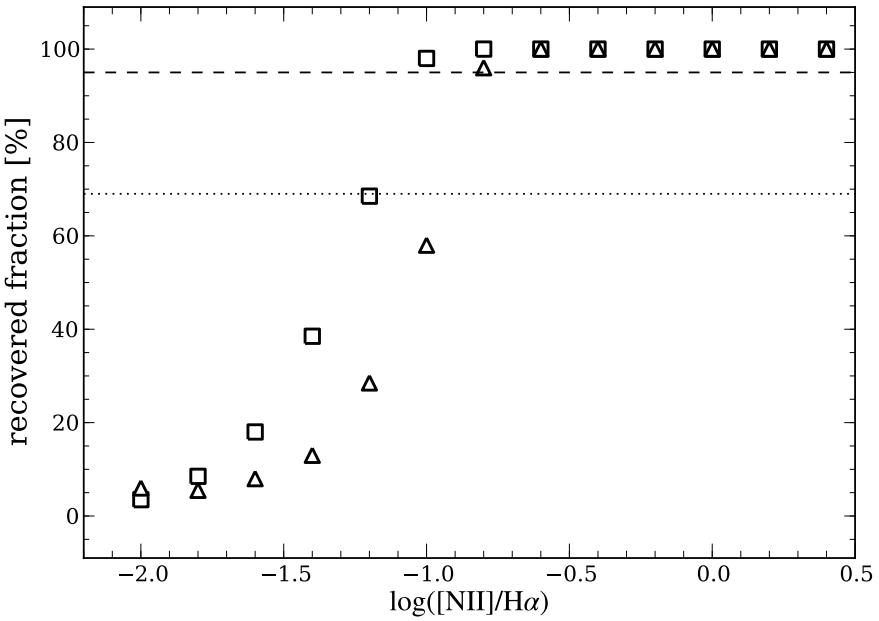

Fig. F.2. Fraction of 3σ [N II] detections among 200 simulated mock spectra as a function of simulated Hα/[N II] ratio. The open squares correspond to simulated QSO spectra and the open triangles correspond to simulated EELR spectra, respectively. The dashed and solid lines highlight the 95% and 68% confidence limits corresponding to a 3σ and 1σ detection limit, respectively.

The recovered host magnitudes can be systematically off by a large factor. Again the *i* band exhibits the strongest deviations from the input values. In all cases, except the *r* band, we found that $\Delta m_{\rm host}$ is decreasing with increasing host brightness, which corresponds to a flux transfer from the PSF to the host component. The systematic offsets and errors matched to the observed parameters of the host in the *r*, *i* and *z* bands are $\Delta m_{{\rm host},r} = 0.00 \pm 0.02$ mag, $\Delta m_{{\rm host},i} = 0.08 \pm 0.04$ mag and $\Delta m_{{\rm host},z} = -0.17 \pm 0.11$, respectively. The recovered host fluxes were in all bands significantly above the 3σ detection limit, except in the *H* band. The 3σ detection limit for the host in the this band depends critically on $r_{\rm e}$ and corresponds to $m_{{\rm host},H} > 18.19$ for $r_{\rm e} = 0\farcs44$.

F.2. Estimation of the [N II] detection limit in the spectra of HE 2158−0107

The [N II] $\lambda\lambda$6548, 6583 doublet could neither be detected in the QSO nor in the EELR spectra obtained for HE 2158−0107 with the PMAS spectrograph. Due to the diagnostic importance of this line we determined robust upper limits for those lines with the aid of dedicated Monte Carlo simulations.

Based on the best-fit Hα model for the QSO and EELR spectrum we generated mock spectra including narrow [N II] $\lambda\lambda$6548, 6583 lines, with the same profile and redshift as the narrow Hα line, within a certain range in Hα/[N II]λ6583 ratios (Hα/[N II] hereafter) . We further added realistic Gaussian noise to the spectra including night sky lines using the variance vector matched to the observed data. 200 mock spectra were generated for each Hα/[N II] ratio.

In order to test for each mock spectrum whether the [N II] lines could be recovered at a certain confidence level, we fitted the spectra with two different models, with and without the [N II] components. The [N II] lines actually add only one additional free parameter to the model, the [N II]λ6583 flux, as the [N II] λ6548/[N II] λ6583 flux ratio is fixed to 1/3 and the line width and redshift were both coupled to the narrow Hα component. We employed the statistical F-test to check whether the model including the [N II] is a significantly better model than the one without based on the χ^2 values for a given simulated spectrum at a 95% confidence level.

In Fig. F.2 we present the fraction of spectra for which the model including a [N II] component was significantly better representing the data as a function of the input Hα/[N II] line ratio. At high Hα/[N II] ratios, the [N II] is detected in 100% of the spectra. This fraction drops at a certain Hα/[N II] ratio below 95% or 69%, which we adopt as our 3σ and σ detection limits, and smoothly decreasing towards zero with decreasing Hα/[N II] ratio as expected. Our simulations imply a 3σ upper limit of Hα/[N II] < -0.8 for the EELR spectrum (Hα/[N II] < -0.8 1σ) and Hα/[N II] < -1.0 for the QSO spectrum (Hα/[N II] < -1.2 1σ), respectively.

Acknowledgements

I would like to take the opportunity to thank my supervisor Lutz Wisotzki for all his support and guidance over the last four years of my PhD time. All our discussions improved my understanding, helped me to develop new ideas and to find the essence of my work I need to concentrate on. He spent a lot of time to check my manuscripts carefully and provided reams of comments and corrections with his language skills, in particular in the last weeks where my concentration was severely hampered by the time pressure to finish this work. I just can say thanks!
Another important person has been Sebastian F. Sánchez. His knowledge about integral field spectroscopy was essential for me to be able to analyse these huge amount of data and to extract as much information from it as possible. I thank him and his family for their hospitality during several visits in Spain. I always felt like being part of his family even during times when he had to struggle with his own personal problems. He simply became a true friend for me. In the same line I thank Knud Jahnke for his thorough reading of my work and fruitful discussions as part of our successful collaboration. I am happy to continue working with all of you!
I thank all the people of our working group, Aldo Dall'Aglio, Asmus Böhm, Daria Dubinovska, Isabelle Gavignaud, Sebastian Kamann, Daniel Kupko, Natasha Maddox, Malte Schramm, Andreas Schulze, Christian Tapken and Jakob Walcher, who were always open for questions. All of them provided helpful comments and proofread parts of this thesis on short notice. In particular I have to set apart my office mates, Aldo, Sebastian, and Christian, who had to bear all my grumbling in times I hated astronomy. Many thanks go to Jakob Walcher, who finished my ESO proposal on the last day when I had to finish my PhD thesis in parallel.
Special thanks are reserved for my family and my girlfriend Anita Ludwig, who always provided a place for me to rest during the stressful time and were able to clear my mind. They have shown me what is really important in life.